Design and Development of Novel Electrochemical Biosensors Based on Metal and Metal Oxides Nano-composites

DOCTOR OF PHILOSOPHY

by

ASHUTOSH KUMAR

JAN 2020

Department of Biosciences and Bioengineering

Indian Institute of Technology Guwahati

Guwahati- 781039, INDIA

TH-2627_166106107

Design and Development of Novel Electrochemical Biosensors Based on Metal and Metal Oxides Nano-composites

A Thesis submitted in partial fulfillment of the requirements for the award of the degree of

DOCTOR OF PHILOSOPHY

by

ASHUTOSH KUMAR

JAN 2020

Department of Biosciences and Bioengineering

Indian Institute of Technology Guwahati

Guwahati- 781039, INDIA

TH-2627_166106107

Dedicated to my family

TH-2627_166106107

Ashutosh Kumar
Registration No. 166106107
Department of Biosciences and Bioengineering
Indian Institute of Technology Guwahati
Guwahati-781039, Assam, INDIA

Statement

I hereby declare that the matter embodied in this thesis is the result of investigations carried out by me at the Department of Biosciences and Bioengineering, Indian Institute of Technology Guwahati, Guwahati, India, under the supervision of **Dr. Pranjal Chandra.** This thesis has not been submitted to any university, institute or elsewhere for the award of the any degree, diploma or associate-ship.

Ashutosh Kumar

Date: 28/01/2020..... **Ashutosh Kumar**

Department of Biosciences and Bioengineering
Indian Institute of Technology Guwahati
Guwahati-781039, Assam, India

Certificate

It is to certify that the work described in the thesis entitled "**Design and Development of Novel Electrochemical Biosensors Based on Metal and Metal Oxides Nano-composites**" done by Mr. Ashutosh Kumar (Roll No - 166106107) for the award of the degree of doctor of philosophy is an authentic record of the results obtained from the research work carried out under my supervision in the Department of Biosciences and Bioengineering, Indian Institute of Technology, Guwahati-India.

The results embodied in this thesis have not been submitted to any other university or institute for the award of any degree.

Jan 2020

Dr. Pranjal Chandra

(Supervisor)

TH-2627_166106107

Acknowledgments

"All praise for the Almighty, the ultimate being."

By the abundant grace and blessings of God and His everlasting light of guidance, I was able to accomplish this work. As I reach another cornerstone in my academic career, I wish to express my eternal feelings to those whose active support and motivation made it possible to present my research work in the form of a dissertation. Finally, at the end of a seemingly endless journey towards producing this thesis, I would like to thank everyone, whose critics, comments, questions, support, and encouragement, personal as well as academic, have left a mark on this thesis work.

First of all, I would like to express my most profound sense of gratitude and special thanks to my supervisor ***Dr. Pranjal Chandra,*** *who believed in, encouraged and supported my efforts, and provided intellectual stimulation, continuing e exhilarating and sagacious guidance throughout the present study. His scholarly suggestions, prudent admonitions, immense interest, constant help, and affectionate behavior have been a beacon of light for me. His cordial behavior, humble attitude, generous mood, friendly nature, cooperativeness, and generosity are some of the exquisite traits, which I would certainly like to cherish and emulate.*

I am also thankful to my doctoral committee members, ***Dr. Manish Kumar, Dr. Narayanasamy Selvaraju****, and* ***Dr. Shankar Prasad Kanaujia****, for their timely and invaluable suggestions, which helped me to improve the work relating to the Ph.D. thesis. I owe my sincere gratitude to* ***Dr. Ananya Srivastava*** *from the National Institute of Pharmaceutical Education and Research Guwahati for her valuable suggestions and motivation, which helped me to improve the research work.*

I owe my thanks to ***Prof. Latha Rangan****, Head of the Department of Biosciences and Bioengineering, Indian Institute of Technology Guwahati, for providing me the necessary facilities*

TH-2627_166106107

to fulfill my Ph.D. thesis objectives. I am also thankful to ***Prof. Kannan Pakshirajan****, former Head of Department of Biosciences and Bioengineering, for his support and motivations. I am also thankful to all the faculty members of the Department of Biosciences and Bioengineering for their guidance and help. I am very much thankful to CIF IIT Guwahati for research facilities. I want to thank* ***Prof. M. Qureshi,*** *Head of the Central Instrumentation Facility, for providing me facilities to book high-end instruments. I am also thankful to Mr. Sujit Deb, Mr. Milan, Mr. Kishore, Mr. Bhasker and other staff of CIF, IIT Guwahati, for helping me to use CIF instruments. I want to thank the Ministry of Human Resource Development, India, and the Indian Institute of Technology Guwahati for providing financial assistance during my Ph.D. tenure.*

I am also thankful to office staff of BSBE, especially Mr. Dipangkar Sharma, Mrs. Prarthana Swaragini, Mr. Dipankar Barman, Mr. Chandan Kumar Nath, Mr. Niranjan Barah, Mr. Nurul Islam, and Mr. Binoy Das for providing me the necessary administrative and official paperwork helps. I also acknowledge the services rendered by Mr. Pankaj for providing ever-possible help.

It was a pleasure to work with my lab members Dr. Sharmili, Dr. Kuldeep, Budhhadev, Anupriya, Monalisha, Mastan, Silveri, Kruthi M, and Riddhipratim. Thanks to them for their suggestions, time, and help in experiments throughout my Ph.D. tenure. I am very much thankful to the Ph.D. friends of my department Pratap, Suvankar, Ratan, Vineet, Deepak, Adhiraj, Manish, Swati, and others providing a soothing and friendly environment during my Ph.D.

Words alone cannot express my gratitude, I owe to my friends, of other departments at IIT Guwahati; Juhi, Jaishree, Pilik Basumatary, Manvendra, Ankit, Vivek, Shubhangi, Rahul, Santosh, Toni, Dr. Ramakrishna Madaka, Dr. Asha Yadav, Dr. Venkanna Kanneboina, and others for providing a soothing environment and helping in the critical situations during my Ph.D., whenever I needed.

TH-2627_166106107

On completion of my thesis, I must acknowledge my childhood friends Mukesh Shukla, Abhishek Dubey, Sujit Tiwari, S.K. Jitendra, Navneet, Satyendra, Deepu, Ravi, and others for their love, encouragement, and support. They were the source of happiness in critical situations during my Ph.D.

I am also very much grateful to my college friends Vishal, Rahul Kumar, Rahul Ratn, Annadaa, Ashish, Abhinav Ashesh, DM Bage, NM Bage, Abhinav, Ashwini Tyagi, Pawan Prabhakar, Nitish, Liya, Sweta Prabha, Nisha, Hasnat, Ayan, Nikhil, Deepmala, Prerna, Astha, Jyoti, Divya, Priyanka Ganguly, Priya, Krishna, Gorav, Priyanka Rani, Pallavi, Vidya, Shweta, and Keshav for their overwhelming help, love, patience, support, and understanding throughout my studies.

Words fall short of expressing my appreciation for my sister and brother whose unconditional love have always cherished in hard times, I express my gratitude to my elder brother ***Dr. Alok K Pandey*** *and elder sister* ***Dr. Nivedita Priyadarshini*** *for their blessings, love, patience, support, and understanding throughout my studies. I am also very much thankful to my brother-in-law* ***Mr. Ravishankar Pandey*** *for his motivation and support during my Ph.D.*

I cannot get through without mentioning my family members and the almighty who installed in me courage, confidence, patience, and firm determination to fulfilling my dreams. With gratitude and reverence, I would like to admire my parents, ***Shri M. M Pandey*** *and* ***Smt. Usha Pandey****, who answered to all I needed, tolerated my idiosyncrasies, and boosted my morale for the successful completion of the project.*

Regret and regards to those who have been close enough to be mentioned but not included by name in this acknowledgment. I also expect their grant of forgiveness and acknowledge their help and support.

Date: …28/01/2020…

Ashutosh Kumar
Member at
Chandra's
Laboratory of Bio/physio Sensors
and Nanobioengineering

TH-2627_166106107

Abstract

Biosensors have found great attention because of their advantages over the traditional lab-based, time-taking, sophisticated diagnostic methods. In order to fabricate an efficient biosensor, there is a requirement of surface engineering at the transducer surface that ultimately play a significant role in attaining better sensitivity. The application of nanomaterials facilitates not only signal amplification but also provides stable immobilization of the bio-receptors, which ultimately aids in providing the sensitive determination of target analyte. In this research work, we have attempted to develop the sensor systems, which not just offer sensitive diagnoses, but it senses the analytes of industrial/clinical importance at significant levels. The nanomaterials were sequentially used to design four sensor systems (from simple to complex) to detect small molecules as well as complex cancer antigen. With the help of nanomaterials, we have tried to develop four sensors to detect food supplements, fatty liver disease, enzyme-free diabetes, and oral cancer.

We have planned the research in four different segments, where in the first segment, we reported for the first time sinapic acid (SA) sensing based on nanocomposite comprising electrochemically tuned gold nanoparticles (EAuNPs) and solvothermally reduced graphene oxide (rGO). The synthesized EAuNPs, rGO, and EAuNPs-rGO nanocomposite were characterized using X-ray diffraction (XRD), transmission electron microscopy (TEM), selected area electron diffraction (SAED), particle size analysis, and Raman spectroscopy. A proof-of-concept electrochemical sensor for SA was developed based on synthesized EAuNPs-rGO nanocomposite, which was characterized by electrochemical techniques such as cyclic voltammetry (CV) and electrochemical impedance spectroscopy (EIS). The developed sensor detected SA with a linear dynamic range (LDR) between 20 µM and 200 µM and detection limit (DL) of 33.43 (±0.21) nM

TH-2627_166106107

(RSD<3.32%). To show the useful purpose of the sensor probe in clinical applications, SA was detected in human urine samples, which showed the percentage recovery between 82.8% and 93.34%. Interferences due to various molecules such as L-cystine, glycine, alanine, serum albumin, uric acid, citric acid, ascorbic acid, and urea were tested. The long-term stability of the sensor probe was examined, which was found to be stable for up to 6 weeks. The sensor fabricated using EAuNPs-rGO nanocomposite has many attractive features such as; simplicity, rapidity, and label-free detection, hence it could be a method of choice for SA detection in diverse matrices.

In the next section, we have attempted to enhance the analytical capabilities of the sensor using bimetallic nanoparticles. For that, we have tried for the first time a microwave-assisted, one-pot, direct, and facile synthesis of monodispersed iron - gold bimetallic nanoparticles (BNP_{Au-Fe}) using glucose as a reducing agent in merely 90 s. The as such synthesized BNP_{Au-Fe} were thoroughly characterized using UV-Vis, XRD, TEM, EDX, elemental mapping, and Raman spectroscopy. These BNP_{Au-Fe} were further impregnated with rGO and coated onto glassy carbon electrode (GCE) to develop a sensor probe for label-free electrochemical detection of acetaminophen, which is considered to be a most potent biomarker related to non-alcoholic fatty liver disease. With the help of CV and EIS, the sensor probe was systematically characterized. The BNP_{Au-Fe}-rGO nanocomposite matrix showed the sensing of acetaminophen with a wide dynamic range between 50 and 800 nM with a detection limit (DL) of 0.14 nM (±0.05) nM (RSD< 4.12%) that was lower compared to previously reported acetaminophen sensors. In order to show the practical application of the sensor probe, acetaminophen was detected in human urine samples, which showed the percentage recovery between 86.65% and 91.32%. To the best of our knowledge, this is the first report where BNP_{Au-Fe} impregnated rGO was used to detect acetaminophen. Interferences due to various molecules such as glucose, serum

TH-2627_166106107

albumin, glycine, glutamic acid, alanine, citric acid, and ascorbic acid were tested individually and in a mixed sample. The long-term stability of the sensor probe was examined, which was found to be stable for up to 12 weeks.

We have replaced the gold from our bimetallic system and designed a new material using gadolinium and iron, which was tested for electro-catalysis of glucose. We tried here one pot, ultrafast, and facile synthesis of monodispersed gadolinium iron oxide (GdFe oxide) nanoparticles using a household microwave oven that was physically characterized using UV-Vis, XRD, TEM, EDX, STEM, and Fourier transform infrared spectroscopy (FTIR) spectroscopy. The GdFe oxide nanomaterial was doped with nafion to form a nanocomposite, which was characterized by electrochemical techniques and tested for proof-of-concept non-enzymatic glucose electrochemical sensor. Unlike other non-enzymatic glucose sensors, the GdFe oxide doped nafion nanocomposite did not require any mediator for sensing and required very low potential to detect glucose. It showed the sensing of glucose with a wide LDR of 66-350 mg/dL and LOD of 9.59 (±0.05) mg/dL (RSD< 4%) that was lower compared to previously reported glucose sensors. Moreover, the sensor was capable of detecting the glucose in blood, and results were comparable to the classical hexokinase method of glucose determination. To the best of our knowledge, this is the first report where GdFe oxide nanoparticles doped nafion was used to detect glucose non-enzymatically. Selectivity was determined with possible interfering agents and the sensor was able to sense the glucose upto 12 weeks. The sensor system fabricated has many outstanding features such as; simplicity, rapidity, label-free and low-cost detection, hence it could be a method of choice for glucose detection in POC detection tools.

In the complex matrices *viz.* urine, blood, serum, *in-vitro*, *ex-vivo*, and *in-vivo* samples, interference and fouling of electrodes are the major concerns. Because of this,

TH-2627_166106107

we have designed a self-signal generating oral cancer biosensor using gadolinium hexacyanoferrate (GdHCF) nanoparticles. In this work, we have employed AuNPs for signal enhancement followed by electrochemically active GdHCF layer. A layer of graphene oxide was used over this to generate a film having functional groups, which was eventually utilized for antibodies immobilization specific to oral cancer. The immunosensor probe was fabricated by covalent coupling of COO^- present in GO with the NH_2 group of antibodies using EDC-NHS chemistry. The fabrication of the sensor probe was confirmed using FTIR, CV, and EIS. The analytical performance of the developed sensor was obtained by recording the differential pulse voltammetry (DPV) responses. To the best of our knowledge, this is the first-ever report where AuNPs, GdHCF, and GO-based electrochemically active label-free immunosensor has been developed and utilized for highly sensitive diagnosis of oral cancer through detecting CYFRA-21-1 directly in human saliva samples. It showed the sensing of glucose with a wide LDR from 02-50 ng/mL of CYFRA-21-1 and LOD of 0.6 ng/mL (±0.012) ((RSD< 4.1%, 95 % confidence level, n=3) that was lower compared to previously reported sensors. Interferences due to various molecules such as glucose, serum albumin, glycine, glutamic acid, alanine, citric acid, and ascorbic acid were studied. The long-term stability of the sensor probe was examined, which was found to be stable for up to 10 weeks.

Thus, this work explores the role of nanomaterials in the design and development of sensitive as well as selective electrochemical biosensing approaches. In the future, these proof-of-concepts models may lead to the commercially acclaimed prototypes for onsite detection in various matrices.

TH-2627_166106107

Contents

TH-2627_166106107

TH-2627_166106107

TH-2627_166106107

TH-2627_166106107

List of figures

TH-2627_166106107

TH-2627_166106107

TH-2627_166106107

List of tables

TH-2627_166106107

Chapter – I

Introduction

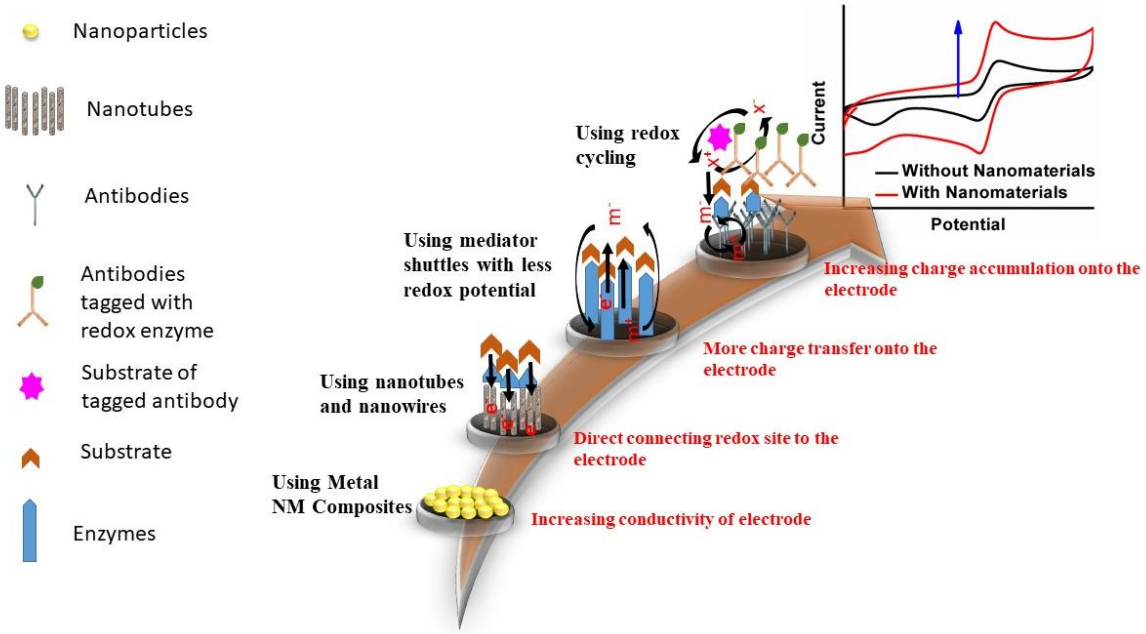

Status:

Part-wise published in

1. *Electroanalysis, Willy, 2019*
2. *MSET, Elsevier, 2018*
3. *RSC, Immunosensors, 2019*

TH-2627_166106107

1. The need for miniaturized diagnostic devices

Amongst numerous, worldwide problems in health management (individual and public), the timely diagnoses of disease are significant cutthroat control to uphold society's well-being. (Snyderman 2012) Detection of pathogenic and lethal components, pollutants, and metabolic intermediates plays a crucial role in contending the disease anticipations. (Fischbach and Dunning 2009) Moreover, the current paradigm of such investigations has been shifted towards the assessment of relevant molecules at a specific stage, where the disease indicators/ biomarkers initiate to appear at the minute level. Hence, there is a severe requirement of simple, operative, cheap, and quantifiable detection apparatus to sanction the rapid accurate diagnosis to check foreign entities or the relevant biomarkers inside the living body even in minute concentrations. (Thévenot et al. 2001) Moreover, it is very important to develop efficient miniaturized diagnostic devices that can perform biomolecular analyses in remote areas with low sample volumes and having the ability to be operated by untrained personnel even in emergency conditions. In view of this, biosensors provide new hope for the design and development of modern diagnostic devices.

2. Introduction to biosensors

In last few decades, the development of interdisciplinary study paved the various methods for diagnosing the diseases. In this perspective, a cheap, rapid, robust, sensitive, and selective diagnostic approach was acquired and developed as a modern biosensor. In simple words, a biosensor is an analytical tool that utilizes several bio-chemical reactions assisted by enzymes, antibodies, cell-organelles, and proteins to sense and transmit the physiological variations in the form of measurable electrical/optical/thermal signals. (Turner et al. 1987) Its key constituents encompass bio-receptor element, transducer, amplifier, and signal processor with output display in broad-spectrum. (Cooper and Cass 2004; Cosnier 2015; Mehrotra 2016) The

TH-2627_166106107

detection mechanism includes the procedure where analyte approaches are in contact with the bio-receptor component. A stimulus is produced, and the transducer converts it into a decipherable output signal, which is further enhanced by the amplifier and processor in the form of an output signal. (Mahato et al. 2018d). With the discovery of antibodies by Paul Ehrlich provided new hope in the development of several new biosensing techniques, which can detect diseases accurately and promptly. (JEAN 2006) Among them, immunoassay has been widely appreciated for its possibilities in medical diagnostics. In an unsophisticated way, an immunoassay can be described as a method that uses antibodies to discover a specific analyte by generating a signal either qualitative or quantitative or both, typically in a mixture of the sample. (O's ullivan et al. 1979) Identifying molecular entities in bio-analytical immunoassays is mainly based on the affinity interactions between antigen and antibody. In addition, the implementation of advanced analytical techniques, along with the recent interdisciplinary research, has shaped these immunoassays into strong, quick, and competent substitutes, which imply the improved sensitivity, selectivity, and precision. The fundamentals of modern biosensors' design and development, specifically the immunosensors, have been taken from these immunoassays. The foremost benefits of biosensors that make them superseding over lab-based detection methods such as requirement of slight sample, rapid and onsite detection, robustness etc., On the basis of bioreceptors and transducers present onto the sensing surface biosensor can be categorized into following types.

TH-2627_166106107

3. Types of biosensors

3.1. On the basis of bioreceptors

Biosensors are mainly categorized into two types based on their bioreceptors

3.1.1. *Affinity-based biosensors:* The biosensor has a bioreceptor specific for its analyte, which catches the analyte molecule present in the clinical samples. Biosensors having antibodies, avidin-biotin, and aptamer-ligand-based bioreceptors are mainly known as affinity-based biosensors.

3.1.2. *Bio-catalytic biosensors:* The biosensors have a bioreceptor that catalyzes the analyte and generates electrons into the sensing matrix. Ultimately, these electrons are being captured with the help of the sensing matrix, and the presence of analyte is confirmed. Enzyme based biosensors and non-enzymatic NMs/composite (Enzyme-mimicking) based catalytic biosensors are known as bio-catalytic biosensors.

3.2. On the basis of transducers

3.2.1. Transduction mechanisms

Generally, in a sensor, the biochemical reactions are converted into a quantifiable electrical signal with the help of a transducer. Based on transducer forms, the sensing mechanism has been classified under the categories of electrochemical, optical, and mechanical types (Mahato et al. 2018c, d). NMs seemed attuned with nearly all transducing mechanisms appropriate for almost every type of sensor. The scientific characteristics of the mostly utilized transducers are explained in the subdivisions below, with an emphasis on the engaged NM.

TH-2627_166106107

3.2.2. Optical transducers

The working principle of optical transducers is based on the variations in optical properties. At the time of antigen binding onto the sensing matrix, the changes occur in phase, polarity, wavelength of input light in reaction to physical or chemical reactions occurring at the sensing probe are measured, and the optical transducer converts it into decipherable signals. These biosensors can be categorized under subcategories of absorption, fluorescence, luminescence techniques based on the optical phenomena associated with signal transduction.(Ligler and Taitt 2002, 2011; Špačková et al. 2016) The biosensors based on the method of absorption and fluorescence are amongst utmost applied for sensing several medically significant biomarkers. In short, the sensing matrix absorbs a specific energy level of the electromagnetic spectrum in the absorption method when exposed to a range of electromagnetic wavelengths. In the existence of the target antigen and effective antigen-antibody immuno-complexation, the absorption shifts to either higher wavelengths or lower wavelengths that yields an output signal. The degree of peak shifts can be associated with respect to analytes concentration for quantification. The reason of the shift in interacting electromagnetic radiations during absorption studies can be caused because of complex structure formation due to antigen-antibody immuno-complexation, which is captivating more energy from the induced electromagnetic spectrum. In the condition where the induced electromagnetic radiations are of the visible region, the shift in wavelengths during immuno-complexation causes a change in visible frequency that can be seen by color change. An optical biosensor shows a change in color with existence of an analyte is known as colorimetric biosensors. The correlational equation for analyte measurement is based on Beer–Lambert's law Eq (1).

TH-2627_166106107

$$\log \frac{I_0}{I} = \varepsilon C \Delta x, \quad (1)$$

*Where "**I**" is representing the final intensity of light; "**I_o**" is showing the incidence intensity of the light; "**ε**" is showing the molar coefficient of the medium; "**C**" is showing the concentration of the analyte, and "**Δx**" is showing the change in path length.*

Fluorescence based detection is another method of optical biosensing in which; the fluorescent properties of molecules are used for the sensing of target molecules. (Strianese et al. 2012) In fluorescent-based biosensors, the absorbed higher energy electromagnetic radiation fluoresce in lower energy electromagnetic radiations. According to Professor Aleksander Jabłoński this phenomenon is free from the absorbance maxima. Besides bio-imaging, numerous other fluorescence-based procedures have also been engaged for biosensing methodologies *viz.* fluorescence resonance energy transfer (FRET), fluorescence recovery after photobleaching (FRAP), *etc.*(Kuznetsova et al. 2006). The chief advantage of biosensors based on fluorescence phenomena is their better selectivity towards analyte since each molecule demonstrates its specific fingerprint spectrum.

Moreover, a number of surface plasmon resonance (SPR) based optical biosensors have also been reported. SPR is a characteristic property in which electrons of the conduction band of the metallic surface show resonating oscillations with respect to positive and negative permittivity when exposed to electromagnetic radiation of a particular wavelength (Homola et al. 1999; Nguyen et al. 2015; Oliverio et al. 2017). Nowadays, NM of several shapes and sizes have been described with adjustable SPR

TH-2627_166106107

properties (Haes and Van Duyne 2002; Hoa et al. 2007). This phenomenon has been utilized to fabricate several sensors, as the SPR of surface changes significantly with respect to selective binding of analyte molecule on sensing matrix (Tao et al. 2017).

3.2.3. Mechanical transducers

An alternative leading transducer type in biosensors is described as mechanical transducers, in which physico-mechanical properties of the sensing platform are exploited to sense the chemical or biological target molecules. Usually, there are three main categories of mechanical transducers, *viz*. surface acoustic wave, quartz crystal microbalance, and nanomechanical systems. (Hwang et al. 2009; Savaliya et al. 2015) Among all mechano-transducers, the nanomechanical arrangement is extensively acknowledged because of extraordinary sensitivity and ability to be miniaturized. The design consists of a cantilever, mechanical transducer, and the processor in these sensors where the signal is processed to acquire better results (Dagdeviren et al. 2016). Characteristic properties of the material, as well as the length of the cantilever, primarily influence the critical performance of these kinds of biosensing platforms. Micro-nano cantilevers-based probes are frequently utilized for biosensing.

Moreover, the mechanical sensors functioned under two fundamental means, which comprise the deflection (static) and resonance (dynamic) approach. The static approach depends on the change in curvature of cantilever because of the stress caused by the analyte receptor complex formation, while the dynamic approach of operation worked on the measurement of resonating frequency shift with respect to change in concentration. Mechanical transducers are constructed in such a way that it can provide response either because of displacement alteration or due to generation of piezoelectricity.(Tamayo et al. 2013) In displacement-based techniques, an optical

TH-2627_166106107

lever is extensively used, where the laser beam is reflected from the cantilever. Subsequently, the reflected beam is perceived by a photodetector sensitive towards the position of the obtained signal. The necessary procedures that are involved in mechanical sensors encompass the mass change, alteration of surface stress, change in young's modulus, and viscoelasticity after bio-molecular immobilization or coupling to the bio-receptor. All of the constraints together change the curving in a static approach and create an alteration in the resonance frequency of the dynamic approach.(Jain et al. 2012)

3.2.4. Electrochemical transducers

Biosensors constructed on electrochemical transduction mechanisms are acquiring escalating consideration because of their extraordinary sensitivity, good reproducibility, outstanding selectivity, and cost-effective operations. These are also very much compatible with modern micromachining technology, which helps design point-of-care devices for biomedical applications. With the expansion of nanotechnology, electrochemical transduction based biosensing not only opened the door to noteworthy sensitivity enhancement but also led in the direction of incorporating additional integral qualities, such as miniaturization of probe, compactness, and the enormous scope of reforms. Together with the bio-receptors (antibodies) and electrochemically active intermediaries, these tactics secure low LOD with relatively rapid responses. While direct electron transfer (DET) in modern biosensors can provide immediate indications in the course of immuno-complex creation, mediator-based sensing probes use signal-generating materials amalgamated into the immuno-complex while assembling the sensing probe. Later one provides sensitive and versatile detection (Liu et al. 2013; Bagbi et al. 2016; Sarkar et al. 2016; Solanki et al. 2017; Mahato et al. 2018a). Nowadays, biosensing

TH-2627_166106107

based on the electrochemical transduction mechanism has gained key expansion, and the use of NM in electrochemical methods has been increased. (Wang 2005a, b) The electrochemical biosensing mechanisms can be evaluated by various techniques, where the charge transfer or electron transport during the redox interaction is measured. These electrochemical methods are explained as follows:

3.2.4.1. Voltammetry/ Amperometry

Voltammetry is one of the widely used techniques in electrochemical methods, in which the generation of current with respect to changing/static potential(s) is measured. In the amperometry, the potential, which is applied through the working and counter electrodes that initialize' redox reactions reliant upon the reduction /oxidation potentials of the analytes. (Delahay and Mamantov 1955) The charge generated during the redox reaction is then transmitted to the electrochemical cell that ultimately produces an electric current. The basis of amperometric sensors on the above-mentioned technique is that the redox reaction generated electrical current is standardized with respect to changing concentrations of the target entities. Another specific amperometric technique, also known as voltammetry, is a potentio-dynamic procedure, in which the current response is quantified with respect to changing potentials. Depending upon the numerous means for potential variance, voltammetry can be applied in diverse procedures comprising cyclic, linear sweep, square wave, and differential pulse voltammetry. Cyclic voltammetry (CV) is the utmost exploited technique in between all other alternatives of the voltammetry and competent enough to give the data of electrochemical redox reactions and their reaction rates in the analyte solution.(Mirceski et al.; Nicholson 1965) These voltammetric techniques provide both qualitative as well as quantitative facts with outstanding accuracies (<1%), sensitivity and wide detection range. The amperometry method relies on the

TH-2627_166106107

current generation as a function of either time or potential applied through the electrodes that provide the assessment of different sensing properties such as response time, detection range, and sensitivity comparable to the other approaches of electrochemical sensing. Typically, amperometric sensors require very less amount of the target molecules; thus, essentially demands that analytes should be of either inherent or tagged with redox mediators. Additionally, the amperometric sensor assembly significantly effects the process of sensing, thus the design used for sensor fabrication decides stability. Moreover, environmental conditions such as pH, temperature and humidity also controls the different sensing parameters *viz*. sensitivity, detection limit, linear range, and limit of quantification etc. (Bandodkar and Wang 2014)

3.2.4.2. Potentiometry

Potentiometry is another well-known method, which is based on the measurement of working electrode charge potential in comparison to the reference electrode when there is no current flow in the electrochemical circuit. The method provides information is about redox reactions occurring inside the electrochemical cells. (Dryhurst 2012) In potentiometry, Nernst Eq (2) directs the mathematical modeling of the potential and the analyte concentration.

$$E_{cell} = E^{0}_{cell} - \frac{RT}{nF}\ln Q \qquad (2)$$

*In the equation, "E_{cell}" is potential of electrochemical cell with zero current; "E^{0}_{cell}" is potential constant of the electrochemical cell; "**R**" is gas constant; "**T**" is absolute temperature; "**n**" is number of electrons transferring through the system during redox*

TH-2627_166106107

*reaction; "**F**" is Faraday constant; and "**Q**" is the ratio of ion concentrations at reduced state and oxidized state.*

A number of potentiometric procedures have been designed to sense the target molecules comprising potentiometric titration, field-effect transistor working on pH variance, and light-addressable potentiometric sensor. (Owicki et al. 1994; Bratov et al. 2010)

3.2.4.3. Impedimetric/conductometry:

Impedimetry is another famous technique used frequently to assess biosensors' analytical performances by measuring the impedance in the electrochemical circuit. In an impedimetric sensor, the electrochemical cell impedance is computed between the working and auxiliary electrodes with the help of a reference electrode to an identified potential. The immobilization of insulating analytes over the conducting sensing electrode receptor surface hampers the charge movement, causing the charge transfer resistance inside the electrochemical circuit. Electrochemical impedance spectroscopy (EIS) is one of the most applied techniques amongst extensively used impedimetric methods for measuring various analytical parameters of numerous biosensors. (Arkan et al. 2015; Lien et al. 2015; Afkhami et al. 2017) Since the procedure needs no detection tags, it is frequently applied for label-free sensing, and the interaction of charge transfer is determined for a sinusoidal changing current. With variation in excitation frequency of sinusoidal potential, the complex impedances can be acquired for a wide range of frequencies. Impedance can be mathematically modeled with following Eq. (3)

$$Z(j\omega) = \frac{U(j\omega)}{I(j\omega)}\ ;\ \omega = 2\pi f \qquad (3)$$

TH-2627_166106107

*In the equation, "**Z**" is showing impedance; "**U**" is showing potential; "**I**" is representing current flows through the circuit; "**ω**" is showing angular frequency of sinusoidal potential and "**f**" is representing the frequency (Hz).*

In electrochemical biosensing, the impedance method has been very valuable for observing the changes during biophysical reactions, causing from numerous bio-recognition events over the surface of the biosensing electrode. (Johari-Ahar et al. 2015; Wang et al. 2015) The variation in the electrode's surface conduction can be quantified because of analyte immobilization and affinity binding reactions occurring on the sensor surface. (Choudhary et al. 2016) On the contrary, the conductometric methods of biosensing worked on the power of the ionic molecules present during analysis in electrochemical cells. Enzyme tagged antibodies mostly accompany the variety of these kinds of biosensors. The enzyme plays a key role in creating a charge transfer species during the enzymatic reaction by cleaving the electroactive agents and ultimately enhancing the signal after antigen-antibody reactions. (Zhang et al. 2016)

It can be seen that the role of various transducers is apparent in the designing of numerous sensors. Different types of transducers can be applied with the necessity of sensing probe. Figure 1.1 is showing the various type of transducers and their application in designing of biosensors.

TH-2627_166106107

Although, electrochemical transducers have notable advantages over other transducers such as ability to be miniaturized, remarkable detectability, requirement very less sample, ultra-fast detection, experimental simplicity, ability to be integrated with handheld devices, and supports precise quantification of analytes. However, there are some limitations with current electrochemical biosensors that needs to be addressed so that a better biosensor can be developed.

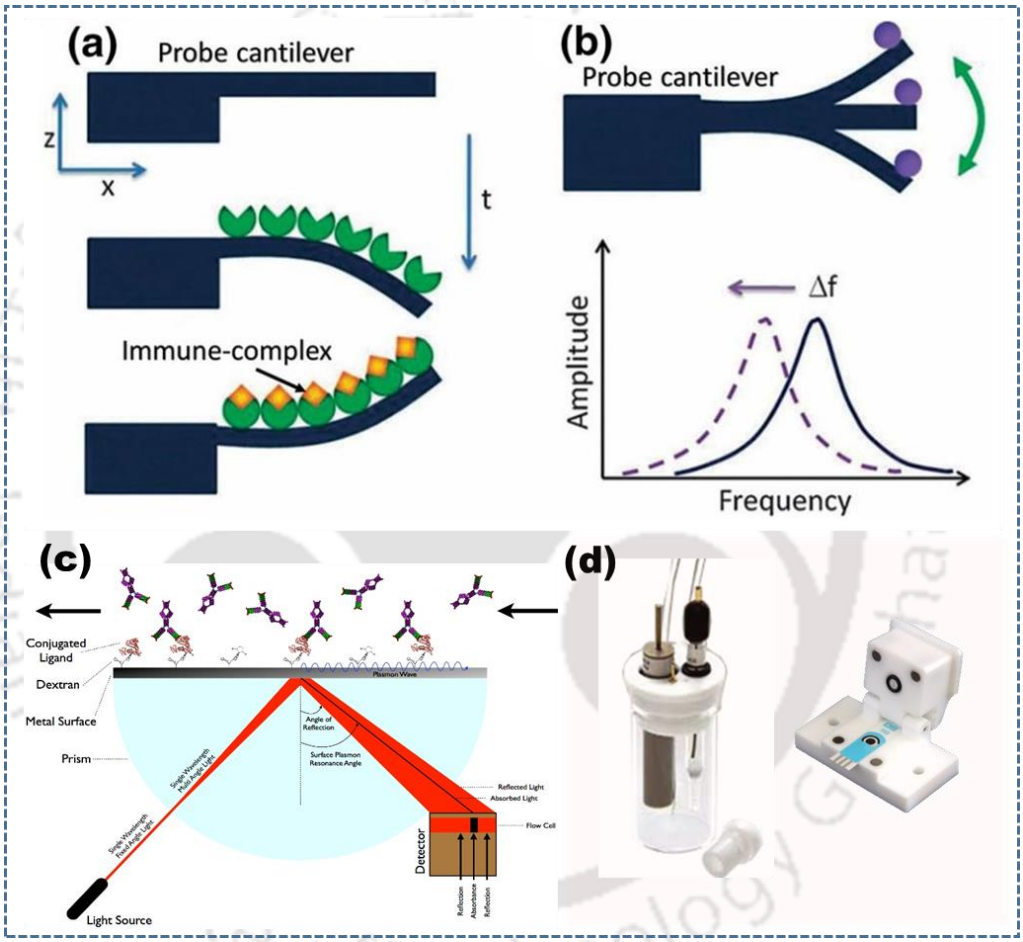

Figure 1.1. Type of transducers used in biosensor fabrication; mechanical transducer having cantilever (a) for stress measurement upon immune-complex formation, (b) for vibrational frequency measurement, (c) optical transducer, and (d) electrochemical transducer

The limitations that affect biosensors' performance are narrow detection range, prone to external environments (*viz.* pH, temperature, and humidity), requirement

TH-2627_166106107

of a more biocompatible material, and requirement of material that can enhance the signal of the biosensor (Signal amplifying material). To address these limitations, several works have been done towards the development of advance engineered nanomaterials (NM) and their composites, which offer high resolution by enhancing electron transfer between the bio-recognition matrix and electrode (Zhu et al. 2010) discussed as Signal amplification strategies (Kumar et al. 2019).

4. Nanomaterials

NMs are all that materials having size < 100nm or any material which is having at least one dimension in the nano level. NMs are a matter of interest now because of their special or unique optical, electrical, magnetic, and chemical properties. These different properties have the potential to have a great impact on the industries of electronics and biomedical fields. Applications of nanoparticles (NP) and their composites are paved new paths in interdisciplinary research, including the development of modern diagnostic tools and novel therapeutic agents. Over the last few decades, NM's amalgamation in interdisciplinary research diaspora has significantly affected possible biomedical applications, including bioimaging, biosensing, and targeted drug delivery. NMs are preferably suitable for drug-delivery as a carrier that may simplify the design and fabrication of a new generation of theranostic biosensors with intricate capabilities to sense chemical and biological molecules. Noteworthy developments have been achieved in synthesis approaches as a result of which it is conceivable to make a range of NM with a considerably manageable dimension (Noh et al. 2012b) shape, surface charge, and physicochemical properties (Wang 2005b, a). NM can be conjugated with conducting polymers and biologically active molecules (*e.g.*, antibodies, biopolymers, peptides, proteins, enzymes, *etc.*) to improve biocompatibility and

TH-2627_166106107

their performance (Baranwal and Chandra 2018). To accomplish accurate targeting, they are progressively engaged in the development of modern biosensors because of their unique electrocatalytic characteristics. NM functionalized with binder entities provide outstanding possibilities for bio-recognition events by transduction into an electrical signal, ultimately designing a new strategy for the fabrication of novel bio-electronic devices. Moreover, it has been perceived that chemical structure, active surface area, surface charge, quality of crystal structure, *etc.* are important factors of NM that cumulatively affect electron transfer at electrode/electrolyte interface (Jianrong et al. 2004; Vaddiraju et al. 2010). Applications of nanoparticles (NP) and their composites are paved new paths in interdisciplinary research, including the development of modern diagnostic tools and novel therapeutic agents. Over the last few decades, NM's amalgamation in interdisciplinary research diaspora has had a significant effect on possible biomedical applications, including bio-imaging, biosensing, and targeted drug delivery. NM is preferably suitable for drug-delivery as a carrier that may simplify the design and fabrication of a new generation of theranostic biosensors with intricate capabilities to sense chemical and biological molecules. Noteworthy developments have been achieved in synthesis approaches as a result of which it is conceivable to make a range of NM with a considerably manageable dimension (Noh et al. 2012b) shape, surface charge, and physicochemical properties (Wang 2005b, a). NM can be conjugated with conducting polymers and biologically active molecules (*e.g.*, antibodies, biopolymers, peptides, proteins, enzymes, *etc.*) to improve biocompatibility and their performance (Baranwal and Chandra 2018). To accomplish accurate targeting, they are progressively being engaged in development of modern biosensors because of their unique electrocatalytic

TH-2627_166106107

characteristics. NM functionalized with binder entities provide outstanding possibilities for bio-recognition events by transduction into an electrical signal, ultimately helping in designing a new strategy for the fabrication of novel bio-electronic devices. Moreover, it has been perceived that chemical structure, active surface area, surface charge, quality of crystal structure *etc.* are important factors of NM that cumulatively effect electron transfer at electrode/electrolyte interface (Jianrong et al. 2004; Vaddiraju et al. 2010). NMs are very much suitable for the development of biosensors as they can provide strong electrocatalytic activity, stability, and miniaturization capability to the sensors. Two significant benefits of NM are their capacity to be employed as noninvasive analytical devices and their ability to be utilized for a combination of multiple functional entities within a single particle (Karim et al. 2018). These properties facilitate far greater sensitivities to be attained, leading to additional transparency and firm understanding, particularly in *in-vitro*, *ex-vivo*, and *in-vivo* diagnostics (Prasad et al. 2016; Deka et al. 2018). The capacity to detect particular cell types or precise anatomical spots inside the human body may portend very sound because of the biosensors conjugated with NM (Noh et al. 2012a; Chandra et al. 2013, 2014; Akhtar et al. 2018). Agreed on their higher sensitivity, agility, and miniaturization, these nano biosensors could function as a novel archetype for medical and point-of-care (POC) analytical instruments (Akhtar et al. 2017). Based on the desired application in sensor, the different type of NMs are used while sensor designing, such as nanoparticles (metallic, metal oxide, polymeric, etc.), quantum dots, carbon based NMs (graphene, nanotubes (CNTs)), and nano-composites (figure 1.2).

To synthesize NMs for sensor fabrication, various synthesis procedure can be adopted. In general, there are two main methods for NMs synthesis; (1) bottom up

TH-2627_166106107

approach and (2) top down approach. In bottom up approach, the NMs are synthesized by self-assembly of atoms and molecules, ultimately leading to the formation of nanostructures, while in top down approach NMs are synthesized via cutting the bulk material into nano dimensional particles. Bottom up approach includes PVD, CVD, Sol-gel method, hydrothermal method, and microwave method etc while top down approach include ball milling, etching, grinding, etc.

4.1. Signal amplification using nanomaterials

The complementary combination of bio-recognition element and transducing surface of biosensor system decides the sensitivity of the designed biosensor but amalgamation of some signal amplification strategies is essential to magnify the output signal particularly when dealing with very small amount of the target analytes (Ding et al. 2013). It is very much desirable to get an enhanced signal that can improve not only the sensitivity of a sensor but also increase the dynamic range of sensing. Signal amplification in an electrochemical sensor can be accomplished by engineering the sensor surface in such a way that increases the conductivity of the electrode (Riepl et al. 1999). These surface modifications can be possible by application of NM while fabrication of sensing platform. Several NM, such as metal gold NP and platinum NP are competent enough to enhance the conductivity of electrode surface (Mahato et al. 2019). Another approach to get enhanced signal in biosensor can be obtained by increasing the charge transfer between sensing surface and electrode. Several NM such as carbon nanotubes, metal nano-rods, and nanowires act as connection between reaction sites and electrode, these not only increase the surface area of electrode but also provide direct connection of electrode with reaction site. Sometimes, NM catalyzes the redox reaction at electrode surface itself and thus facilitate in generation of more charge species. The catalytic activity,

TH-2627_166106107

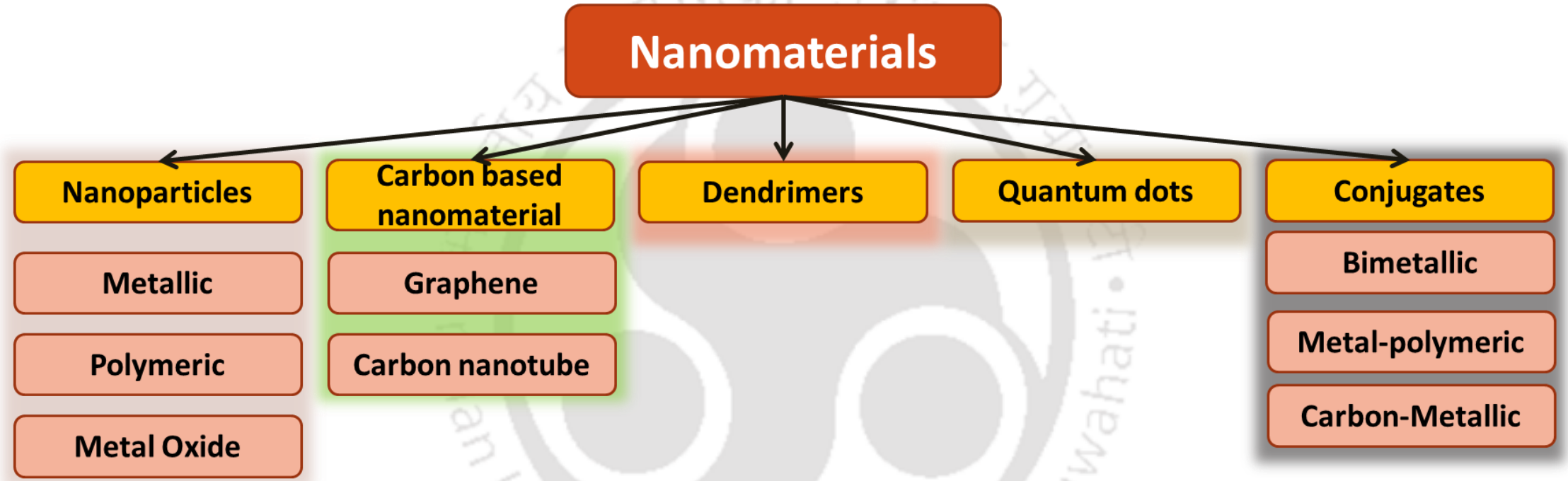

Figure 1.2. Types of nanomaterials

TH-2627_166106107

ultimately enhance the dynamic range of sensor system because of more charge transfer onto the sensing electrode.

Another way to get amplified signal in electrochemical sensor system can be attained by using a suitable mediator charge carrier. When the mediator molecule or the redox couple, used as shuttle molecule between reaction site and electrode, itself have lower redox potential. In other words, it has the capacity to be oxidized or reduced easily with requirement of less electrochemical potential; this can enhance the electrochemical response, as the signal can be captured in lower energy condition as well. Similar to this, sometimes two or more than two redox couples are used in electrochemical system to act synergistically, which ultimately increase the generation of charge species inside the electrochemical cell because of redox cycling (Das et al. 2007; Akanda et al. 2013; Liu et al. 2014; Park et al. 2014; Xia et al. 2015). Nowadays, redox cycling has fascinated many researchers across the globe as signal enhancing mechanism in electrochemical sensing (Liu et al. 2009). Sometimes, these surface modification leads to increase in the background current of the sensor system, which ultimately aids in the sensitivity improvement of the electrochemical sensors (Rajamani and Peter 2018). In these kind of surface modifications, researchers have used various nano-composites to enhance the charge transfer across the sensor surface. Since, LOD is inversely proportional to sensitivity of sensing probe; the background current enhancement can provide a better sensitivity and lower LOD to the sensor system (Lee et al. 2019).

Conclusively, signal enhancement in biosensor plays a crucial role to determine the presence of analyte where sensitivity is low and affinity of analyte towards bioreceptor is not adequate. A detailed description of signal enhancement strategies adopted in electrochemical sensors has been comprehensively described in figure

TH-2627_166106107

1.3. NM plays a critical role in getting the enhanced signal and application of NM onto the sensor surface require their functionalization that will not only establish the proper anchoring of bioreceptor onto the sensing platform but also provide biocompatibility and stability to the sensor system. In the upcoming section, we have discussed some widely used functionalization strategies of NM for sensitive detection of various molecules.

4.2. Functionalization of nanomaterials

The physical properties expressed by NP, *e.g.* color, surface plasmon resonance, electrical conductivity and binding affinity are considerably improved or altered when they are subjected to functionalization with appropriate metals, organic or bio-molecular functional groups (Zeng et al. 2011; Upadhyayula 2012). This step not only decides the functionality of NP used in the sensor system but also offers the option to design modern biosensors with smart and enhanced sensing capabilities. The shape, size, curvature, and structure of NM may influence the surface functionalization. To properly adapt and modify the exterior of NM, material scientist have formulated different approaches to incorporate the desired functionality onto the NM (Sapsford et al. 2013). General procedures that are routinely used for functionalization of NP as emphasized in figure 1.4. In figure 1.4 (i) electrostatic interaction by the use of a peptide has been shown. In this approach opposite charges on the NP surface and the peptide (biomolecule) are used to mediate charge-based NP-peptide assembly. In figure 1.4 (ii) direct interaction method has been shown, which is widely used for gold NP (AuNP) functionalization. In this approach, some peptide motifs can bind to or coordinate with the NP surface because of high affinity, for example, the binding of free thiols with the surface of AuNP. In figure 1.4 (iii) secondary interactions has been shown,

TH-2627_166106107

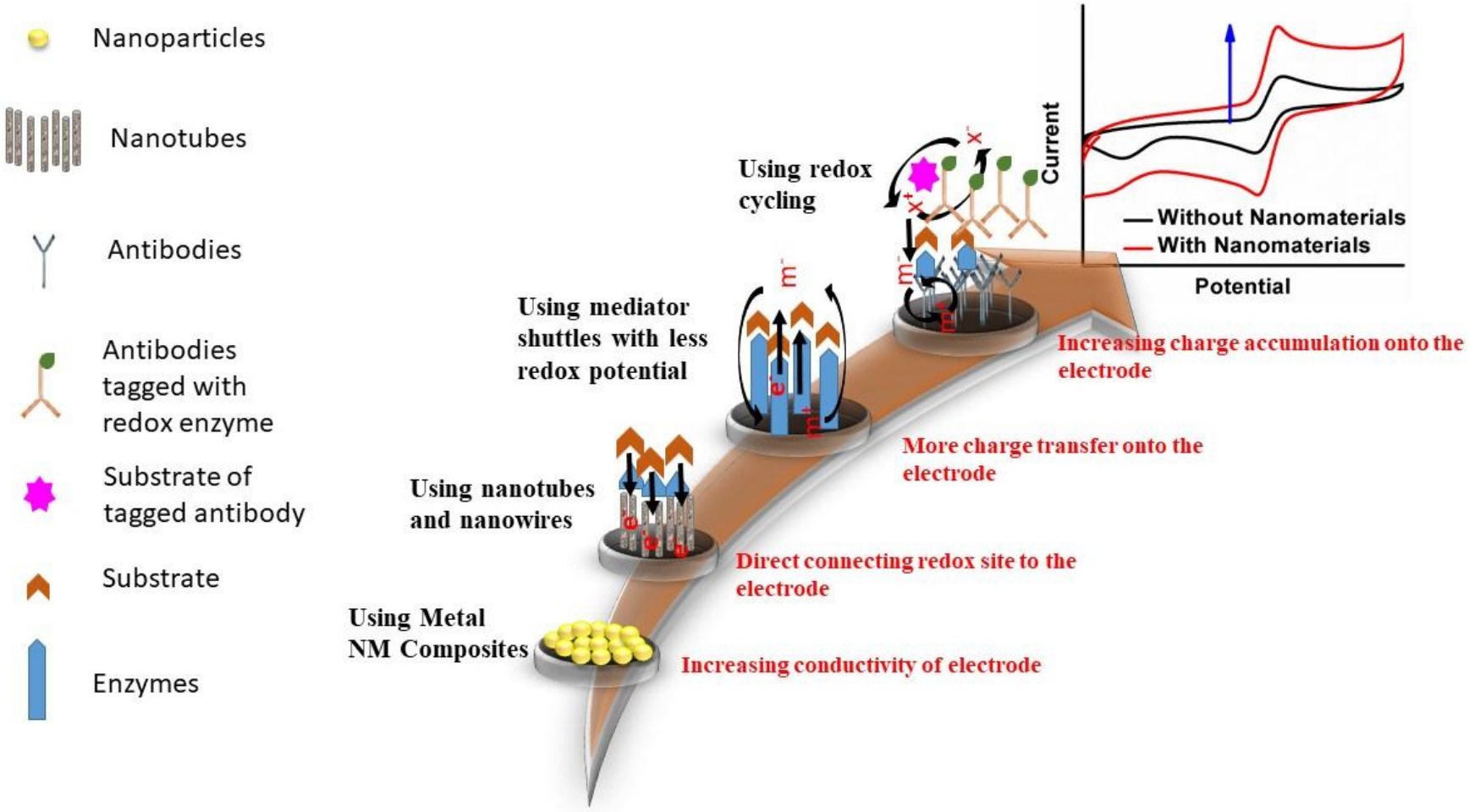

Figure 1.3: Signal enhancement strategies in electrochemical biosensors

this approach utilizes specific ligand–receptor interactions as demonstrated by biotin–streptavidin interactions. In figure 1.4 (iv) covalent chemical attachment method has been shown, it exploits the classical bio-conjugation chemistry such as EDC-based coupling of amines to carboxyl or NHS- and maleimide-mediated conjugation to amines and thiols. In figure 1.4 (v) encapsulation method has been elucidated, in this approach peptide may go inside the NP, which may happen during synthesis or after the NM is formed. Nowadays, NM have been extensively functionalized with a range of materials like as artificial polymers, biopolymers, dendrimers and small molecules using above mentioned functionalization strategies. Getting a particular functional group such as amine, carboxyl, thiol, and alcohol is very much important for anchoring enzymes and antibodies onto the NM, and the functionalizing agent determines it (Hao et al. 2010). To get amine group onto the NM, amine group containing compounds are used such as 3-Aminotriethoxy propyl silane (APTES), chitosan, serine etc. Similarly, to get carboxyl group, compound with carboxylic acid are used. To immobilize the antibodies for immunosensor fabrication it is very much important to determine the functionalizing compound as its structure may regulate the charge transfer across the electrode, which ultimately affect the signal amplification of the sensor. The immobilization of a biological component onto a matrix refers to restricting the gross movement of bio-receptor while keeping it in a relatively defined region resulting enhanced stability and reusability, which requires proper functionalization of sensing surface (Sapsford et al. 2013). In simple words, to exploit NM in biomedical applications, the outer surface of the NP needs to be functionalized appropriately to provide firmness, biocompatibility and functionality. In the upcoming section, we have explained some recent sensor fabrication with different

TH-2627_166106107

types of NM, using several functionalization steps to get an enhanced and better signal.

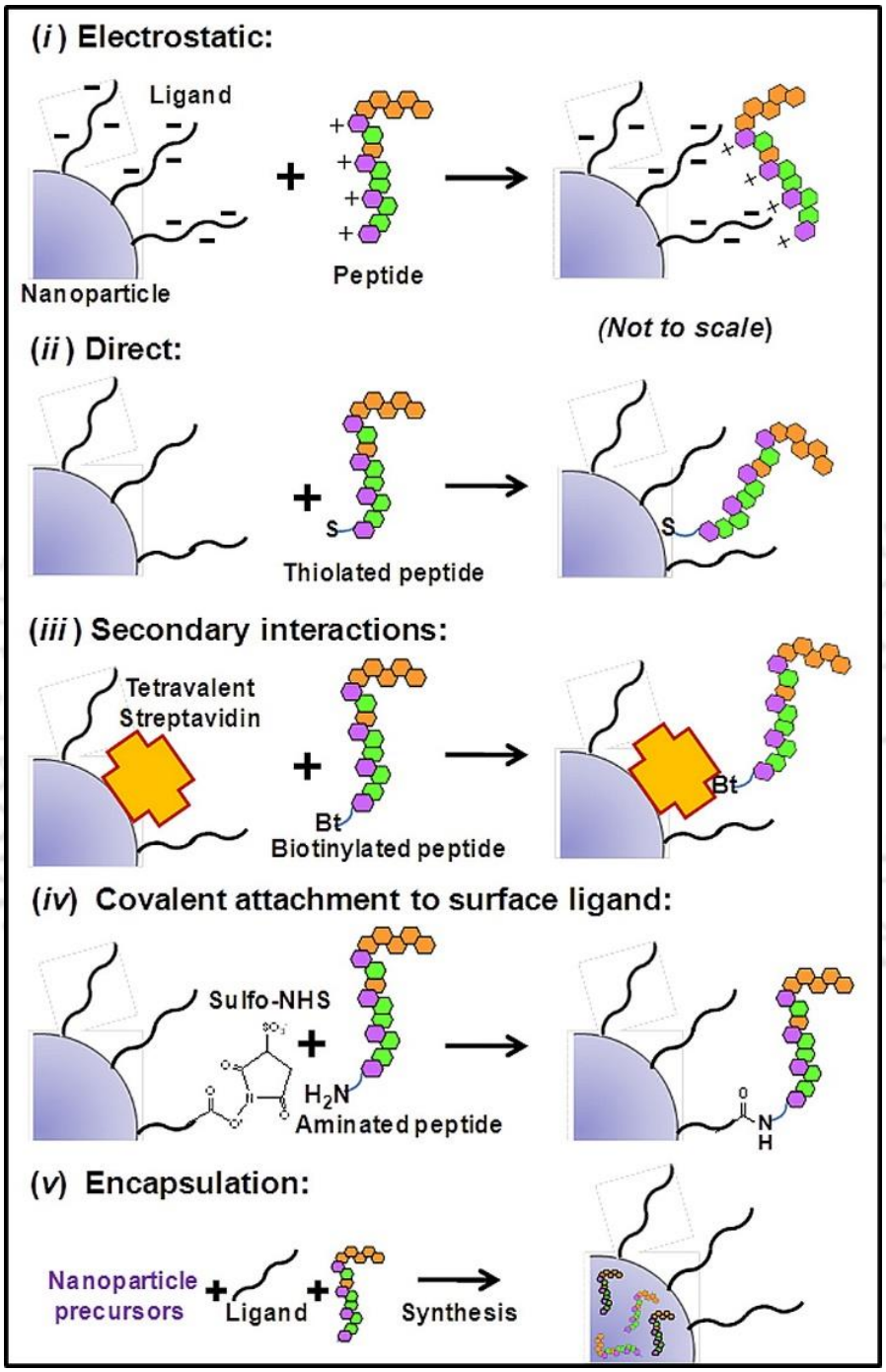

Figure 1.4: Functionalization methods (i) Electrostatic attachment, (ii) direct attachment, (iii) secondary interactions, (iv) covalent attachment, and (v) encapsulation.

TH-2627_166106107

4.3. Characterization and analytical techniques

The synthesized NMs and sensor surfaces are characterized for their physical and electrochemical properties using various characterization techniques. The NPs and nano-composites synthesized for the sensor fabrication are physically characterized with UV-Vis spectroscopy, XRD, TEM, EDX and elemental mapping, FTIR spectroscopy, and Raman spectroscopy (Ruiz-Hitzky et al. 2008).

4.3.1. UV-Vis spectroscopy:

In UV-Vis spectroscopy analysis, absorbance or reflectance are studied while illuminating the sample with UV and the adjacent visible spectrum (Ruiz-Hitzky et al. 2008). The absorption / reflectance in the visible range indicates the apparent color of the NPs. During UV-Vis analysis, the atoms and molecules present in the NPs experience electronic transitions from ground state to excited state. The resonance between the absorbance wavelength and electronic transitions occurring in the NMs leads to the characteristic surface plasmonic resonance (SPR) generation. The SPR generated by NMs can be studied with Beer–Lambert law; which states that with increase in the concentration of NMs, the absorbance intensity increases while keeping all other parameters constant.

4.3.2. X-ray diffraction study:

X-ray diffraction analysis is a tool to study the atomic and molecular structure of a crystal. In this a beam of X-ray applied on a material, diffract to many specific directions, by determining the intensity and diffraction angle, a 3-dimensional image of the atomic electron density inside the crystal can be obtained (Guinier 1994; Jenkins et al. 1996). From this, we can determine the mean atomic position inside the crystal as well as chemical bonds and various crystallographic disorders. In simple words, a non-destructive analytical method reveal facts about the crystal,

TH-2627_166106107

chemical composition, and physical properties of NMs and thin films. XRD helps in crystallite size and domain study of the NMs.

4.3.3. Transmission electron microscopy:

TEM is one of the main characterization techniques in the physical, chemical and biological sciences. It is a non-destructive advanced microscopy method in which an electron beam transmitted through the sample is used to form an image (Thomas et al. 2017). Usually, the TEM sample is an ultrathin slice having thickness less than 100 nm or a suspension on a copper grid. As the electron beam transmitted through the sample, an image is formed due to electron interactions with the specimen (Reimer 2013). The obtained image is magnified as well as focused onto imaging devices, like as a fluorescent screen, photographic film, or a scintillator attached to a charge-coupled device. TEM are able to capture the image at a significantly high resolution compare to light microscopes, due to the smaller de Broglie wavelength of electrons, which empowers the instrument to capture fine details even as small as a single stake of atoms (d fringes).

4.3.4. Energy dispersive x ray spectroscopy and elemental mapping:

EDX is a fundamental characterization technique used to determine elemental analysis / chemical composition of specimen. The principle behind EDX analysis relies on unique atomic structure of each element present in periodic table that ultimately lead to generation of unique set of peaks on its electromagnetic emission spectrum (Ruiz-Hitzky et al. 2008). To release a characteristic X-rays from the sample, a highly-energised beam of charged particles such as electrons / protons, or a high energy X-rays beam is focused onto the specimen. An electron from inner shell can be excited due to beam of high energy charged particles, which eventually eject it from the inner shell and generate a hole at the position of electron (Deepak

TH-2627_166106107

et al. 2015). To fill this place an electron from outer, higher-energy shell releases its energy in the form of discreate x-rays. It can be used to determine relative abundance elements present in the sample. With the help of EDX of a particular area, elemental mapping can be performed to determine the site-specific presence of particular element in the sample.

4.3.5. Fourier-transform infrared spectroscopy:

FTIR is an analytical technique used to acquire an absorption or emission infrared spectrum of solid/liquid/gas samples. In this method, FTIR spectrometer illuminate the sample with a beam comprising numerous frequencies of light at once and determines how much of that electromagnetic beam is absorbed by the specimen. Subsequently, the electromagnetic beam is altered to contain a different combination of frequencies, generating a second data point. This process is quickly repeated several times over a short duration. Next, in a computer all data is analysed using Fourier-transformation to conclude the absorption at each wavelength. The FTIR characterization study during sensor development not only helps in determination of functional groups presence onto the functionalized NMs but also confirms the attachment of bioreceptors onto the sensor surface (Nikolic 2011).

4.3.6. Raman spectroscopy:

Raman is an analytical technique, which is characteristically used to determine molecular vibrational frequencies present in the sample, though rotational as well as other low-frequency modes can also be detected. Raman spectroscopy depend on inelastic scattering of applied photon, recognized as Raman scattering (Kumar 2012). Usually, a monochromatic laser either visible or near infrared is used as source of light. The applied laser interacts with molecular vibrations as well as

TH-2627_166106107

phonons of the sample, that ultimately, results in the energy shift of the applied laser photons which provides the data about the vibrational frequencies of the system. Generally, Raman spectroscopy is applied in material science to determine a specific structural fingerprint by which molecules can be identified.

4.3.7. Electrochemical characterizations:

The electrochemical valuation of sensors is performed using traditional three electrode system comprising working, counter, and reference electrodes (Bard et al.,1980). For electrochemical biosensors, the charge transfer behaviour between electrode and electrolyte interface plays a significant role that has been evaluated by using various electrochemical studies. Rendles Sevcik, Brown Anson, and Laviron models are extensively recognized to study the charge transfer behaviour at electrode surface and interface. To evaluate with these models, the voltammetric responses at every fabrication step is measured and the value of anodic / cathodic peak currents (I_{pa} / I_{pc}) are used for further study to infer the charge transfer phenomenon at the electrode surfaces. The stability of biosensing probe and charge transfer dynamics at the electrode surface are inferred by scan-rate study. Furthermore, the electrochemical impedance spectroscopy has also been applied to evaluate the sensor probe with respect to resistance in charge transfer, particularly in instance of deposition /functionalization onto the electrode surface.

4.4. Analytical performance of biosensors:

The analytical performance of a biosensor is measured by several constraints, including dynamic range, detection limit, quantification limit, interference study, shelf-life, sensitivity, reproducibility, and the capacity to detect target in complex physiological samples (Mahato et al. 2018e). The scientific modelling for these studies is usually done with regression plot. In this model, regression line is drawn

TH-2627_166106107

for the different intensities of signals with changing concentrations of the analyte (shown in Figure 1.5).

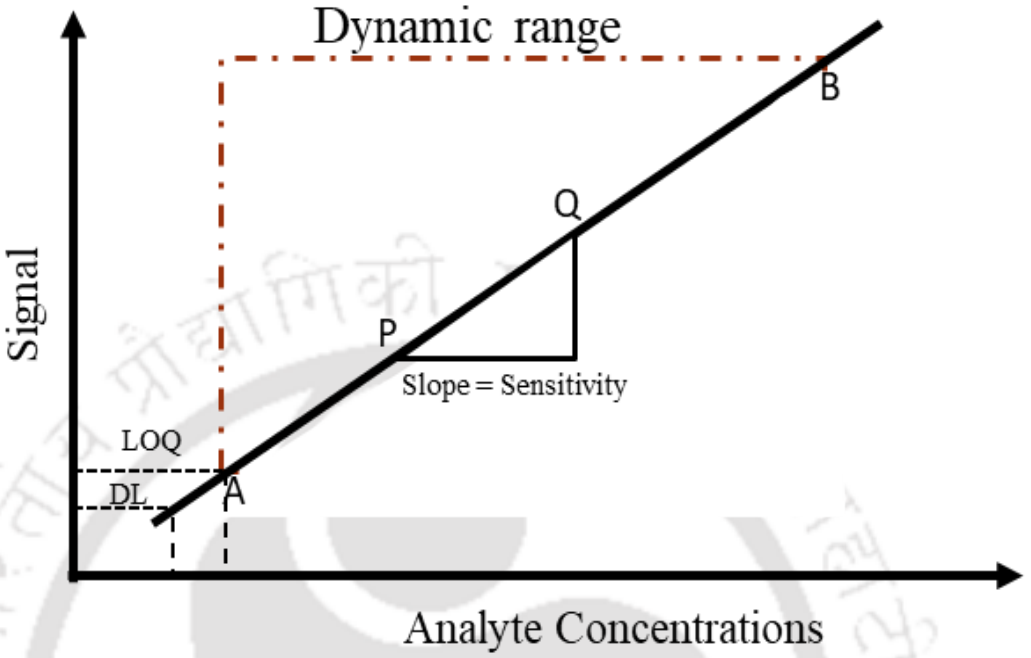

Figure 1.5. Standard calibration plot used for calculating LOD, LOQ, Sensitivity and the dynamic range.

4.4.1. **Dynamic Range:** It is a range in the calibration plot, where analyte signal is directly proportional to the analyte concentrations. The broader the dynamic range, the better will be the clinical importance, as a greater number of concentrations can be extrapolated by these values for quantitative detection (Mahato et al. 2018e).

4.4.2. **Detection Limit:** DL is the statistical minimum amount of analyte that can be detected because of the biochemical reaction happening at the sensor surface. This is generally calculated by using the equation 4

$$DL = \frac{3\sigma_b}{m} \quad \ldots\ldots\ldots\ldots\ldots\ldots\ldots\ldots\ldots\ldots\ldots\ldots(4)$$

Where, DL is detection limit, σ_b is standard deviation of blank, and m is slope of the calibration curve.

TH-2627_166106107

4.4.3. **Limit of Quantification:** LOQ is minimum amount of analyte that can be quantified by the sensor. Usually, LOQ is

$$LOQ = \frac{10\sigma_b}{m} \quad \ldots\ldots\ldots\ldots\ldots\ldots (5)$$

Where, LOQ is limit of quantification, σ_b is standard deviation of blank, and m is slope of the calibration curve.

4.4.4. **Interference study:** It is the most significant standard for the biosensor assessment. It is the capability of sensor for discriminating out the non-specific molecules from the analytical sample. Sensor should be selective towards its analyte only and to determine the selectivity the responses of potential interfereing molecule is studied.

4.4.5. **Shelf-life study:** Shelf-life study is performed to determine the lifetime of the developed sensor. It represents the stability of developed sensor in terms of retainment of activity of bio-recognition elements and life-time of the coupled transducers (Mahato et al. 2018c).

4.4.6. **Sensitivity:** This is the property of a sensor by virtue of which it responses towards the minute change in the analyte concentrations. It is explained by the slope of the regression curve, where sharper slope indicates the better sensitivity. It indicate the property of sensor in differentiating even small change of analyte. The scientific expression of sensitivity can be explained as follows (equation 5).

$$Sensitivity = slope\ of\ the\ regression\ curve = \frac{Y_q - Y_p}{X_q - X_p} \quad \ldots\ldots\ldots(5)$$

Y_p, Y_q, X_p, and X_q are the coordinates of two points (P and Q) in the calibration plot, related to analyte concentrations and their corresponding signals.

TH-2627_166106107

4.4.7. **Reproducibility:** For the translational viability of any sensor there is a need of reproducibility study. In reproducibility, the signal responses of several seperate sensing platforms, prepared using similar protocol is studied (Mahato et al. 2018e).

4.4.8. **Real sample analysis**: After physical and electrochemical characterization of developed sensor followed by determining the sensing capabilities in standard conditions, the analytical performances in the real matrices are analyzed (Mahato et al. 2018b). It is performed by sensing the target analyte in numerous real sample matrices *viz.* beverages, blood serum, urine, saliva, tears *etc*. Occasionally, unavailability or complexity of medical samples leads to irregularities in various levels of study. To study such issues, spike-recovery and standard addition approaches have been employed for real sample analysis. These approaches, examine the analytical performances in mimicked real matrices, where these specimens are prepared with the natural interfering integral molecules.

4.4.8.1. Spike recovery method

In this procedure, a known quantity of the analyte is injected to the collected real samples and the percentage recoveries were estimated by designed sensor. The significantly lesser level of percentage recovery deduces a strong interference from the matrix molecules, which are limiting the performance of the developed sensor. If the percentage recovery is adjacent to the spiked concentration, biosensing probe does not experience any interference from the matrices, whereas the significantly higher percentage recovery deduces the intrinsic presence of target analytes in the test sample.

The scientific calculation of % recovery and its explanation are given below.

$$\% \text{ recovery} = \frac{Observed - \text{Neat}}{Expected} \quad \ldots\ldots\ldots\ldots (6)$$

TH-2627_166106107

Where "Observed" signifies the value of analyte concentration recorded after spiking of analyte; "Neat" signifies the value of analyte concentration present in sample before spiking. The "Expected" is exact concentration of analyte spiked into the sample.

4.4.8.2. Standard addition method

In several real matrices, the intrinsic presence of target molecules raised the % recoveries. In order to measure the unknown concentrations of the intrinsic target molecules, standard addition method is utlized (Mahato et al. 2018e). In this experiment, the sensor is utilized to acquire the signal while injecting the known concentraion of the target molecules, ultimately, leads to generation of a concentration dependent regression curve, which is extrapolated to determine the intrinsic concentration of target molecules in the real sample matrices. By this assessment, the credibility of the biosensor is evaluated for its biomedical applications.

4.4.8.3. Clinical relevancy test

The sensing ability of a sensor should be better or comparable to the traditional diagnostic devices and the results obtained from developed sensor should be comparable to the clinical results. In view of this, sensor is tested for real sample and the same specimen is tested with traditional hospital based diagnostic instruments. The results obtained in both cases are compared to determine the clinical relevancy of developed sensor.

TH-2627_166106107

5. Objectives and goals of the study:

The objectives of the doctoral research are to attain improved sensitivity and sensor performances of biosensors by using the advanced engineered nanomaterial inside the sensing matrix. We have also tried to develop sensor systems, which not just offer very wide dynamic ranges, but it essentially detects the analyte in clinically significant levels. Simultaneously, this thesis work is motivated to resolve few serious issues, such as sinapic acid sensing and silent clinical diseases *viz.* liver and bone diseases, diabetes, and oral carcinoma. The effort done in this doctoral research was intended towards designing the miniaturized, deliverable, fast, and precise biosensors for the ultrasensitive diagnosis of clinical biomarkers utilizing novel metallic and metal oxide nano-composites. In the research work, different metal and metal oxide NMs are utilized in context of sensor development, and the role of the NMs in biosensing has been extensively elucidated. Stress has been given on the fundamentals and advances of engineered materials such as NM comprising different morphologies. Consideration has been paid to not only numerous applications of NM in a particular detection process but also to the design and transduction approaches that have anticipated perceptions for further improvement.

TH-2627_166106107

5.1. Research objectives:

Objective #1: Design and Development of Ultrafast Sinapic Acid Sensor Based on Electrochemically Nanotuned Gold Nanoparticles and Solvothermally Reduced Graphene Oxide.

Objective #2: Gold - Iron Bimetallic Nanoparticles Impregnated Reduced Graphene Oxide Based Nanosensor For Label-free Detection Of Biomarker Related To Non-alcoholic Fatty Liver Disease.

Objective #3: Novel Non-enzymatic Electrochemical Glucose Biosensor Based on Gadolinium-Iron Bimetallic Nanocomposite.

Objective #4: Design and Development of Noninvasive Oral Cancer Sensor Based on Electrochemically Active Gadolinium Hexacyannoferrate Nanoparticles.

TH-2627_166106107

Thesis Overview

TH-2627_166106107

Thesis Overview

Objective 1

Nanotuning and sinapic acid sensor fabrication

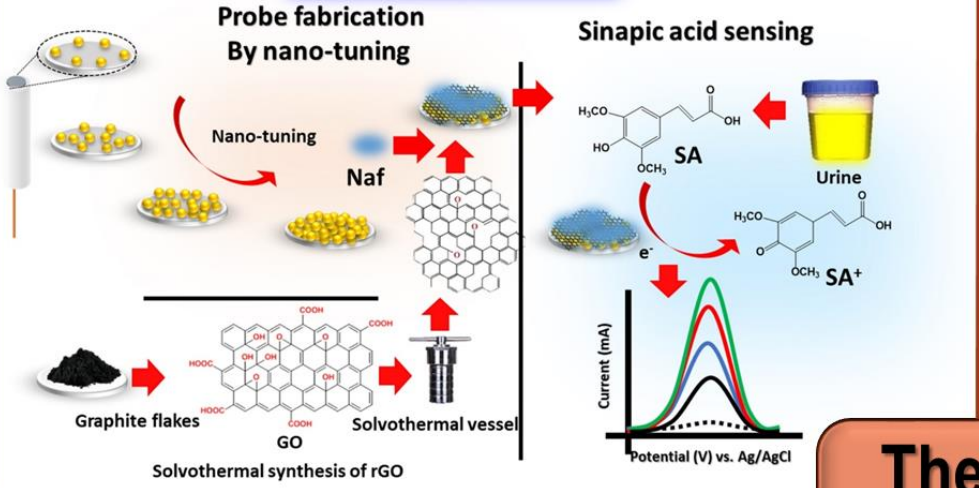

Objective 2

BNP synthesis and fatty liver disease sensor fabrication

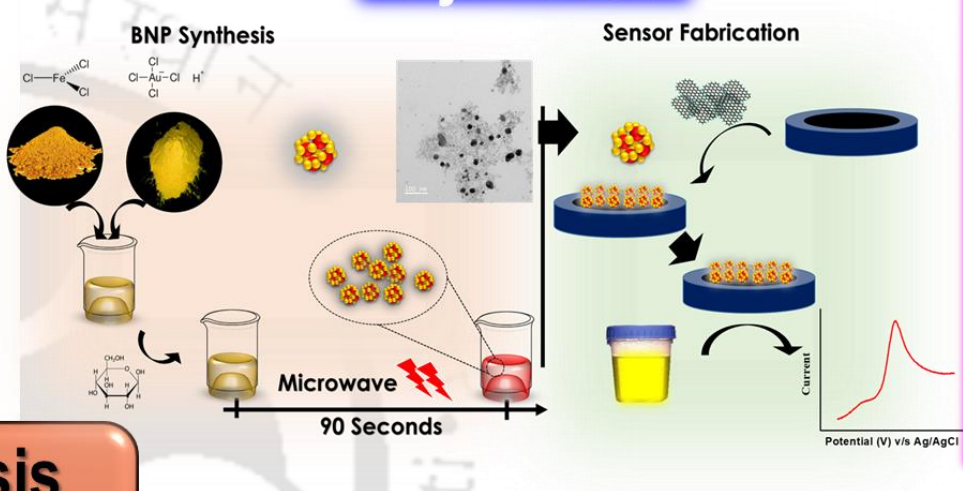

Objective 3

Non-enzymatic glucose sensor fabrication

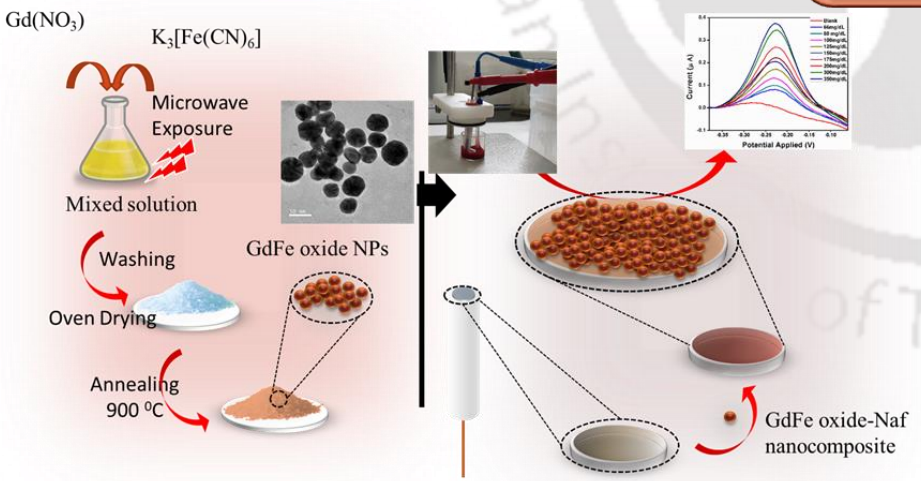

Objective 4

Non-invasive Oral cancer sensor fabrication

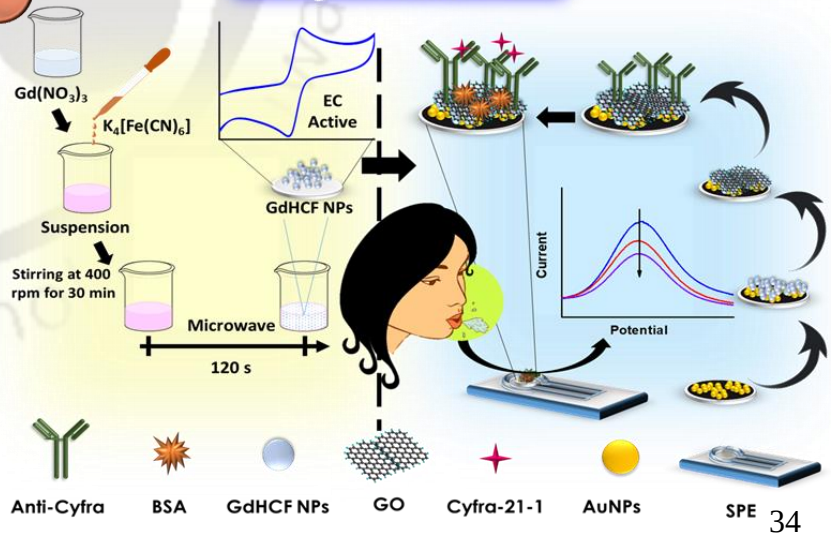

TH-2627_166106107

6. *References*

Afkhami A, Hashemi P, Bagheri H, et al (2017) Impedimetric immunosensor for the label-free and direct detection of botulinum neurotoxin serotype A using Au nanoparticles/graphene-chitosan composite. Biosens Bioelectron 93:124–131.

Akanda MR, Tamilavan V, Park S, et al (2013) Hydroquinone Diphosphate as a Phosphatase Substrate in Enzymatic Amplification Combined with Electrochemical–Chemical–Chemical Redox Cycling for the Detection of E. coli O157:H7. Anal Chem 85:1631–1636.

Akhtar MH, Hussain KK, Gurudatt NG, et al (2018) Ultrasensitive dual probe immunosensor for the monitoring of nicotine induced-brain derived neurotrophic factor released from cancer cells. Biosens Bioelectron 116:108–115.

Akhtar MH, Hussain KK, Gurudatt NG, Shim Y-B (2017) Detection of Ca2+-induced acetylcholine released from leukemic T-cells using an amperometric microfluidic sensor. Biosens Bioelectron 98:364–370.

Arkan E, Saber R, Karimi Z, Shamsipur M (2015) A novel antibody--antigen based impedimetric immunosensor for low level detection of HER2 in serum samples of breast cancer patients via modification of a gold nanoparticles decorated multiwall carbon nanotube-ionic liquid electrode. Anal Chim Acta 874:66–74.

Bagbi Y, Sharma A, Bohidar HB, Solanki PR (2016) Immunosensor based on nanocomposite of nanostructured zirconium oxide and gelatin-A. Int J Biol Macromol 82:480–487.

Bandodkar AJ, Wang J (2014) Non-invasive wearable electrochemical sensors: a review. Trends Biotechnol 32:363–371.

Baranwal A, Chandra P (2018) Clinical implications and electrochemical biosensing of

TH-2627_166106107

monoamine neurotransmitters in body fluids, in vitro, in vivo, and ex vivo models. Biosens Bioelectron 121:137–152.

Bratov A, Abramova N, Ipatov A (2010) Recent trends in potentiometric sensor arrays—A review. Anal Chim Acta 678:149–159.

Chandra P, Noh H-B, Shim Y-B (2013) Cancer cell detection based on the interaction between an anticancer drug and cell membrane components. Chem Commun 49:1900–1902.

Chandra P, Suman P, Airon H, et al (2014) Prospects and advancements in C-reactive protein detection. World J Methodol 4:1–5.

Choudhary M, Yadav P, Singh A, et al (2016) CD 59 targeted ultrasensitive electrochemical immunosensor for fast and noninvasive diagnosis of oral cancer. Electroanalysis 28:2565–2574.

Cooper J, Cass T (2004) Biosensors. Oxford University Press, USA.

Cosnier S (2015) Electrochemical biosensors. CRC Press.

Dagdeviren C, Joe P, Tuzman OL, et al (2016) Recent progress in flexible and stretchable piezoelectric devices for mechanical energy harvesting, sensing and actuation. Extrem Mech Lett 9:269–281.

Das J, Jo K, Lee JW, Yang H (2007) Electrochemical Immunosensor Using p-Aminophenol Redox Cycling by Hydrazine Combined with a Low Background Current. Anal Chem 79:2790–2796.

Deka S, Saxena V, Hasan A, et al (2018) Synthesis, characterization and in vitro analysis of $α$-Fe2O3-GdFeO3 biphasic materials as therapeutic agent for magnetic hyperthermia applications. Mater Sci Eng C 92:932–941.

TH-2627_166106107

Delahay P, Mamantov G (1955) Voltammetry at Constant Current: Review of Theoretical Principles. Anal Chem 27:478–483.

Ding L, Bond AM, Zhai J, Zhang J (2013) Utilization of nanoparticle labels for signal amplification in ultrasensitive electrochemical affinity biosensors: A review. Anal Chim Acta 797:1–12.

Dryhurst G (2012) Electrochemistry of biological molecules. Elsevier.

Fischbach FT, Dunning MB (2009) A manual of laboratory and diagnostic tests. Lippincott Williams & Wilkins.

Haes AJ, Van Duyne RP (2002) A nanoscale optical biosensor: sensitivity and selectivity of an approach based on the localized surface plasmon resonance spectroscopy of triangular silver nanoparticles. J Am Chem Soc 124:10596–10604.

Hao R, Xing R, Xu Z, et al (2010) Synthesis, Functionalization, and Biomedical Applications of Multifunctional Magnetic Nanoparticles. Adv Mater 22:2729–2742.

Hoa XD, Kirk AG, Tabrizian M (2007) Towards integrated and sensitive surface plasmon resonance biosensors: a review of recent progress. Biosens Bioelectron 23:151–160.

Homola J, Yee SS, Gauglitz G (1999) Surface plasmon resonance sensors. Sensors Actuators B Chem 54:3–15.

Hwang KS, Lee S-M, Kim SK, et al (2009) Micro-and nanocantilever devices and systems for biomolecule detection. Annu Rev Anal Chem 2:77–98.

Jain A, Nair PR, Alam MA (2012) Flexure-FET biosensor to break the fundamental sensitivity limits of nanobiosensors using nonlinear electromechanical coupling. Proc Natl Acad Sci 109:9304–9308.

TH-2627_166106107

JEAN L (2006) SENIOR OVERVIEWS. Scand J Immunol 19:281–285.

Jianrong C, Yuqing M, Nongyue H, et al (2004) Nanotechnology and biosensors. Biotechnol Adv 22:505–518.

Johari-Ahar M, Rashidi MR, Barar J, et al (2015) An ultra-sensitive impedimetric immunosensor for detection of the serum oncomarker CA-125 in ovarian cancer patients. Nanoscale 7:3768–3779.

Karim MN, Anderson SR, Singh S, et al (2018) Nanostructured silver fabric as a free-standing NanoZyme for colorimetric detection of glucose in urine. Biosens Bioelectron 110:8–15.

Kumar A, Purohit B, Maurya PK, et al (2019) Engineered Nanomaterial Assisted Signal-amplification Strategies for Enhancing Analytical Performance of Electrochemical Biosensors. Electroanalysis 31:1615–1629.

Kuznetsova S, Zauner G, Schmauder R, et al (2006) A Förster-resonance-energy transfer-based method for fluorescence detection of the protein redox state. Anal Biochem 350:52–60.

Lee W, Kim K, Gurudatt NG, et al (2019) Biosensors and Bioelectronics Comparison of enzymatic and non-enzymatic glucose sensors based on hierarchical Au-Ni alloy with conductive polymer. Biosens Bioelectron 130:48–54.

Lien TTN, Takamura Y, Tamiya E, Mun'delanji CV (2015) Modified screen printed electrode for development of a highly sensitive label-free impedimetric immunosensor to detect amyloid beta peptides. Anal Chim Acta 892:69–76.

Ligler FS, Taitt CAR (2002) Optical biosensors: present and future. Gulf Professional Publishing.

Ligler FS, Taitt CR (2011) Optical biosensors: today and tomorrow. Elsevier.

TH-2627_166106107

Liu J, Liu J, Yang L, et al (2009) Nanomaterial-Assisted Signal Enhancement of Hybridization for DNA Biosensors: A Review. Sensors 9:7343–7364.

Liu L, Xia N, Liu H, et al (2014) Highly sensitive and label-free electrochemical detection of microRNAs based on triple signal amplification of multifunctional gold nanoparticles, enzymes and redox-cycling reaction. Biosens Bioelectron 53:399–405.

Liu Y, Du Y, Li CM (2013) Direct Electrochemistry Based Biosensors and Biofuel Cells Enabled with Nanostructured Materials. Electroanalysis 25:815–831.

Mahato K, Baranwal A, Srivastava A, et al (2018a) Smart Materials for Biosensing Applications. In: Pawar PM, Ronge BP, Balasubramaniam R, Seshabhattar S (eds) Techno-Societal 2016. Springer International Publishing, Cham, pp 421–431.

Mahato K, Kumar S, Srivastava A, et al (2018b) Chapter 14 - Electrochemical Immunosensors: Fundamentals and Applications in Clinical Diagnostics. In: Vashist SK, Luong JHT (eds) Handbook of Immunoassay Technologies. Academic Press, pp 359–414.

Mahato K, Maurya PK, Chandra P (2018c) Fundamentals and commercial aspects of nanobiosensors in point-of-care clinical diagnostics. 3 Biotech 8:149.

Mahato K, Nagpal S, Shah MA, et al (2019) Gold nanoparticle surface engineering strategies and their applications in biomedicine and diagnostics. 3 Biotech 9:57.

Mehrotra P (2016) Biosensors and their applications--A review. J oral Biol craniofacial Res 6:153–159.

Mirceski V, Gulaboski R, Lovric M, et al Square-Wave Voltammetry: A Review on the Recent Progress. Electroanalysis 25:2411–2422.

Nguyen HH, Park J, Kang S, Kim M (2015) Surface plasmon resonance: a versatile technique

TH-2627_166106107

for biosensor applications. Sensors 15:10481–10510.

Nicholson RS (1965) Theory and application of cyclic voltammetry for measurement of electrode reaction kinetics. Anal Chem 37:1351–1355.

Noh H-B, Chandra P, Kim Y-J, Shim Y-B (2012a) A Simple Separation Method with a Microfluidic Channel Based on Alternating Current Potential Modulation. Anal Chem 84:9738–9744.

Noh H-B, Lee K-S, Chandra P, et al (2012b) Application of a Cu–Co alloy dendrite on glucose and hydrogen peroxide sensors. Electrochim Acta 61:36–43.

O'sullivan MJ, Bridges JW, Marks V (1979) Enzyme immunoassay: a review. Ann Clin Biochem 16:221–239.

Oliverio M, Perotto S, Messina GC, et al (2017) Chemical functionalization of plasmonic surface biosensors: a tutorial review on issues, strategies, and costs. ACS Appl Mater Interfaces 9:29394–29411.

Owicki JC, Bousse LJ, Hafeman DG, et al (1994) The light-addressable potentiometric sensor: principles and biological applications. Annu Rev Biophys Biomol Struct 23:87–114.

Park S, Singh A, Kim S, Yang H (2014) Electroreduction-Based Electrochemical-Enzymatic Redox Cycling for the Detection of Cancer Antigen 15-3 Using Graphene Oxide-Modified Indium–Tin Oxide Electrodes. Anal Chem 86:1560–1566.

Prasad A, Mahato K, Chandra P, et al (2016) Bioinspired Composite Materials: Applications in Diagnostics and Therapeutics. J Mol Eng Mater 4:1640004.

Rajamani AR, Peter SC (2018) Novel Nanostructured Pt/CeO2@Cu2O Carbon-Based Electrode To Magnify the Electrochemical Detection of the Neurotransmitter Dopamine and Analgesic Paracetamol. ACS Appl Nano Mater 1:5148–5157.

TH-2627_166106107

Riepl M, Mirsky VM, Novotny I, et al (1999) Optimization of capacitive affinity sensors: drift suppression and signal amplification. Anal Chim Acta 392:77–84.

Sapsford KE, Algar WR, Berti L, et al (2013) Functionalizing Nanoparticles with Biological Molecules: Developing Chemistries that Facilitate Nanotechnology. Chem Rev 113:1904–2074.

Sarkar T, Rawat K, Bohidar HB, Solanki PR (2016) Electrochemical immunosensor based on PEG capped iron oxide nanoparticles. J Electroanal Chem 783:208–216.

Savaliya R, Shah D, Singh R, et al (2015) Nanotechnology in disease diagnostic techniques. Curr Drug Metab 16:645–661.

Snyderman R (2012) Personalized health care: From theory to practice. Biotechnol. J. 7:973–979.

Solanki PR, Singh J, Rupavali B, et al (2017) Bismuth oxide nanorods based immunosensor for mycotoxin detection. Mater Sci Eng C 70:564–571.

Špačková B, Wrobel P, Bocková M, Homola J (2016) Optical biosensors based on plasmonic nanostructures: a review. Proc IEEE 104:2380–2408.

Strianese M, Staiano M, Ruggiero G, et al (2012) Fluorescence-Based Biosensors. In: Bujalowski WM (ed) Spectroscopic Methods of Analysis: Methods and Protocols. Humana Press, Totowa, NJ, pp 193–216.

Tamayo J, Kosaka PM, Ruz JJ, et al (2013) Biosensors based on nanomechanical systems. Chem Soc Rev 42:1287–1311.

Tao S, Jia T-W, Yang Y, Chu L-Q (2017) BSA-sugar conjugates as ideal building blocks for SPR-based glycan biosensors. ACS sensors 2:57–60.

TH-2627_166106107

Thévenot DR, Toth K, Durst RA, Wilson GS (2001) Electrochemical biosensors: recommended definitions and classification. Anal Lett 34:635–659.

Turner A, Karube I, Wilson GS (1987) Biosensors: fundamentals and applications. Oxford university press. London.

Upadhyayula VKK (2012) Functionalized gold nanoparticle supported sensory mechanisms applied in detection of chemical and biological threat agents: A review. Anal Chim Acta 715:1–18.

Vaddiraju S, Tomazos I, Burgess DJ, et al (2010) Emerging synergy between nanotechnology and implantable biosensors: a review. Biosens Bioelectron 25:1553–1565.

Wang D, Hu W, Xiong Y, et al (2015) Multifunctionalized reduced graphene oxide-doped polypyrrole/pyrrolepropylic acid nanocomposite impedimetric immunosensor to ultra-sensitively detect small molecular aflatoxin B1. Biosens Bioelectron 63:185–189.

Wang J (2005a) Nanomaterial-based amplified transduction of biomolecular interactions. Small 1:1036–1043.

Wang J (2005b) Nanomaterial-based electrochemical biosensors. Analyst 130:421–426.

Xia N, Zhang Y, Wei X, et al (2015) An electrochemical microRNAs biosensor with the signal amplification of alkaline phosphatase and electrochemical–chemical–chemical redox cycling. Anal Chim Acta 878:95–101.

Zeng S, Yong K-T, Roy I, et al (2011) A Review on Functionalized Gold Nanoparticles for Biosensing Applications. Plasmonics 6:491.

Zhang Y, Zhang B, Ye X, et al (2016) Electrochemical immunosensor for interferon-$γ$ based on disposable ITO detector and HRP-antibody-conjugated nano gold as signal tag. Mater Sci Eng C 59:577–584.

TH-2627_166106107

Zhu Y, Son JI, Shim Y-B (2010) Amplification strategy based on gold nanoparticle-decorated carbon nanotubes for neomycin immunosensors. Biosens Bioelectron 26:1002–1008.

भारतीय प्रौद्योगिकी संस्थान गुवाहाटी • Indian Institute of Technology Guwahati •

TH-2627_166106107

TH-2627_166106107

Chapter – II

Design and Development of Ultrafast Sinapic Acid Sensor Based on Electrochemically Nanotuned Gold Nanoparticles and Solvothermally Reduced Graphene Oxide.

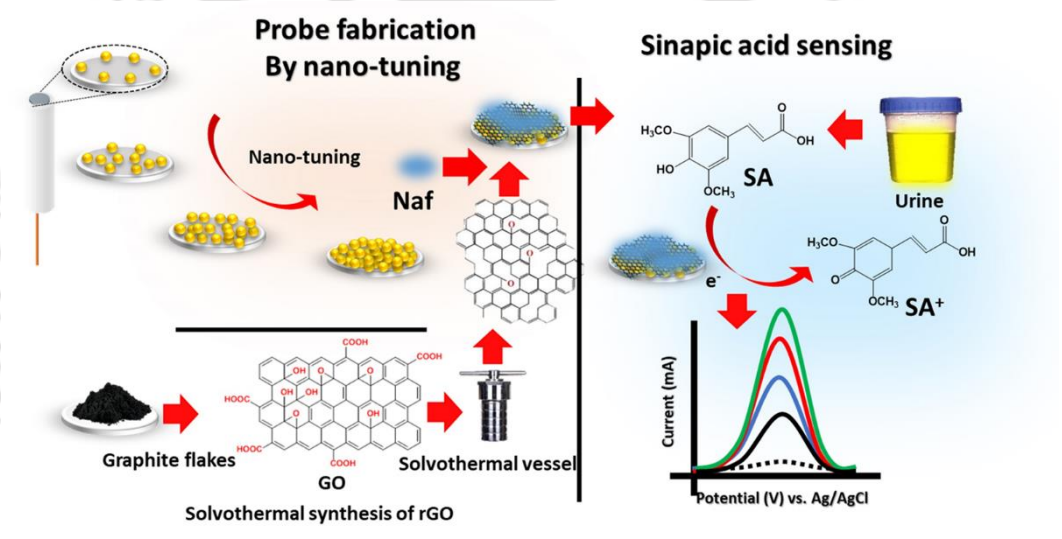

Status:

Published in Electroanalysis, Willy, 2020

TH-2627_166106107

1. Introduction

In our first objective, we have attempted to develop first electrochemical sensor for SA using electrochemically tuned AuNPs and solvothermally reduced rGO. The main reason for the electrochemical sensor fabrication was to develop a POC sensing system with low detection limit and have clinically relevant dynamic range that can be utilized for onsite detection of SA. Nowadays, replacing the nutritional supplements with natural food has attracted researchers to investigate the levels of chemicals / biochemicals in fruits, vegetables and other agricultural resources along with various supplementary drugs having health benefits. Among various nutritional supplements, SA has gained huge interest in human health due to its excellent antioxidant activity. SA majorly found in rapeseed, red wine, coffee, tea leaves, various kinds of citrus fruits including lemon and Indian gooseberry, canola oil, vegetables, whole grains or cereals *etc.*(Thiyam et al. 2006; Siger et al. 2013). It has been reported that SA could be considered as preservative of cosmetics, pharmaceuticals, and various foods (Kroon, Paul A and Williamson 1999). Moreover, numerous studies has also been reported about the useful applications of SA as therapeutic agents in various oxidative stress related diseases like depression, inflammation, and atherosclerosis. Even in cancer diagnosis, levels of SA provides better understandings about the disease diagnosis and prognosis (Fresco et al. 2006). Furthermore, low level of SA in body fluids is also related with human behaviour such as depression, anxiety, and neurological disorders *viz.* Alzheimer's and Parkinson's disease (Nićiforović and Abramovič 2014). This clearly shows the importance of the SA in food as well as in various clinical conditions. In view of such importance, several analytical methods have been developed for its detection in diverse samples. Conventionally, SA has been detected using high-pressure liquid chromatography (HPLC), liquid chromatography – mass spectrometery (LC-MS), and gas chromatography-mass spectrometry (GC-MS)

TH-2627_166106107

techniques (Zhang and Zuo 2004; Thiyam et al. 2009). These techniques are extremely powerful and provide reliable detection of SA, but they are complicated, tedious, less sensitive, require bulky instruments, expensive reagents, and involve multiple steps; hence not appropriate for onsite quick analysis of SA. It is, therefore, desirable to develop a facile, robust, sensitive, selective, and economically feasible method for SA detection that can be operated onsite. SA has a unique chemical structure composed of various functional groups that can be oxidised / reduced at a certain electrode potential; hence, an electrochemical sensor based on its direct electron transfer process can be attempted. To the best of our knowledge, electrochemical sensor for SA has not been reported until now. The signal enhancement in an electrochemical sensor can be achieved by incorporating various highly conducting and stable nanostructures onto the electrode surface (Kumar et al. 2018, 2019a). There are several nanomaterials such as complex carbon nanostructures (fullerenes), multi-metallic nano-alloys, nanotubes *etc.* that can be synthesized and employed onto the surface of the electrode (Dakshayini et al. 2019; Kumar et al. 2019b; Shetti et al. 2019c, a, d, b), but they require multi step synthesis procedure and several purification processes (Cao and Wang 2004; Ignat 2008; Ali et al. 2010). In recent years, direct deposition of metal nanoparticles onto the electrode surface has gained much interest as they are direct and merely require few minutes to synthesize under the optimum conditions without any external reducing agents (Noh et al. 2012a, b; Chandra et al. 2015; Pallela et al. 2016). Among various metallic nanoparticles, AuNPs has gained considerably great importance due to its stability, inertness, and highly conducting nature (Verma et al. 2019). The performance of these AuNPs can be further improved by electrochemically tuning them under the optimized conditions (Mahato et al. 2018a, 2019). The nanotuning assists towards the improvement of the geometry / morphology of the AuNPs, which may facilitate the specific reactions improving their electronic as well as electrocatalytic

TH-2627_166106107

properties (Chandra et al. 2013; Baranwal and Chandra 2018; Mahato et al. 2018c, b; Mandal et al. 2018). However, it has also been argued that metal surfaces or metallic nanoparticles deposited surfaces fouls due to the presence of proteins, particularly in real sample analysis (Bhakta et al. 2015). Therefore, layering of other nanostructures onto the metallic nanoparticles may improve the performance of sensor in real sample matrices. In this context, reduced graphene oxide could be a promising candidate due to its fast electron transfer behaviour, stability, and unique two-dimensional matrix that provides stable interactions with metallic nanoparticles, eventually forming a highly conducting and stable sensor surface. rGO has been considered as better electronic conductor as compare to GO, which have more oxygen content in the structure than rGO. It is therefore required to use rGO for sensor matrix formation to enhance the conductivity. There are several approaches to reduce GO, out of which solvothermal treatment results better reduction (Nethravathi and Rajamathi 2008; Hailiang et al. 2009).

In the present study, we report a nanosensor for SA detection based on EAuNPs – rGO nanocomposite coated on glassy carbon electrode (GCE). The EAuNPs deposition was optimized to obtain the maximum signal followed by coating of rGO, which was synthesized by a facile solvothermal technique. The synthesized EAuNPs, rGO, and EAuNPs-rGO nanocomposite were characterized using XRD, TEM, SAED, particle size analysis, and Raman spectroscopy. A proof-of-concept electrochemical sensor for SA was developed based on EAuNPs-rGO nanocomposite, which was characterized by electrochemical techniques such as; CV and EIS. Subsequently, the designed sensor was applied for dose dependent detection of SA to measure its analytical performance, *i.e.* LDR and DL using differential pulse voltammetry (DPV). The response time of the sensor was evaluated by performing continues injection chrono-amperometry at a specific applied potential. The practical applicability of the fabricated sensor was examined by testing SA

TH-2627_166106107

directly in unprocessed human urine using spike and recovery method. Interference due to various biochemicals was investigated. The long-term stability and reproducibility of fabricated sensor were also tested.

2. Materials and methods

2.1. Materials, apparatus, and reagent preparation

Graphite powder, Ortho-phosphoric acid (H_3PO_4), Hydrochloric acid (HCl), SA, and Chloro-auric acid ($HAuCl_4$) were purchased from SRL, India. Deionised water was obtained from Millipore unit (Elix USA) having 18.2 MΩ.cm resistance. Glucose, ethanol, potassium ferrocyanide ($K_4[Fe(CN)_6]$), and potassium ferricyanide ($K_3[Fe(CN)_6]$) were obtained from Himedia, India. Hydrogen peroxide (H_2O_2), and potassium permanganate ($KMnO_4$) were purchased from Merck. Nafion and SA were purchased from Sigma. Sodium dihydrogen phosphate (NaH_2PO_4) and sodium phosphate (Na_2HPO_4) were purchased from Merck and SRL, respectively. Indium tin oxide (ITO) coated glass substrates were purchased from Techinstro Pvt. Limited. All the chemicals were of AR grade and utilized without any additional purification.

2.2. Solvothermal synthesis of rGO

For the rGO synthesis, graphite powder was first oxidized to get graphene oxide (GO) using acid exfoliation method. Briefly, in this process, H_2SO_4 and H_3PO_4 were mixed in volume ratio of 9:1 (27mL: 3mL) and stirred for half hour. 0.225 g of graphite powder was added into mixing solution under stirring condition followed by slowly addition of 1.32 g of $KMnO_4$. The reaction mixture was uninterruptedly stirred for 6 hours until the final solution became blackish dark green. To neutralize the excess of $KMnO_4$, 0.675 mL of H_2O_2 was added dropwise while stirring in cold environment for 10 minutes. Thereafter, 10 mL of HCl and 30 mL of deionized water was added into the solution and centrifuged

TH-2627_166106107

at 5000 rpm for 7 minutes. The supernatant was emptied and the residuals were then washed again with HCl and deionized water for five times followed by drying in a hot air oven at 90 °C for 24 hours to get the GO powder. Colloidal dispersion of GO was prepared using 100 mg of GO in 50 mL of ethanol followed by sonication in a bath sonicator for half an hour. The colloidal solution was transferred to a stainless steel hydrothermal vessel and heated at 200 °C in oven for 48 hours [34]. The product obtained after solvothermal treatment was washed three times with acetone and deionized water followed by oven drying at 65 °C. The obtained powder was kept in airtight container for further applications.

2.3. Fabrication of GCE/EAuNPs/rGO/Naf sensing probe

The first step towards the development the sensing probe was to tune the density of EAuNPs onto the GCE. We have adopted an electrochemical potential step method in which AuNPs were formed onto the electrode surface. The first layer of the AuNPs were electrochemically deposited onto the GCE in an acidic solution (0.6 M H_2SO_4) containing 0.003% $HAuCl_4$ by performing linear sweep voltammetry (LSV) from +1.5 to +0.4 (V) vs. Ag/AgCl. The provided conditions for AuNPs electrodeposition are as follows: 60.0 s deposition time, −0.6 V deposition potential, 0.1 V s^{-1} scan rate. After deposition, the electronic property of the electrode was investigated by recording CV as well as EIS in a 5 mM $[Fe(CN)_6]^{-3/-4}$ solution prepared in PBS. Thereafter, AuNPs were tuned by successive LSVs for four sweeps (optimized) and the surface is termed as GCE/$EAuNPs_4$. Thereafter, 1.0 mg / mL of rGO was prepared in 0.01% nafion solution and coated onto GCE/$EAuNPs_4$. The electrode was kept in dark for 30 minutes followed by its rinsing with deionised water, forming the final sensing electrode as GCE/$EAuNPs_4$/rGO/Naf. The EAuNPs, rGO synthesis, and sensor probe fabrication has been shown in scheme 2.

TH-2627_166106107

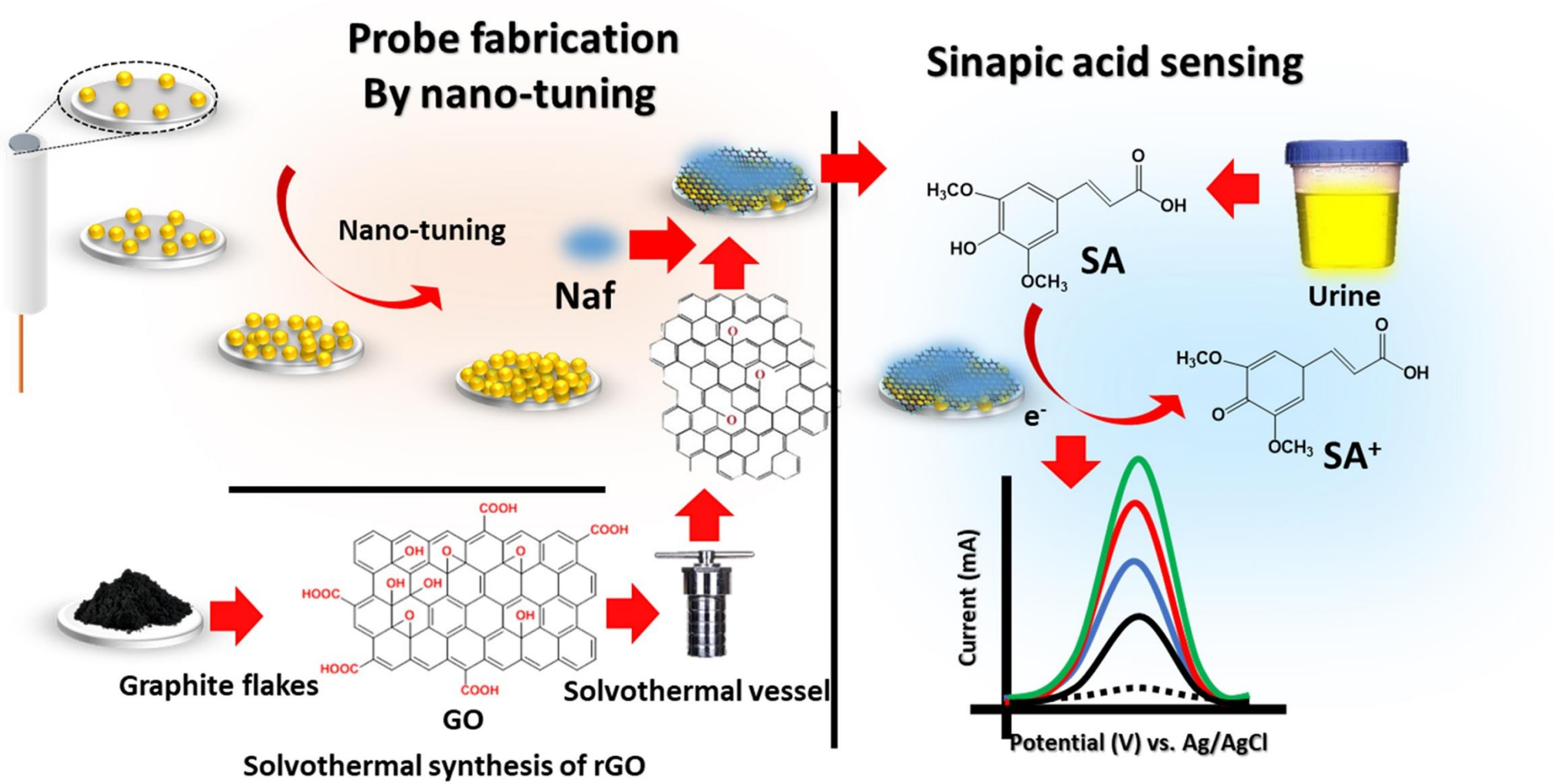

Scheme 2. Scheme of GCE/EAuNPs$_4$/rGO/Naf sensing probe fabrication using nanotuned EAuNPs and solvothermally synthesized rGO.

2.4. Characterization of EAuNPs-rGO nanocomposite and sensor probe

2.4.1. *X-ray* diffraction *analysis:*

To check the crystallinity of EAuNPs, rGO, and EAuNPs-rGO, XRD has been performed at 2θ Bragg's angle in the range between 10° to 60° with a scan rate of 10° per minute on Rigaku MiniFlex 300, while operating the machine in film reading mode. For XRD studies, three separate films of EAuNPs, rGO, and EAuNPs-rGO were prepared onto the ITO coated glass.

2.4.2. *Transmission electron microscopy imaging and analyses:*

To know the shape, size, and electron diffraction analyses of EAuNPs, FE-TEM (JEOL JEM-2100F TEM) has been utilized. A well dispersed solution of EAuNPs was obtained using sonication and was loaded onto the surface of carbon coated copper grid (300 mesh) followed by drying at 37°C for 12 hours.

2.4.3. *Raman Spectroscopy:*

EAuNPs, rGO, and nanocomposite EAuNPs-rGO were characterized for Raman scattering using Raman spectrophotometer (Laser Micro Raman System Horiba Jobin Vyon, Model LabRam HR). For Raman analysis, three separate films of EAuNPs, rGO and EAuNPs-rGO were prepared onto the ITO coated glass. A Co laser of 488 nm has been applied with 10 s reaction time to measure the Raman scattering in the range of 1200 to 2500 cm^{-1}.

2.4.4. *Electrochemical characterization:*

Electrochemical characterizations of bare GCE, GCE/$EAuNPs_1$, GCE/$EAuNPs_2$, GCE/$EAuNPs_3$, GCE/$EAuNPs_4$, and GCE/$EAuNPs_4$/rGO/Naf probe sensor was performed by CV, LSV, and EIS using Metrohm

TH-2627_166106107

electrochemical analyser (Autolab potentiostat galvanostat). A phosphate buffer saline (PBS pH 7.6 and 0.9% NaCl) solution containing 5 mM $[Fe(CN)_6]^{-3/-4}$ was used as an electrolyte to perform all electrochemical characterization using Ag/AgCl as a reference electrode and Pt wire as a counter electrode.

3. Results and discussions

3.1. Physical Characterization of EAuNPs and rGO

3.1.1. *XRD studies*:

To confirm the nature of crystallinity of EAuNPs, rGO, and nanocomposite EAuNPs-rGO, we have performed XRD. Three thin films were prepared onto the ITO coated glass. Later, it was tested for XRD while operating the instrument in film reading mode. The X-ray diffraction pattern of EAuNPs (figure 2.1 (a)) depicts the diffracted peaks corresponding to the (111) and (200) diffraction planes of gold, which is due the cubic phase of gold that has been well indexed with JCPDS No: 65-2870 (Narayanan and Sakthivel 2008). The average crystallite size was estimated as ~ 12.11 (±0.5) nm using all diffraction peaks with the help of Debye-Scherrer's equation.

$$D = \frac{0.9\lambda}{\beta\cos\theta} \quad \ldots. (1)$$

Where λ=1.5460Å is the wavelength of target Cu-Kα, θ is the Bragg's angle of diffraction and β is the full-width half maximum of diffraction peak.

Thereafter, the XRD of rGO coated ITO was performed (figure 2.1 (b)), a characteristic diffraction peak was observed showing the (002) crystal plane of rGO (Nethravathi and Rajamathi 2008). Further, the XRD of EAuNPs-rGO nanocomposite was performed in same range and characteristic diffraction peaks were recorded (figure 2.1 (c)). It is interesting to note that in the case of EAuNPs-rGO nanocomposite, diffraction peaks of

TH-2627_166106107

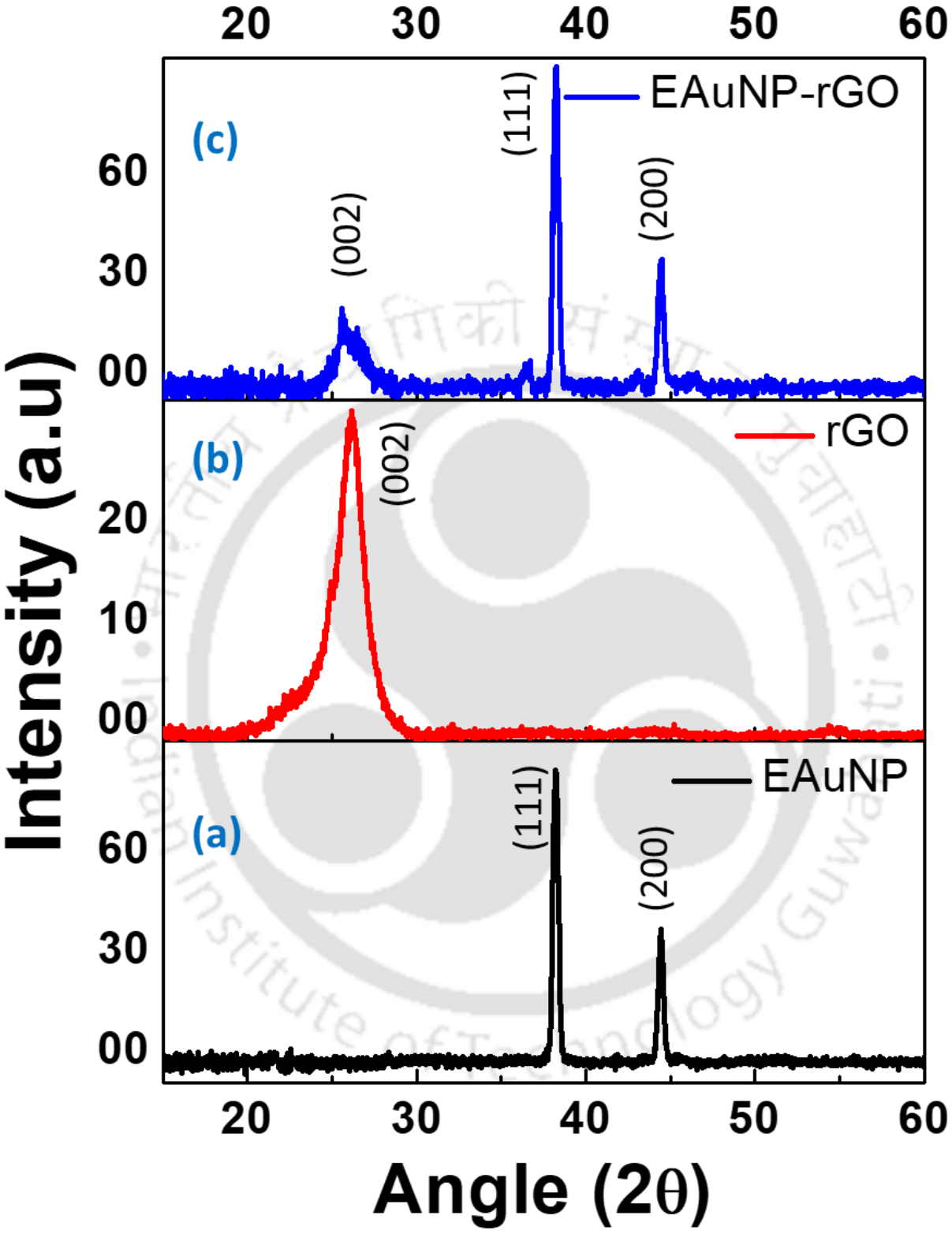

Figure 2.1: XRD analysis of (a) EAuNPs, (b) rGO, and (c) EAuNPs-rGO nanocomposite.

TH-2627_166106107

both of the materials has been observed (*i.e.* (002) of rGO and (111) and (200) of EAuNPs), indicating the proper conjugation of rGO with EAuNPs.

3.1.2. *TEM imaging and analyses:*

In order to characterize the size, shape, and distribution, TEM analyses of EAuNPs were performed (Figure 2.2 (a) and (b)). Clear dark spherical structures were observed in the whole field of imaging. These are of gold, as gold is a heavy metal and therefore, the amount of electron absorbed by gold is large (Nakaji et al. 2005). In inset of figure 2.2 (b)

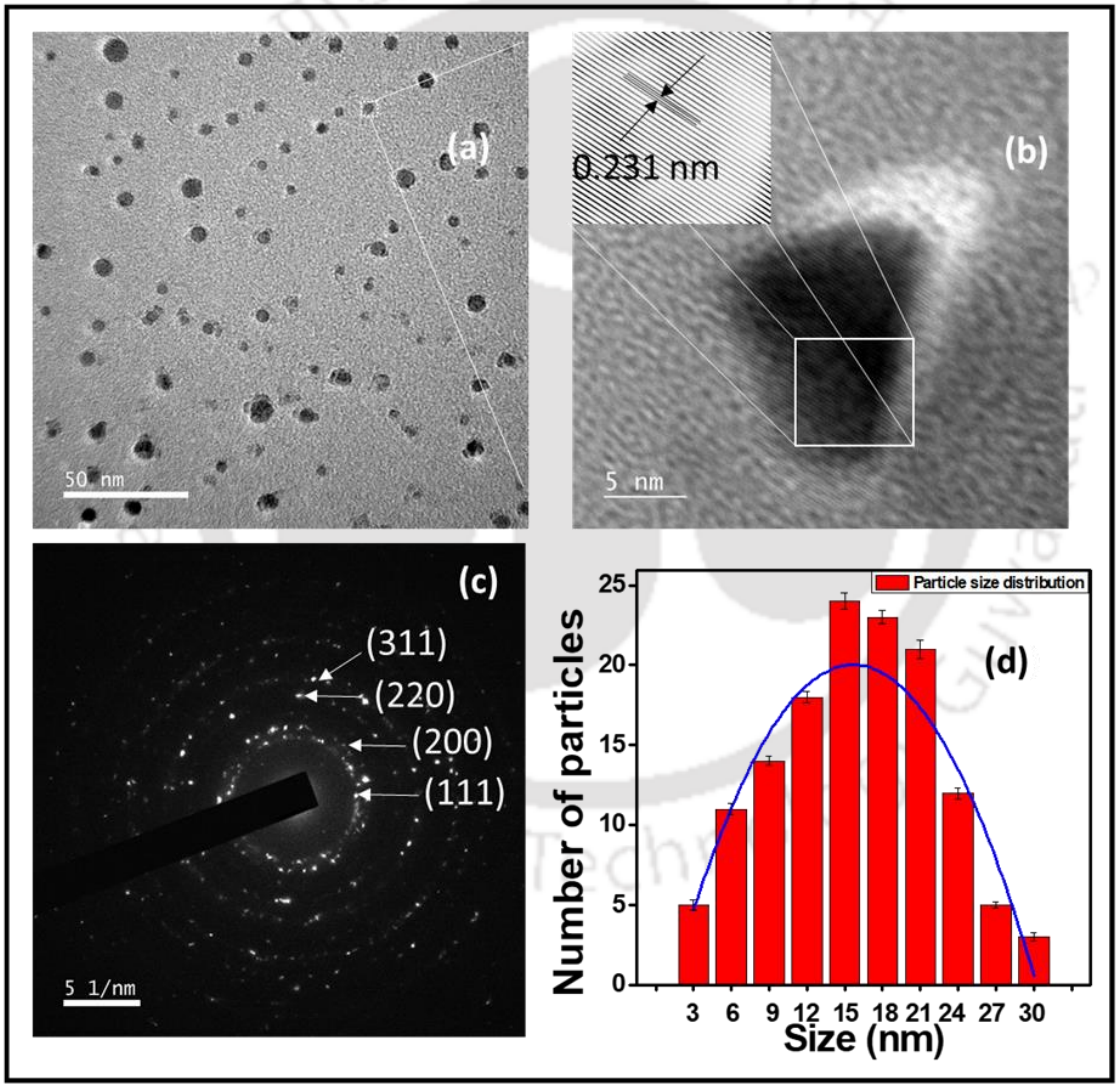

Figure 2.2: (a) TEM image of the EAuNPs-rGO, (b) HRTEM image of a single particle, (c) SAED pattern and d-fringes, (d) size distribution of the particles.

TH-2627_166106107

the d-fringes has been shown, where the interplanner distance of 0.231 nm was obtained indicating the (111) crystal plane (Smitha et al. 2009), which compliments to the XRD analysis. In order to validate the crystalline nature of EAuNPs, we have performed SAED using TEM (figure 2.2 (c)). SAED of the EAuNPs showed the concentric diffraction pattern, which reveal the polycrystalline nature of the nanoparticles. In our case, we got the concentric rings that corresponds to lattice planes (111), (200), (220), and (311) of gold. Interestingly, we have obtained the crystal planes (111) and (200) in SAED, that is in well agreement of the results what we obtained in XRD (Smitha et al. 2009). Thereafter, we calculated the size distribution of EAuNPs considering 130 particles using image-processing tool (ImageJ), where mean size of the particles were obtained with the diameter of 15.5 nm (figure 2.2 (d)).

3.1.3. Raman spectroscopy analysis:

In order to obtain the chemical and structural information about EAuNPs-rGO nanocomposite; we have performed Raman spectroscopy (Figure 2.3). For EAuNPs (black) multiple faint aberrations were observed, which is most likely due to the noise associated with EAuNPs. In the second spectrum, the two peaks were observed at 1353 cm^{-1} and 1593 cm^{-1}, which corresponds to the characteristic peaks of rGO (red; designated as D and G peaks, respectively) (Srivastava et al. 2016). In the next spectrum when EAuNPs-rGO nanocomposite was evaluated the appearance of similar peaks with the enhanced intensity was observed (blue). This is most likely due to the presence EAuNPs in nanocomposite that is enhancing the Raman scattering. Similar observation has also been reported, where metallic nanostructure had shown increase in the Raman scattering of rGO (Jasuja and Berry 2009). The I_D/I_G ratios for rGO and EAuNPs-rGO were found

TH-2627_166106107

to be 0.74 and 1.21, respectively. The greater ratio for EAuNPs-rGO suggests that defects in EAuNPs-rGO have increased. This could be attributed to the fact that even though there is partial reformation of the C=C network in EAuNPs-rGO, the disruptions of sp^2 domains due to interaction of gold with rGO induces more defects in the rGO structure and more carbon atoms are free to interact with EAuNPs (Zhang et al. 2011).

3.2. Electrochemical characterizations

The suitability of EAuNPs-rGO has been tested electrochemically, where the change in the electrochemical response because of the surface modification of electrodes were carried out by performing CV at a scan rate of 0.05 V s^{-1} in 3 mL PBS (pH 7.6) containing 5 mM $[Fe(CN)_6]^{-3/-4}$. Figure 2.4 (a) shows the CV responses for bare GCE (black), one time tuned GCE/$EAuNPs_1$ (olive green), two times tuned GCE/$EAuNPs_2$ (green), three times tuned GCE/$EAuNPs_3$ (blue), four time tuned GCE/$EAuNPs_4$ (pink), and GCE/$EAuNPs_4$/rGO/Naf (red) surfaces. Representative voltamogram due to the redox process of $[Fe(CN)_6]^{-3/-4}$ was observed at bare GCE, while anodic (I_{pa}) and cathodic (I_{pc}) peak currents increased from first to four tuning. This could be due to presence of higher density of EAuNPs onto the GCE surface, which increases the conductivity and surface area of electrodes. We have further increased the loading of EAuNPs onto the electrode surface, where no increase in the current has been observed most likely due to the saturation effect. This means that tune four is the optimized condition to obtain the maximum signal in our case. Further, rGO nanosheets were coated onto the GCE/$EAuNPs_4$ and CV was recorded. Interestingly, we observed further the increase in I_{pa} and I_{pc}, indicating that the rGO is capable of giving amplified signal, which could be due to the synergistic effect of $EAuNPs_4$ and rGO. The oxidation peak current of each electrode has been shown in the figure 2.4 (b). In order to investigate the charge transfer behaviour and

TH-2627_166106107

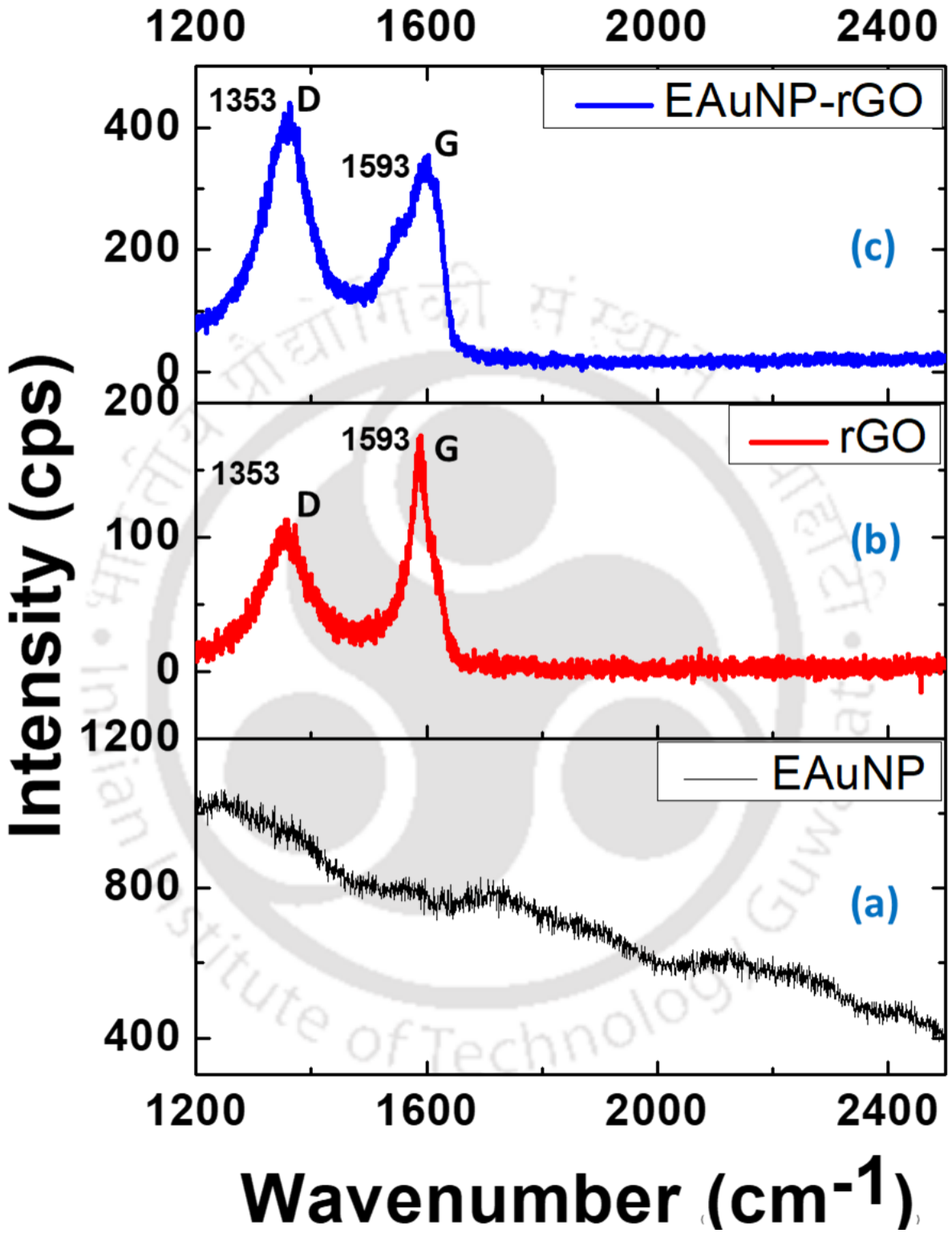

Figure 2.3: Raman analysis of (a) EAuNPs, (b) rGO, and (c) EAuNPs-rGO.

TH-2627_166106107

stability of final sensing probe for electrochemical analysis, we have performed scan rate studies at bare GCE, GCE/EAuNPs$_1$, GCE/EAuNPs$_2$, GCE/EAuNPs$_3$, GCE/EAuNPs$_4$, and GCE/EAuNPs$_4$/rGO/Naf modified electrodes. The diffusion coefficient of electrode surfaces were calculated using Randles-Sevcik equation (Verma et al. 2017).

$$I_p = (2.69\times10^5)\, n^{3/2} A D^{1/2} C \upsilon^{1/2} \quad \text{..... (2)}$$

Where I_p is the peak current of the electrode, n is the number of electrons transferred (n=1), A is the working electrode surface area, D is the diffusion coefficient, C is the concentration of the redox couple $[Fe(CN)6]^{-3/-4}$, and υ is the scan rate (0.05V s^{-1}).

The diffusion coefficient was calculated as 5.56 ×10^{-10}, 1.02 ×10^{-9}, 1.63 ×10^{-9}, 1.82 ×10^{-9}, 2.1 ×10^{-9}, and 2.6 ×10^{-9} cm^2 s^{-1} for GCE, GCE/EAuNPs$_1$, GCE/EAuNPs$_2$, GCE/EAuNPs$_3$, GCE/EAuNPs$_4$, and GCE/EAuNPs$_4$/rGO/Naf respectively. It is worth mentioning that the diffusion coefficient of GCE/EAuNPs$_4$/rGO/Naf modified electrode was found to be 4.67 times greater than that of the bare GCE, indicating the fastest charge transfer at final probe.

In the next step, the electrochemical interface kinetics study of GCE/EAuNPs$_4$/rGO/Naf electrode (Figure 2.4 (c)) was recorded at different scan rate (10 to 100 mV s^{-1}) in 5mM $[Fe(CN)_6]^{-3/-4}$. It was observed that both I_{pa} and I_{pc} peak currents varied linearly with the square root of scan rate figure 2.4 (d), indicating the diffusion controlled process. The slopes and intercepts were given by the following equations:

I_{pa} (GCE/EAuNPs$_4$/rGO/Naf) = [4.65μA(s mV^{-1}) (± 0.47) × scan rate (mVs^{-1})] + 12.44 (± 0.63) μA, R^2=0.999…..... (3)

TH-2627_166106107

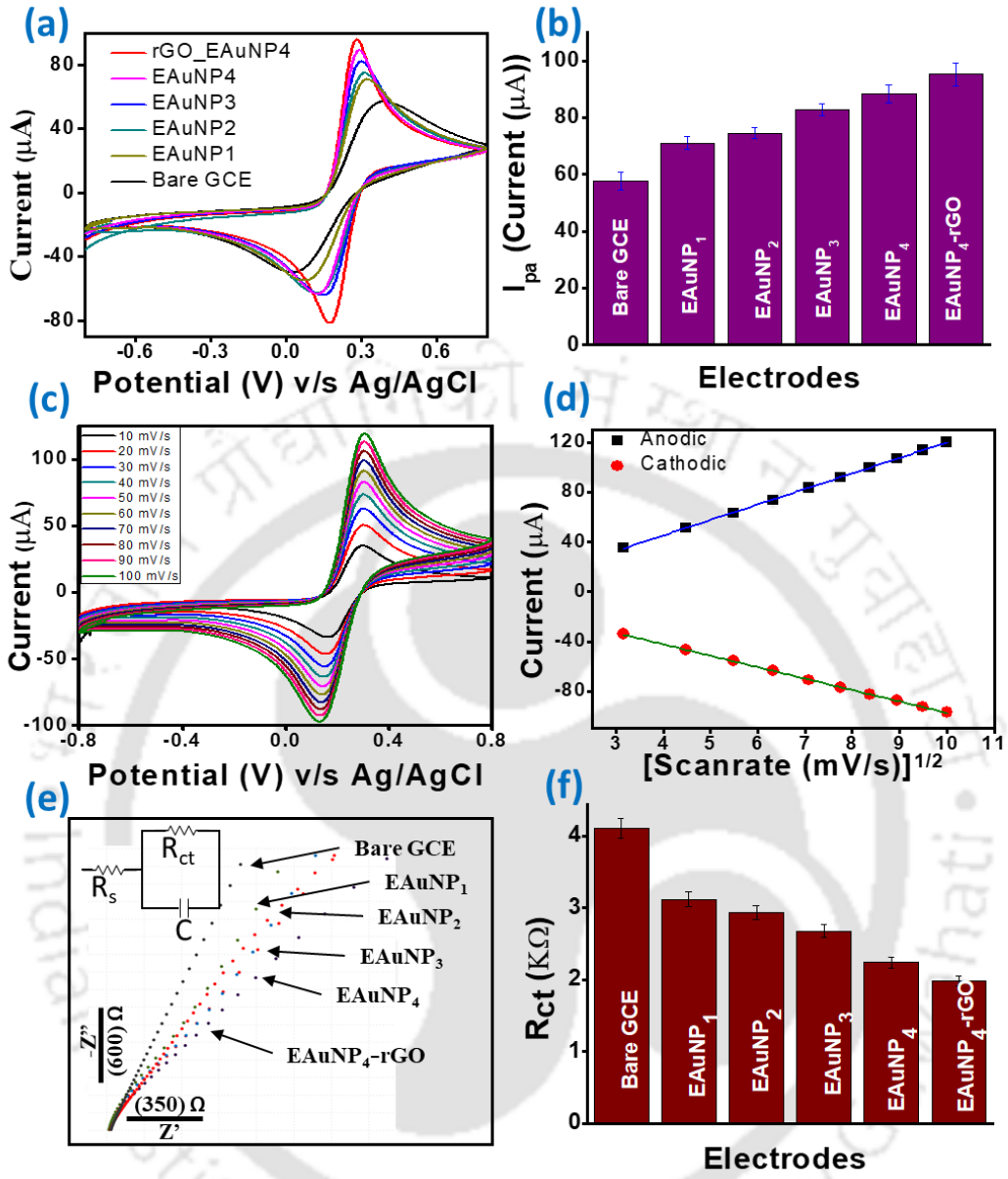

Figure 2.4: (a) Shows the CV responses for bare GCE (black), one time tuned GCE/EAuNPs$_1$ (olive green), two times tuned GCE/EAuNPs$_2$ (green), three times tuned GCE/EAuNPs$_3$ (blue), four time tuned GCE/EAuNPs$_4$ (pink), and GCE/EAuNPs$_4$/rGO/Naf (green) surfaces, (b) corresponding histogram of peak currents, (c) scan rate study of EAuNPs$_4$-rGO from 10 mV/s to 100 mV/s, (d) anodic and cathodic peak currents with respect to square root scan rate, (e) EIS study of electrodes, and (f) corresponding R_{ct} histogram of electrodes.

TH-2627_166106107

I_{pc} (GCE/EAuNPs$_4$/rGO/Naf) = - [5.493 µA(s mV^{-1}) (± 0.43) × scan rate (mVs^{-1})] – 9.18µA (± 0.58), R^2=0.999 …….. (4)

The results obtained by CV were also validated using the EIS, where spectra in the Nyquist plot were recorded for bare GCE, GCE/EAuNPs$_1$, GCE/EAuNPs$_2$, GCE/EAuNPs$_3$, GCE/EAuNPs$_4$, and GCE/EAuNPs$_4$/rGO/Naf modified electrodes to obtain the resistance in charge transfer (Rct) as shown in figure 2.4 (e). The R_{ct} values obtained were 4112± 34.832 Ω, 3121 ± 57.31 Ω, 2937.5 ± 67.97 Ω, 2679.5 ± 27.7 Ω, 2243.5 ± 75.97 Ω, and 1982 ± 33.10 Ω for the bare GCE, GCE/EAuNPs$_1$, GCE/EAuNPs$_2$, GCE/EAuNPs$_3$, GCE/EAuNPs$_4$, and GCE/EAuNPs$_4$/rGO/Naf, respectively (figure 2.4 (f)). It is interesting to note that the lowest R_{ct} was obtained for GCE/EAuNPs$_4$/rGO/Naf surface compared to other tested surfaces. This was due to the fastest electron transfer at electrode- electrolyte interface in this case. The results obtained in EIS also compliments with the results obtained in the CV.

Since, electrocataysis phenomena are surface charge dependent, the concentration of ionic species at electrode surface plays an important role. Therefore, in order to assess the concentration of ionic species (I^*), Brown-Anson model (Equation 5) has been applied (Nenkova et al. 2013).

$$I_p = \frac{n^2 F^2 I^* A V}{4RT} \qquad \ldots\ldots (5)$$

Where n is number of electrons (n=1, in this case), F is Faraday constant (96485.34 C mol^{-1}), T is 298 K, and I_p/V is the slope of calibration (scan rate value), A is surface area of the electrode (0.01 cm^2), and R is gas constant.

I^* for bare GCE, GCE/EAuNPs$_1$, GCE/EAuNPs$_2$, GCE/EAuNPs$_3$, GCE/EAuNPs$_4$, and GCE/EAuNPs$_4$/rGO/Naf was calculated as 1.81×10^{-7} M/cm^2, 2.07×10^{-7} M/cm^2, 2.29×10^{-}

TH-2627_166106107

^{7} M/cm^2, 2.41×10^{-7} M/cm^2, 2.69×10^{-7} M/cm^2, and 2.86 ×10^{-7} M/cm^2, respectively. These results clearly indicates that GCE/EAuNPs$_4$/rGO/Naf modified electrode has highest surface charge density compare to other surfaces. Further, the reaction kinetics at modified electrode surfaces was evaluated by using Laviron model (equation. 6), in order to find diverse electron transfer rate constant (K_s) (Verma et al. 2017).

$$K_s = mnFv/RT \quad \text{..... (6)}$$

Where m is slope, n is number of electrons (n=1, in this case), F is Faraday constant (96485.34 C mol^{-1}), T is 298 K, υ is the scan rate (0.05V s^{-1}), and R is gas constant.

The calculated K_s for the bare GCE, GCE/EAuNPs$_1$, GCE/EAuNPs$_2$, GCE/EAuNPs$_3$, GCE/EAuNPs$_4$, and GCE/EAuNPs$_4$/rGO/Naf modified electrode surfaces was obtained to be 1.67 s^{-1}, 1.02 s^{-1}, 0.91 s^{-1}, 0.78 s^{-1}, 0.52 s^{-1} and 0.39 s^{-1}, respectively. From the above studies, the GCE/EAuNPs$_4$/rGO/Naf surface was found as the best in terms of conductivity and diffusion of charged species, as compare to bare GCE, GCE/EAuNPs$_1$, GCE/EAuNPs$_2$, GCE/EAuNPs$_3$, GCE/EAuNPs$_4$, electrodes. These above electrochemical characterizations showed that the sensor composed of GCE/EAuNPs$_4$/rGO/Naf surface is assisting in the charge transfer, hence most suitable for electrochemical sensing applications.

3.3. Analytical performance of sensing electrode

The sensing capability of GCE/EAuNPs$_4$/rGO/Naf sensor probe was assessed for the detection of SA. For that, the fabricated probe was tested towards SA detection using LSV. Firstly, bare GCE was dipped in 5 mM PBS (pH 7.6) (Blank) and LSV was recorded by sweeping the potentials between 0.05 and 0.8 V. In this case, no peak was observed (Figure 6(a) dotted line), however, when we added 150 μM SA in the electrochemical cell, a peak

TH-2627_166106107

around 0.47 V was observed, which was most likely due to the electrochemical oxidation of SA (Figure 6(a) green curve). In the case of GCE/EAuNPs$_4$ modified electrode, amplified current response at lower potential of 0.44 V was observed, that signifies the role of EAuNPs in the sensing matrix towards easier electrochemical oxidation of SA (Figure 6(a) blue curve). Similarly, in the case of GCE/rGO/Naf electrode the oxidation peak shifted towards lower potential of 0.44 V that is due to the increase in electro-conductivity of electrode (Figure 6(a) red curve). In the case of final sensor probe *i.e.* GCE/EAuNPs$_4$/rGO/Naf, a distinguished sharp peak was observed at lower potential, which was around 0.41 V. This clearly shows the importance of EAuNPs$_4$-rGO nanocomposite as an electro-catalytic and conducting sensing matrix, which is assisting towards sensitive detection of SA (Figure 2.5 (a) black curve). In order to validate the peak at 0.41V was merely due to the SA, two control experiments were performed. In the first control, four concentration of SA were tested, where the signal response increases linearly with concentrations of SA between 125 and 200 μM. The linear regression equation for concentration dependent plot is expressed as follows: ΔI (μA) = 0.0415 (± 0.008) + 2..46 x 10^{-4} (± 4.91 x10^{-5}) Conc. [SA (μM)] with the correlation coefficient of 0.98, indicating the ability of GCE/EAuNPs$_4$/rGO/Naf sensor for SA detection. In the second control experiment, a scan rate dependent study was performed at 150 μM of SA between 10 and 100 mV s^{-1} (Figure 2.5 (b). It was observed that peak currents (inset figure 2.5 (b)) increased linearly with the square root of scan rates, validating the diffusion control electrochemical process due to SA only. After validating the electronic properties and controls the analytical performance of GCE/EAuNPs$_4$/rGO/Naf electrode was evaluated by sensing SA at a scan rate of 0.05 V s^{-1} using DPV, as DPV is considered to be a more sensitive technique compared to LSV (Bard et al. 1980),(Chandra et al. 2011). Figure 2.5 (c) shows the representative DPV curves, where the current response increases with the

TH-2627_166106107

increase in SA concentrations. Based on the DPV responses, a calibration curve was ploted that shows the LDR from 20 to 200 µM for SA detection (Figure 6 (d)). The linear regression equation of the calibration plot for SA sensing was expressed as follows:

$$\Delta I\ (\mu A) = 0.0262\ (\pm\ 0.007) + 8.46 \times 10^{-4}\ (\pm\ 6.15 \times 10^{-5})\ \text{Conc. [SA (µM)]} \ldots\ldots\ldots (7)$$

with the regression coefficient of 0.968. The DL of SA was determined to be 33.43 nM (±0.21) nM (RSD<3.32%, 95 % confidence level, n=3) using equation 8.

$$DL = \frac{3\sigma_b}{m} \ldots\ldots\ldots\ldots\ldots\ldots\ldots\ldots\ldots\ldots\ldots\ldots (8)$$

Where, σ_b is standard deviation of blank and m is slope of the calibration curve.

Notably, in our case lower DL has been obtained for SA sensing, that is comparable to conventional HPLC and GC-MS methods, indicating the immense clinical importance of the fabricated sensor.

Rapidity is an important criteria for the commercial success of any sensor (Chandra 2015; Chandra and Segal 2016). Hence, we have investigated the response time of GCE/EAuNPs$_4$/rGO/Naf sensor probe, by performing chronoamperometry at 0.4V vs. Ag/AgCl in dynamic mode. Inset of figure 2.5 (d) shows the amperometric response recorded after addition of SA on a stabilized current, a sharp jump in the current was observed between 44 and 44.5 s, indicating that the sensor was able to detect SA in ≤ 0.50 s. It is important to note that a stable and considerably higher current value was observed after the saturation of the signal. It is worth mentioning that the detection time of ≤ 0.5 s

TH-2627_166106107

in our case is ultrafast and significantly lower to the traditional methods of SA detection based on HPLC, GC-MS, and LC-MS.

3.4. Selectivity study

To evaluate the commercial importance of any sensor, it is important to investigate its selectivity of sensor towards various possible interfering molecules (Mahato et al. 2018c). In order to determine the interfering effects, GCE/EAuNPs$_4$/rGO/Naf probe was tested towards glycine, L-cystine, alanine, serum albumin, uric acid, citric acid, ascorbic acid, and urea, which may potentially coexist with SA in real matrices. For the experiment, a continuous chronoamperometeric study was performed in which 0.4 V potential was applied onto the sensing electrode with respect to Ag/AgCl refernce electrode. Initially, a 200 µM SA was spiked into the electrochemical cell after the getting constant current, a sharp increase in the current was observed. After getting plateau in current, interfering molecules were sequentially injected in the running condition. No significant signal response was observed for the tested interfering compounds due to either their inherent electro-inactive behaviour (*e.g.* BSA) or due to the specific operational potential, where the tested molecules doesn't show any electrochemical response. The selectivity of GCE/EAuNPs$_4$/rGO/Naf probe was statistically inferred by determining the selectivity coefficient using equation 9 (Verma et al. 2019).

$$k_{sel} = \frac{(Signal)interfernt}{(Signal)sa} \text{ ---------- (9)}$$

Where k_{sel} is the coefficient of selectivity, $(Signal)_{interfernt}$ is the signal strength of sensor when treated with the interfering molecules and $(Signal)_{sa}$ is signal strength of SA.

The calculated k_{sel} values for interfering molecules were extremely low (<< 1), indicating that the fabricated sensor is highly selective towards SA detection. Figure 2.5 (e) shows

TH-2627_166106107

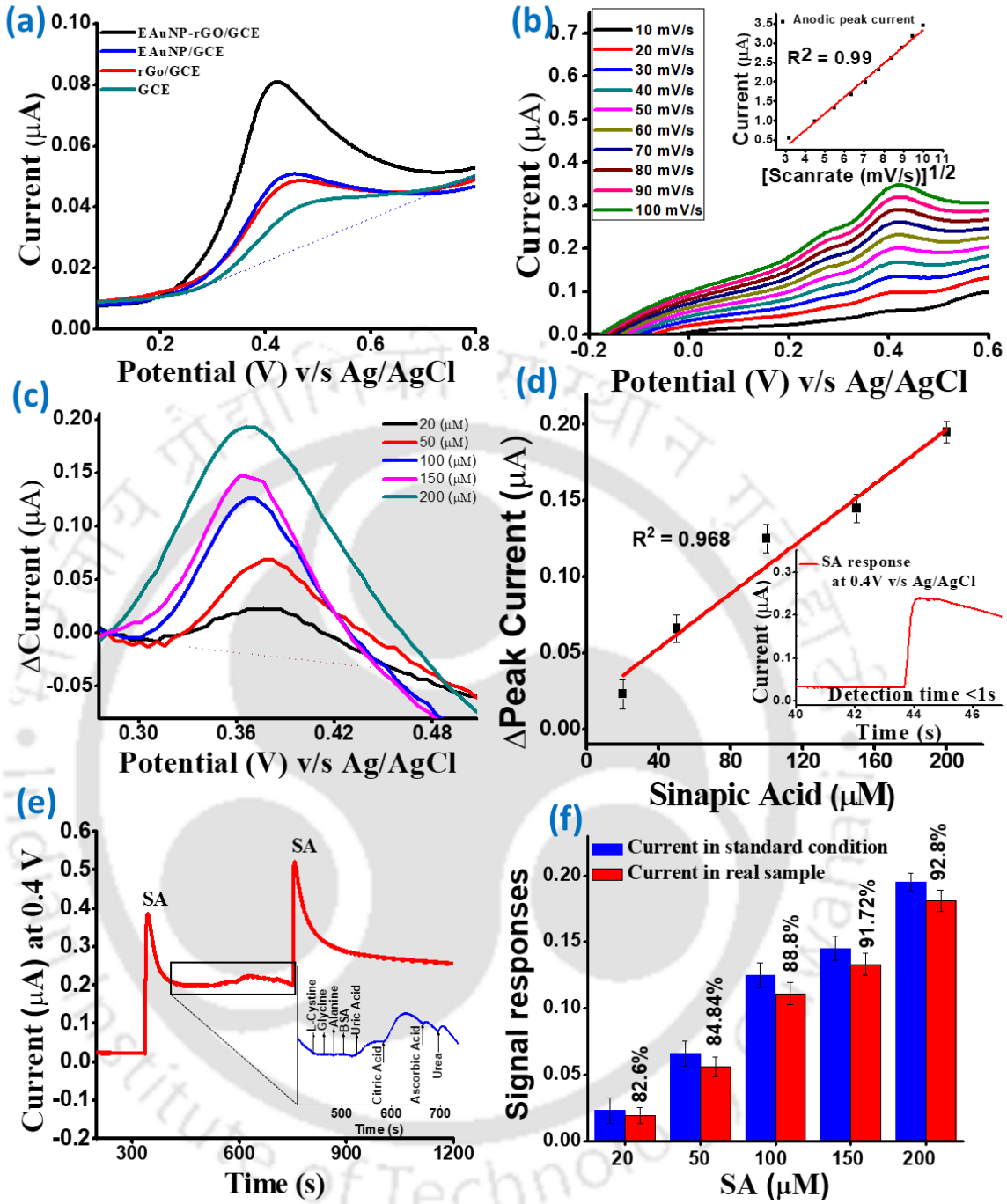

Figure 2.5: (a) Electrode responses with 200 µM SA, (b) Scan rate of GCE/EAuNPs4/rGO/Naf sensor in 200 µM SA, (c) response study of GCE/EAuNPs4/rGO/Naf sensor with respect to concentrations of SA, (d) corresponding calibration curve (inset: detection time of GCE/EAuNPs4/rGO/Naf sensor) (e) interference study of GCE/EAuNPs4/rGO/Naf sensor, and (f) real sample analysis onto the GCE/EAuNPs4/rGO/Naf sensor.

TH-2627_166106107

the chronoamperometeric response for SA and different interfering molecules tested at the sensor probe. Since, SA may coexist with other interfering molecules in a real system; therefore, we have also performed SA detection in mixed sample. After adding all the interfering molecules, 200 µM SA was added into this mixed sample. In this case, the signal was 98.9% similar to SA when it was detected initially. These results clearly indicates that the developed sensor was not only able to detect SA separately but also in mixed sample effectively. The interference study with chronoamperometeric technique not only confirms about the selectivity of the sensor but also describes the stability of the sensor in complex matrices.

3.5. Real sample analysis

The level of SA in urine has been tremendously studied in various clinical as well as pharmacological conditions (Kern et al. 2003; Nićiforović and Abramovič 2014). Therefore, we selected urine as a real sample matrix to show the practical applicability of the fabricated sensor. Moreover, tesing in urine provide pain-free (non-invasive) detection of SA. Initially, urine samples were equiliberated with PBS and SA was spiked into the electrochemical cell followed by its detection using the GCE/EAuNPs$_4$/rGO/Naf sensor. It is worth to mention that the urine samples were not subjected for any pretreatment step such as filtration or centrifugation in our study, hence the sensor developed in the present study has great potential of direct application in clinics. The results of these experiments were analyzed and % recoveries of SA were calculated using equation 10.

$$\text{Percentage recovery} = \frac{[S]sa - [B]sa}{[SS]sa} \quad \ldots\ldots\ldots\ldots (10)$$

Where, $[S]_{sa}$ and $[B]_{sa}$ are the analytical responses of SA in spiked and blank urine, respectively, and $[SS_{sa}]$ is the analytical response of SA in PBS solution.

TH-2627_166106107

Figure 2.5 (f) shows signal responses of SA detected in urine samples, where peak currents increased linearly with increase in the SA concentrations from 20 to 200 µM. Remarkably, the fabricated sensor is able to detect 82.8 to 93.34 % of SA from the urine samples. Table 2.1 indicates the percentage recovery on differnent concentrations of SA. Based on the dose dependent SA detection in urine, a calibration plot was obtained, which shows the linear regression equation as follows: ΔI (µA) = 0.0265 (± 0.006) + 8.04 x 10^{-4} (± 5.01 x10^{-5}) Conc. [SA (µM)] with the correlation coefficient of 0.95. The DL of 52.31 (± 0.02) µM was obtained in urine sample based on the standard deviation of three times consecutive analyses of the blank (95.21% confidence level; n=3).

This shows the fabricated sensor is highly capable of detecting SA even in complex biological matrices. A negligible higher DL (*i.e.* low sensitivity) in case of urine sample compare to blank buffer analysis was most likely due to the matrix effect of urine components.

3.6. Reproducibility and stability studies

For the translational viability of any sensor, reproducibility and stability evaluation is very important (Mahato et al. 2016). In this regard, we have tested our sensor for reproducibility by checking the current responses at three seperate electrodes prepared using similar protocol. The reproducibility of the sensor was evaluated, which showed the RSD < 5.1% (n = 3) and probe to probe RSD was < 4.2% even when the same fabrication process was followed (figure 2.6 (a)). These minor deviations were most likely due to the negligible variation in the sensor fabrication process and/ or handling errors. We have also tested long-term stability of our sensor, where the sensor retained almost 97.11 ± 2 % (RSD < 6.1 %) of its original response upto 6 weeks (Figure 2.6 (b)). Over this period, current

TH-2627_166106107

decreased with time, suggesting that the developed GCE/EAuNPs$_4$/rGO/Naf sensor is stable up to 6 weeks.

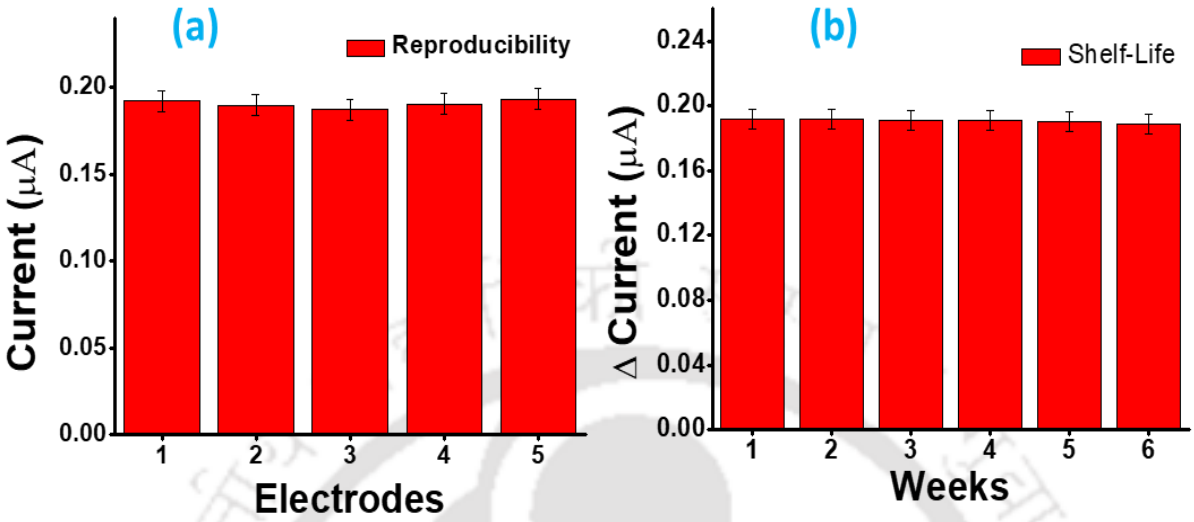

Figure 2.6: (a) The reproducibility of the GCE/EAuNPs$_4$/rGO/Naf sensor and (b) Long-term stability of GCE/EAuNPs$_4$/rGO/Naf sensor.

Sample	Spiked	Recovered	RSD %	% Recoveries
1.	20	16.57 ± 2.21	8.32	82.8 %
2.	50	46.67 ± 3.12	6.05	93.34 %
3.	100	88.91 ± 5.32	5.04	88.91 %
4.	150	138.54 ± 7.82	3.09	92.36 %
5.	200	181.73 ± 6.52	2.82	92.31 %

Table. 2.1. Percentage recovery of SA in real sample

TH-2627_166106107

4. Conclusions

In this study, we have fabricated a novel nanosensor for SA detection in human urine. The nanotuned EAuNPs and rGO were synthesized followed by their characterization using XRD, TEM, and Raman spectroscopy. The EuNPs-rGO nanocomposite were further characterized using electrochemical techniques and tested for electrochemical sensor fabrication using SA as a model compound. The EuNPs-rGO matrix showed the sensing of SA with a wide LDR of 20 - 200 µM and DL of 33.43 nM (±0.21) nM (RSD<3.32%, 95 % confidence level, n=3). Interestingly, this sensor was able to detect the SA in real sample with % recovery between 82.8 and 93.34 % in unprocessed human urine. To the best of our knowledge this is the first report where EuNPs-rGO nanocomposite has been used to detect SA. The GCE/EAuNPs$_4$/rGO/Naf is highly reproducible and the long-term stabality of the sensor was found upto 6 weeks. The sensor system fabricated has many outstanding features such as; simplicity, rapidity, label-free and low-cost detection, hence it could be a method of choice for SA detection in various clinical and pharmaceutical applications. In the next chapter we have tried to incorporate another material along with gold to make a bimetallic nanocomposite and designed a sensor for liver diseases.

TH-2627_166106107

5. *References*

Ali N, Oechsner A, Ahmed W (2010) Carbon Based Nanomaterials: Handbook. Trans Tech Publishers.

Baranwal A, Chandra P (2018) Clinical implications and electrochemical biosensing of monoamine neurotransmitters in body fluids, in vitro, in vivo, and ex vivo models. Biosens Bioelectron 121:137–152.

Bard AJ, Faulkner LR, Leddy J, Zoski CG (1980) Electrochemical methods: fundamentals and applications. wiley New York.

Bhakta SA, Evans E, Benavidez TE, Garcia CD (2015) Protein adsorption onto nanomaterials for the development of biosensors and analytical devices: A review. Anal Chim Acta 872:7–25.

Cao G, Wang Y (2004) Nanostructures and nanomaterials: synthesis. Prop Appl 2. Imperial college press, London.

Chandra P (2015) Electrochemical Nanobiosensors for Cancer Diagnosis. J Anal Bioanal Tech 6:.

Chandra P, Noh H-B, Pallela R, Shim Y-B (2015) Ultrasensitive detection of drug resistant cancer cells in biological matrixes using an amperometric nanobiosensor. Biosens Bioelectron 70:418–425.

Chandra P, Noh H-B, Won M-S, Shim Y-B (2011) Detection of daunomycin using phosphatidylserine and aptamer co-immobilized on Au nanoparticles deposited conducting polymer. Biosens Bioelectron 26:4442–4449.

Chandra P, (2016) Nanobiosensors for personalized and onsite biomedical diagnosis. The Institution of Engineering and Technology, Stevenage.

TH-2627_166106107

Chandra P, Singh J, Singh A, et al (2013) Gold Nanoparticles and Nanocomposites in Clinical Diagnostics Using Electrochemical Methods.

Dakshayini BS, Reddy KR, Mishra A, et al (2019) Role of conducting polymer and metal oxide-based hybrids for applications in ampereometric sensors and biosensors. Microchem J 147:7–24.

Fresco P, Borges F, Diniz C, Marques MPM (2006) New insights on the anticancer properties of dietary polyphenols. Med Res Rev 26:747–766.

Hailiang W, Joshua Tucker R, Xiaolin L, Hongjie D (2009) Solvothermal reduction of chemically exfoliated graphene sheets. J Am Chem Soc 131:9910.

Ignat M carbon nanotubes. A.Farcas,A.Vasile,E. Propovici, (2008) Calixarene-modified multi-wall carbon nanotubes Stud Surf Sci Catal 174:389–392.

Jasuja K, Berry V (2009) Implantation and Growth of Dendritic Gold Nanostructures on Graphene and Raman Enhancement. ACS Nano 3:2358–2366.

Kern SM, Bennett RN, Mellon FA, et al (2003) Absorption of hydroxycinnamates in humans after high-bran cereal consumption. J Agric Food Chem 51:6050–6055.

Kroon, Paul A and Williamson G (1999) Hydroxycinnamates in plants and food: current and future perspectives. J Sci Food Agric 79:355–361.

Kumar A, Purohit B, Maurya PK, et al (2019a) Engineered Nanomaterial Assisted Signal-amplification Strategies for Enhancing Analytical Performance of Electrochemical Biosensors. Electroanalysis 31:1615–1629.

Kumar A, Sharma S, Pandey LM (2018) Nanoengineered material based biosensing electrodes for enzymatic biofuel cells applications. Mater Sci Energy Technol 1:38–48.

TH-2627_166106107

Kumar S, Bukkitgar SD, Singh S, et al (2019b) Electrochemical Sensors and Biosensors Based on Graphene Functionalized with Metal Oxide Nanostructures for Healthcare Applications. ChemistrySelect 4:5322–5337.

Mahato K, Baranwal A, Srivastava A, et al (2018a) Smart Materials for Biosensing Applications. In: Pawar PM, Ronge BP, Balasubramaniam R, Seshabhattar S (eds) Techno-Societal 2016. Springer International Publishing, Cham, pp 421–431.

Mahato K, Kumar A, Maurya PK, Chandra P (2018b) Shifting paradigm of cancer diagnoses in clinically relevant samples based on miniaturized electrochemical nanobiosensors and microfluidic devices. Biosens Bioelectron 100:411–428.

Mahato K, Maurya PK, Chandra P (2018c) Fundamentals and commercial aspects of nanobiosensors in point-of-care clinical diagnostics. 3 Biotech 8:149.

Mahato K, Nagpal S, Shah MA, et al (2019) Gold nanoparticle surface engineering strategies and their applications in biomedicine and diagnostics. 3 Biotech 9:57.

Mahato K, Prasad A, Maurya P, Chandra P (2016) Nanobiosensors: next generation point-of-care biomedical devices for personalized diagnosis. J Anal Bioanal Tech 7:e125.

Mandal R, Baranwal A, Chandra P (2018) Evolving trends in bio / chemical sensors fabrication incorporating bimetallic nanoparticles. Biosens Bioelectron 117:546–561.

Nakaji D, Grillo V, Yamamoto N, Mukai T (2005) Contrast analysis of dislocation images in TEM-cathodoluminescence technique. J Electron Microsc (Tokyo) 54:223–230.

Narayanan KB, Sakthivel N (2008) Coriander leaf mediated biosynthesis of gold nanoparticles. Mater Lett 62:4588–4590.

Nenkova R, Wu J, Zhang Y, Godjevargova T (2013) Influence of different nanozeolite particles on the sensitivity of a glucose biosensor. Anal Biochem 439:65–72.

TH-2627_166106107

Nethravathi C, Rajamathi M (2008) Chemically modified graphene sheets produced by the solvothermal reduction of colloidal dispersions of graphite oxide. Carbon N Y 46:1994–1998.

Nićiforović N, Abramovič H (2014) Sinapic acid and its derivatives: Natural sources and bioactivity. Compr Rev Food Sci Food Saf 13:34–51.

Noh H-B, Chandra P, Moon JO, Shim Y-B (2012a) In vivo detection of glutathione disulfide and oxidative stress monitoring using a biosensor. Biomaterials 33:2600–2607.

Noh H-B, Lee K-S, Chandra P, et al (2012b) Application of a Cu–Co alloy dendrite on glucose and hydrogen peroxide sensors. Electrochim Acta 61:36–43.

Pallela R, Chandra P, Noh H-B, Shim Y-B (2016) An amperometric nanobiosensor using a biocompatible conjugate for early detection of metastatic cancer cells in biological fluid. Biosens Bioelectron 85:883–890.

Shetti NP, Bukkitgar SD, Reddy KR, et al (2019a) Nanostructured titanium oxide hybrids-based electrochemical biosensors for healthcare applications. Colloids Surfaces B Biointerfaces 178:385–394.

Shetti NP, Bukkitgar SD, Reddy KR, et al (2019b) ZnO-based nanostructured electrodes for electrochemical sensors and biosensors in biomedical applications. Biosens Bioelectron 141:111417.

Shetti NP, Malode SJ, Ilager D, et al (2019c) A Novel Electrochemical Sensor for Detection of Molinate Using ZnO Nanoparticles Loaded Carbon Electrode. Electroanalysis 31:1040–1049.

Shetti NP, Malode SJ, Nayak DS, et al (2019d) Nanostructured silver doped TiO2/CNTs

TH-2627_166106107

hybrid as an efficient electrochemical sensor for detection of anti-inflammatory drug, cetirizine. Microchem J 150:104124.

Siger A, Czubinski J, Dwiecki K, et al (2013) Identification and antioxidant activity of sinapic acid derivatives in Brassica napus L. seed meal extracts. Eur J Lipid Sci Technol 115:1130–1138.

Smitha SL, Philip D, Gopchandran KG (2009) Green synthesis of gold nanoparticles using Cinnamomum zeylanicum leaf broth. Spectrochim Acta - Part A Mol Biomol Spectrosc 74:735–739.

Srivastava A, Agarwal A, Gupta SK, Jain N (2016) Graphene oxide decorated with Cu(i)Br nanoparticles: A reusable catalyst for the synthesis of potent bis(indolyl)methane based anti HIV drugs. RSC Adv 6:23008–23011.

Thiyam U, Claudia P, Jan U, Alfred B (2009) De-oiled rapeseed and a protein isolate: Characterization of sinapic acid derivatives by HPLC-DAD and LC-MS. Eur Food Res Technol 229:825–831.

Thiyam U, Stöckmann H, Schwarz K (2006) Antioxidant activity of rapeseed phenolics and their interactions with tocopherols during lipid oxidation. JAOCS, J Am Oil Chem Soc 83:523–528.

Verma S, Choudhary J, Singh KP, et al (2019) Uricase grafted nanoconducting matrix based electrochemical biosensor for ultrafast uric acid detection in human serum samples. Int J Biol Macromol 130:333–341.

Verma S, Singh A, Shukla A, et al (2017) Anti-IL8/AuNPs-rGO/ITO as an Immunosensing Platform for Noninvasive Electrochemical Detection of Oral Cancer. ACS Appl Mater Interfaces 9:27462–27474.

TH-2627_166106107

Zhang K, Zuo Y (2004) GC-MS Determination of Flavonoids and Phenolic and Benzoic Acids in Human Plasma after Consumption of Cranberry Juice. J Agric Food Chem 52:222–227.

Zhang Z, Chen H, Xing C, et al (2011) Sodium citrate: A universal reducing agent for reduction / decoration of graphene oxide with au nanoparticles. Nano Res 4:599–611.

भारतीय प्रौद्योगिकी संस्थान गुवाहाटी • Indian Institute of Technology Guwahati •

TH-2627_166106107

TH-2627_166106107

Chapter – III

Gold - Iron Bimetallic Nanoparticles Impregnated Reduced Graphene Oxide Based Nano-sensor for Label-free Detection of Biomarker Related to Non-alcoholic Fatty Liver Disease.

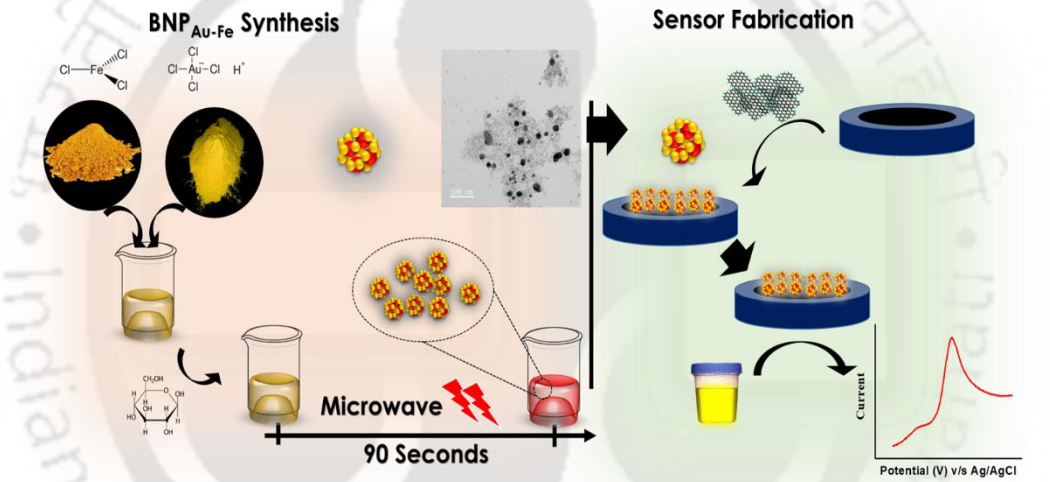

Status:

Published in Electroanalysis, Willy, 2019

TH-2627_166106107

1. Introduction

In this chapter, we have tried to develop a novel bimetallic nanomaterial for the detection of fatty liver disease. We have added iron with gold to target a potent drug that can be used for fatty liver disease biomarker. Over the last few decades, the amalgamation of nanosciences and biotechnology has had a significant impact on biomedical applications, including bio-imaging, biosensing, and targeted drug delivery (Chandra 2013; Tech et al. 2016; Mahato et al. 2018b). Recent advancements in application of nanomaterials (NM) in interdisciplinary research diaspora has transformed the paradigm of sensing of analytes of biological importance due to their exceptional optoelectronic properties (Ajayan 1999b; Nethravathi and Rajamathi 2008; Solanki et al. 2011; Pan et al. 2017; Shetti et al. 2019). Moreover, it has been perceived that chemical structure, active surface area, surface charge, quality of crystal structure and orientation of crystal in nanoparticles, etc. cumulatively effect electron transfer in electrochemical sensors (Zhu et al. 2012; Choudhary et al. 2016; Baranwal et al. 2018a; Mahato et al. 2018a; Kumar et al. 2019a, b). To accomplish the accurate sensing; they are progressively being engaged in development of modern sensors because of their unique electro-catalytic behavior. (Baranwal et al. 2018b; Kumar et al. 2018, 2019b) The synthesis of advanced engineered NM and their composites for the faster electron transfer at the transducing surface can pave a new dimension in the designing of enhanced modern sensors (Ajayan 1999a; Cao 2004; Cao and Wang 2004; Lu et al. 2010; Chandra et al. 2013). Among various engineered NM, mono-metallic viz. gold, silver, and platinum, are comprehensively considered as potent matrix materials that have been utilized to design many electrochemical sensors (Mandal et al. 2018). Recently, there has been increase in the researches on the development of NM having two or more than two metals to get the synergistic properties of constituent elements (Maduraiveeran et al. 2018). Bimetallic nanoparticles particularly of iron and gold ($BNP_{Au\text{-}Fe}$) has been widely synthesized which require several complex synthetic

procedures. There are number of reports on the synthesis of core shell BNP_{Au-Fe} for catalytic applications. Usually, the synthesis approaches for this BNP_{Au-Fe} require multi-step processes including high-end instruments, complex filtration, sequential synthesis, and time taking protocols (Ramachandran et al. 2016). Involvement of multi-step process, lengthy reaction time, expensive instruments, limit the quick synthesis of such BNP_{Au-Fe} and their composites. Moreover, the application of BNP_{Au-Fe} has not been widely explored in the domain of sensing, especially for clinically relevant molecules. There are only few reports on electrochemical sensors where BNP_{Au-Fe} has been used in the sensing matrices, which are based on direct electron transfer (DET) (Darabdhara et al. 2017). These sensors also suffer due to lengthy electrode preparation and low sensor sensitivity (Mandal et al. 2018). Therefore, there is a requirement of a simplistic approach for BNP_{Au-Fe} synthesis, which can be further applied to develop sensitive and stable electrochemical sensors.

In view of this, we have attempted to synthesize BNP_{Au-Fe} through a facile microwave assisted technique by using glucose as a reducing agent. The synthesized BNP_{Au-Fe} was characterized using UV-Vis spectroscopy (UV-Vis), X-ray diffraction (XRD), transmission electron microscopy (TEM), and Raman spectroscopy. Further, a proof-of-concept electrochemical sensor was developed by impregnating BNP_{Au-Fe} to rGO for electrochemical detection of acetaminophen. The sensor probe/material was characterized using TEM, CV, and EIS. Subsequently, the designed sensor was applied for dose dependent detection of acetaminophen to assess its analytical performance, i.e. linear dynamic range (LDR) and DL using differential pulse voltammetry (DPV). The practical applicability of the fabricated sensor was examined by testing acetaminophen in human urine samples using spike and recovery method. Interference due to various components was studied and the long-term stability of fabricated sensor was also evaluated.

2. Materials and methods

2.1. Materials, apparatus, and reagent preparation

Chloro-auric acid ($HAuCl_4$) and ferric chloride ($FeCl_3$,) were purchased from SRL, India. Deionized water was obtained from Millipore unit (Elix USA) having 18.2 MΩ cm resistance. Graphite powder, Hydrochloric acid (HCl), Ortho phosphoric acid (H_3PO_4) were obtained from SRL, India. Glucose, potassium ferrocyanide ($K_4[Fe(CN)_6]$), and potassium ferricyanide ($K_3[Fe(CN)_6]$) were obtained from Himedia, India. Hydrogen peroxide (H_2O_2), and potassium permanganate ($KMnO_4$) were purchased from Merck. Nafion 117 solution was purchased from Sigma. Sodium dihydrogen phosphate (NaH_2PO_4) and sodium phosphate (Na_2HPO_4) were purchased from Merck and SRL, respectively. All the chemicals were of AR grade and utilized without any additional purification.

2.2. $BNP_{Au\text{-}Fe}$ synthesis

Gold and Iron salt solutions were prepared separately and fresh every time for the $BNP_{Au\text{-}Fe}$ synthesis. A one-pot synthesis process was adapted, where 50 mL salt solution comprising gold and iron salt solutions in 1:4 molar ratio (optimized) taken and was stirred vigorously for 30 minutes using Hot plate magnetic stirrer (Tarson India; Spinot). Thereafter, 100 mM glucose solution (optimized) was prepared for reduction of metal ions in salt solution. The salt and reducing solutions were mixed to make final reaction mixture. To synthesize $BNP_{Au\text{-}Fe}$, the reaction mixture was then exposed to household microwave oven (LG, India; MC-8083MLR) and heated for 90 s at 900 W power. It was then 5 times washed with deionized water using Sigma (3-30K) centrifuge to remove the impurities followed by oven (Equitron) drying at 40°C for 12 hours. The optimization process for the formation of $BNP_{Au\text{-}Fe}$ with respect to the concentration of reducing agent and molar ratio of salt solution was monitored using UV-Vis spectrophotometer (Agilent USA; Carry 60).

2.3. Synthesis of rGO

For the rGO synthesis, graphite powder was first oxidized to form graphene oxide (GO) using modified Hummer's method (Choi et al. 2010; Lu et al. 2010; Murali et al. 2010). Briefly, in this process, H_2SO_4 and H_3PO_4 were mixed in volume ratio of 9:1 (27mL: 3mL) and stirred for 30 minutes. Then 0.225 g of graphite powder was added into mixing solution under stirring condition. 1.32 g of $KMnO_4$ was then added slowly into the solution. The mixture was uninterruptedly stirred for 6 hours until the final solution became blackish dark green. To neutralize the excess of $KMnO_4$, 0.675 mL of H_2O_2 was added dropwise while stirring in cold environment for 10 minutes. Thereafter, 10 mL of HCl and 30mL of deionized water was added into the solution and centrifuged at 5000 rpm for 7 minutes. The supernatant was emptied and the residuals were then washed again with HCl and deionized water for three times to obtain GO solution. The washed solution was dried in an oven at 90 °C for 24 hours to get the GO powder. After drying, the GO powder was exposed to microwaves to get rGO using the same domestic microwave oven at 900 W for 60 s. The rGO was instantly placed inside an oxygen free container to prevent its oxidation.

2.4. Fabrication of BNP_{Au-Fe} impregnated rGO sensing probe

For the fabrication of sensing probe, firstly a mixture solution of BNP_{Au-Fe} (0.5 mg) and rGO (1 mg) in 1 mL of 0.1% nafion solution was prepared. The mixture was sonicated for 3 hours in ultrasonic bath sonicator (Tempo 4A) at ambient conditions while maintaining temperature below 40°C. Thereafter, the sensor was fabricated by spin-coating the BNP_{Au-Fe}-rGO nanocomposite onto the previously cleaned GCE; area $0.01cm^2$. Precisely, 5 µl of the nanocomposite solution was deposited onto the GCE and allowed to dry in closed container for 3 hours to form the final sensing probe as BNP_{Au-Fe}-rGO/GCE. The details of BNP_{Au-Fe} synthesis and step-by-step electrode fabrication has been shown in scheme 3.

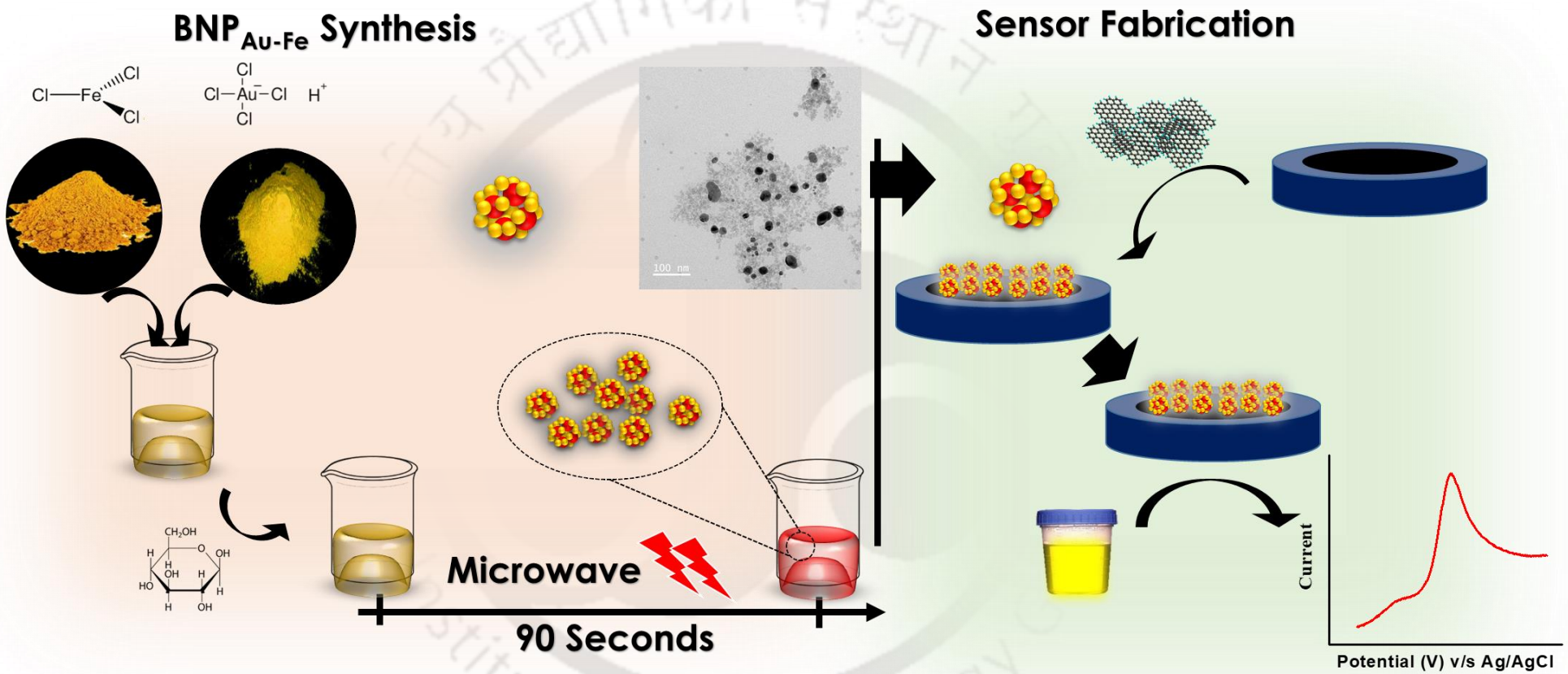

Scheme 3. Scheme of synthesis of BNP_{Au-Fe} and BNP_{Au-Fe} -rGO/GCE sensor fabrication.

2.5. Characterization of BNP_{Au-Fe}

2.5.1. UV-Visible (UV-Vis) spectroscopy analysis:

UV-Vis spectrophotometer (Carry 60) was used to determine the formation of BNP_{Au-Fe} present in the reaction mixture by scanning the aliquots between 200 and 800 nm range.

2.5.2. X-ray diffraction (XRD) analysis:

The crystalline nature of the BNP_{Au-Fe} was determined through a powder X-ray diffractometer (Rigaku MiniFlex 300), where, XRD analysis was performed at 2θ Bragg's angle by maintaining the range between 30° to 80° with a scan rate of 3° per minute.

2.5.3. Transmission electron microscopy (TEM) imaging and analyses:

Shape, size, dispersity, elemental mapping, and electron diffraction analyses of BNP_{Au-Fe} were performed on FE-TEM (JEOL JEM-2100F TEM). Samples were prepared by drop casting the well dispersed BNP_{Au-Fe} (in ethanol) onto the surface of carbon coated copper grid (300 mesh) and allowing it to dry at 37°C for 12 hrs.

2.5.4. Raman Spectroscopy:

BNP_{Au-Fe} and BNP_{Au-Fe} impregnated rGO were characterized for Raman scattering using Raman spectrophotometer (Laser Micro Raman System Horiba Jobin Vyon, Model LabRam HR). For Raman analysis, three separate films of BNP, rGO and BNP impregnated rGO were prepared onto the ITO

coated glass. A Co laser of 488 nm has been applied with 10 s reaction time to measure the Raman scattering in the range of 1200 to 2500 cm^{-1}.

2.5.5. Electrochemical characterization:

Electrochemical characterizations of bare GCE, GCE/ BNP_{Au-Fe}, GCE/rGO, and GCE/ BNP_{Au-Fe}-rGO probe was performed by CV, LSV, and EIS using Metrohm electrochemical analyser (Autolab potentiostat galvanostat). A phosphate buffer saline (PBS pH 7.6 and 0.9% NaCl) solution containing 5 mM $[Fe(CN)_6]^{-3/-4}$ was used as an electrolyte to perform all electrochemical characterization using Ag/AgCl as a reference electrode and Pt wire as a counter electrode.

3. Result and discussions

3.1. Physical Characterization of BNP_{Au-Fe}

3.1.1. UV- Visible spectroscopy:

The indication of BNP_{Au-Fe} formation has been observed with the change in the color of reaction mixture, which was changed from amber yellow to purple. Further, it was confirmed using UV-Vis spectrophotometer, the spectrum of sample was observed with the broad peak around 551 ± 3 nm. This is in conformity with the existing literature where researchers have reported peak of core shell iron and gold nanoparticles at about 555 nm (Sun et al. 2017). The broad peak is also indicative of the existence of iron and gold together in one nanoparticle (Sun et al. 2017). In order to further confirm that the peaks at 551 ± 3 nm is merely due to the

BNP_{Au-Fe} not the monometallic nanoparticles of gold or iron or their precursors or the glucose, we performed control experiments as follows:

1. Only $HAuCl_4$ solution without glucose with microwave exposure (Au+MW)
2. Only $FeCl_3$ solution with glucose with microwave exposure (Fe+Glu+MW)
3. Both $FeCl_3$ and $HAuCl_4$ solutions without glucose with microwave exposure (Fe+Au+MW)
4. Glucose only without any salt solution with microwave exposure (Glu+MW)

All four controls were subjected to the same reaction conditions and post reaction UV-Vis wavelength scan was taken for every control. No absorbance was observed in entire spectrum when $HAuCl_4$ without glucose was exposed to microwaves (control 1). Similarly, $FeCl_3$ salt solution did not give any peak in 400 to 700 nm range (control 2). This is indicating that iron was not being reduced under our experimental conditions and hence it can be inferred that monometallic iron nanoparticles were not formed. Similarly, no significant absorbance was obtained when both salt solutions together were exposed to microwaves without glucose (control 3). In the next control study, no absorbance was observed, when only glucose was exposed with microwave (control 4). However, $HAuCl_4$ under the given experimental conditions gave a peak at around 515 ± 2 nm, which was comparable to the spectrum of monometallic Au nanoparticles (Khlebtsov 2008; Information and Amendola 2009). This indicates that Au was reduced by the glucose under our experimental parameters. It is worth mentioning, there is a significant difference in absorbance wavelength in the case of BNP_{Au-Fe} formation that has been only possible because of iron salt

in the solution. These results clearly indicates the successful formation of BNP_{Au-Fe} in our experimental settings. It is possible to hypothesize that during this bimetallic synthesis, iron may acted as a catalytic partner in the formation of the BNP_{Au-Fe}. Considering the controls and test experiments it was found that the absorbance peak at 551 ± 3 nm was only because of BNP_{Au-Fe} formation, which was also confirmed using other characterization techniques discussed in later sections. Thereafter, we optimized the reducing agent concentration in the reaction by comparing the peak absorbance of the reaction solution at 551 ± 3 nm. The glucose concentration was varied from 10 mM to 100 mM and a linear plot was obtained in the range of 40 to 100 mM. At 100 mM glucose, the peak absorbance was maximum while over this concentration no further increase in the absorbance was observed. Hence, the maximum yield of BNP_{Au-Fe} was attained at 100 mM reducing agent concentration, and therefore, for further synthesis the same concentration was used. A comparative histogram of the absorbance at 551 ± 3 nm for the discussed controls and test is shown; it is worth to mention that the *p-value* obtained is less than 0.001 that is clearly indicating the BNP_{Au-Fe} synthesis was accurate and no possibility of formation monometallic nanoparticles in our experimental settings.

3.1.2. XRD studies:

To check the crystallinity of BNP_{Au-Fe}, we have performed X-ray diffraction study. A thin film of BNP_{Au-Fe} was made onto the glass substrate and it was tested while operating the instrument in film reading mode. The X-ray diffraction pattern of BNP_{Au-Fe} depicts the diffracted peaks corresponding to the (111), (200), (220), and (311) diffraction planes of gold, which is due the cubic phase of gold in BNP_{Au-Fe} that has been well indexed with JCPDS No: 65-2870 (Yan

et al. 2005; Jayaseelan et al. 2013). Furthermore, no peaks corresponds to iron were observed that is most likely due to formation of non-crystalline iron nanoparticles along with gold nanoparticles in BNP_{Au-Fe}. However, the presence of iron in BNP_{Au-Fe} was confirmed using other analytical techniques discussed in section 3.1.3. The average crystallite size was estimated as ~ 20 (±2) nm using all diffraction peaks with the help of Debye-Scherrer's equation.

$$D = \frac{0.9\lambda}{\beta\cos\theta} \qquad \ldots. (1)$$

Where λ=1.5460Å is the wavelength of target Cu-Kα, θ is the Bragg's angle of diffraction and β is the full-width half maximum of diffraction peak.

3.1.3. TEM imaging and analyses:

In order to characterize the size, shape, and distribution, TEM analyses of BNP_{Au-Fe} were performed. Clear dark spherical structures were observed in the whole field of imaging. These are presumably of gold, as gold is a heavy metal and therefore, the amount of electron absorbed by gold is large (Nakaji et al. 2005). Lighter diffused particulate structures were found around the gold nanoparticles, could be of iron particles. It is interesting to note that no such structures were observed in the area, where gold nanoparticle was absent. This clearly suggest that these structures are related to the bimetallic iron and gold nanocluster system, which was further confirmed by elemental mapping.

In order to validate the crystalline nature of BNP_{Au-Fe}, we have performed selected area electron diffraction (SAED) using TEM. SAED of the BNP_{Au-Fe} clearly showed the concentric diffraction pattern, which reveal the polycrystalline nature of the nanoparticles. In our case, we got the concentric rings that corresponds to lattice planes (111), (200), and (220) of gold, that is in well agreement of the results what we obtained in XRD. It is interesting to note that there has been formation of some diffused diffraction pattern also around the central maxima, most likely due to the electron diffraction from the amorphous iron present in BNP_{Au-Fe}. The d-fringes has been taken, where the interplanner distance of 0.251 nm was obtained, which corroborates to the XRD analysis, indicating the presence of (111) crystal plane. Thereafter, we calculated the size distribution of BNP_{Au-Fe} considering 151 particles using image-processing tool (ImageJ), where mean size of the particles were obtained with the diameter of 21 nm. The energy dispersive x-ray spectroscopy (EDX) was performed to further validate the presence of iron and gold in BNP_{Au-Fe}. EDX results showed the presence of 31.16% and 68.84 % iron and gold in the tested sample by weight, respectively, re-confirming the synthesis of BNP_{Au-Fe}. To validate the formation of BNP_{Au-Fe} nanoparticles, we have performed elemental mapping study. For elemental mapping, electron beam was focused onto the area having one dark particle in the centre. Each element has been highlighted by a different colour individually to show the presence of iron and gold in BNP_{Au-Fe}. The combined view of elemental mapping was also analyzed, which gives the position and distribution of a particular element in a given field.

This confirms two things: (i) the BNP_{Au-Fe} contains both metals and (ii) the dense dark regions are of gold surrounded by iron, confirming the iron coating onto the gold.

3.1.4. Raman Analysis:

In order to obtain the chemical and structural information about BNP_{Au-Fe}, rGO, and BNP_{Au-Fe}-rGO nanocomposite; we have performed raman spectroscopy. For BNP_{Au-Fe} multiple faint aberrations were observed, which is most likely due to the noise associated with BNP_{Au-Fe}. In the second spectrum, the two peaks were observed at 1323.3 and 1587.2 cm^{-1}, which corresponds to the characteristic peaks of rGO (designated as D and G peaks, respectively). In the next spectrum when BNP_{Au-Fe}-rGO nanocomposite was evaluated the appearance of similar peaks with the three-fold, enhanced intensity was observed. This is most likely due to the presence BNP_{Au-Fe} in nanocomposite that is enhancing the Raman scattering. Similar observation has also been reported, where metallic nanostructure had shown increase in the Raman scattering of rGO (Jasuja and Berry 2009). This is most likely due to the presence EAuNPs in nanocomposite that is enhancing the Raman scattering. Similar observation has also been reported, where metallic nanostructure had shown increase in the Raman scattering of rGO (Jasuja and Berry 2009). The I_D/I_G ratios for rGO and BNP_{Au-Fe}-rGO were found to be 0.74 and 0.71, respectively. The almost similar ratio for BNP_{Au-Fe}-rGO suggests that BNP_{Au-Fe} is not damaging the carbon sp^2 structure in graphene. In other words, the nanocomposite is quite stable and firm. (Zhang et al. 2011).

3.2. Electrochemical Characterizations

The suitability of BNP_{Au-Fe}-rGO has been tested electrochemically, where the change in the electrochemical response because of the surface modification of electrode was carried out by performing CV at a scan rate of 0.05 V/s in 3 mL PBS (pH 7.6) containing 5 mM $[Fe(CN)_6]^{-3/-4}$ solution. Figure 3.5 (a) shows the CV responses for bare GCE (blue), BNP_{Au-Fe}/GCE (black), rGO/GCE (red), and BNP_{Au-Fe}-rGO/GCE (green) surfaces. Representative voltamogram due to the redox process of $[Fe\ (CN)_6]^{-3/-4}$ was observed at bare GCE, while anodic (I*pa*) and cathodic (I*pc*) peak currents increased when BNP_{Au-Fe}/GCE surface was examined. This could be due to presence of gold nanoparticles of BNP_{Au-Fe} on the GCE surface, which increases the conductivity and surface area of electrode. Further, a separate bare GCE was modified with only rGO nanosheets and CV was recorded. Interestingly, we observed the increase in I*pa* and I*pc* compare to the bare GCE and BNP_{Au-Fe}/GCE surfaces, indicating that rGO is capable of giving amplified signal. Further, BNP_{Au-Fe}-rGO/GCE electrode was examined where maximum current response was observed compare to other tested electrodes (green), indicating that the electrode was best among all in term of conductivity, which could be due to the synergistic effect of BNP_{Au-Fe} and rGO (Niu et al. 2017). The peak current of each electrode has been shown in the inset of figure 3.5 (a). In order to investigate the charge transfer behaviour and stability of final sensing probe for electrochemical analysis, we performed scan rate studies at bare GCE, BNP_{Au-Fe}/GCE, rGO/GCE, and BNP_{Au-Fe}-rGO/GCE modified electrodes. The diffusion coefficient of electrode surfaces were calculated using Randles-Sevcik equation.

$$I_p = (2.69\times10^5)\ n^{3/2}AD^{1/2}C\upsilon^{1/2} \qquad \text{..... (2)}$$

Where I_p is the peak current of the electrode, n is the number of electrons transferred (n=1), A is the working electrode surface area, D is the diffusion coefficient, C is the concentration of the redox couple $[Fe(CN)6]^{-3/-4}$, and υ is the scan rate ($0.05 V\ s^{-1}$).

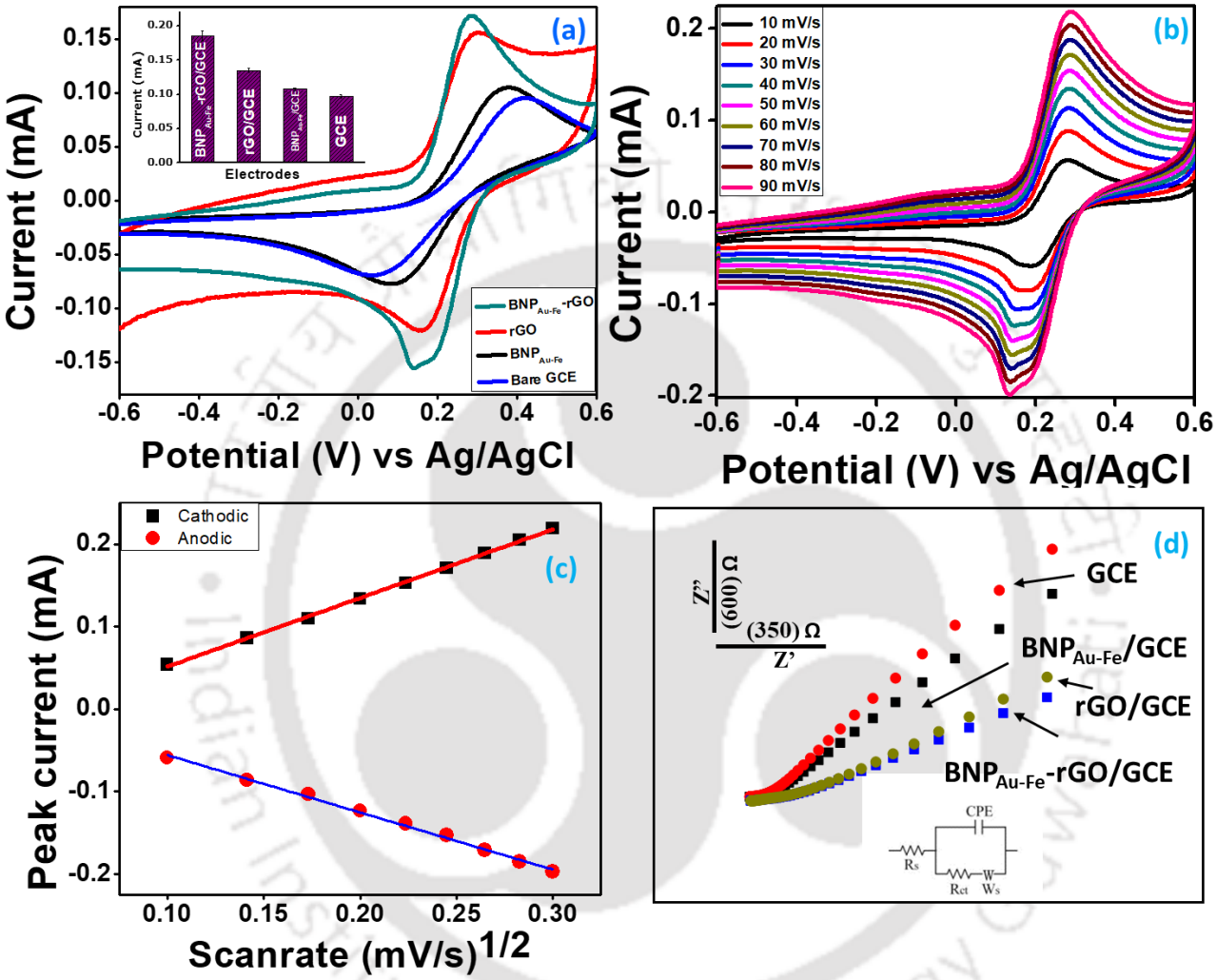

Figure 3.1: Electrochemical response of electrodes (a) CV for bare GCE (blue) BNP_{Au-Fe}/GCE (black), rGO/GCE (red), and BNP_{Au-Fe}-rGO/GCE (green) (inset anodic peak current), (b) scan rate response of BNP_{Au-Fe}-rGO/GCE electrode from 10 mV/s to 90 mV/s in Zobell solution, (c) Linear plot of I_{pc} and I_{pa} with repect to square root of scan rate, and (d) EIS plot for GCE (red), BNP_{Au-Fe}/GCE (black), rGO/GCE (olive green), and BNP_{Au-Fe}-rGO/GCE (blue).

Where the diffusion coefficient calculated as 8.65 $\times 10^{-10}$, 1.1 $\times 10^{-9}$, 1.9 $\times 10^{-9}$, and 3.1 $\times 10^{-9}$ $cm^2\ s^{-1}$ for GCE, BNP_{Au-Fe}/GCE, rGO/GCE, and BNP_{Au-Fe}-rGO/GCE, respectively. It is worth to mention that diffusion coefficient of BNP_{Au-Fe}-rGO/GCE modified electrode was found to be 3.87 times greater than that of the bare GCE, indicating the faster charge transfer in final probe. In the next step, the electrochemical interface kinetics study of BNP_{Au-Fe}-rGO/GCE electrode (Figure 3.5 (b)) was recorded at different scan rate (10 to 90 mV s^{-1}) in 5mM $[Fe(CN)_6]^{-3/-4}$. It was observed that both I_{pa} and I_{pc} peak currents varied linearly with the square root of scan rate figure 3.5 (c), indicating the diffusion-controlled process. The slopes and intercepts were given by the following equations:

I_{pa} (BNP_{Au-Fe}-rGO/GCE) = [0.83 µA(s mV^{-1}) (± 0.00869) × scan rate (mVs^{-1})] - 0.0315 (± 0.00194) µA, R^2=0.999…..... (3)

I_{pc} (BNP_{Au-Fe}-rGO/GCE) = - [0.6938 µA(s mV^{-1}) (± 0.01549) × scan rate (mVs^{-1})] – 0.013µA (± 0.00346), R^2=0.996 …….. (4)

The results obtained by CV were also validated using the EIS, where spectra in the Nyquist plot were recorded for bare GCE, BNP_{Au-Fe}/GCE, rGO/GCE, and BNP_{Au-Fe}-rGO/GCE modified electrode surfaces to obtain the resistance in charge transfer (Rct) as shown in figure 3.5 (d). The R_{ct} values obtained were 4441± 64.832 Ω, 3120 ± 42.31 Ω, 1298.5 ± 57.97 Ω, and 950 ± 23.10 Ω for the bare GCE (red), BNP_{Au-Fe}/GCE (black), rGO/GCE (green), BNP_{Au-Fe}-rGO/GCE (blue) surfaces, respectively. It is interesting to note that the lowest R_{ct} was obtained for BNP_{Au-Fe}-rGO/GCE (blue) surface compared to other tested surfaces. This was due to the fastest electron transfer kinetics at electrode/electrolyte interface in this case. The results obtained in EIS also corroborates with the results of CV analysis.

Since, electrocatalysis phenomena are surface charge dependent, the concentration of ionic species at electrode surface plays an important role. Therefore, in order to assess the

concentration of ionic species (I^*) using Brown-Anson model (Equation 5) is used (Verma et al. 2017).

$$I_p = \frac{n^2 F^2 I^* AV}{4RT} \qquad \ldots\ldots (5)$$

Where n is number of electrons (n=1, in this case), F is Faraday constant (96485.34 C mol^{-1}), T is 298 K, and I_p/V is the slope of calibration (scan rate value), A is surface area of the electrode (0.01 cm^2), and R is gas constant.

I^* for GCE, $BNP_{Au\text{-}Fe}$/GCE, rGO/GCE, and $BNP_{Au\text{-}Fe}$-rGO/GCE electrode was calculated as 1.95×10^{-7} M/cm^2, 2.03×10^{-7} M/cm^2, 2.27×10^{-7} M/cm^2, and 2.96×10^{-7} M/cm^2, respectively. These results clearly indicates that $BNP_{Au\text{-}Fe}$-rGO/GCE modified electrode has highest surface charge density compare to other surfaces. Further, the reaction kinetics at modified electrode surfaces was evaluated by using Laviron model (equation. 6), in order to find diverse electron transfer rate constant (K_s) (Verma et al. 2017).

$$K_s = mnFv/RT \qquad \ldots\ldots\ldots (6)$$

The calculated K_s for the GCE, $BNP_{Au\text{-}Fe}$/GCE, rGO/GCE, and $BNP_{Au\text{-}Fe}$-rGO/GCE modified electrode surfaces was obtained to be 1.37 s^{-1}, 1.04 s^{-1}, 0.79 s^{-1}, and 0.31 s^{-1},which indicate the $BNP_{Au\text{-}Fe}$-rGO/GCE modified electrode surfaces is capable of 4.5 times faster charge transfer compare to GCE.

From the above studies, the $BNP_{Au\text{-}Fe}$-rGO/GCE was found as the best electrode in term of conductivity and diffusion of charged species, as compare to GCE, rGO/GCE, and $BNP_{Au\text{-}Fe}$/GCE electrodes. These above electrochemical characterizations showed that the sensor composed of BNP-rGO nanocomposite is assisting in the charge transfer, hence most suitable for electrochemical sensing applications.

3.3. Analytical performance of BNP_{Au-Fe}-rGO/GCE sensor probe

The sensing capability of BNP_{Au-Fe}-rGO/GCE sensor probe was assessed for the detection of acetaminophen. For that, the fabricated probe was tested towards acetaminophen detection using LSV. Firstly, bare GCE was dipped in 5 mM PBS (pH 7.6) (Blank) and LSV was recorded by sweeping the potentials between - 0.05 and 0.65 V. In this case, no peak was observed (Figure 3.6 (a) black curve), however, when we added 800 nM acetaminophen in the electrochemical cell, a peak around 0.32 V was observed, which was most likely due to the electrochemical oxidation of acetaminophen (Figure 3.6 (a) pink curve), since some previous reports suggest the oxidation of acetaminophen near this potential (Su and Cheng 2010; Karikalan et al. 2016). In the case of BNP_{Au-Fe} modified electrode, a sharp increase in the oxidation current was observed at lower potential that is signifying the role of BNP_{Au-Fe} in the sensing matrix towards easier electrochemical detection of acetaminophen (Figure 3.6 (a) green curve). Similarly, in case of rGO/GCE the oxidation peak shifted towards lower potential that is due to the increase in electro-conductivity of electrode (Figure 3.6 (a) blue curve). In the case of final sensor probe *i.e.* BNP_{Au-Fe}-rGO/GCE, a distinguished sharp peak was observed at lower potential, which was around 0.22V. This clearly shows the importance of BNP_{Au-Fe}-rGO nanocomposite as an electro-catalytic sensing matrix, which may assist towards sensitive detection of acetaminophen (Figure 3.6 (a) red curve). In order to validate the peak was merely due to the acetaminophen two control experiments were performed. In the first control, three concentration of acetaminophen were tested, where the signal response increases linearly with concentrations of acetaminophen between 600 and 800 nM. The linear regression equation for concentration dependent plot is expressed as follows: $\Delta I\ (\mu A) = 0.124\ (\pm 0.00341) + 0.003\ (\pm 0.00471)$ Conc [Acetaminophen (nM)] with the correlation coefficient of 0.97, indicating the ability of BNP_{Au-Fe}-rGO/GCE sensor for acetaminophen detection. In the second control experiment, a scan rate dependent study was performed at 600 nM of

acetaminophen between 10 and 90 mV s^{-1} (Figure 3.6 (b)). It was observed that I_{pa} peak currents (inset figure 3.6 (b)) varied linearly with the square root of scan rate, validating the diffusion control electrochemical process of acetaminophen only. After validating the electronic properties of the developed sensor, the electrochemical response of $BNP_{Au\text{-}Fe}$-rGO/GCE electrode was measured as a function of acetaminophen concentration (50 to 800 nM) in 3 mL PBS at a scan rate of 0.05 V s^{-1} using DPV technique as DPV is considered to be a more sensitive technique compared to LSV (Bard et al. 1980)(Chandra et al. 2011). Figure 3.6 (c) shows the representative DPV curves, where the current response increases with the increase in acetaminophen concentrations. Based on the DPV responses, a calibration curve was ploted that shows the LDR from 50 to 800 nM of acetaminophen (Figure 3.6 (d)). The linear regression equation of the calibration plot for acetaminophen sensing was expressed as follows:

$$\Delta I\ (\mu A) = 3.04\ (\pm\ 0.3202) + 0.012\ (\pm\ 8.5 \times 10^{-5})\ \text{Conc. [acetaminophen (nM)]} \quad \ldots.(7)$$

with the regression coefficient of 0.971. The DL of acetaminophen was determined to be 0.14 nM (±0.05) (RSD< 4.12 %, 95 % confidence level, n=3) using equation 8.

$$DL = \frac{3\sigma_b}{m} \quad \ldots\ldots\ldots\ldots\ldots\ldots\ldots\ldots\ldots\ldots\ldots\ldots\ldots\ldots(8)$$

Where, σ_b is standard deviation of blank and m is slope of the calibration curve.

Notably, in our case obtained DL is lower and/or comparable to the recently reported acetaminophen sensors as shown in table 3.1 (Maduraiveeran et al. 2018; Zhang et al. 2018). It is worth mentioning, the detection range obtained in this case falls at the urine acetaminophen concentrations of patients suffering from non-alcoholoic fatty liver diseases (upto 1.3 M),(Barshop et al. 2011) indicating the immense clinical importance of the fabricated sensor.

Table 3.1. A detailed account of the comparative analytical performances of recently reported acetaminophen sensors.

Sl No.	Sensor probe design	LDR	DL	Real sample		Detection technique	References
1.	NiO-CuO	4 – 400 µM	1.33 µM	Yes	Serum	Square wave voltammetry	(Liu et al. 2016)
2.	ERG/GCE	5 nM – 800 µM	2.13 nM	Yes	Serum	Amperometric and DPV	(Adhikari et al. 2015)
3.	P-rGO/GCE	1.5 – 120 µM	0.36 µM	Yes	Drug	DPV	(Zhang et al. 2018)
4.	Graphite-polystyrene composite film modified electrode	0.02 – 100 µM	0.034 µM	Yes	Urine	DPV	(Khaskheli et al. 2013)
5.	AuNP-PGA/SWCNT/naf-nitrocellulose paper	50 – 300 µM	15 µM	Yes	Drug	DPV	(Lee et al. 2016)
6.	Pd/GO nanocomposite	0.005 – 0.5 µM and 0.5 – 80 µM	2.2 nM	Yes	Urine	DPV	(Li et al. 2014)
7.	Ti/AuNi NPs	0.00 – 1.75 µM	0.51 nM	Yes	Serum	Amperometric	(Maduraiveeran et al. 2018)
8.	Pt-Den-PANI-CNT Platinum dendrimer polyaniline carbon nanotube	20 – 1 mM	NR	NR	NR	Amperometric	(Deb et al. 2016)
9.	**BNP_{Au-Fe}-rGO/GCE**	**50 – 800 nM**	**0.14 nM (±0.05)**	**Yes**	**Urine**	**DPV**	**This Work**

3.4. Selectivity study

To evaluate the commercial importance of any sensor, it is important to investigate the selectivity of sensor towards various possible interfering molecules (Mahato et al. 2018c). In order to determine the interfering effects, $BNP_{Au\text{-}Fe}$-rGO/GCE probe was tested towards glycine, L-cystine, glutamic acid, alanine, glucose, BSA, citric acid, and ascorbic acid, which potentially coexist with acetaminophen in real matrix. No significant signal response was observed for the tested interfering compounds due to either their inherent electro-inactive behaviour (*e.g.* glucose, BSA) or due to the different operational potential window. The selectivity of $BNP_{Au\text{-}Fe}$-rGO/GCE probe was statistically inferred by determining the selectivity coefficient using equation 9.

$$k_{sel} = \frac{(Signal)interfernt}{(Signal)acetaminophen} \text{ ---------- (9)}$$

Where k_{sel} is the coefficient of selectivity, $(Signal)_{interfernt}$ is the signal strength of sensor when treated with the interfering molecules and $(Signal)_{acetaminophen}$ is signal strength of acetaminophen.

The calculated k_{sel} values for interfering molecules were extremely low (<< 1), indicating that the fabricated sensor is highly selective towards acetaminophen detection. Figure 3.6 (e) shows the comparatives histograms obtained from DPV responses of acetaminophen and different interfering molecules at the sensor probe. We have also performed acetaminophen detection in a mixed sample. In this case, the signal was 94.3% similar to acetaminophen when it was detected separately. These results clearly indicates that the developed sensor was not only able to detect acetaminophen separately but also in mixed sample, effectively.

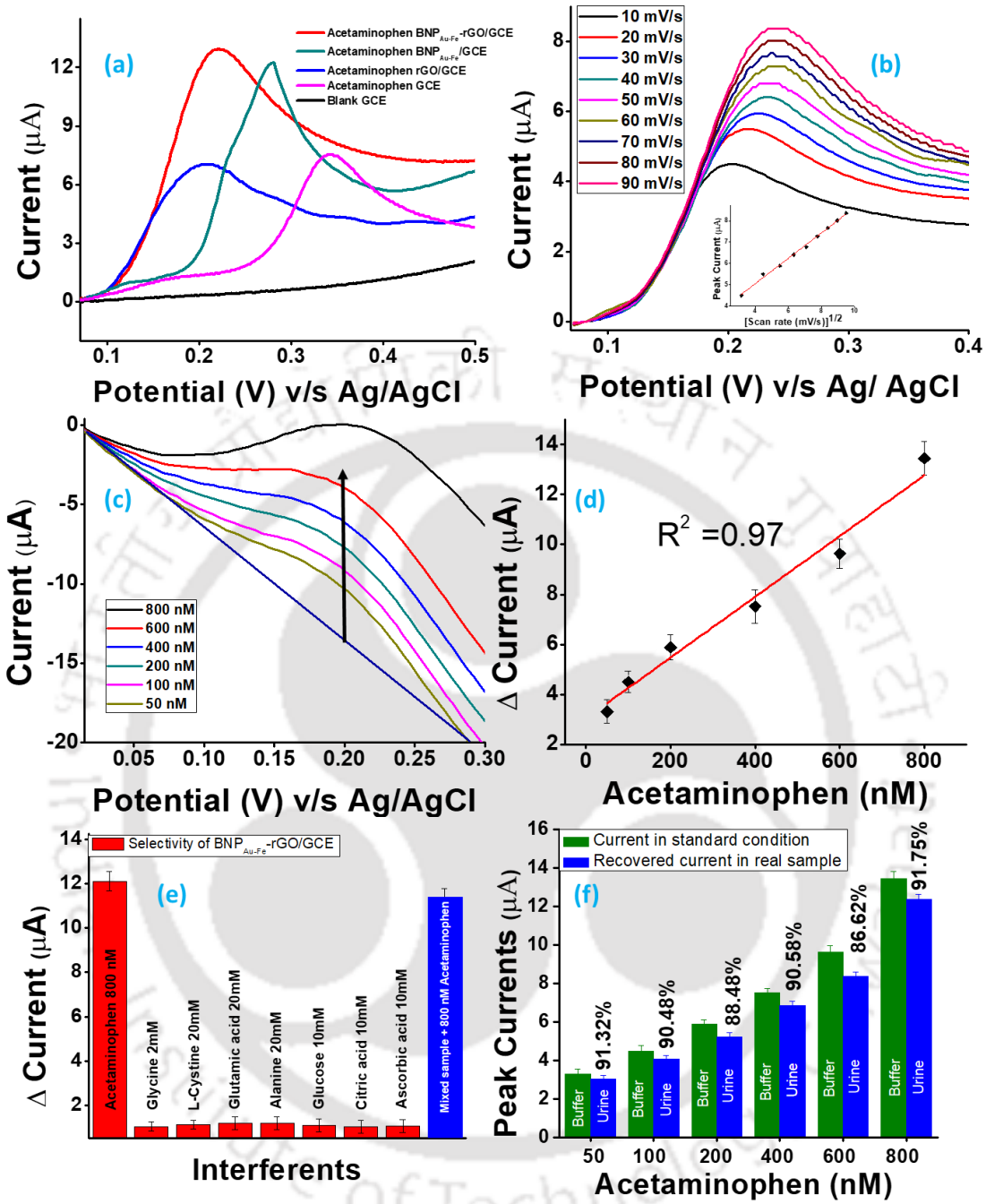

Figure 3.2: (a) Electrochemical responses of acetaminophen at various modified surfaces, (b) scan rate study of BNP_{Au-Fe}-rGO/GCE sensor with acetaminophen (inset shows the corresponding plot), (c) response study of BNP_{Au-Fe}-rGO/GCE sensor with respect to concentrations of acetaminophen, (d) corresponding calibration curve, (e) interference study of BNP_{Au-Fe}-rGO/GCE, and (f) real sample analysis onto the BNP_{Au-Fe}-rGO/GCE.

3.5. Real sample analysis

In hospitals, acetaminophen levels are often analyzed in urine samples in various clinical conditions (Barshop et al. 2011) such as non-alcoholoic fatty liver diseases (Benson 1983; Mitic-Zlatkovic and Stefanovic 1999; Barshop et al. 2011).Therefore, we selected urine as a real sample matrix to show the practical applicability of the fabricated sensor. Initially, urine samples were equiliberated with PBS and acetaminophen was spiked into the electrochemical cell followed by its detection using the $BNP_{Au\text{-}Fe}$-rGO/GCE sensor. It is worth to mention that the urine samples were not subjected for any pretreatment step such as filtration or centrifugation in our study, hence the sensor developed in the present study has great potential of direct application in clinics. The results of these experiments were analyzed and % recoveries of acetaminophen were calculated using equation 10.

$$\text{Percentage recovery} = \frac{[S]aceta - [B]aceta}{[SS]aceta} \quad \ldots\ldots\ldots\ldots (10)$$

Where, $[S]_{aceta}$ and $[B]_{aceta}$ are the analytical responses of acetaminophen in spiked and blank urine, respectively, and $[SS]_{aceta}$ is the analytical response of acetaminophen in PBS solution.

Sample	Spiked	Recovered	RSD %	% Recoveries
1.	50	46.07 ± 4.21	5.12	91.32 %
2.	100	91.11 ± 6.32	4.02	90.48 %
3.	200	178.91 ± 12.21	6.04	88.48 %
4.	400	364.94 ± 17.82	5.04	90.58 %
5.	600	522.89 ± 16.92	3.06	86.62 %
6.	800	736.81 ± 20.12	3.21	91.75 %

Table. 3.2. Percentage recovery of acetaminophen in urine sample

Figure 3.6 (f) shows signal responses of acetaminophen detected in urine samples, where peak currents increased linearly with increase in the acetaminophen concentrations from 50 to 800 nM. Remarkably, the fabricated sensor is able to detect 86.65 % to 91.32% of acetaminophen from the urine samples. Based on the dose dependent acetaminophen detection in urine, a calibration plot was obtained, which shows the linear regression equation as follows: ΔI (μA)= 2.71(±0.41) + 0.1104 (±0.00103) Conc [acetaminophen (nM)] with the correlation coefficient of 0.958. The DL of 2.31 (± 0.01) nM was obtained in urine sample based on the standard deviation of three times consecutive analyses of the blank (94.12% confidence level; n=3). This shows the fabricated sensor is highly capable of detecting acetaminophen even in complex biological matrices. A negligible higher DL (*i.e.* low sensitivity) in case of urine sample compare to blank buffer analysis was most likely due to the matrix effect of urine components.

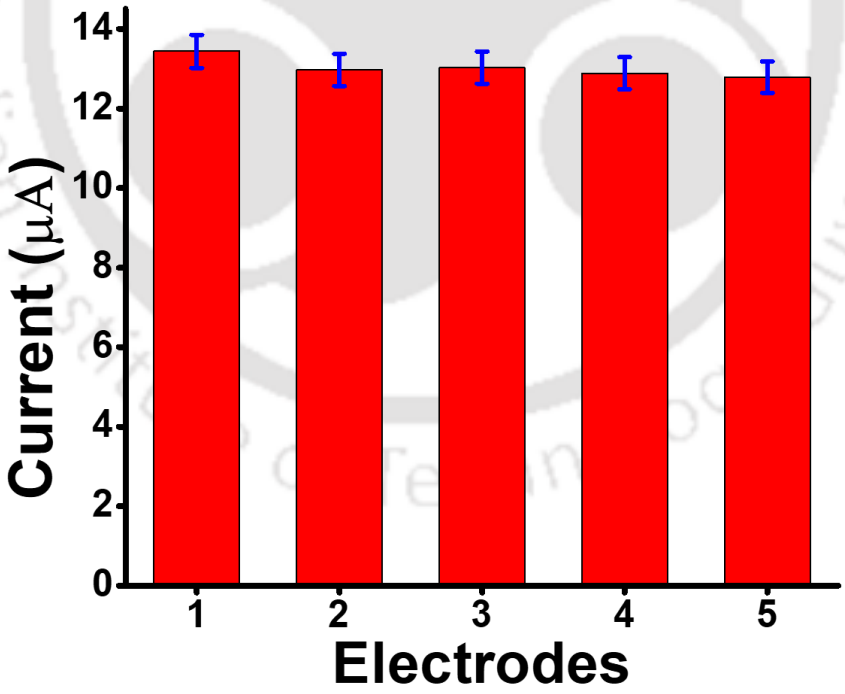

Figure 3.3: The reproducibility of the $BNP_{Au\text{-}Fe}$-rGO/GCE sensor.

3.6. Reproducibility and stability studies

For the translational viability of any sensor, reproducibility and stability is of major concern (Mahato et al. 2018c). In this regard, we have tested our sensor for reproducibility by checking the current responses with three seperate electrodes, prepared using similar protocol. The reproducibility of the sensor was evaluated, which showed the RSD < 4.4% (n = 3) and probe to probe RSD was < 6.8% even when the same fabrication process was followed as shown in figure 3.7. This minor variation was most likely due to the negligible variation in the sensor fabrication process and handling errors. We have also tested long-term stability of our sensor, it was observed that the sensor retained almost 93.11 ± 2 % (RSD < 5.1 %) of its original response over 10 weeks as shown in figure 3.8. Over the period, current decreased with time, suggesting that, the developed $BNP_{Au\text{-}Fe}$-rGO/GCE sensor is stable up to 10 weeks. The stability of the sensor is possibly due to the absence of any biological molecules which may denatures during the storage conditions.

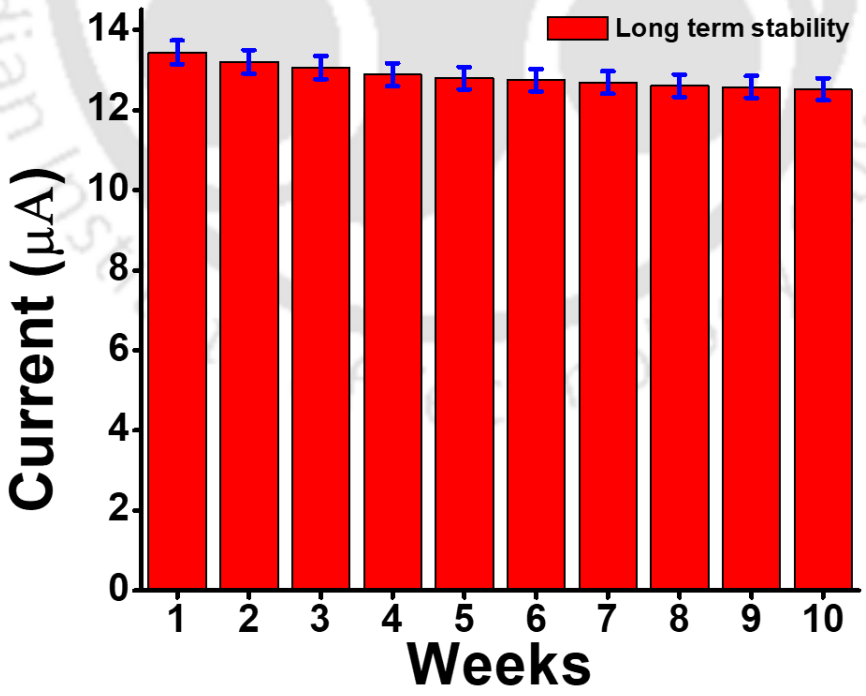

Figure 3.4: Long-term stability of $BNP_{Au\text{-}Fe}$-rGO/GCE sensor.

4. Conclusions

In this study we have synthesized BNP_{Au-Fe} using a facile and stable process of microwave irradiation within 90s in presence of glucose. The BNP_{Au-Fe} was characterized using UV-Vis, XRD, TEM, EDX, elemental mapping, and raman spectroscopy. The BNP_{Au-Fe} was further characterized using electrochemical techniques and tested for electrochemical sensor fabrication using acetaminophen as a model compound. The BNP_{Au-Fe} impregnated rGO matrix showed the sensing of acetaminophen with a wide LDR of 50 – 800 nM and DL of 0.14 nM (±0.05) nM (RSD< 4.12%) that was lower compared to previously reported acetaminophen sensors. Moreover, the sensor was capble to detect the acetaminophen in real sample with % recovery between 86.65 and 91.32% in unprocessed human urine. To the best of our knowledge this is the first report where BNP_{Au-Fe} impregnated rGO was used to detect acetaminophen. The sensor was able to sense the acetaminophen upto 10 weeks. The sensor system fabricated has many outstanding features such as; simplicity, rapidity, label-free and low-cost detection, hence it could be a method of choice for acetaminophen detection in various clinical and pharmaceutical samples. In future, as prepared BNP_{Au-Fe}-rGO nanocomposite based sensor can be utilized to make a miniaturized point-of-care diagnostic device for diagnosis of non-alcoholic fatty liver diseases related to acetaminophen. In the next chapter we have replaced the gold from our system to make it more cost-effective and developed a new sensor for glucose, which has more commercial acclamation.

5. *References*

Adhikari BR, Govindhan M, Chen A (2015) Sensitive detection of acetaminophen with graphene-based electrochemical sensor. Electrochim Acta 162:198–204.

Ajayan PM (1999a) Nanotubes from carbon. Chem Rev 99:1787–1800.

Amendola V (2009) Size Evaluation of Gold Nanoparticles by UV # vis Spectroscopy Size Evaluation of Gold Nanoparticles by UV - vis Spectroscopy. Journ. Phy. Chem. C. Support Inf 2:1–5.

Baranwal A, Chiranjivi AK, Kumar A, et al (2018a) Design of commercially comparable nanotherapeutic agent against human disease-causing parasite, Leishmania. Sci Rep 8:8814.

Baranwal A, Kumar A, Priyadharshini A, et al (2018b) Chitosan: An undisputed bio-fabrication material for tissue engineering and bio-sensing applications. Int J Biol Macromol 110:110–123.

Bard AJ, Faulkner LR, Leddy J, Zoski CG (1980) Electrochemical methods: fundamentals and applications. wiley New York.

Barshop NJ, Capparelli E V, Sirlin CB, et al (2011) Acetaminophen pharmacokinetics in children with nonalcoholic fatty liver disease. J Pediatr Gastroenterol Nutr 52:198.

Benson GD (1983) Acetaminophen in chronic liver disease. Clin Pharmacol Ther 33:95–101.

Cao G (2004) Nanostructures & nanomaterials: synthesis, properties & applications. Imperial college press, London.

Cao G, Wang Y (2004) Nanostructures and nanomaterials: synthesis. Prop Appl 2: Imperial college press, London.

Chandra P (2013) Advances in clinical diagnosis through electrochemical aptamer sensors. J Bioanal Biomed 5:5–6.

Chandra P, Noh H-B, Won M-S, Shim Y-B (2011) Detection of daunomycin using phosphatidylserine and aptamer co-immobilized on Au nanoparticles deposited conducting polymer. Biosens Bioelectron 26:4442–4449.

Chandra P, Singh J, Singh A, et al (2013) Gold Nanoparticles and Nanocomposites in Clinical Diagnostics Using Electrochemical Methods.

Choi W, Lahiri I, Seelaboyina R, Kang YS (2010) Synthesis of graphene and its applications: A review. Crit Rev Solid State Mater Sci 35:52–71.

Choudhary M, Yadav P, Singh A, et al (2016) CD 59 targeted ultrasensitive electrochemical immunosensor for fast and noninvasive diagnosis of oral cancer. Electroanalysis 28:2565–2574.

Darabdhara G, Sharma B, Das MR, et al (2017) Cu-Ag bimetallic nanoparticles on reduced graphene oxide nanosheets as peroxidase mimic for glucose and ascorbic acid detection. Sensors Actuators B Chem 238:842–851.

Deb AK, Das SC, Saha A, et al (2016) Ascorbic acid , acetaminophen , and hydrogen peroxide detection using a dendrimer-encapsulated Pt nanoparticle carbon nanotube

Jasuja K, Berry V (2009) Implantation and Growth of Dendritic Gold Nanostructures on Graphene and Raman Enhancement. ACS Nano 3:2358–2366.

Jayaseelan C, Ramkumar R, Rahuman AA, Perumal P (2013) Green synthesis of gold nanoparticles using seed aqueous extract of Abelmoschus esculentus and its antifungal activity. Ind Crops Prod 45:423–429.

Karikalan N, Karthik R, Chen SM, et al (2016) Electrochemical properties of the

acetaminophen on the screen printed carbon electrode towards the high performance practical sensor applications. J Colloid Interface Sci 483:109–117.

Khaskheli AR, Fischer J, Barek J, et al (2013) Differential pulse voltammetric determination of paracetamol in tablet and urine samples at a micro-crystalline natural graphite-polystyrene composite film modified electrode. Electrochim Acta 101:238–242.

Khlebtsov NG (2008) Determination of size and concentration of gold nanoparticles from extinction spectra. Anal Chem 80:6620–6625.

Kumar A, Purohit B, Mahato K, Chandra P (2019a) CHAPTER 11. Advance Engineered Nanomaterials in Point-of-care Immunosensing for Biomedical Diagnostics. Immunosensors RSC 238–266.

Kumar A, Purohit B, Maurya PK, et al (2019b) Engineered Nanomaterial Assisted Signal-amplification Strategies for Enhancing Analytical Performance of Electrochemical Biosensors. Electroanalysis 31:1615–1629.

Kumar A, Sharma S, Pandey LM (2018) Nanoengineered material based biosensing electrodes for enzymatic biofuel cells applications. Mater Sci Energy Technol 1:38–48.

Lee SH, Lee JH, Tran VK, et al (2016) Determination of acetaminophen using functional paper-based electrochemical devices. Sensors Actuators, B Chem 232:514–522.

Li J, Liu J, Tan G, et al (2014) Biosensors and Bioelectronics High-sensitivity paracetamol sensor based on Pd / graphene oxide nanocomposite as an enhanced electrochemical sensing platform. Biosens Bioelectron 54:468–475.

Liu B, Ouyang X, Ding Y, et al (2016) Electrochemical preparation of nickel and copper oxides-decorated graphene composite for simultaneous determination of dopamine, acetaminophen and tryptophan. Talanta 146:114–121.

Lu W, Slesarev A, Sun Z, et al (2010) Improved Synthesis of Graphene Oxide. ACS Nano 4:4806–4814.

Maduraiveeran G, Rasik R, Sasidharan M, Jin W (2018) Bimetallic gold-nickel nanoparticles as a sensitive amperometric sensing platform for acetaminophen in human serum. J Electroanal Chem 808:259–265.

Mahato K, Baranwal A, Srivastava A, et al (2018a) Smart Materials for Biosensing Applications. In: Pawar PM, Ronge BP, Balasubramaniam R, Seshabhattar S (eds) Techno-Societal 2016. Springer International Publishing, Cham, pp 421–431.

Mahato K, Kumar S, Srivastava A, et al (2018b) Chapter 14 - Electrochemical Immunosensors: Fundamentals and Applications in Clinical Diagnostics. In: Vashist SK, Luong JHT (eds) Handbook of Immunoassay Technologies. Academic Press, pp 359–414.

Mahato K, Maurya PK, Chandra P (2018c) Fundamentals and commercial aspects of nanobiosensors in point-of-care clinical diagnostics. 3 Biotech 8:149.

Mandal R, Baranwal A, Srivastava A, Chandra P (2018) Evolving trends in bio/chemical sensor fabrication incorporating bimetallic nanoparticles. Biosens Bioelectron 117:546–561.

Mitic-Zlatkovic M, Stefanovic V (1999) Acute effects of acetaminophen on renal function and urinary excretion of some proteins and enzymes in patients with kidney disease. Ren Fail 21:525–532.

Murali S, Suk JW, Li X, et al (2010) Graphene and Graphene Oxide: Synthesis, Properties, and Applications. Adv Mater 22:3906–3924.

Nakaji D, Grillo V, Yamamoto N, Mukai T (2005) Contrast analysis of dislocation images in

TEM-cathodoluminescence technique. J Electron Microsc (Tokyo) 54:223–230.

Nethravathi C, Rajamathi M (2008) Chemically modified graphene sheets produced by the solvothermal reduction of colloidal dispersions of graphite oxide. Carbon N Y 46:1994–1998.

Niu X, Zheng W, Yin C, et al (2017) Electrochemical DNA biosensor based on gold nanoparticles and partially reduced graphene oxide modified electrode for the detection of Listeria monocytogenes hly gene sequence. J Electroanal Chem 806:116–122.

Pan LH, Kuo SH, Lin TY, et al (2017) An electrochemical biosensor to simultaneously detect VEGF and PSA for early prostate cancer diagnosis based on graphene oxide/ssDNA/PLLA nanoparticles. Biosens Bioelectron 89:598–605.

Ramachandran K, Babu KJ, others (2016) Ni-Co bimetal nanowires filled multiwalled carbon nanotubes for the highly sensitive and selective non-enzymatic glucose sensor applications. Sci Rep 6:36583.

Shetti NP, Malode SJ, Nayak DS, et al (2019) Nanostructured silver doped TiO2/CNTs hybrid as an efficient electrochemical sensor for detection of anti-inflammatory drug, cetirizine. Microchem J 150:104124.

Solanki PR, Kaushik A, Agrawal V V., Malhotra BD (2011) Nanostructured metal oxide-based biosensors. NPG Asia Mater. 3:17–24.

Su WY, Cheng SH (2010) Electrochemical oxidation and sensitive determination of acetaminophen in pharmaceuticals at poly(3,4-ethylene-dioxythiophene)-modified screen-printed electrodes. Electroanalysis 22:707–714.

Sun K, Cheng T, Wu L, et al (2017) Ultrahigh mass activity for carbon dioxide reduction enabled by gold--iron core--shell nanoparticles. J Am Chem Soc 139:15608–15611.

Mahato K, Prasad A, et al (2016) Nanobiosensors: Next Generation Point-of-Care Biomedical Devices for Personalized Diagnosis. J Anal Bioanal Tech 7.

Verma S, Singh A, Shukla A, et al (2017) Anti-IL8/AuNPs-rGO/ITO as an Immunosensing Platform for Noninvasive Electrochemical Detection of Oral Cancer. ACS Appl Mater Interfaces 9:27462–27474.

Yan W, Petkov V, Mahurin SM, et al (2005) Powder XRD analysis and catalysis characterization of ultra-small gold nanoparticles deposited on titania-modified SBA-15. Catal Commun 6:404–408.

Zhang X, Wang KP, Zhang LN, et al (2018) Phosphorus-doped graphene-based electrochemical sensor for sensitive detection of acetaminophen. Anal Chim Acta 1036:26–32.

Zhang Z, Chen H, Xing C, et al (2011) Sodium citrate: A universal reducing agent for reduction / decoration of graphene oxide with au nanoparticles. Nano Res 4:599–611.

Zhu Y, Chandra P, Shim Y-B (2012) Ultrasensitive and selective electrochemical diagnosis of breast cancer based on a hydrazine--Au nanoparticle--aptamer bioconjugate. Anal Chem 85:1058–1064.

TH-2627_166106107

Chapter – IV

Novel Non-enzymatic Electrochemical Glucose Biosensor Based on Gadolinium-Iron Bimetallic Nanocomposite.

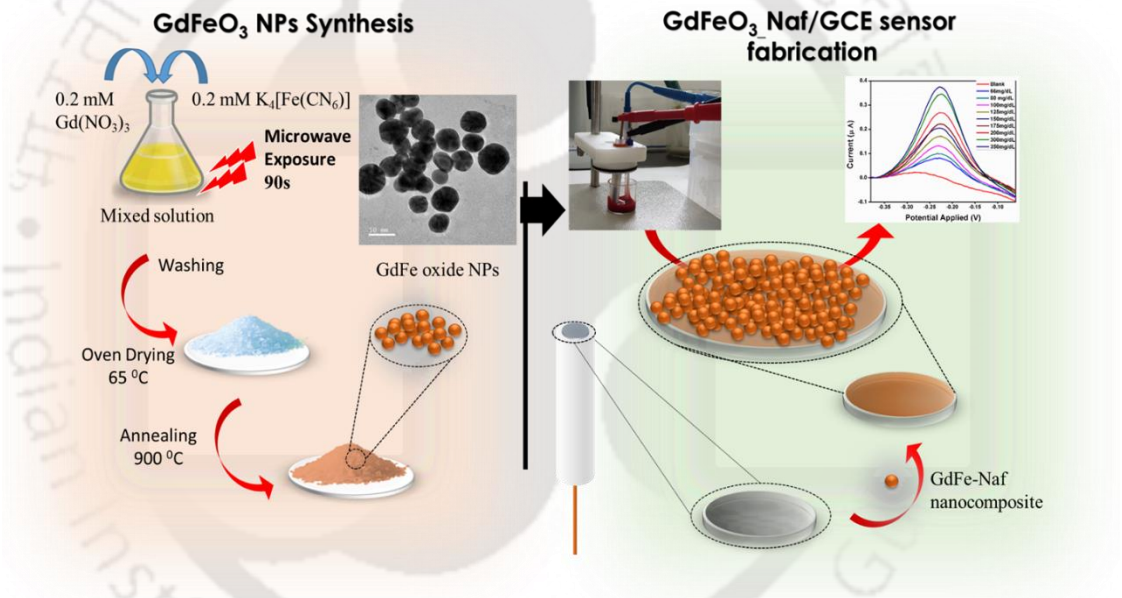

Status:

Manuscript submitted

TH-2627_166106107

1. Introduction

In this chapter, we have replaced gold with gadolinium to develop a new bimetallic nanocomposite and tried to develop a nonenzymatic glucose biosensor. As we know, diabetes or hyperglycemia (an elevated level of glucose in the blood), is one of the profoundly affecting disease found among various developing and developed countries, which is categorized into two major categories, insufficient insulin production either in the body (Type 1 diabetes) or by the incapacity of body's to consume its produced insulin (Type 2 diabetes). (Kenneth and Cummings 2012; Nichols et al. 2013).

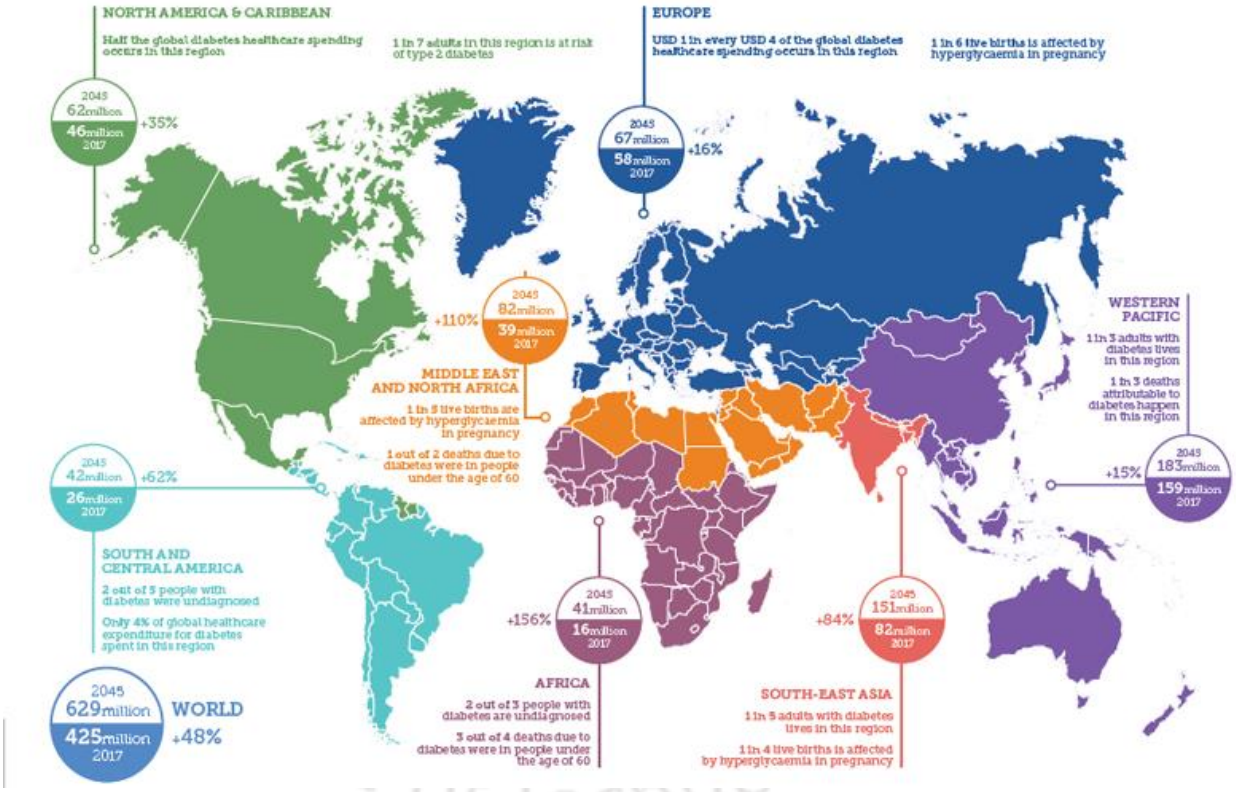

Figure 4.1. World Diabetic Map indicates the rate of diabetes among all countries (source: https://www.idf.org/aboutdiabetes/what-is-diabetes/facts-figures.html).

According to the International Diabetic Federation and World Health Organization, almost 350 million people globally have diabetes, and, based on current predictions, diabetes will be the 7th leading reason for death as of 2030. (WHO. World Health Organisation. 2010; Danaei et al. 2011) Both accurate observation and cautious control of blood glucose levels

TH-2627_166106107

are critical for the appropriate diagnosis and treatment of diabetes. Consequently, regular testing of physiological glucose levels is important to avoid diabetic emergencies, hypoglycemic (deficient blood sugar levels) shock, and prevent long-term complications from high-level blood glucose that include heart attack, stroke, high blood pressure, kidney failure, blindness, and limb amputation. (Chase and Maahs 2006; Frier and Fisher 2007) Because of this, a diabetic patient is recommended to test their blood glucose levels numerous times a day to ascertain a safe blood glucose range. Thus, for the proper care and management of diabetes, precise blood glucose measurement is crucial. These measurements are usually performed using a blood test or glucose monitoring test strips.(Shaw and Cummings 2012) Among all types of biomedical instruments, glucose biosensors are considered very effective for diabetes diagnosis due to its robustness, small size, user-friendly operation, and ability to be a tool for personalized diagnosis. (Mahato et al. 2016, 2018c) Glucose biosensor is an analytical device that uses biochemical reactions facilitated by enzymes, catalysts, and proteins to detect the physiological changes in the form of quantifiable electrical/optical/thermal signals (Mahato et al. 2018a, b, 2019). Most of the commercialized glucose biosensor is enzyme based amperometric sensors, which have glucose dehydrogenase either (GDH) or Glucose oxidase (GOx) immobilized onto the sensing matrix. As these enzymes are highly selective towards glucose, they offer better selectivity to the enzymatic glucose biosensors (Kumar et al. 2018). Moreover, GOx is quite firm compared with other enzymes; the glucose sensors based on GOx are always exposed to the possible thermal and chemical deformation during fabrication, storage, or use. The activity of GOx drops quickly below pH 2 and above pH 8. On exposure to a temperature above 40 °C can cause serious damages to the enzyme. Also, it has been found that ionic detergents deactivate GOx. (Wilson and Turner 1992) Moreover, the short shelf life of an enzyme not only limits the performance of these enzymatic sensors but also causes

TH-2627_166106107

commercial use. Since the sensitivity of enzyme-based glucose sensors principally determined by the enzyme activity immobilized onto the chip, the reproducibility is still a serious question for quality control. Moreover, the drawbacks, such as inadequate stability, originated from the nature of the enzymes that are barely overcome, demanded a need that can address these issues. Nowadays, there is a vast demand for the development and improvement of glucose sensors. There has been an increment in the number of diabetic patients over the last 20 years. Therefore, the demand to make a sensor that is both biocompatible and has enhanced sensing abilities and stability compared to present enzymatic sensors. (Albareda-Sirvent et al. 2000; Oliver et al. 2009; Chen et al. 2013) In view of this, the nonenzymatic glucose detection can pave a new dimension in developing more robust and stable glucose biosensors.(Rahman et al. 2010) The interest in practical nonenzymatic glucose sensor has been centered on the efforts to find out the breakthrough in electrocatalysis (Atta et al. 2019; Bao et al. 2019; Liu et al. 2019; Sharma et al. 2019; Wang et al. 2019; Zhang et al. 2020). In traditional sensors, the enzyme such as GOx is applied as a catalyst, while, in non–enzymatic sensors, atoms at the surface of the electrode themselves act as the electrocatalysts.(Park et al. 2006) However, the mechanism of nonenzymatic oxidation of glucose at the electrode surface still needs a lot of research. Until now, there are two main models, which have been projected to clarify the above process. According to one model, which is also known as activated chemisorption model, the process of oxidation is instigated by the glucose adsorption onto the electrode surface. Eventually, glucose forms a bond with the sensing surface, where the electrocatalysts attached to the sensing electrode help in glucose oxidation. During electrocatalysis, hydrogen of hemiacetal carbon is extracted. Once removed, the hydrogen atom bonds with the sensor surface at a place near to the chemically adsorbed glucose; this causes a change in the oxidation state, which leads to the change in the metal-glucose interaction, in that way dropping the glucose–

TH-2627_166106107

metal bond strength, resulting into glucose desorption. A bond of intermediate strength is anticipated, as it is promising for both the adsorption (bond forming) and desorption (bond breaking) processes.(Pletcher 1984) Burke proposed the second model, known as the 'Incipient Hydrous Oxide Adatom Mediator' (IHOAM) model. He initially expressed this model founded on the observation that active metal atoms on the electrode surface have low lattice stabilization and enhanced reactivity. These atoms undergo a pre-monolayer oxidation step, during which an incipient hydrous oxide layer is formed, which is believed to mediate the oxidation of glucose at the electrode surface (Burke 1994). Till now, there are several reports of nonenzymatic biosensors; most of them require mediator molecules either in the solution or onto the electrode, which not only limits their practical applications but also their point of care applicability (Park et al. 2006; Tian et al. 2014). Nanomaterials (NMs) have been found to have fascinating opto-electronic properties due to electron and phonon confinement, high surface-to-volume ratio, high surface reaction activity, high catalytic efficiency, and strong adsorption ability (Kumar et al. 2019c, a, b, d; Purohit et al. 2019). There are still many challenges ahead to make the practical utilization of nonenzymatic glucose sensors in the human body before the commercialization of these techniques (Hsu et al. 2017; Lee et al. 2019).

In view of this, we have tried to synthesize a novel Gadolinium iron oxide ($GdFeO_3$) nanomaterial (NM), using a facile, ultrafast, one-pot, and microwave-assisted synthesis procedure. As prepared GdFe oxide, NM was thoroughly characterized using, UV-Vis spectrophotometer, X-ray diffractometer, TEM, STEM, and FTIR spectrometer. We have tried to fabricate a glucose sensor using the GdFe doped Nafion nanocomposite as a matrix material in the next step. It was electrochemically characterized using cyclic voltammetry (CV) and scan rate study. Consequently, we have performed glucose sensing by the fabricated probe to evaluate its analytical performance, *i.e.*, LDR and LOD using differential

TH-2627_166106107

pulse voltammetry (DPV). We have also tested the fabricated sensor's practical applicability by checking glucose in human blood and compared its performance with clinical results. Selectivity because of various real sample components was also studied, and the long-term stability of the designed sensor was evaluated.

2. Materials and methods

2.1. Materials, apparatus, and reagent preparation

Gadolinium nitrate ($Gd(NO_3)_3$) was purchased from SRL, India. Deionized water was obtained from Milli Q, Millipore unit (Elix USA) of 18.2 MΩ resistance. Glucose was purchased from Himedia. Potassium ferrocyanide ($K_4[Fe(CN)_6]$) and potassium ferricyanide ($K_3[Fe(CN)_6]$) were obtained from Himedia and SRL, respectively. Hydrogen peroxide (H_2O_2), Nafion 117 solution, was procured from Sigma. Sodium dihydrogen phosphate (NaH_2PO_4) and sodium phosphate (Na_2HPO_4) were purchased from Merck and SRL, respectively. All the chemicals were of AR grade and utilized without any additional purification. Instruments that were used in synthesis, hot plate magnetic stirrer (Tarson India; Spinot), household microwave oven (LG, India; MC-2846BCT), for washing BR-Biochem (BR-60) centrifuge, for high-temperature annealing, a muffle furnace, and to dry samples a hot air (Equitron -7051-150) oven was used.

2.2. Synthesis of $GdFeO_3$ nanoparticles

An equimolar solution of $Gd(NO_3)_3$ and $K_4[Fe(CN)_6]$ were prepared separately using Milli-Q Millipore unit having 18.2 MΩ resistance. A reaction solution of 70 mL was made of $Gd(NO_3)_3$ and $K_4[Fe(CN)_6]$, in a 1:1 ratio. The reaction mixture was vigorously stirred upto 2 hours until the colour of mixture solution became milky white. The reaction mixture was then exposed to 120 s of microwave irradiation using a household LG microwave oven while

TH-2627_166106107

setting the power of the machine to 900 W. The microwave exposure time was optimized with the change in the color of reaction mixture. Microwave was irradiated in a flash fashion, 30 s on followed by 30 s off, for four times. The milky white reaction mixture changes its color from milky white to greenish white. Further, it was centrifuged and washed four times using milli Q water followed by alcohol. The pellet obtained during centrifugation was dried into hot air oven overnight at 65 °C. The powder obtained after drying was grinded into fine powder using a mortar-pestle. Powder was then annealed using a high temperature muffle furnace while setting the annealing temperature 900 °C for 6 hours. After annealing the colour of powder again changed from greenish white to reddish brown. After annealing, material was grinded with mortar-pestle and stored in a tight container in moisture free environment.

2.3. Preparation $GdFeO_3$ nanoparticles based glucose sensing electrode

Initially, 2 mg of $GdFeO_3$ NPs in 1 mL of 0.1% nafion 117 solution was prepared. The purpose of nafion 117 solution was to bind the $GdFeO_3$ NPs onto the electrode surface. This mixture was sonicated for 3 hours in ultrasonic bath sonicator at 45°C. Care was taken to maintain the temperature of the water in the sonicator. To prepare the sensing matrix, we used a glassy carbon electrode (GCE) and it was used for all other electrochemical characterizations. Initially, GCE was thoroughly cleaned using alumina powder. The $GdFeO_3$-Naf/GCE nanocomposite material was then used for making the thin film onto the GCE by drop-casting/spin-coating. The composite was used for electrode fabrication. Precisely, 2 µl of this solution was used onto the conducting surface of the GCE and let the electrode dry in closed container for 3 hours to form the $GdFeO_3$-Naf/GCE sensing electrode. Scheme 4 shows the schematic of $GdFeO_3$ NPs synthesis and electrode fabrication.

TH-2627_166106107

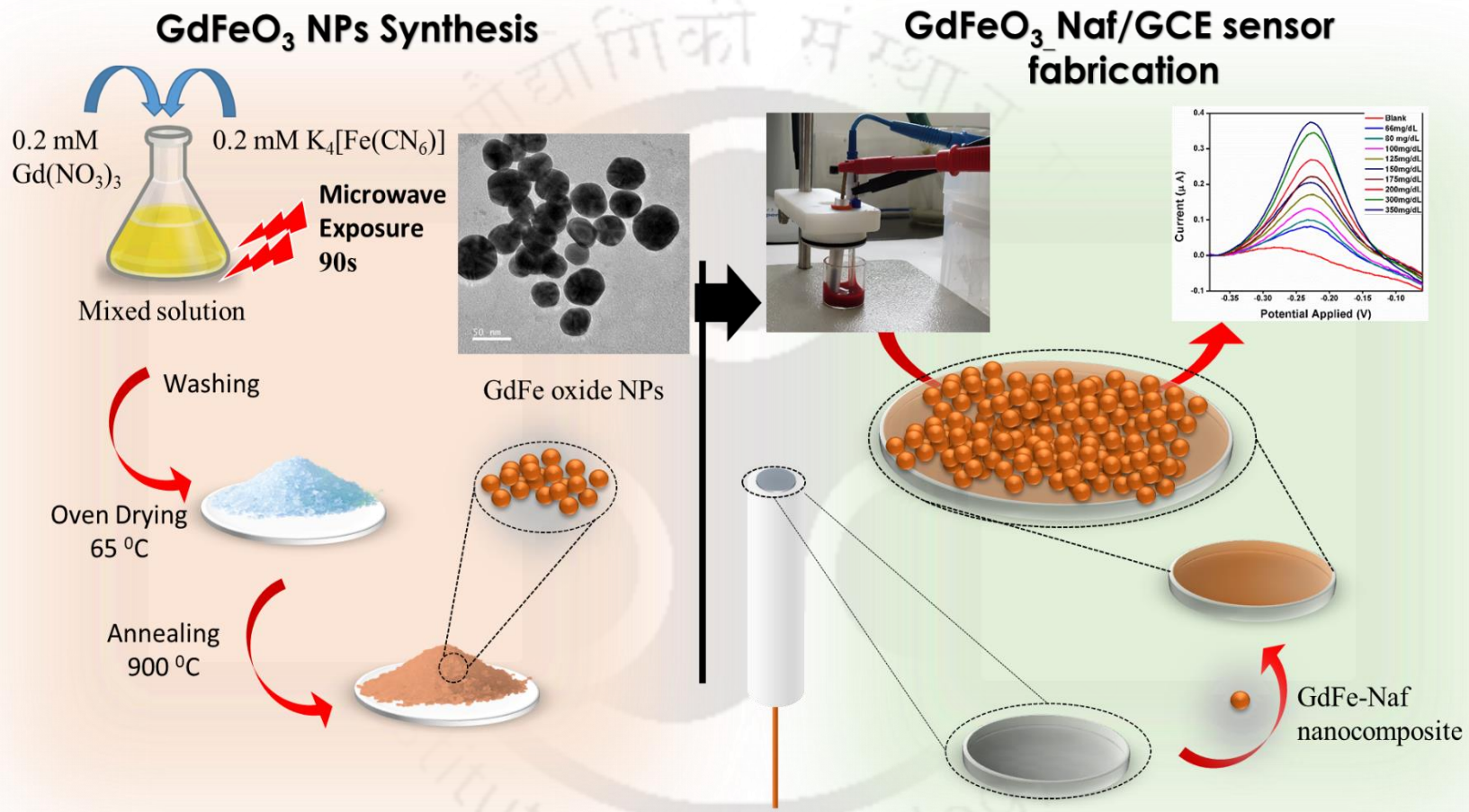

Scheme 4. Scheme of synthesis of $GdFeO_3$ NPs and $GdFeO_3$-Naf/GCE glucose sensor fabrication.

2.4. Characterization of $GdFeO_3$ nanoparticles

2.4.1. X-ray diffraction (XRD) analysis:

The crystalline nature of the $GdFeO_3$ NPs was determined through a powder X-ray diffractometer (Rigaku MiniFlex 300), where, XRD analysis was performed at 2θ Bragg's angle by maintaining the range between 30° to 80° with a scan rate 20° per minute.

2.4.2. Transmission electron microscopy (TEM) imaging and analyses:

$GdFeO_3$ NPs shape, size, dispersivity, energy dispersive X-ray (EDX) study, and electron diffraction analyses were performed with FE-TEM (JEOL JEM-2100F TEM). Sample was prepared by drop-casting the well dispersed GdFe oxideNPs in ethanol onto the surface of carbon coated copper grid (300 mesh) and allowing it to dry at 37°C for 12 hrs.

2.4.3. Scanning tunneling electron microscopy (STEM) analysis:

To determine the presence of elements and their position in the sample; (elemental mapping), the STEM module of FE-TEM (JEOL JEM-2100F TEM) was used. Sample was prepared on 300 mesh containing carbon coated copper grid.

2.4.4. Fourier-transform infrared (FTIR) spectroscopy:

$GdFeO_3$ NPs were characterized for IR spectroscopy using FTIR spectrometer (Cary- 630). For FTIR studies, the diamond ATR mode of operation was selected in the FTIR spectrometer. $GdFeO_3$ NPs were placed onto the diamond ATR and scanned for transmittance in the range of 400 cm^{-1} to 4000 cm^{-1}

TH-2627_166106107

2.4.5. Electrochemical characterizations:

The $GdFeO_3$-Naf/GCE sensing electrode was electrochemically characterized using Metrohm electrochemical analyzer (Autolab potentiostat galvanostat) with the help of various electrochemical techniques such as CV, differential pulse voltammetry (DPV), and EIS. A phosphate buffer saline (PBS pH 7.6 and 0.9% NaCl) solution containing 5 mM $[Fe(CN)_6]^{-3/-4}$ was used as electrolyte to perform all electrochemical characterization using Ag/AgCl as a reference electrode and Pt wire as counter electrode.

3. Result and discussions

3.1. Physical characterization of $GdFeO_3$ nanoparticles

3.1.1. XRD studies:

To determine the crystallinity of our $GdFeO_3$ NPs, we have performed X-ray diffraction study. 50 mg of $GdFeO_3$ NPs powder was utilized to check the diffraction pattern. The machine was set into powder mode of measurement. The XRD pattern of NPs (Figure 4.2) depicts the diffracted peaks corresponding to (020), (111), (200), (121), (002), (022), (131), (202), (230), (311), (123), (331) (242), (313), and (161) diffraction planes of GdFe oxide NPs, which are well indexed with JCPDS No: 78-0451. The XRD pattern shown the formation of a $GdFeO_3$ NPs. The average crystallite size was estimated as ~ 19 (±2) nm using all diffraction peaks with the help of Debye-Scherrer's equation.

$$D = \frac{0.9\lambda}{\beta\cos\theta} \qquad \ldots. (1)$$

TH-2627_166106107

Where λ=1.5460Å is the wavelength of target Cu-Kα, Θ is the Bragg's angle of diffraction and β is the full-width half maximum of diffraction peak.

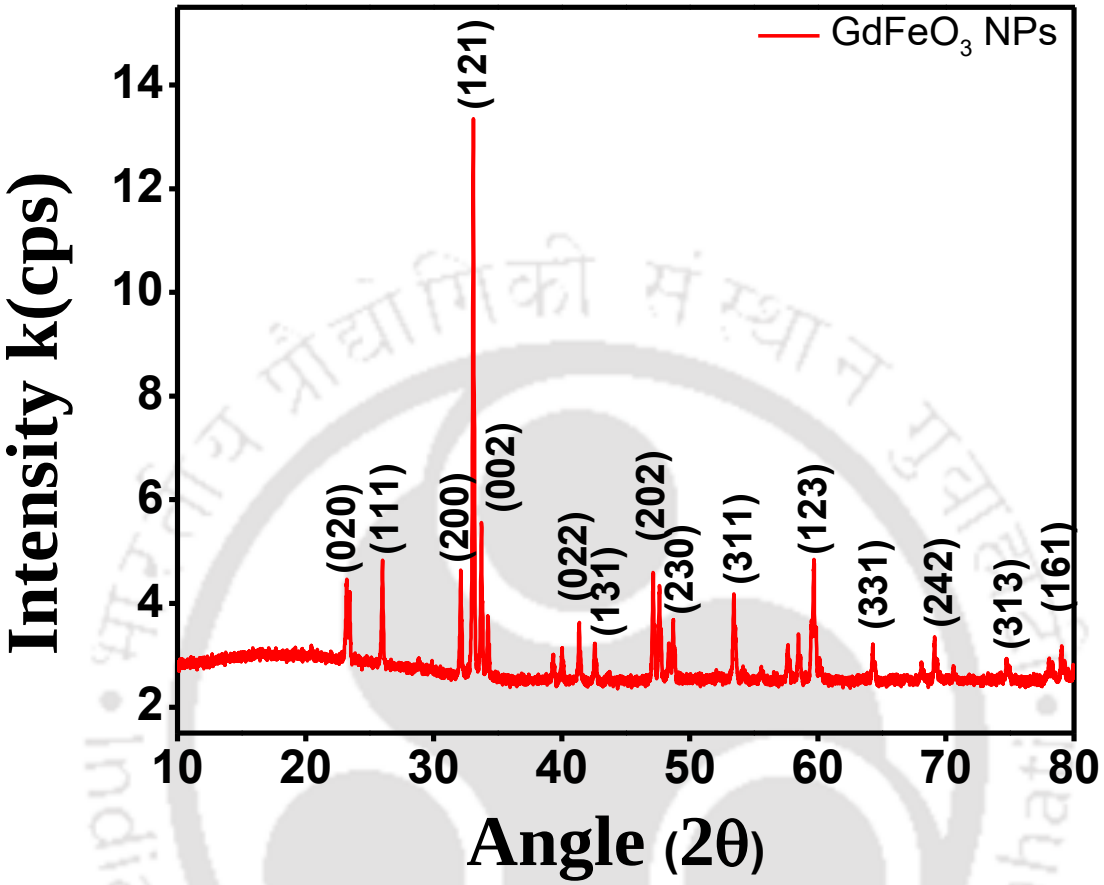

Figure 4.2: XRD analysis of $GdFeO_3$ NPs

3.1.2. TEM imaging and analyses:

TEM images were taken of our synthesized $GdFeO_3$ NPs (Figure 4.3). Dark spherical regions were seen scattered about the whole field of imaging (Figure 4 (a) and (b)), where the NPs found to be monodispersed. In figure 4.3 (c), we tried to get d-fringes using the TEM machine in high-resolution mode. We get the interplanar distance of 0.26 nm, which shows the (002) diffraction plane of the crystal. It was complimenting the data of what we have observed in XRD. We have also tested our sample for energy dispersive x-ray (EDX); our

TH-2627_166106107

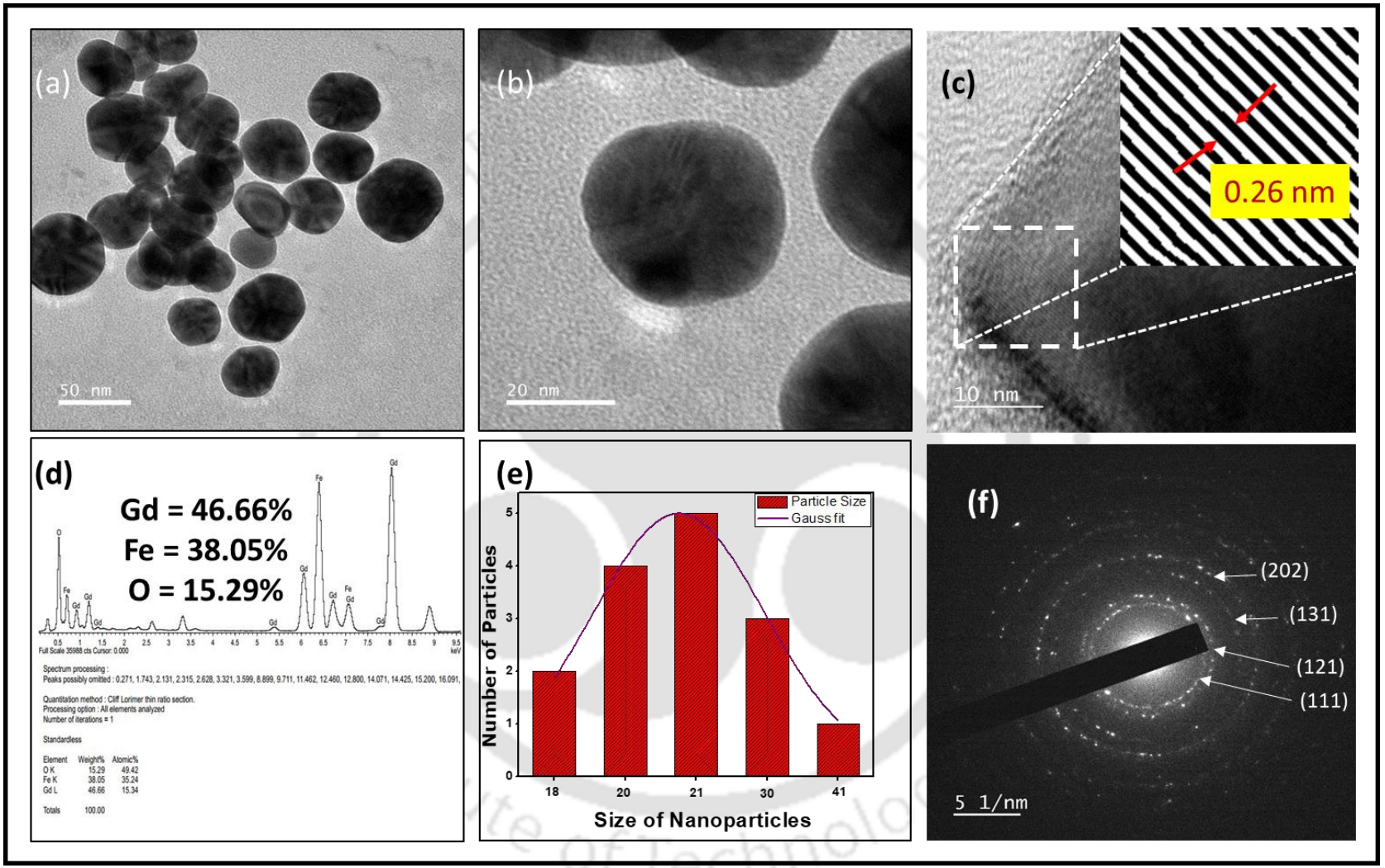

Figure 4.3: (a) TEM image of the $GdFeO_3$ NPs, (b) HRTEM image of a single particle, (c) d-fringes on a single particle, (d) EDX of the particles, (e) particle size distribution of the particles, and (f) SAED of $GdFeO_3$ NPs.

TH-2627_166106107

sample showed there was 46.66% of Gd, 38.05% of Fe, and 15.21% of O by weight percentage. It was further complimenting the fact of bimetallic nanoparticles synthesis.

We calculated the average size of the $GdFeO_3$ NPs and found their size distribution considering 110 particles in different fields. Diameter of $GdFeO_3$ NPs were measured with the help of open-source software (ImageJ). It was found that $GdFeO_3$ NPs were of 18 nm to 41 nm, and most of them were of 21 nm, as shown in figure 4 (e). Further, we have tested our sample for electron diffraction, which provided information about our sample's crystallinity. We have obtained concentric diffraction rings. The concentric rings from the central maxima represent the polycrystalline nature of $GdFeO_3$ NPs. The diffraction rings were assigned with the diffraction planes (111), (121), (131), and (202). This is further in good agreement with the data that we have obtained from XRD. With the data obtained from XRD and TEM, we found the crystalline nature of our sample, and both studies complement each other.

3.1.3. STEM analysis:

To determine the position of elements present in single $GdFeO_3$ NP, STEM elemental mapping was performed. Sample was prepared with the same procedure as what we have done in the case of TEM sample preparation. During imaging in the TEM machine, the mode of operation was changed from bright field imaging to bright field STEM imaging. The elemental mapping was performed using software (INCA) preloaded in the TEM machine. Initially, a single spherical NP was captured, and X-ray detector was

TH-2627_166106107

switched on to capture the counts of element-specific X-rays. The mixed image (figure 4.4 (a)) shows the presence of all three elements in a single particle. Figure 4.4 (b) shows the presence of gadolinium, (c) shows the presence of iron, and figure 4.4 (d) shows the presence of oxygen. Interestingly, we did not obtain any X-ray outside the spherical NP, indicating the formation of $GdFeO_3$ NPs.

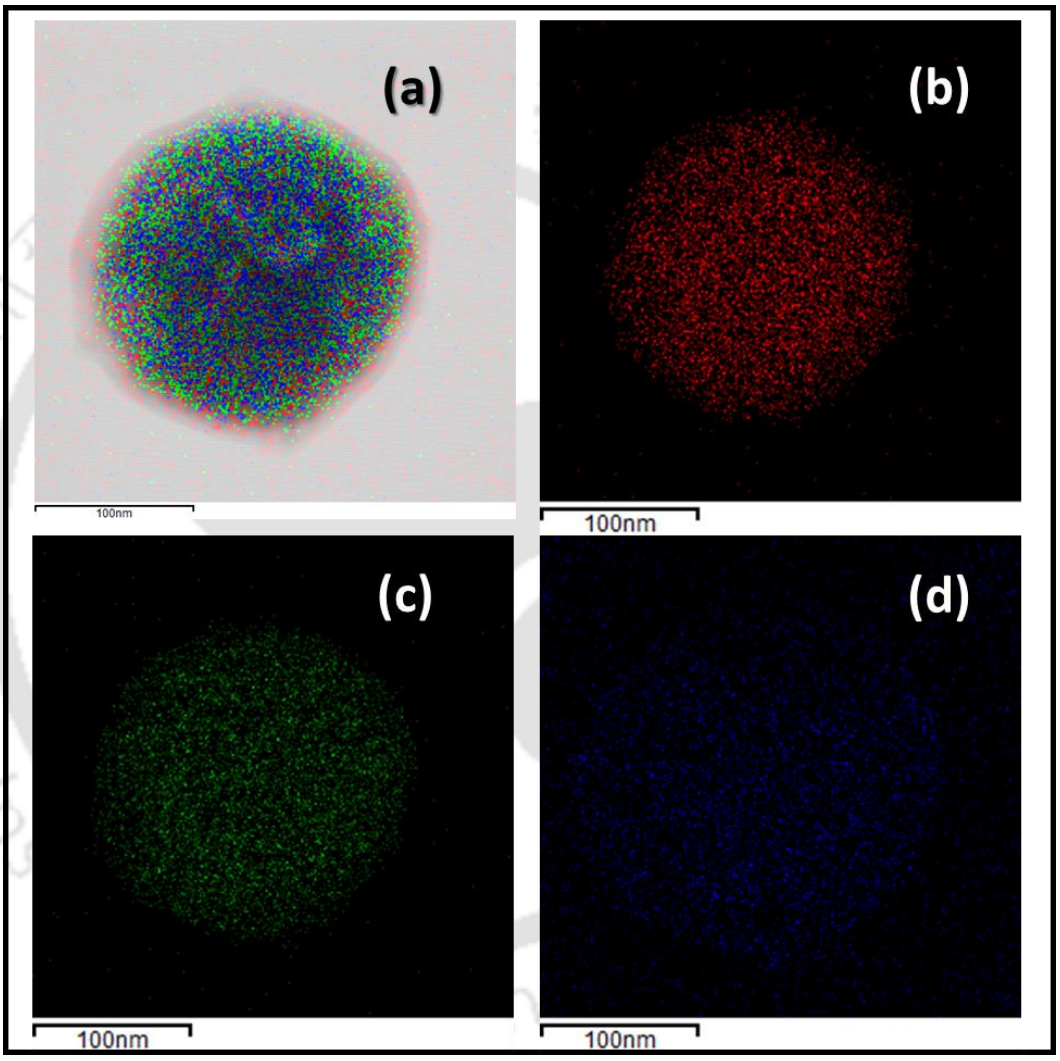

Figure 4.4: Elemental mapping study (a) STEM mixed image of the $GdFeO_3$ NP, (b) presence of gadolinium in the particle (red), (c) presence of iron in the nanoparticle (green), and (d) presence of oxygen (blue).

TH-2627_166106107

3.1.4. FTIR Analysis:

The synthesis of $GdFeO_3$ NPs was monitored with FTIR as well. During synthesis, the greenish white powder and after 900 °C annealing the sample was examined for IR transmittance with Cary 630 FTIR spectrophotometer. It was found that before giving the heat treatment, there was presence of a sharp peak around 2123 cm^{-1} designated for cyanide (C-N) group in the material. We anticipate that this was coming from precursor chemical K_4 $[Fe(CN)_6]$. After annealing, the characteristic FTIR peak of C-N along with (O-H) from the material moisture got disappeared, as shown in figure 4.5. Only a peak of around 540 cm^{-1} was observed at the peak of metal oxides (Figure 4.5). Hence, our material $GdFeO_3$ NPs were formed only after annealing treatment.

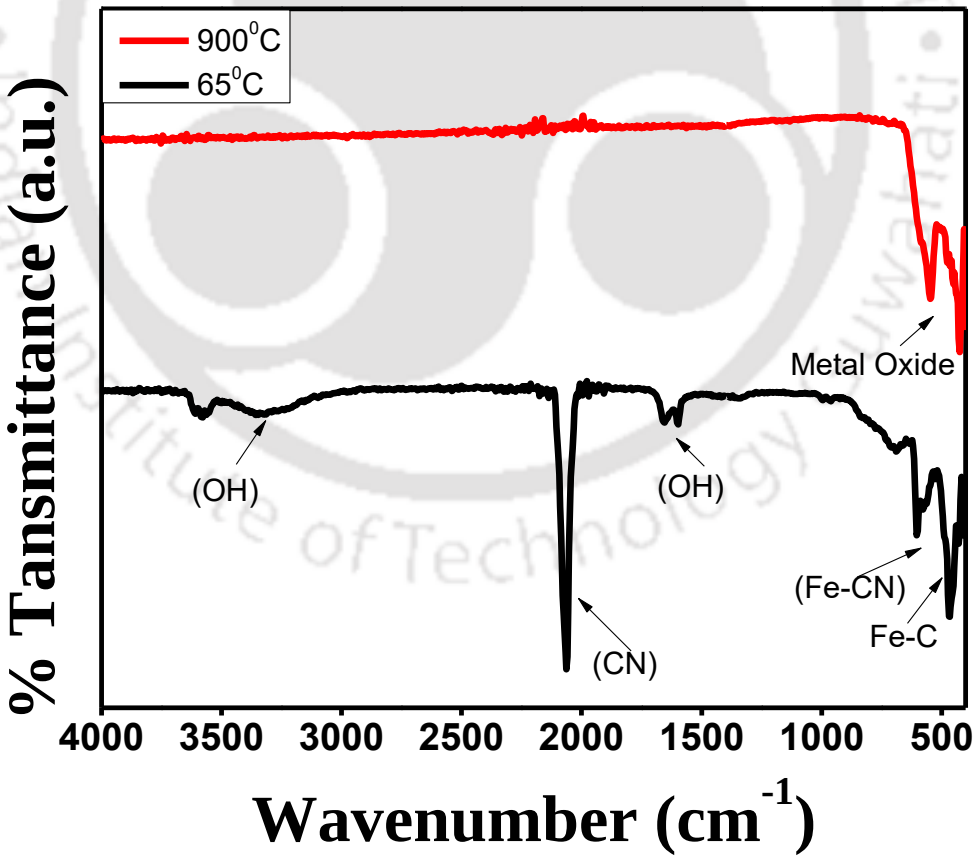

Figure 4.5: FTIR graphs of the material before and after annealing

TH-2627_166106107

3.2. Electrochemical Characterizations

The change in the electrochemical response of the $GdFeO_3$-Naf/GCE sensing electrode was studied using CV with a scan rate of 0.05 V/s in 3 mL PBS containing 0.9% NaCl. A characteristic redox peak appeared at -0.24V and -0.26 V showing oxidation and reduction, respectively, as shown in figure 4.6. These redox peaks were not present in the bare GCE. It showed that our material was electrochemically active, and there was something in the nanocomposite that was oxidizing and reducing onto the electrode surface. The oxidation peaks were in at low potential showing the novelty of our material.

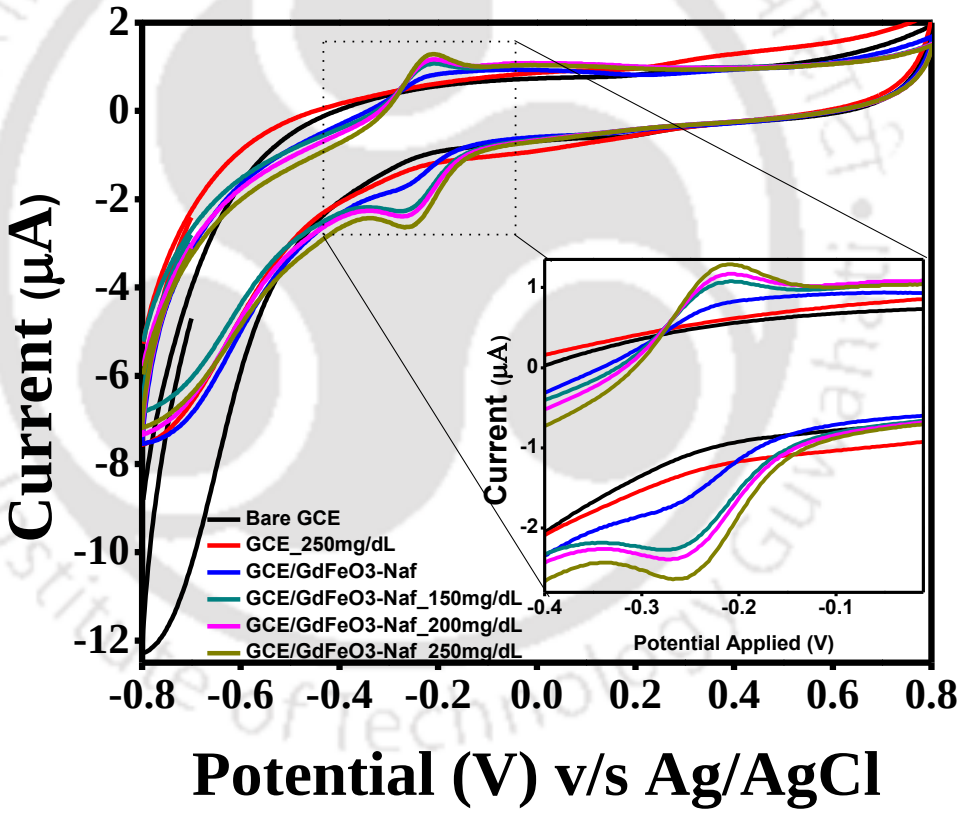

Figure 4.6: Electrode study in PBS: Bare GCE (black), GCE in 250 mg/dL glucose red), GCE/$GdFeO_3$ (blue), GCE/$GdFeO_3$_150mg/dL glucose (green), GCE/$GdFeO_3$_200mg/dL glucose (pink), GCE/$GdFeO_3$_250mg/dL glucose (olive green)

TH-2627_166106107

To the best of our knowledge, this is the first report showing this kind of electrochemical behavior of $GdFeO_3$-Naf/GCE nanocomposite. The possible mechanism of glucose detection could be either of the models, as explained earlier. We tested our modified electrode, whether it was showing any response to small molecules. Surprisingly, our system showed an increase in the current with glucose addition (150 mg/dL); it seems like our material was catalyzing the glucose, and electrons were generating electrons into the system. To check whether this was merely due to the glucose not from anything else, we added the concentration of glucose (200 and 250 mg/dL) into the electrochemical cell; with an increase in glucose concentration, the oxidation current increased.

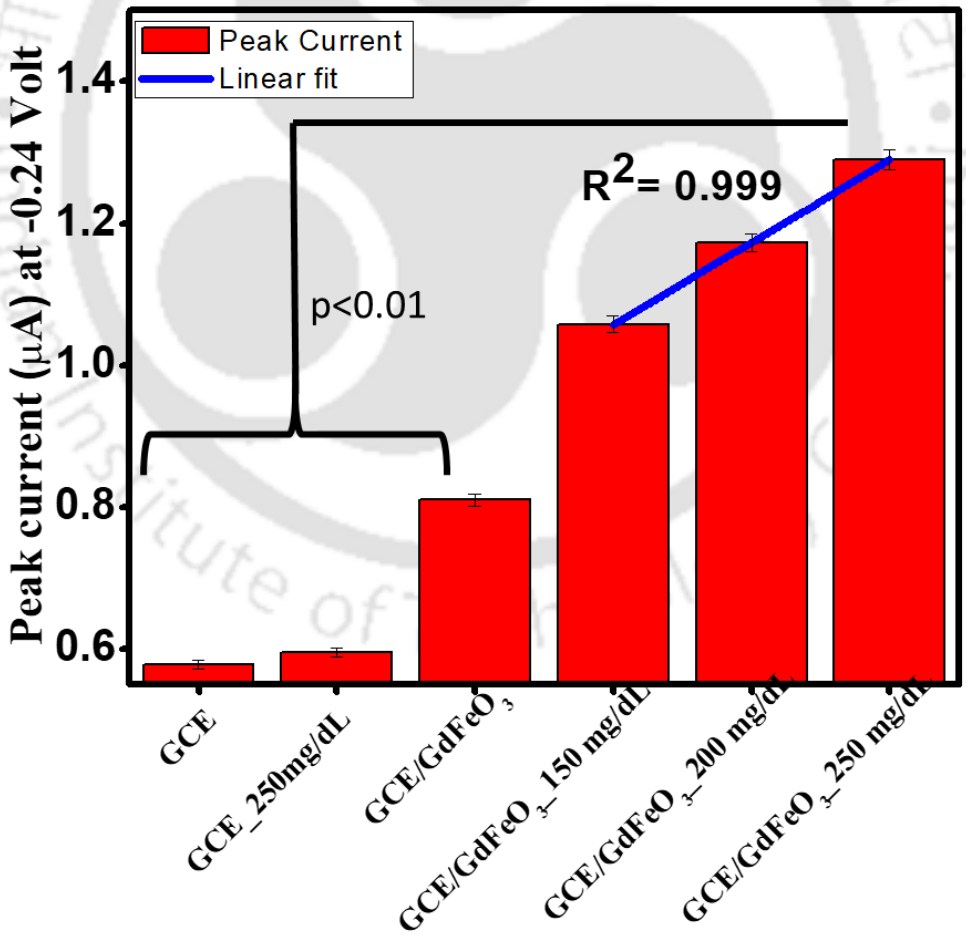

Figure 4.7: Peak currents of electrodes with glucose concentrations.

TH-2627_166106107

A calibration curve was plotted using these three responses, and it was showing an excellent linear regression, with coefficient $R^2 = 0.999$, as shown in figure 4.7. With this result, we found that our system could be useful for glucose testing.

To determine the GdFeO3-Naf/GCE sensing electrode's stability, we have performed the scan rate studies (Figure 4.8. (a)). 100 mg/dL of glucose was dissolved in 2 mL PBS (pH 7.0 and 0.9% NaCl) and it was tested with variable scan rate from (10mV/s to 100mV/s). With an increase in scan rate, the oxidation and reduction current increase, suggesting the GdFeO3-Naf/GCE sensing matrix is highly stable. The cathodic and anodic peaks were in good linearity with respect to scan rates as well as having regression coefficient ($R^2 = 0.96$) and ($R^2 = 0.96$), respectively (Figure 4.8 (b)), showing that it was because of on surface oxidation-reduction.

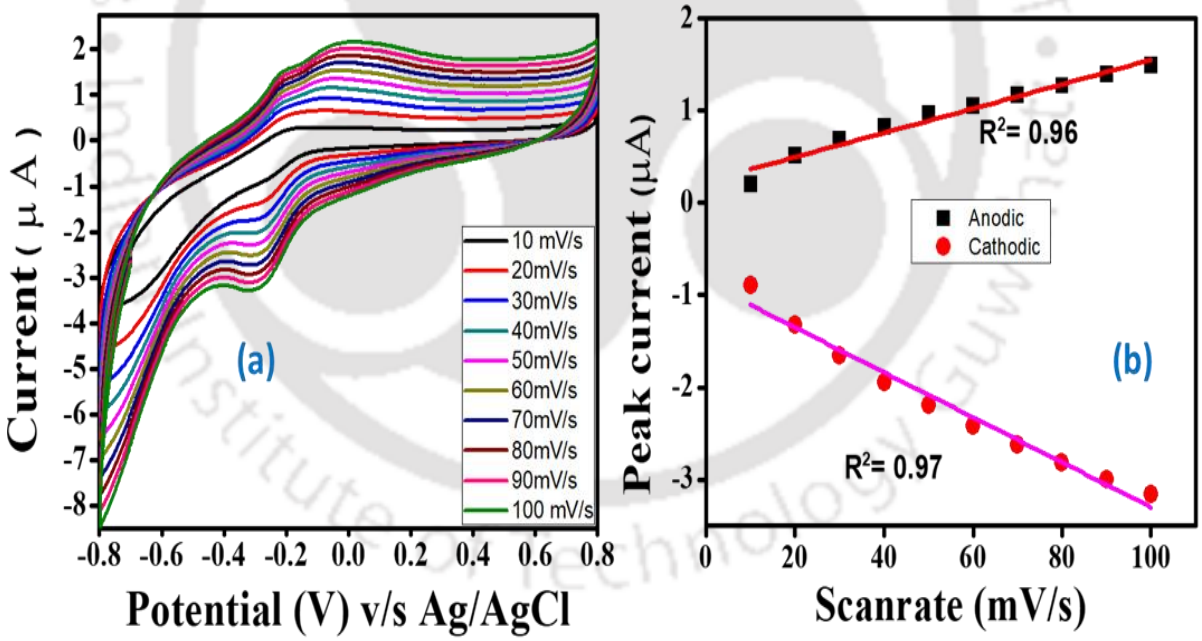

Figure 4.8: (a) Scan rate study of $GdFeO_3$-Naf/GCE glucose sensing electrode in the presence of 150 mg/dL glucose. (b) corresponding anodic and cathodic peak currents

TH-2627_166106107

3.3. Analytical performance of $GdFeO_3$-Naf/GCE sensor probe

After confirming the electrochemical properties of the $GdFeO_3$-Naf/GCE electrode, the electrochemical response of $GdFeO_3$-Naf/GCE electrode was measured as a function of glucose concentration (66-350 mg/dL) in 2 mL PBS at a scan rate of 0.05 V s^{-1}, from -0.4V to 0V, using DPV technique (Figure 4.9 (a)). There was an oxidation peak around -0.22 V, which was coming because of glucose, as obtained in the CV. Figure 4.9 (a) shows the representative DPV curves, where the current response increases with the increase in glucose concentrations.

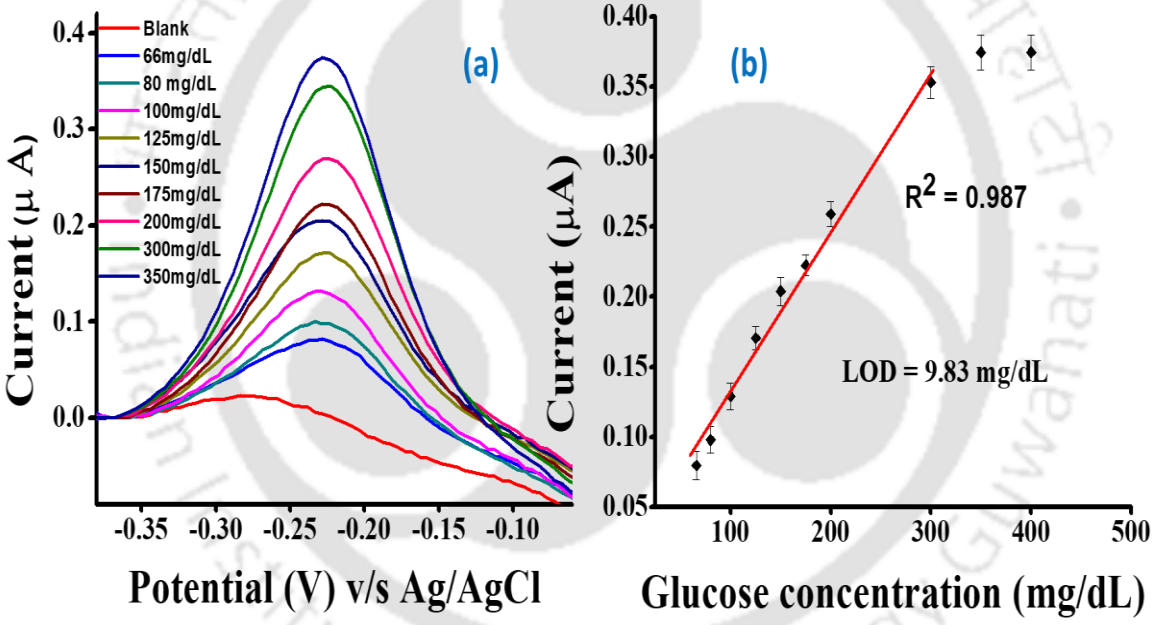

Figure 4.9: (a) Response of $GdFeO_3$-Naf/GCE glucose sensing electrode with respect to different concentrations of glucose in DPV and (b) corresponding calibration curve.

TH-2627_166106107

Table 4.1. A detailed account of the comparative analytical performances of recently reported enzyme-less glucose sensors.

Sl. No.	Sensor probe design	LDR	DL	Real sample		Detection technique	References
1.	CuO-ZnO NR/FTO	0.001 – 3.45 mM	0.40 µM	Yes	Serum	Amperometric	(Ahmad et al. 2017)
2.	AgNPs/NSC electrode	5 µM – 3 mM	0.046 mM	Not reported	-	Amperometric	(Khalaf et al. 2019)
3.	Cu-NGr/GCE	0.01 – 100 µM	10 nM	Yes	In food items	Amperometric	(Shabnam et al. 2017)
4.	Cu@C/Nafion/GCE	40 µM – 40 mM	21.35 µM	Yes	Serum	Amperometric	(Ye et al. 2019)
5.	$NiGa_2O_4$@NF electrode	0.03 – 2.5 mM	5 µM	Not reported	-	Amperometric	(Ding et al. 2019)
6.	PdNi@rGO/GCE	0.05 –1.1 mM	0.15 µM	Yes	Serum	Amperometric	(Şavk et al. 2019)
7.	NiO@ Fe_3O_4-SH/PPAH-SDS/GCE	0.1 – 10.0 µM and 10.0 – 300.0 µM	0.13 µM	Yes	Serum	DPV	(Baghayeri et al. 2018)
8.	ZnO@C/GCE	0.1 – 13.8 mM	1 mM	Yes	Blood	CV and Amperometric	(Chung et al. 2017)
9.	**$GdFeO_3$-Naf/GCE**	**66 – 350 mg/dL**	**9.83 mg/dL (±0.05)**	**Yes**	**Blood**	**DPV**	**This Work**

TH-2627_166106107

Based on the DPV responses, a calibration plot was acquired that shows the linear detection range (LDR) from 66-350 mg/dL of glucose (Figure 4.9 (b)). The linear regression equation of the calibration plot for glucose sensing was expressed as follows:

$$\Delta I\ (\mu A)= 0.02\ (\pm 2.841 \times 10^{-4}) + 0.001\ (\pm 3.78 \times 10^{-5})\ \text{Conc. [glucose (mg/dL)]} \quad ....(2)$$

The regression coefficient was calculated as 0.987, which shows good linearity. The limit of detection (LOD) of glucose was determined to be 9.83 mg/dL (±0.05) ((RSD< 4%, 95 % confidence level, n=3) using the following equation.

$$\text{LOD} = \frac{3\sigma_b}{m} \quad .... (3)$$

Where, σ_b *is the standard deviation of blank, and m is the slope of the calibration curve.*

Notably, in our case obtained, LOD is significant enough to detect glucose even in low concentrations. A comparative table of different nonenzymatic glucose is shown in table 4.1. The GdFeO3-Naf/GCE sensor's dynamic range can cover the hypoglycemic condition to hyperglycemic conditions, indicating the immense clinical importance of the fabricated sensor.

3.4. Selectivity study

To evaluate any sensor's commercial importance, it is essential to investigate the sensor's selectivity towards various possible interfering molecules (Mahato et al. 2018c). To determine the interfering effects, $GdFeO_3$-Naf/GCE probe was tested towards glycine, cystine, glutamic acid, alanine, glucose, BSA, citric acid, and ascorbic acid, which potentially coexist with acetaminophen in the real matrix. No significant signal response

was observed for the tested interfering compounds due to either their inherent electro-inactive behavior (*e.g.*, glucose, BSA) or due to the different operational potential window (Chandra et al. 2011; Noh et al. 2012; Agrawal et al. 2013; Yadav et al. 2014). The GdFeO3-Naf/GCE probe's selectivity was statistically inferred by determining the selectivity coefficient using equation 4.

$$k_{sel} = \frac{(Signal)interfernt}{(Signal)glucose} \text{ ---------- (4)}$$

Where k_{sel} is the coefficient of selectivity, $(Signal)_{interferent}$ is the signal strength of sensor when treated with the interfering molecules, and $(Signal)_{glucose}$ is the signal strength of glucose.

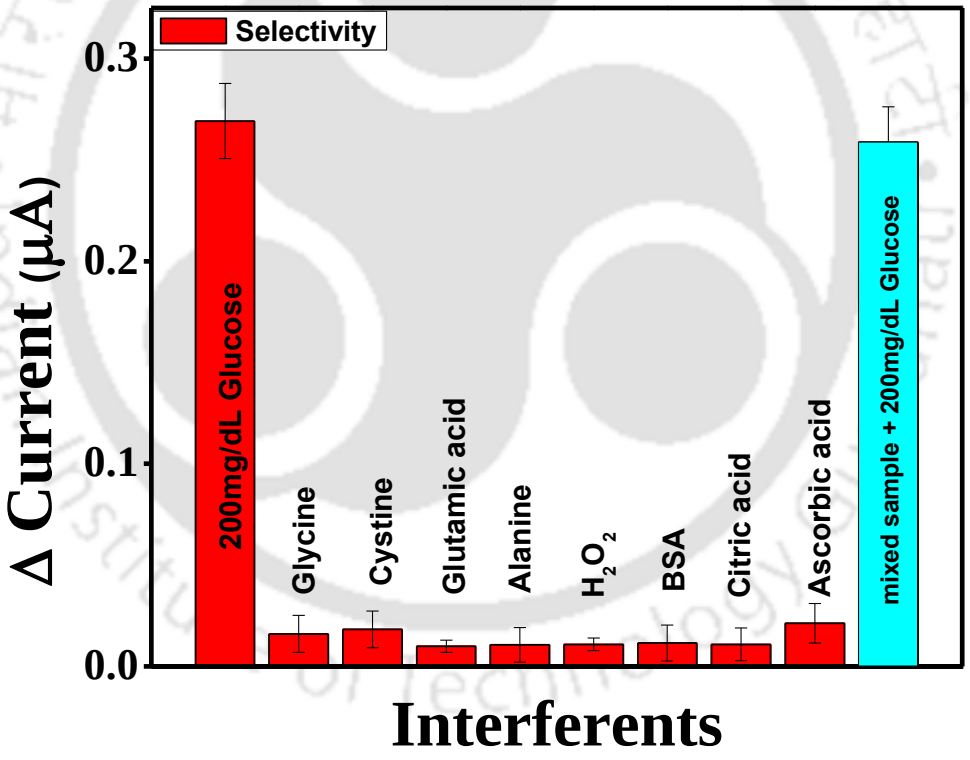

Figure 4.10: Interference study of $GdFeO_3$-Naf/GCE sensor

The calculated k_{sel} values for interfering molecules were extremely low (<< 1), indicating that the fabricated sensor is highly selective towards glucose detection. Figure 4.10 shows the comparatives histograms obtained from DPV responses of glucose and different

TH-2627_166106107

interfering molecules at the sensor probe. We have also performed glucose detection in a mixed sample. In this case, the signal was 94.3% similar to glucose when it was detected separately. These results clearly indicate that the developed $GdFeO_3$-Naf/GCE sensor was not only able to detect glucose separately but also in a mixed sample, effectively.

3.5. Real sample analysis

For a diabetic patient, continuous glucose level monitoring is very much required; therefore, we have the sensor extensively for real sample analysis after taking all ethical clearance. Initially, we tested the GdFeO3-Naf/GCE sensor's performance using spike and recovery real sample analysis method. In this method, a healthy 28-year male volunteer provided blood for sensing. The blood was equilibrated with PBS and kept for 15 minutes to settle down. It was then tested for glucose sensing. A similar amount of glucose was spiked into the electrochemical cell, and the calibration curve was obtained. Based on the concentration-dependent glucose detection in blood, a calibration plot was obtained which shows the linear regression equation as follows: ΔI (μA) = 0.0361(±0.0201) + 0.0014 (±0.000115) Conc [gluco (mg/dL)] with the correlation coefficient of 0.928. The LOD of 12.31 (± 0.01) mg/dL was obtained in blood based on the standard deviation of three consecutive analyses of the blank (95% confidence level; n=3), which shows the fabricated sensor is powerful for real sample analysis and highly reproducible. The results of these experiments were analyzed, and % recoveries of glucose were calculated using equation 5.

$$\% \text{ recovery} = \frac{[S]\text{gluco} - [B]\text{gluco}}{[SS]\text{gluco}} \quad \ldots\ldots\ldots\ldots (5)$$

Where $[S]_{gluco}$ and $[B]_{gluco}$ are the analytical responses of glucose in spiked and blank urine, respectively, and [SS]gluco is the analytical response of glucose in PBS solution.

TH-2627_166106107

Interestingly, the $GdFeO_3$-Naf/GCE sensor showed 102.5% to 112.3% recoveries in the range of 66 mg/dL to 350 mg/dL (Figure 4.11 (a)). More than 100% recoveries were achieved due to the presence of residual glucose in the blood of volunteers; hence, the sensor developed in the present study has great potential for direct application in clinics, as shown in table 4.2.

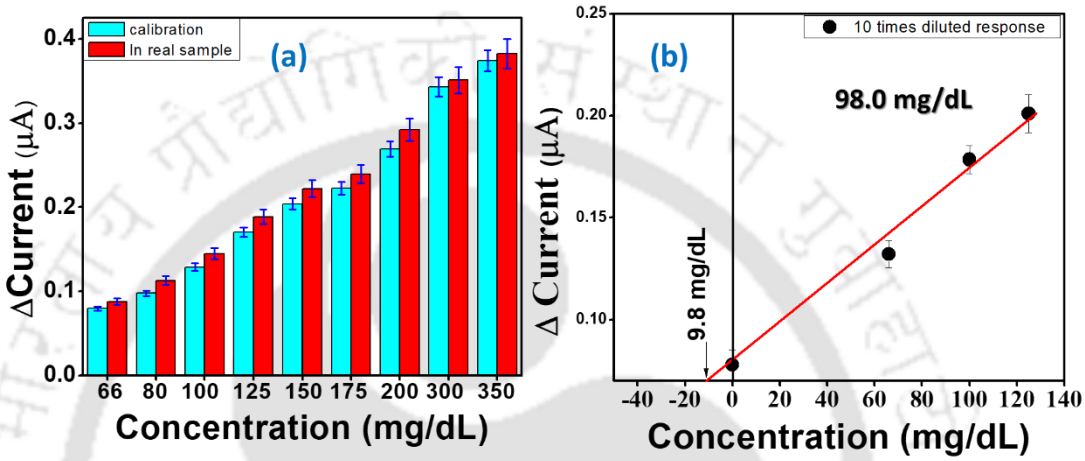

Figure 4.11: $GdFeO_3$-Naf/GCE sensor real sample analysis (a) using the spike-recovery method and (b) standard addition method.

The real sample analysis of the $GdFeO_3$-Naf/GCE sensor was also tested using the standard addition method. In this study, blood from a 26-year healthy volunteer was taken and ten times diluted with PBS, a known concentration of glucose was added into the electrochemical cell, and current responses were recorded. The peak currents were extrapolated with linear fitting, and the initial concentration of glucose was determined to be 9.8 mg/dL, which was a diluted concentration, as shown in figure 4.11 (b). To determine the undiluted glucose concentration, dilution factor was multiplied with observed concentration. It was found to be 98 mg/dL. The calculated concentration was in well agreement with hospital based glucose test.

TH-2627_166106107

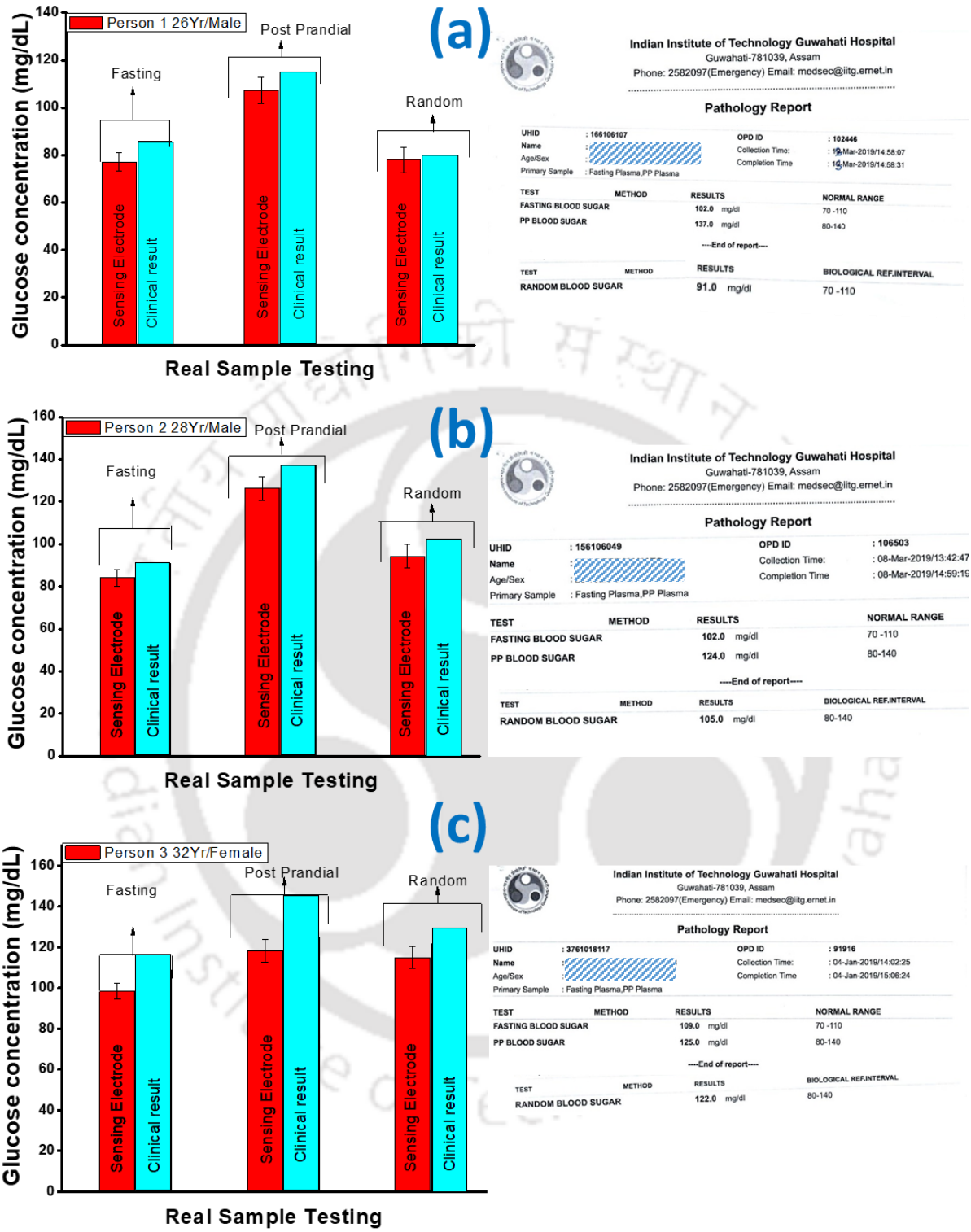

Figure 4.12: $GdFeO_3$-Naf/GCE sensor clinical relevancy test with hospital lab data (a) 26 year male, (b) 28 year male, and (c) 32 year female.

TH-2627_166106107

Sample	Spiked	Recovered	RSD %	% Recoveries
1.	66	70.87 ± 2.21	2.12	107.39 %
2.	80	90.36 ± 1.32	4.02	112.95 %
3.	100	110.61 ± 3.21	6.04	110.61 %
4.	125	136.50 ± 1.82	5.04	109.20 %
5.	150	161.47 ± 2.32	3.06	107.64 %
6.	175	186.48 ± 2.12	3.21	106.56 %
7	200	215.23 ± 3.16	2.07	107.61 %
8.	300	304.80 ± 1.21	3.15	101.60 %
9.	350	355.32 ± 2.16	2.03	101.52 %

Table. 4.2. The percentage recovery of glucose in the blood serum sample

Clinical relevancy test is very much required to test the practical applicability of developed sensors. In this regard, we have tested our $GdFeO_3$-Naf/GCE sensor for glucose concentrations parallel to the hospital-based glucose testing. Three healthy volunteers, including a 32 year old female, were selected and tested for glucose levels using $GdFeO_3$-Naf/GCE sensor while the same blood was tested in the IIT Guwahati hospital (Figure 4.12). The response showed by $GdFeO_3$-Naf/GCE sensor was comparable to IIT Guwahati hospital lab test results.

3.6. Reproducibility and stability studies

For the commercial viability of a sensor, it must have to be highly reproducible and stable (Mahato et al. 2018c). In this regard, we have tested our sensor for reproducibility by checking the current responses with five separate electrodes prepared using similar protocol. The sensor's reproducibility was evaluated, which showed the RSD < 4.32% (n = 3) and probe to probe RSD was < 3.8% even when the same fabrication process was followed. This minor variation was most likely due to the negligible variation in the sensor fabrication process and handling errors. We have also tested the long-term stability of our sensor; it was observed that the sensor retained almost 96.11 ± 2 % (RSD < 5.1 %) of its initial response over ten weeks. Over the period, the current decreased with time, suggesting that the developed $GdFeO_3$-Naf/GCE sensor is stable up to 10 weeks.

TH-2627_166106107

4. Conclusions

With the above study, we conclude that $GdFeO_3$ NPs can be synthesized with a facile, fast, and stable microwave irradiation process. $GdFeO_3$ NPs were physically characterized using XRD, TEM, EDX, elemental mapping, and FTIR spectroscopy. The $GdFeO_3$-Naf nanocomposite material was further characterized using electrochemical techniques and tested for POC glucose electrochemical sensor fabrication. As prepared $GdFeO_3$-Naf nanocomposite showed electrocatalysis of glucose at very low potential. The $GdFeO_3$-Naf/GCE matrix showed the sensing of glucose with a wide LDR of 66-350 mg/dL and LOD of 9.83 mg/dL (±0.05) (RSD< 4%, 95 %), which is comparable to be applied for clinical implication. This is the first report where GdFeO3-Naf was used to detect glucose to the best of our knowledge. The sensor was able to detect the glucose for up to ten weeks. The sensor system fabricated has many outstanding features such as; simplicity, rapidity, label-free, and low-cost detection; hence it could be a method of choice for glucose detection in POC applications. In the next chapter, we have tried to develop an oral cancer biosensor by applying the initially formed gadolinium and iron NMs in this experiment.

TH-2627_166106107

5. *References*

Agrawal B, Chandra P, Goyal RN, Shim YB (2013) Detection of norfloxacin and monitoring its effect on caffeine catabolism in urine samples. Biosens Bioelectron 47:307–312.

Ahmad R, Tripathy N, Ahn MS, et al (2017) Highly Efficient Nonenzymatic Glucose Sensor Based on CuO Modified Vertically-Grown ZnO Nanorods on Electrode. Sci Rep 7:1–10.

Albareda-Sirvent M, Merkoçi A, Alegret S (2000) Configurations used in the design of screen-printed enzymatic biosensors. A review. Sensors Actuators B Chem 69:153–163.

Atta NF, Galal A, Ekram H (2019) Effect of B-site doping on Sr2PdO3 perovskite catalyst activity for nonenzymatic determination of glucose in biological fluids. J Electroanal Chem 113523.

Baghayeri M, Amiri A, Alizadeh Z, et al (2018) Nonenzymatic voltammetric glucose sensor made of ternary NiO/Fe3O4-SH/para-amino hippuric acid nanocomposite. J Electroanal Chem 810:69–77.

Bao J, Qi Y, Huo D, et al (2019) A Sensitive and Selective Nonenzymatic Glucose Sensor based on AuNPs/CuO NWs-MoS2 Modified Electrode. J Electrochem Soc 166:B1179--B1185.

Burke LD (1994) Premonolayer oxidation and its role in electrocatalysis. Electrochim Acta 39:1841–1848.

Chandra P, Zaidi SA, Noh HB, Shim YB (2011) Separation and simultaneous detection of anticancer drugs in a microfluidic device with an amperometric biosensor. Biosens Bioelectron 28:326–332.

Chase HP, Maahs DM (2006) Understanding diabetes: a handbook for people who are living with diabetes. Children's Diabetes Foundation Denver.

TH-2627_166106107

Chen C, Xie Q, Yang D, et al (2013) Recent advances in electrochemical glucose biosensors: a review. RSC Adv 3:4473–4491.

Chung RJ, Wang AN, Liao QL, Chuang KY (2017) Nonenzymatic glucose sensor composed of carbon-coated nano-zinc oxide. Nanomaterials 7:36.

Danaei G, Finucane MM, Lu Y, et al (2011) National, regional, and global trends in fasting plasma glucose and diabetes prevalence since 1980: Systematic analysis of health examination surveys and epidemiological studies with 370 country-years and 2·7 million participants. Lancet 378:31–40.

Ding L, Yan J, Zhao Z, Li D (2019) Synthesis of NiGa2O4 nanosheets for nonenzymatic glucose electrochemical sensor. Sensors Actuators, B Chem 296:126705.

Frier BM, Fisher M (2007) Hypoglycaemia in clinical diabetes. John Wiley & Sons.

Hsu C-L, Lin J-H, Hsu D-X, et al (2017) Enhanced nonenzymatic glucose biosensor of ZnO nanowires via decorated Pt nanoparticles and illuminated with UV/green light emitting diodes. Sensors Actuators B Chem 238:150–159.

Kenneth S, Cummings M (2012) Read: Diabetes Chronic Complications. In: John Wiley Sons Ltd.

Khalaf N, Ahamad T, Naushad M, et al (2019) Chitosan polymer complex derived nanocomposite (AgNPs/NSC) for electrochemical nonenzymatic glucose sensor. Int J Biol Macromol.

Kumar A, Purohit B, Mahato K, et al (2019a) Design and Development of Ultrafast Sinapic Acid Sensor Based on Electrochemically Nanotuned Gold Nanoparticles and Solvothermally Reduced Graphene Oxide. Electroanalysis, 32:59 – 69.

Kumar A, Purohit B, Mahato K, et al (2019b) Gold-Iron Bimetallic Nanoparticles Impregnated

TH-2627_166106107

Reduced Graphene Oxide Based Nanosensor for Label-Free Detection of Biomarker Related to Non-Alcoholic Fatty Liver Disease. Electroanalysis, 31:2417–2428.

Kumar A, Purohit B, Mahato K, Chandra P (2019c) CHAPTER 11. Advance Engineered Nanomaterials in Point-of-care Immunosensing for Biomedical Diagnostics. Immunosensors RSC 238–266.

Kumar A, Purohit B, Maurya PK, et al (2019d) Engineered Nanomaterial Assisted Signal-amplification Strategies for Enhancing Analytical Performance of Electrochemical Biosensors. Electroanalysis 31:1615–1629.

Kumar A, Sharma S, Pandey LM (2018) Nanoengineered material based biosensing electrodes for enzymatic biofuel cells applications. Mater Sci Energy Technol 1:38–48.

Lee W, Kim K, Gurudatt NG, et al (2019) Biosensors and Bioelectronics Comparison of enzymatic and nonenzymatic glucose sensors based on hierarchical Au-Ni alloy with conductive polymer. Biosens Bioelectron 130:48–54.

Liu S, Zeng W, Li Y (2019) Synthesis of ZnCo2O4 microrods grown on nickel foam for nonenzymatic glucose sensing. Mater Lett 126820.

Mahato K, Kumar A, Maurya PK, Chandra P (2018a) Shifting paradigm of cancer diagnoses in clinically relevant samples based on miniaturized electrochemical nanobiosensors and microfluidic devices. Biosens Bioelectron 100:411–428.

Mahato K, Kumar S, Srivastava A, et al (2018b) Chapter 14 - Electrochemical Immunosensors: Fundamentals and Applications in Clinical Diagnostics. In: Vashist SK, Luong JHT (eds) Handbook of Immunoassay Technologies. Academic Press, pp 359–414.

Mahato K, Maurya PK, Chandra P (2018c) Fundamentals and commercial aspects of

TH-2627_166106107

nanobiosensors in point-of-care clinical diagnostics. 3 Biotech 8:149.

Mahato K, Nagpal S, Shah MA, et al (2019) Gold nanoparticle surface engineering strategies and their applications in biomedicine and diagnostics. 3 Biotech 9:57.

Mahato K, Prasad A, Maurya P, Chandra P (2016) Nanobiosensors: next generation point-of-care biomedical devices for personalized diagnosis. J Anal Bioanal Tech 7:e125.

Nichols SP, Koh A, Storm WL, et al (2013) Biocompatible materials for continuous glucose monitoring devices. Chem. Rev. 113:2528–2549.

Noh HB, Lee KS, Chandra P, et al (2012) Application of a Cu-Co alloy dendrite on glucose and hydrogen peroxide sensors. Electrochim Acta 61:36–43.

Oliver NS, Toumazou C, Cass AEG, Johnston DG (2009) Glucose sensors: A review of current and emerging technology. Diabet Med 26:197–210.

Park S, Boo H, Chung TD (2006) Electrochemical nonenzymatic glucose sensors. Anal Chim Acta 556:46–57.

Pletcher D (1984) Electrocatalysis: present and future. J Appl Electrochem 14:403–415.

Purohit B, Mahato K, Kumar A, Chandra P (2019) Sputtering enhanced peroxidase like activity of a dendritic nanochip for amperometric determination of hydrogen peroxide in blood samples. Microchim Acta 186:658.

Rahman MM, Ahammad AJS, Jin JH, et al (2010) A comprehensive review of glucose biosensors based on nanostructured metal-oxides. Sensors 10:4855–4886.

Şavk A, Cellat K, Arıkan K, et al (2019) Highly monodisperse Pd-Ni nanoparticles supported on rGO as a rapid, sensitive, reusable and selective enzyme-free glucose sensor. Sci Rep 9:1–9.

TH-2627_166106107

Shabnam L, Faisal SN, Roy AK, et al (2017) Doped graphene/Cu nanocomposite: A high sensitivity nonenzymatic glucose sensor for food. Food Chem 221:751–759.

Sharma D, Lee J, Shin H (2019) Gold Nanostructure Decorated 3D Porous Carbon Architectures as a Nonenzymatic Glucose Sensor. In: 2019 IEEE 32nd International Conference on Micro Electro Mechanical Systems (MEMS). pp 580–583.

Shaw KM, Cummings MH (2012) Diabetes: chronic complications. John Wiley & Sons.

Tian K, Prestgard M, Tiwari A (2014) A review of recent advances in nonenzymatic glucose sensors. Mater Sci Eng C 41:100–118.

Wang Q, Chen Y, Zhu R, et al (2019) One-step synthesis of Co (OH) F nanoflower based on micro-plasma: as an effective nonenzymatic glucose sensor. Sensors Actuators B Chem 127282.

WHO. World Health Organisation., Organisation. WWH, Who (2010) Global status report on noncommunicable diseases. World Health 176.

Wilson R, Turner APF (1992) Glucose oxidase: an ideal enzyme. Biosens Bioelectron 7:165–185.

Yadav SK, Agrawal B, Chandra P, Goyal RN (2014) In vitro chloramphenicol detection in a Haemophilus influenza model using an aptamer-polymer based electrochemical biosensor. Biosens Bioelectron 55:337–342.

Ye J, Deng D, Wang Y, et al (2019) Well-aligned Cu@C nanocubes for highly efficient nonenzymatic glucose detection in human serum. Sensors Actuators, B Chem 305:127473.

Zhang Y, Li N, Xiang Y, et al (2020) A flexible nonenzymatic glucose sensor based on copper nanoparticles anchored on laser-induced graphene. Carbon N Y 156:506–513.

TH-2627_166106107

TH-2627_166106107

Chapter – V

Design and Development of Non-invasive Oral Cancer Sensor Based on Electrochemically Active Gadolinium Hexacyannoferrate Nanoparticles.

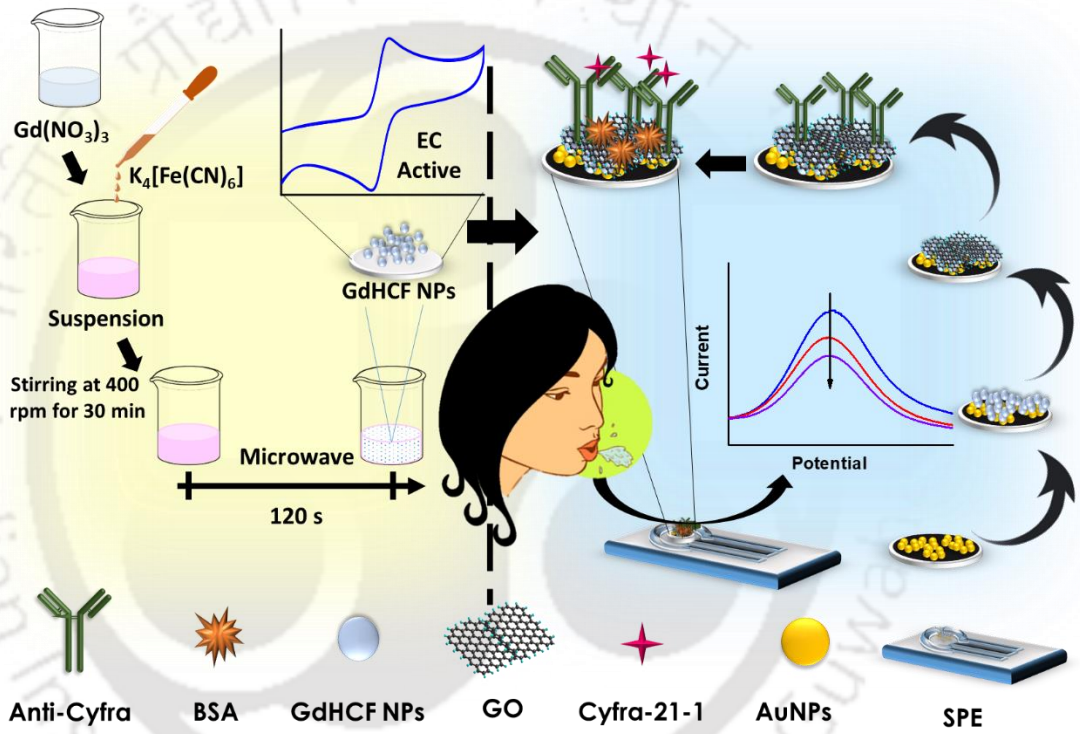

Status:

Manuscript submitted

TH-2627_166106107

1. Introduction

Oral cancer (OC) has been known as one of the most dominant cancers around the globe, and which causes more than 11,000 deaths per year in U.S. only (Brawley 2009; Siegel et al. 2012). OC can be deadly if not diagnosed and treated earlier. Usually, OC initiates in the form of cancer of squamous cell on tongue or mouth that can spread to other body parts if left untreated (Punyani and Sathawane 2013). In spite of the fact that oral cavity is reachable for visual inspection; these cases are typically diagnosed in their advanced stages as patients do not show any symptoms at the initial stage of OC. Though, with time, symptoms like ulcer in oral cavity, teeth loosening, and voice hoarsening are known to develop in the patient (Scully et al. 2008; Mehrotra and Gupta 2011; Brocklehurst et al. 2013).

The primary reasons behind OC development are tobacco chewing, smoking, liquor intake, gastro-oesophageal reflux disorde, human papilloma virus, and hazardous chemicals contact (e.g. formaldehyde and asbestos) (Brawley 2009; Nugent and Moore 2010). These high-risk causes may change the p16, APC, and p53 genes expression, ultimately causing OC (Gonzalez et al. 1997). OC and its premalignant tumours are well-defined for clinical investigation even though high death rates of OC patients are because of late diagnosis (Patton et al. 2008).

In the view of such deadly clinical situation, numerous techniques have been established for OC analysis, which comprises visual inspection, staining with toluidine blue, brush biopsy, bio-imaging by chemiluminescence, fluorescence imaging, computerized tomography, and magnetic resonance imaging (Scully et al. 2008; Arya and Bhansali 2011; Mehrotra and Gupta 2011; Brocklehurst et al. 2013). These detection techniques are useful, though, they have limited point-of-care clinical applications as these are multistep,

TH-2627_166106107

time consuming protocols, need sophesticated fabrication instruments as well as highly trained professionals (Chandra 2015). Moreover, these systems lack the ability to be miniaturized for very sensitive onsite detection. In this regard, biosensors offer a reliable, comprehensible, rapid, sensitive, minimal sample requirement, as well as point-of-care applicability (Chandra and Segal 2016). Nowadays, cancer diagnosis based on biomarkers has gained much importance because of rapid and accurate diagnoses. In last decade, electrochemical sensors have been extremely established for sensitive, selective, easy to operate, and point-of-care cancer analysis. So, to attain a highly sensitive point-of-care OC sensor based on particular OC biomarker would be fascinating to attempt(Prasad et al. 2016; Baranwal et al. 2018; Mahato et al. 2018a; Mandal et al. 2018).

Presently, the biomarkers, such as interleukin-8 (IL-8), interleukin-6 (IL-6), vascular endothelial growth factor, and epidermal growth factor receptor are being applied for OC detection (Gonzalez et al. 1997; Pickering et al. 2007; Malhotra et al. 2010). Though, only a few researches are existing for salivary biomarkers sensing using electrochemical biosensors . Usually, these OC biomarkers are secreted in very minute amount ($pgmL^{-1}$), thus, hard to detect by conventional diagnostic approaches (Mehrotra and Gupta 2011). Moreover, variation in their concentration during OC is not very much evident. Diagnosing OC using serum biomarker makes the diagnosis painful and costly. Hence, OC diagnosis with biomarkers present in human saliva offers a non-invasive and pain-free substitute (Choudhary et al. 2016).

A proteinaceous OC biomarker CYFRA-21-1, (also recognized as cytokeratin-19) is a affiliated to keratin family, which has been recognized as a protein that sustain structural integrity of the epithelial cells (Céruse et al. 2005; Arya and Bhansali 2011). The 40 kDa water soluble proteinaceous OC biomarker is encoded by *KRT19* gene. For healthy human, CYFRA-21-1 cutoff concentration in saliva is 3.8 ng mL^{-1} , while OC patients have been

TH-2627_166106107

found to have CYFRA-21-1 concentration as high as 17.46 ng mL^{-1}. In view of this, an electrochemical biosensor based on CYFRA-21-1 would provide a better opportunity to diagnose OC earlier (Kawaguchi et al. 2000; Zhong et al. 2007; Alkotyfan et al. 2010; Rajkumar et al. 2015; Malhotra et al. 2016). In previous reports of CYFRA-21-1 immunosensor fabrication, there has been continuos use of redox shuttle (usually 5 mM $[Fe(CN)_6]^{-3/-4}$) to carry the charge across the electrodes, which limits the sensor performance because of redox couple stability and activity (Kumar et al. 2015, 2016b, c, a, 2018b; Choudhary et al. 2016).

To design a firm and robust electrochemical sensor, an appropriate support matrix functionalized with desired biomolecules at bioreceptor interaction site leading to an electrical readout signal is very important (Ajayan 1999; Wang 2005; Ignat 2008; Shao et al. 2010). Choice of immobilization platform shows a significant role during sensor assembly in terms of signal transduction, stability of bioreceptors (e.g. antibody), reproducibility, and sensor regeneration. Desired bio recognition element can be attached on wide range of suitable support matrices such as; metallic electrodes, biopolymers, conducting polymers, and self-assembled monolayers. Nanomaterials (NMs) have been found to have fascinating opto-electronic properties due to electron and phonon confinement, high surface-to-volume ratio, high surface reaction activity, high catalytic efficiency, and strong adsorption ability (Kumar et al. 2018a, 2019b, a, c). Thus, the NMs can be utilized for increased loading of desired biomolecules per unit mass of particles . Some NMs shows electrochemically activity such as gadolinium hexacyanoferrate (GdHCF) that not only provide the sensing capacity but also do not require redox couples (Oliver-Tolentino et al. 2018). These NMs can be applied for sensor matrix fabrication, which may provide better sensitivity and stability. Thus, designing a redox-couple free, self-signal generating sensing matirix would be intresting to investigate.

TH-2627_166106107

In the current study, a highly sensitive, self-signal generating, robust and ultrasensitive immunosensor has been designed using AuNPs and GdHCF NPs along with graphene oxide (GO) immobilized anti-CYFRA-21-1antibodies onto screen printed electrodes. The immunosensor probe was fabricated by covalent coupling of COO^- present in GO with NH_2 group of antibodies using EDC NHS chemistry. The step wise assembly of sensing probe was investigated by fourier transform infrared spectroscopy (FTIR), cyclic voltammetry (CV), and electrochemical impedance spectroscopy (EIS). The analytical performance of the designed sensor was obtained bymeasuring the differential pulse voltammetry (DPV) responses. To the best of our knowledge this is the first ever report where AuNPs, GdHCF, and GO based electrochemically active label free immunosensor has been developed and utilized for highly sensitive diagnosis of OC through detecting CYFRA-21-1 directly in human saliva samples.

2. Materials and methods

2.1. Chemicals and instruments

Gadolinium nitrate ($Gd(NO_3)_3$) was purchased from SRL, India. Deionized water was obtained from Milli Q, Millipore unit (Elix USA) of 18.2 MΩ resistance. Glucose was purchased from Himedia. Potassium ferrocyanide ($K_4[Fe(CN)_6]$) and potassium ferricyanide ($K_3[Fe(CN)_6]$) were obtained from Himedia and SRL, respectively. Hydrogen peroxide (H_2O_2), Nafion 117 solution, was procured from Sigma. Sodium dihydrogen phosphate (NaH_2PO_4) and sodium phosphate (Na_2HPO_4) were purchased from Merck and SRL, respectively. CYFRA-21-1 antigens and Anti-CYFRA-21-1 antibodies were purchased from Raybiotech, India. All the chemicals were of AR grade and utilized without any additional purification. Instruments that were used in synthesis, hot plate magnetic stirrer (Tarson India; Spinot), household microwave oven (LG, India; MC-

TH-2627_166106107

2846BCT), for washing BR-Biochem (BR-60) centrifuge, for high-temperature annealing, a muffle furnace, and to dry samples a hot air (Equitron -7051-150) oven was used.

2.2. Synthesis of GdHCF nanoparticles

Equimolar solution of $Gd(NO_3)_3$ and $K_4[Fe(CN)_6]$ were prepared separately using Milli-Q Millipore unit having 18.2 MΩ resistance. A reaction solution of 70 mL was made of $Gd(NO_3)_3$ and $K_4[Fe(CN)_6]$, in 1:1 ratio. Reaction mixture was vigorously stirred upto 2 hours until the colour of mixture solution became milky white. The reaction mixture was then exposed to 120 s of microwave irradiation using household LG microwave oven while setting the power of the machine 900 W. The microwave exposure time was optimized with the change in the color of reaction mixture. Microwave was irradiated in a flash fashion, 30 s on followed by 30 s off, for four times. The milky white reaction mixture changes its color from milky white to greenish white. Further, it was centrifuged and washed four times using milli Q water followed by alcohol. The pellet obtained during centrifugation was dried into hot air oven overnight at 65 °C. The powder obtained after drying was grinded into fine powder using a mortar-pestle and stored in a tight container.

2.3. Synthesis of GO

For the GO synthesis, graphite powder was first oxidized to get graphene oxide (GO) using modified Hummer's method . Briefly, in this process, H_2SO_4 and H_3PO_4 were mixed in volume ratio of 9:1 (27mL: 3mL) and stirred for half hour. 0.225 g of graphite powder was added into mixing solution under stirring condition followed by slowly addition of 1.32 g of $KMnO_4$. The reaction mixture was uninterruptedly stirred for 6 hours until the final solution became blackish dark green. To neutralize the excess of $KMnO_4$, 0.675 mL of H_2O_2 was added dropwise while stirring in cold environment for 10 minutes. Thereafter, 10 mL of HCl and 30 mL of deionized water was added into the solution and centrifuged

TH-2627_166106107

at 5000 rpm for 7 minutes. The supernatant was emptied and the residuals were then washed again with HCl and deionized water for five times followed by drying in a hot air oven at 90 °C for 24 hours to get the GO powder.

2.4. Preparation SPE/AuNP/GdHCF/GO/Anti-Cyfra sensing electrode

The first step towards the development the sensing probe was to deposit AuNPs onto the SPE. We have adopted an electrochemical potential step method in which AuNPs were formed onto the electrode surface, similar to objective 1. The first layer of the AuNPs were electrochemically deposited onto the GCE in an acidic solution (0.6 M H_2SO_4) containing 0.003% $HAuCl_4$ by performing linear sweep voltammetry (LSV) from +1.5 to +0.4 (V) vs. Ag/AgCl. The provided conditions for AuNPs electrodeposition are as follows: 60.0 s deposition time, −0.6 V deposition potential, 0.1 V s^{-1} scan rate. After four-layer deposition we coated the SPE/AuNP electrode with GdHCF NPs. Precisely, 2.5 µl of GdHCF in 0.05% nafion solution was used onto the conducting surface of the SPE and let the electrode dry in closed container for 3 hours to form the SPE/AuNP/GdHCF electrode. In similar way GO was deposited onto the SPE/AuNP/GdHCF electrode using 2.5 µl of GO in 0.05% nafion solution to form SPE/AuNP/GdHCF/GO electrode. After electrode drying, antibodies of Anti-CYFRA-21-1 were covalently attached to SPE/AuNP/GdHCF/GO electrode using EDC-NHS chemistry. In the EDC-NHS covalent immobilization method SPE/AuNP/GdHCF/GO electrode was treated with freshly prepared EDC/NHS (143–100 mM) ultimately causing the COO^- present in GO to attach with NH_2 group of antibodies. BSA was used to block non specific site to avoid non specific interactions. The final sensing electrode was termed as SPE/AuNP/GdHCF/GO/Anti-Cyfra that was used for electrochemical immunosensing of CYFRA-21-1. The GdHCF NPs and SPE/AuNP/GdHCF/GO/Anti-Cyfra OC sensor fabrication has been shown in scheme 5.

TH-2627_166106107

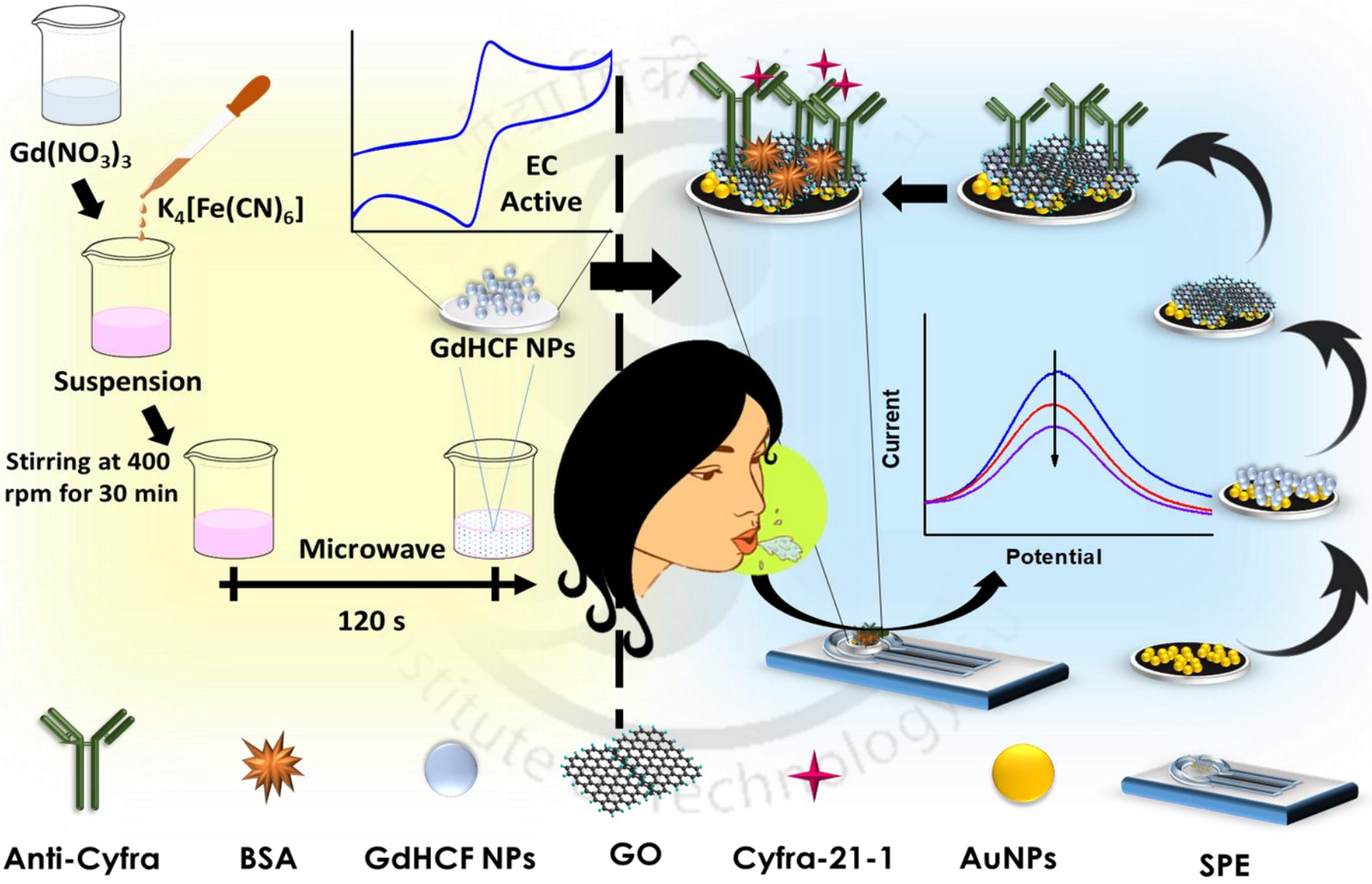

Scheme 5. Scheme of synthesis of GdHCF NPs and SPE/AuNP/GdHCF/GO/Anti-Cyfra OC sensor fabrication.

TH-2627_166106107

2.5. Characterization of GdHCF NPs and SPE/AuNP/GdHCF/GO/Anti-Cyfra sensing electrode

2.5.1. X-ray diffraction (XRD) analysis:

The crystalline nature of the GdHCF NPs was determined through a powder X-ray diffractometer (Rigaku Smart Lab), where, XRD analysis was performed at 2θ Bragg's angle by maintaining the range between 30° to 80° with a scan rate 20° per minute.

2.5.2. Uv-Vis spectroscopy:

UV-Vis spectrophotometer (Carry 60) was used to determine the formation of GdHCF NPs present in the reaction mixture by scanning the aliquots between 250 and 450 nm range.

2.5.3. Transmission electron microscopy (TEM) imaging and analyses:

GdHCF NPs shape, size, dispersivity, energy dispersive X-ray (EDX) study, and electron diffraction analyses were performed with FE-TEM (JEOL JEM-2100F TEM). Sample was prepared by drop casting the well dispersed GdHCF NPs in ethanol onto the surface of carbon coated copper grid (300 mesh) and allowing it to dry at 37°C for 12 hrs.

2.5.4. Raman Spectroscopy:

GdHCF NPs, GO, AuNP/GdHCF/GO and AuNP/GdHCF/GO/Anti-Cyfra nanocomposites were characterized for Raman scattering using Raman spectrophotometer (Laser Micro Raman System Horiba Jobin Vyon, Model LabRam HR). For Raman analysis, separate films of GdHCF NPs, GO,

TH-2627_166106107

AuNP/GdHCF/GO and AuNP/GdHCF/GO/Anti-Cyfra were prepared onto the SPE. A Co laser of 512 nm has been applied with 10 s reaction time to measure the Raman scattering in the range of 1200 to 2500 cm^{-1}.

2.5.5. *Fourier-transform infrared (FTIR) spectroscopy:*

GdHCF NPs and step wise electrode surface modifications were characterized for IR spectroscopy using FTIR spectrometer (Cary- 630). For FTIR studies, the diamond ATR mode of operation was selected in the FTIR spectrometer. GdHCF NPs were placed onto the diamond ATR and scanned for transmittance in the range of 400 cm^{-1} to 4000 cm^{-1}.

2.5.6. *Electrochemical characterizations:*

The SPE, SPE/AuNP, SPE/AuNP/GdHCF, SPE/AuNP/GdHCF/GO, and SPE/AuNP/GdHCF/GO/Anti-Cyfra electrodes were electrochemically characterized using Metrohm electrochemical analyser (Autolab potentiostat galvanostat) with the help of various electrochemical techniques such as CV, differential pulse voltammetry (DPV), and EIS. A phosphate buffer saline (PBS pH 7.6 and 0.9% NaCl) solution was used as electrolyte to perform all electrochemical characterization using Ag/AgCl as a reference electrode and carbon paste as counter electrode printed onto the SPE.

TH-2627_166106107

3. Result and discussions

3.1. Physical Characterization of GdHCF nanoparticles

3.1.1. XRD studies:

To determine the crystallinity of our GdHCF NPs, we have performed X-ray diffraction study. 50 mg of GdHCF NPs powder was used to check the diffraction pattern. The machine was set into powder mode of measurement. The XRD pattern of GdHCF NPs didn't show any diffraction pattern, most likely due to amorphous nature of GdHCF NPs (data not shown).

3.1.2. UV-Vis analysis:

The indication of GdHCF NPs formation has been observed with the change in the color of reaction mixture, which was changed from trasnsparent to milky white. Further, it was confirmed using UV-Vis spectrophotometer, the spectrum of sample was observed with the broad peak around 300 ± 3 nm (Figure 5.1 (a)). To test whether the peak is coming merely due GdHCF NPs we have tested with controls. We gradually increases the GdHCF NPs concentration in cuvette (figure 5.1. (b)). Interestingly, we found increase in the absorbance at 300 nm, indicating the peak was merely due to GdHCF NPs. A calibration curve was plotted with reapect to GdHCF NPs concentration that follows a linear plot with R^2 of 0.96, [Absorbance (Y) = 0.377 (±0.0319) [concentration of GdHCF NPs] – 0.0209 (±0.079)]. We have performed the UV-Vis absorbance study for diluted $Gd(NO_3)_3$ and $K_4[Fe(CN)_6]$ salt solutions that didn't show any significance absorbance near 300 nm (figure 5.1. (c) and

TH-2627_166106107

(d)). It further confirm the formation of GdHCF NPs with microwave irradiation technique.

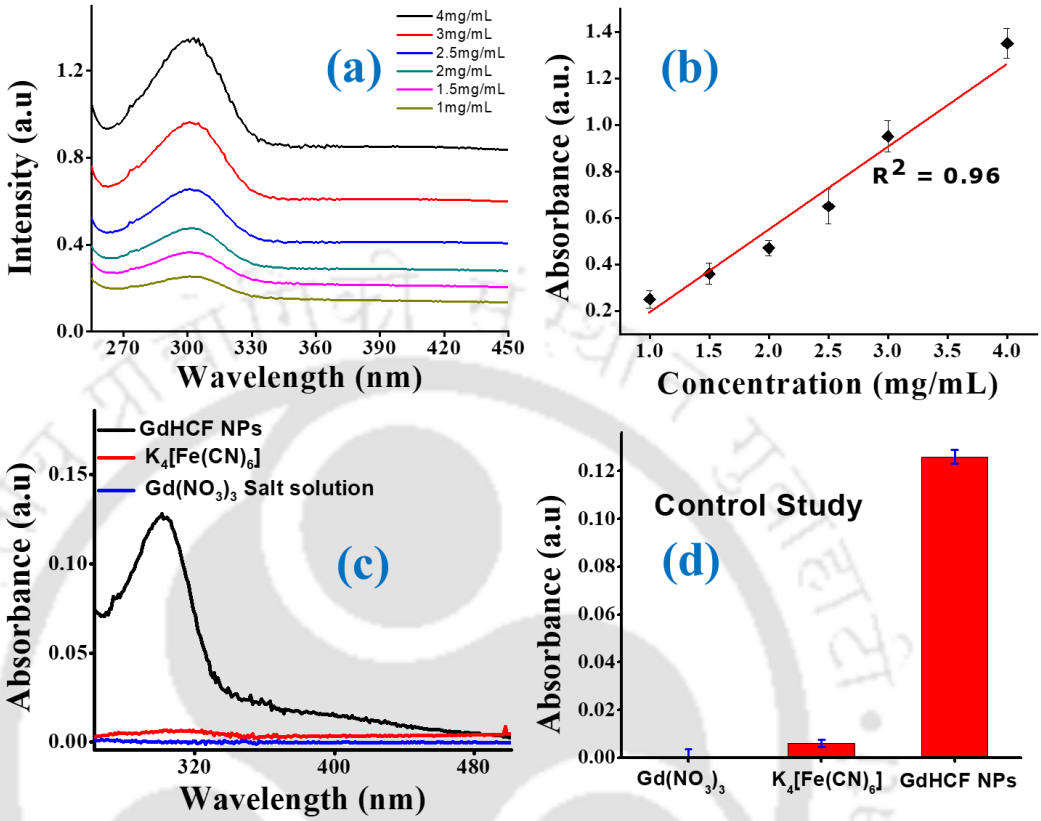

Figure 5.1: (a) UV-Vis absorbance spectrum of GdHCF NPs of different concentrations, (b) corresponding calibration curve, (c) UV-Vis absorbance of GdHCF NPs with respect to controls, and (d) corresponding absorbance histograms.

3.1.3. TEM imaging and analyses:

In order to characterize the size, shape, and distribution, TEM analyses of GdHCF NPs were performed (Figure 5.2 (a)). Clear dark spherical structures were observed in the whole field of imaging. In order to validate the crystalline nature of GdHCF NPs, we have performed selected area electron diffraction

TH-2627_166106107

(SAED) using TEM. SAED of the GdHCF NPs did not show any diffraction pattern, which reveal the amorphous nature of the GdHCF NPs (Figure 5.2 (b)).

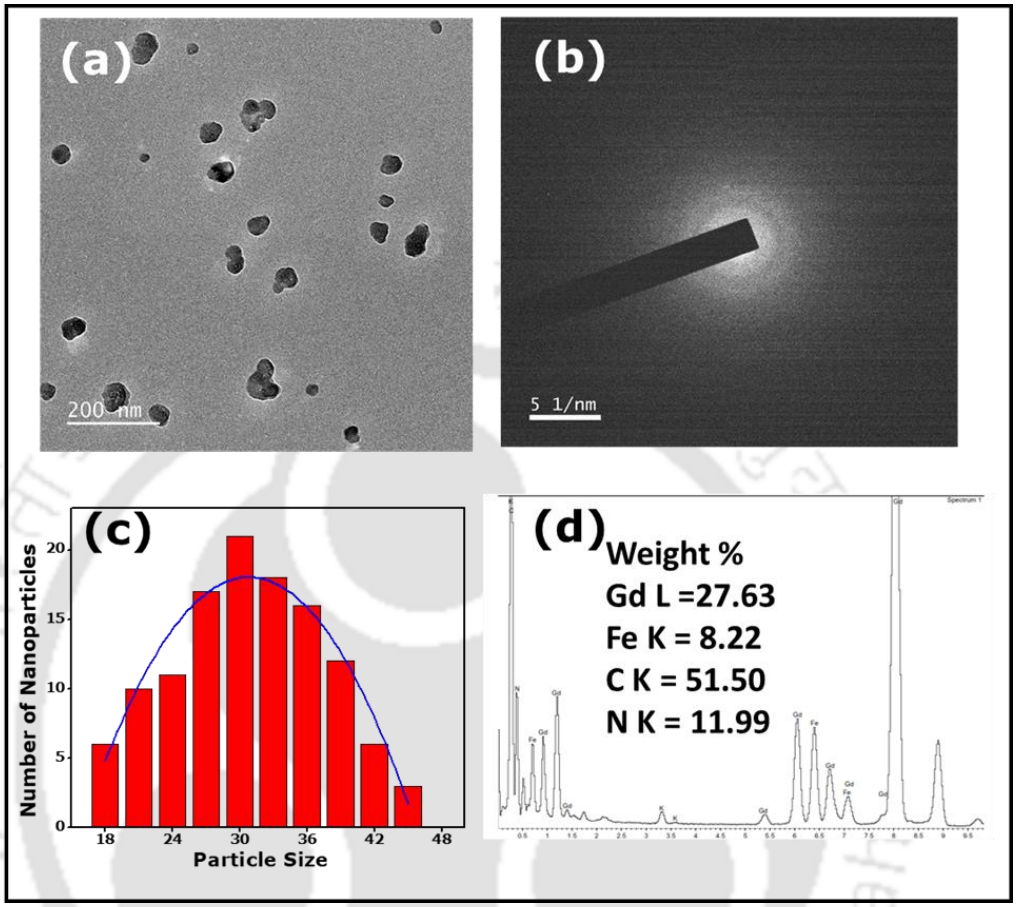

Figure 5.2: (a) TEM image of the GdHCF NPs, (b) SAED pattern, (c) size distribution of the particles, and (d) EDX of the particles

The result of SAED is in well agreement to XRD data, which re-confirm the amorphous nature of GdHCF NPs. Thereafter, we calculated the size distribution of GdHCF NPs considering 121 particles using image-processing tool (ImageJ), where mean size of the particles were obtained with the diameter of 33 nm (Figure 5.2 (c)). The energy dispersive x-ray spectroscopy (EDX) was performed to further validate the presence of iron, carbon, nitrogen, and gadolinium in GdHCF NPs that has been shown in figure 5.2 (f). EDX results

TH-2627_166106107

showed the presence of 27.63 %, 8.22 %, 51.55 % , and 11.99 % gadolinium, iron, carbon, and nitrogen in the tested sample by weight, respectively, re-confirming the synthesis of GdHCF NPs.

3.1.4. Raman Analysis:

In order to obtain the chemical and structural information about GdHCF NPs, GO, AuNP/GdHCF/GO and AuNP/GdHCF/GO/Anti-Cyfra nanocomposites; we have performed Raman spectroscopy (Figure 5.3) using SPE as a substrate for all the films. For GdHCF NPs (black) three characterstic peaks T_{1u}, E_g, and A_{1g} were observed around 2080, 2100, and 2130 cm^{-1}, which is most likely due to the functional groups present in the GdHCF NPs (Figure 5.3 (a)). The vibrational energy study with Raman analysis indicates the σ-donor ability of the $C{\equiv}N^-$ group present in the compound, which is transferring electrons to the metal bonded by coordination bond with N terminal. The transfer of electron occurs through the σ orbital that has a definite antibonding property. The metal coordinated to carbon terminal showed π bonding interaction that involves the t_2g electrons of the metal and the π and π* orbitals of the ligand (Oliver-Tolentino et al. 2018). These interacitons permits the oxidation of internal and external metals in the cyano complex. In the second spectrum, the two peaks were observed at 1323.3 and 1587.2 cm^{-1}, which corresponds to the characteristic peaks of GO (green; designated as D and G peaks, respectively) (Figure 5.3 (b)). In the next spectrum, when AuNP/GdHCF/GO nanocomposite was evaluated, peaks associated with GO and GdHCF appears together indicating the presence of both NMs onto the surface (Figure 5.3 (c) blue curve).

TH-2627_166106107

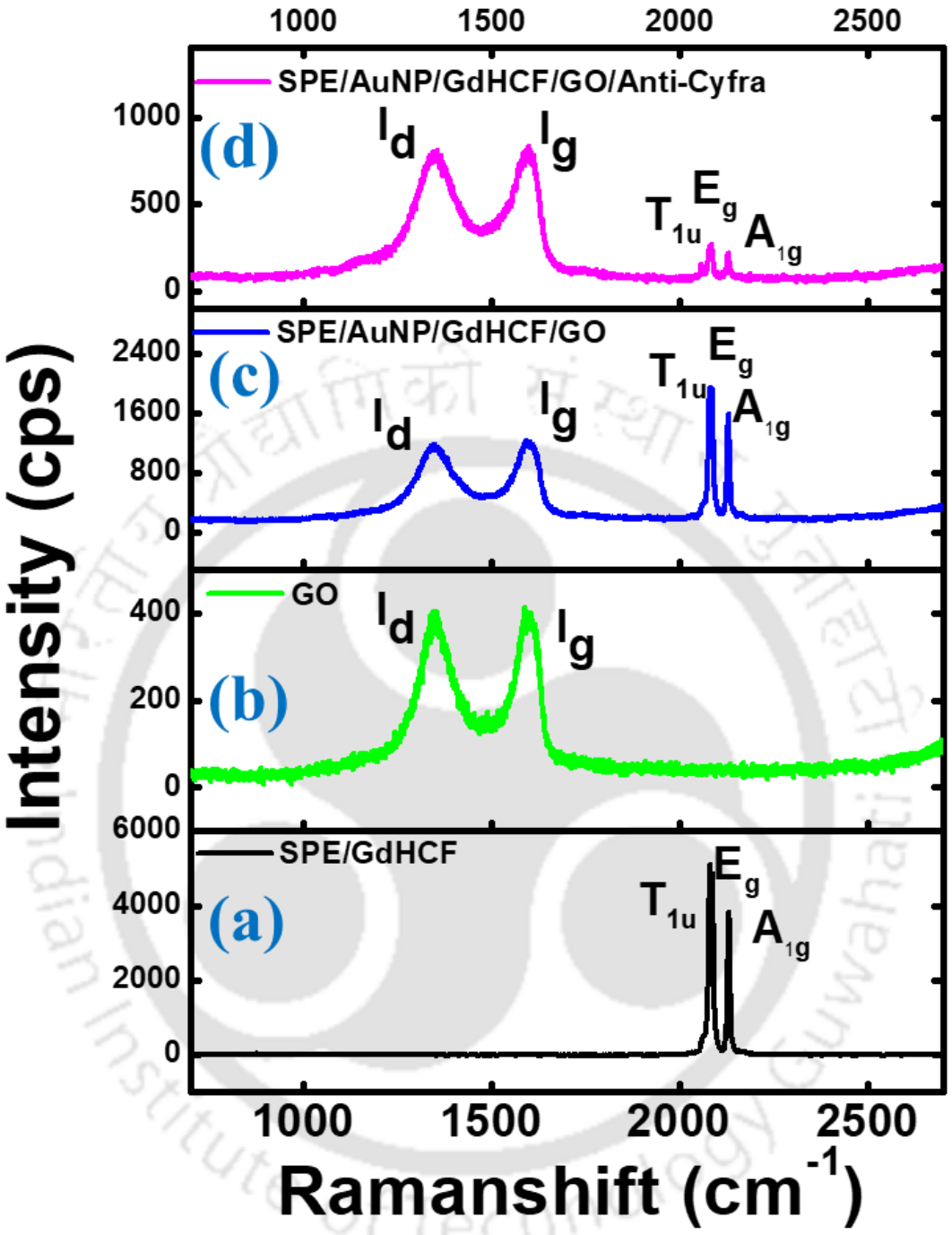

Figure 5.3: Raman analysis of (a) GdHCF NPs, (b) GO, (c) AuNP/GdHCF/GO, and (d) AuNP/GdHCF/GO/Anti-Cyfra nanocomposites.

TH-2627_166106107

Intrestingly, there was no change in I_d/I_g ratio, which indicate that GdHCF NPs were not damaging the sp^2 structure of GO (Zhang et al. 2011). In the next spectrum, AuNP/GdHCF/GO/Anti-Cyfra, similar peaks were obtained, indicating the presence of all constieuent materials (Figure 5.3 (d) pink curve).. It is worth to mention that the T_{1u}, E_g, and A_{1g} GdHCF NPs peaks are present even after complex protein immobilization. This also explain the redox activity present in the final probe (Jasuja and Berry 2009).

3.1.5. FTIR Analysis:

FTIR study was performed to check the presence of functional molecules and to confirm the fabrication in every critical step (Figure 5.4). The FT-IR spectrum of bare SPE showed no vibrational band indicating no polar molecule is present over SPE (Figure 5.4 (a) black). After AuNP deposition we did not get any change in the FTIR spectrum that shows there is absence of chemical bond between AuNPs and SPE (data not shown). After deposition of GdHCF NPs over SPE/AuNP electrode, a characteristic peak of C≡N was observed around 2065 cm^{-1} and the absorption bands appeared at 3350 cm^{-1} and 3575 cm^{-1} corresponded to the O-H present in the GdHCF (Figure 5.4 (b) red). The faint peaks appeared around 1588 and 1650 cm^{-1} are also indicates the O-H present in coordination compond. Intrestingly, when GO was deposited over SPE/AuNP/GdHCF electrode, the functional groups of GO appeared along with the GdHCF NPs peaks (Figure 5.4 (c) blue). The peaks around 2885 and 2972 cm^{-1} corresponds to C-H bond stretching along with the characteristic peak of C≡N around 2065 cm^{-1} was observed. The peaks around 1385 and 1438 cm^{-1} also corresponds to C-H bond present in GO. Bands appeared near 1384 cm^{-1} was assigned to stretching of $–COO^-$ stretch. The sharp peaks around 1035

TH-2627_166106107

and 1089 cm^{-1} exhibits the presence of C-C-C bond on the electrode surface. The FTIR peaks around 1671 cm^{-1} shows the presence of COO^- groups of the GO. When Anti-CYFRA-21-1 antibodies were immobilized onto the SPE/AuNP/GdHCF/GO electrode the FTIR spectrum changed and some new peaks appeared (Figure 5.4 (d) green). The intensity of peak around 1668 cm^{-1} was increased indicating the presence of CO group. A new peak around 1547 cm^{-1} was observed indicating the presence of NH_2 onto the sensor surface along with the characteristic peak of C≡N. The FTIR analysis not only confirmed the step wise surface modifications but also the immobilization of Anti-CYFRA-21-1onto the electrode surface.

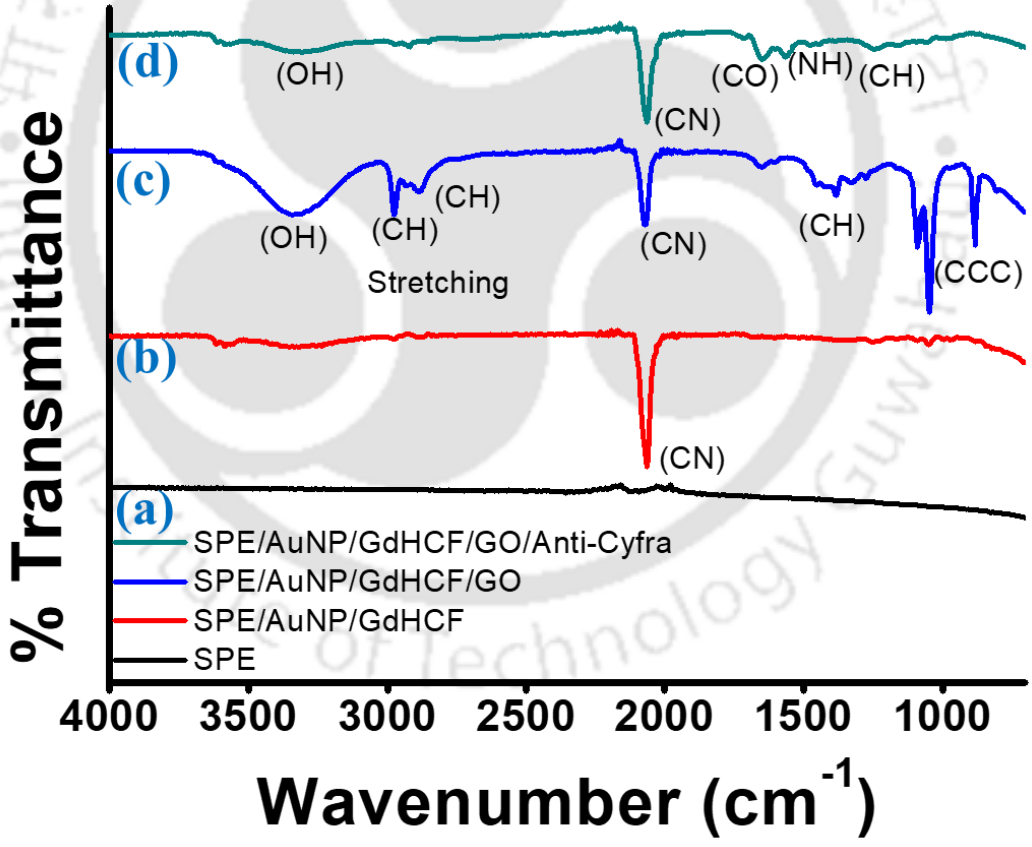

Figure 5.4: FTIR graphs (a) SPE, (b) SPE/AuNP/GdHCF, (c) SPE/AuNP/GdHCF/GO, and (d) SPE/AuNP/GdHCF/GO/Anti-CYFRA-21-1.

TH-2627_166106107

3.2. Electrochemical Characterizations

The change in the electrochemical response of SPE, SPE/AuNP, SPE/AuNP/GdHCF, SPE/AuNP/GdHCF/GO, and SPE/AuNP/GdHCF/GO/Anti-CYFRA-21-1 electrodes were studied using CV with a scan rate of 0.05 V/s in 3 mL PBS containing 0.9% NaCl from -0.8 V to 0.8 V. In the case of bare SPE (Figure 5.5 (a) black curve), there was no current observed, indicating the absence of redox couple into the system. Similar, response was observed when SPE/AuNP electrode was tested (data not shown). When SPE/GdHCF electrode was tested, an oxidaion peak around 0.2 V and a reduction peak 0.03 V was observed, showing the electrode surface has capacity to be oxidized and reduced. When SPE/AuNP/ GdHCF electrode was tested an increase in the current was observed, indicating the increase in the electrode surface conductivity (Figure 5.5 (a) red curve). When electrode SPE/AuNP/GdHCF was modified with GO, redox current was decreased indicating formation of insulating over electrode (Figure 5.5 (a) green curve). Again, when SPE/AuNP/GdHCF/GO electrode was immobilized with Anti-CYFRA-21-1 and after BSA blocking, a decrease in the current was observed, indicating an insulating layer formation over electrode (Figure 5.5 (a) pink curve). Histogram of peak current with respect to electrode fabrication is shown in figure 5.5 (b). The CV study of SPE, SPE/AuNP, SPE/AuNP/GdHCF, SPE/AuNP/GdHCF/GO, and SPE/AuNP/GdHCF/GO/Anti-CYFRA-21-1 electrodes, indicate the importance of GdHCF as a electrochemically active surface that is not only assisting in signal generation but also have the capacity to provide signal even after complex bioreceptor immobilization.

TH-2627_166106107

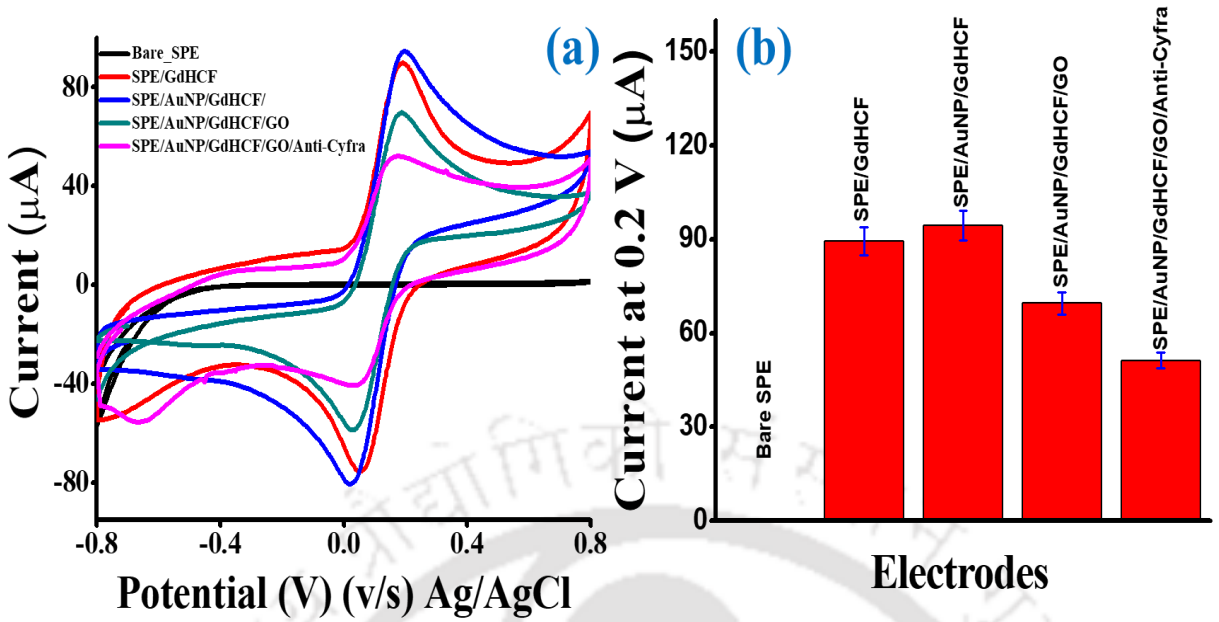

Figure 5.5: (a) Electrode study in PBS and (b) corresponding peak current histograms

The results obtained by CV were also validated using the EIS, where spectra in the Nyquist plot were recorded for bare SPE, SPE/GdHCF, SPE/AuNP/GdHCF, SPE/AuNP/GdHCF/GO, and SPE/AuNP/GdHCF/GO/Anti-CYFRA-21-1 electrode surfaces to obtain the resistance in charge transfer (Rct) as shown in figure 5.6 (a). The R_{ct} values obtained were 81098.2 ± 2103.25 Ω, 11121.3 ± 656.99 Ω, 9113.2 ± 892.53 Ω, 14325.4 Ω ± 659.84, and 17591.1 ± 764.67 Ω for the bare SPE, SPE/GdHCF, SPE/AuNP/GdHCF, SPE/AuNP/GdHCF/GO, and SPE/AuNP/GdHCF/GO/Anti-CYFRA-21-1 electrodes, respectively figure 5.6 (b). It is interesting to note that the low R_{ct} was obtained as compare to SPE for SPE/AuNP/GdHCF/GO/Anti-CYFRA-21-1 surface, indicating the potential of final probe. This was due to the fastest electron transfer kinetics

TH-2627_166106107

at electrode/electrolyte interface in this case. The results obtained in EIS also corroborates with the results of CV analysis.

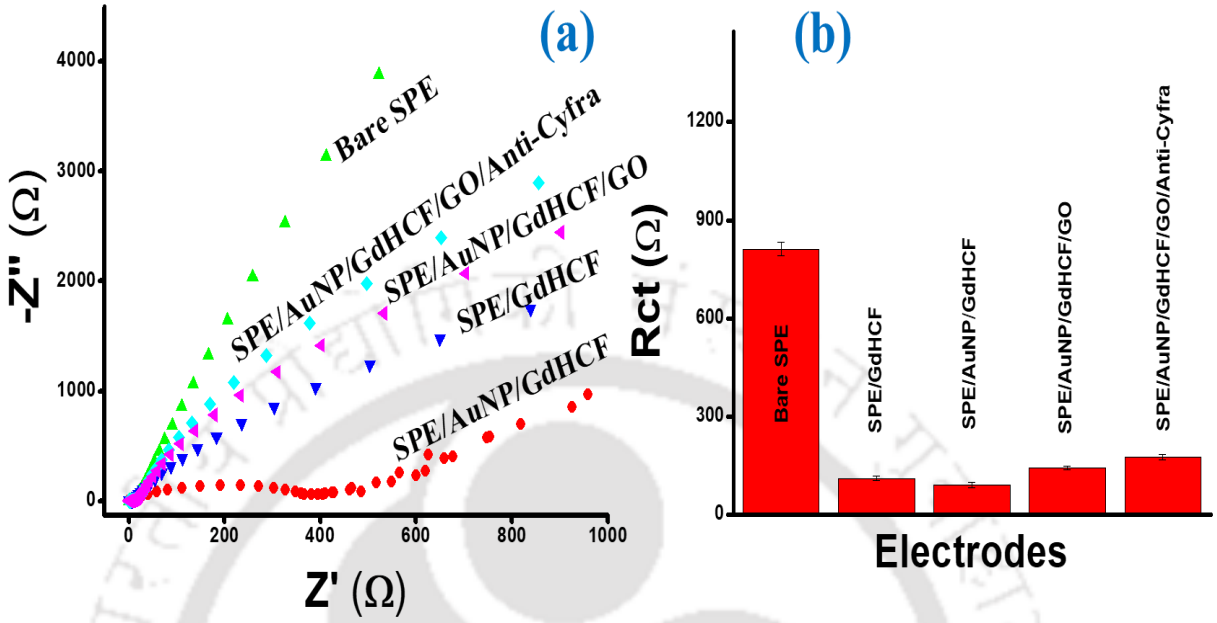

Figure 5.6: (a) EIS study of electrodes in PBS and (b) corresponding R_{ct} histograms

To determine the stability of SPE/AuNP/GdHCF/GO/Anti-CYFRA-21-1 sensing electrode, we have performed the scan rate studies (Figure 5.7. (a)). SPE/AuNP/GdHCF/GO/Anti-CYFRA-21-1 was tested with variable scan rates from (20 mV/s to 100 mV/s) in 2 mL PBS (pH 7.0 and 0.9% NaCl). With increase in scan rate, the oxidation and reduction current increases, suggesting the SPE/AuNP/GdHCF/GO/Anti-CYFRA-21-1 sensing matrix highly stable. The cathodic and anodic peak were in good linearity with respect to scan rates as well as having regression coefficient (R^2 = 0.996) and (R^2 = 0.998), respectively (figure 5.7 (b)), showing that it was because of on surface oxidation and reduction.

TH-2627_166106107

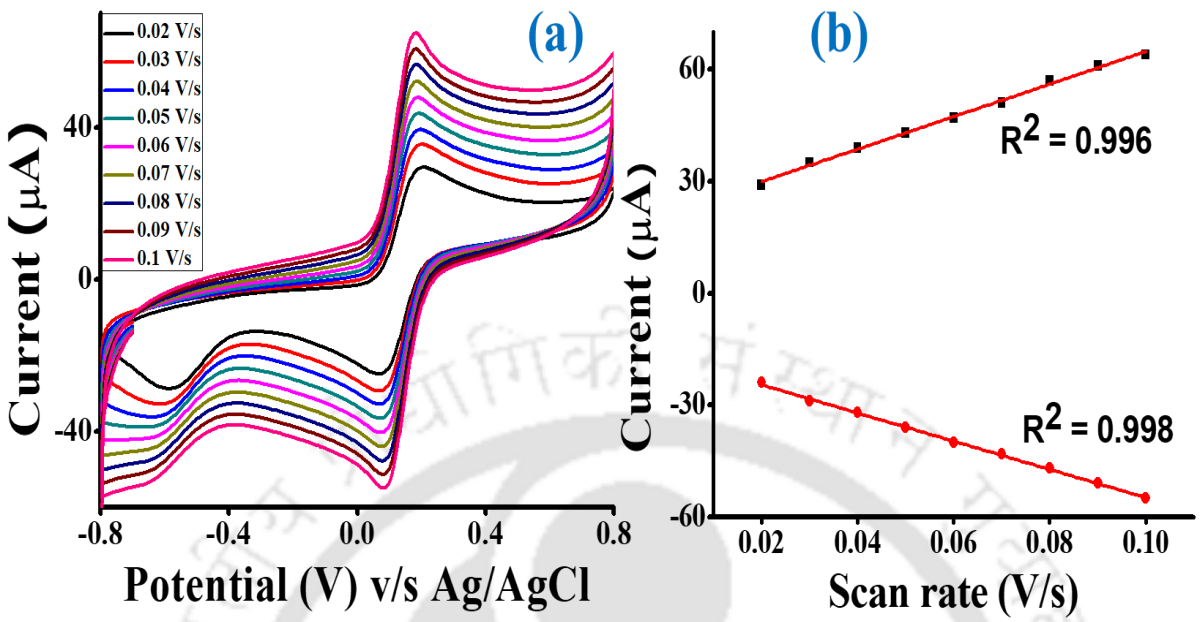

Figure 5.7: (a) Scan rate study of SPE/AuNP/GdHCF/GO/Anti-CYFRA-21-1 sensing electrode and (b) corresponding anodic and cathodic peak currents.

Since, electrochemical properties are surface charge dependent, the concentration of ionic species at electrode surface plays an important role. Therefore, in order to assess the concentration of ionic species (I^*) using Brown-Anson model (Equation 1) is used (Verma et al. 2017).

$$I_p = \frac{n^2F^2I^*AV}{4RT} \quad \text{..... (1)}$$

Where n is number of electrons (n=1, in this case), F is Faraday constant (96485.34 C mol^{-1}), T is 298 K, and I_p/V is the slope of calibration (scan rate value), A is surface area of the electrode (0.01 cm^2), and R is gas constant.

I^* for SPE, SPE/GdHCF, SPE/AuNP/GdHCF, SPE/AuNP/GdHCF/GO, and SPE/AuNP/GdHCF/GO/Anti-CYFRA-21-1 was calculated as 1.85×10^{-7} M/cm^2, 2.93×10^{-7}

TH-2627_166106107

M/cm^2, 3.07×10^{-7} M/cm^2, 2.56×10^{-7} M/cm^2, and 2.23 ×10^{-7} M/cm^2, respectively. These results clearly indicates that SPE/AuNP/GdHCF/GO/Anti-CYFRA-21-1 modified electrode has appriciable surface charge density compare to bare SPE. Further, the reaction kinetics at modified electrode surfaces was evaluated by using Laviron model (equation. 2), in order to find diverse electron transfer rate constant (K_s) (Verma et al. 2017).

$$K_s = mnFv/RT \quad \text{..... (2)}$$

The calculated K_s for the SPE, SPE/GdHCF, SPE/AuNP/GdHCF, SPE/AuNP/GdHCF/GO, and SPE/AuNP/GdHCF/GO/Anti-CYFRA-21-1 modified electrode surfaces was obtained to be 1.87 s^{-1}, 0.84 s^{-1}, 0.78 s^{-1}, 1.21 s^{-1}, and 1.32 s^{-1}, which indicate the SPE/AuNP/GdHCF/GO/Anti-CYFRA-21-1modified electrode surfaces is capable of 0.75 times faster charge transfer compare to SPE.

3.3. Analytical performance of SPE/AuNP/GdHCF/GO/Anti-CYFRA-21-1 sensor probe

After confirming the electrochemical properties of the SPE/AuNP/GdHCF/GO/Anti-CYFRA-21-1 electrode, the electrochemical response of SPE/AuNP/GdHCF/GO/Anti-CYFRA-21-1 electrode was measured as a function of CYFRA-21-1 concentration (02-50 ng/mL) in 2 mL PBS at a scan rate of 0.05 V s^{-1}, from -0.05V to 0.35 V, using DPV technique (Figure 5.8 (a)). There was an oxidation peak around 0.1 V, which was coming because of redox capability of GdHCF NPs as obtained in CV. Figure 5.8 (a) shows the representative DPV curves, where the current response decreases with the increase in CYFRA-21-1 concentration, indicating the gradulation formation of insulating layer over sensor surface. Intrestingly, the current saturated over 50 ng/mL, showing the saturation of binding sites present in SPE/AuNP/GdHCF/GO/Anti-CYFRA-21-1 sensing electrode. Based on the DPV responses, a calibration plot was acquired that shows the linear

TH-2627_166106107

detection range (LDR) from 02-50 ng/mL of CYFRA-21-1 (Figure 5.8 (b)). The linear regression equation of the calibration plot for CYFRA-21-1 sensing was expressed as follows:

$$\Delta I\ (\mu A) = 7.62\ (\pm\ 1.86 \times 10^{-1}) - 0.1535\ (\pm\ 5.89 \times 10^{-3})\ \text{Conc. [CYFRA-21-1 (ng/mL)]} \quad \ldots\ldots(3)$$

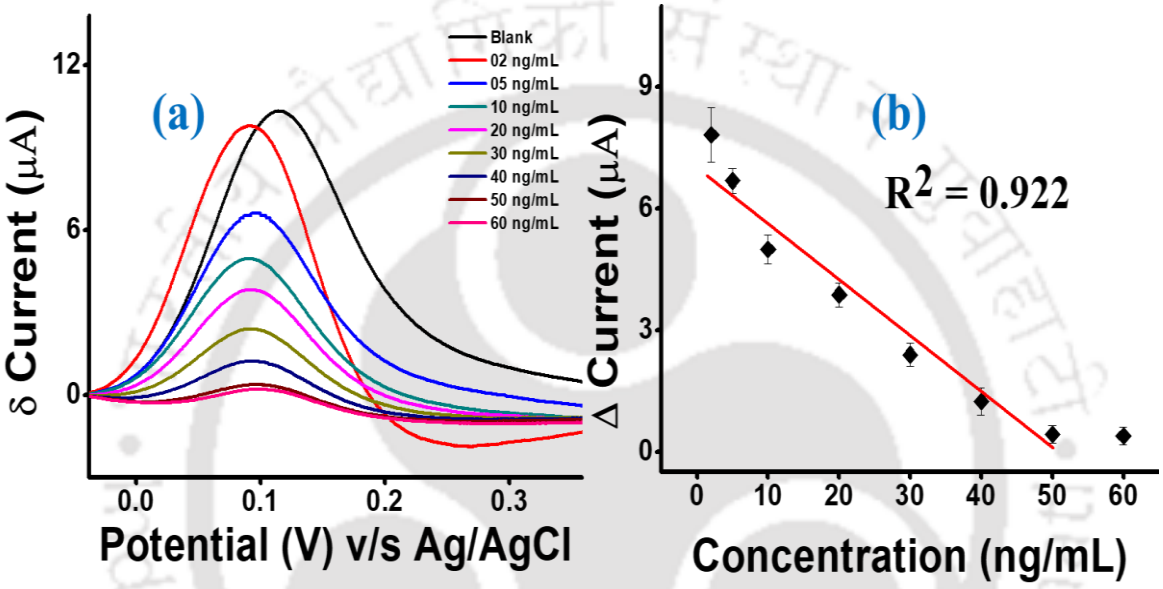

Figure 5.8: (a) Response study of SPE/AuNP/GdHCF/GO/Anti-CYFRA-21-1 sensor electrode and (b) corresponding calibration plot.

The regression coefficient was calculated as 0.922, which shows the good linearity. The limit of detection (LOD) of CYFRA-21-1 was determined to be 0.6 ng/mL (±0.012) ((RSD< 4.1%, 95 % confidence level, n=3) using following equation.

$$\text{LOD} = \frac{3\sigma_b}{m} \quad \ldots\ldots\ldots\ldots\ldots\ldots\ldots\ldots\ldots\ldots\ldots\ldots\ldots\ldots\ldots\ldots\ldots\ldots (3)$$

Where, σ_b is standard deviation of blank and m is slope of the calibration curve.

TH-2627_166106107

Notably, in our case obtained LOD is significant enough to detect CYFRA-21-1 even in low concentrations. The dyanamic range of SPE/AuNP/GdHCF/GO/Anti-CYFRA-21-1 sensor can cover the normal as well cancerous conditions, indicating the immense clinical importance of the fabricated sensor.

3.4. Selectivity study

To evaluate the commercial importance of any sensor, it is important to investigate the selectivity of sensor towards various possible interfering molecules (Mahato et al. 2018b). In order to determine the interfering effects, SPE/AuNP/GdHCF/GO/Anti-CYFRA-21-1 probe was tested towards glycine, cystine, glutamic acid, alanine, glucose, BSA, citric acid, ascorbic acid, and CEA, which may potentially coexist with CYFRA-21-1 in real matrix. No significant signal response was observed for the tested interfering compounds due to either their inherent electro-inactive behaviour (*e.g.* glucose, BSA) or due to the different operational potential window (Chandra et al. 2011; Noh et al. 2012; Agrawal et al. 2013; Yadav et al. 2014). The selectivity of SPE/AuNP/GdHCF/GO/Anti-CYFRA-21-1 probe was statistically inferred by determining the selectivity coefficient using equation 4.

$$k_{sel} = \frac{(Signal)interfernt}{(Signal)CYFRA} \text{ ---------- (4)}$$

Where k_{sel} is the coefficient of selectivity, $(Signal)_{interfernt}$ is the signal strength of sensor when treated with the interfering molecules and $(Signal)_{CYFRA}$ is signal strength of CYFRA-21-1.

TH-2627_166106107

Sr. No:	Interfering molecule	Selectivity coefficient (k_{sel})	Signalling magnitude (times lesser)
01.	Cysteine	0.209	4.78
02.	Alanine	0.214	4.66
03.	Glycine	0.217	4.60
04.	Glucose	0.225	4.44
05.	Urea	0.230	4.34
06.	Ascorbic Acid	0.233	4.29
07.	Glutamic Acid	0.231	4.32
08.	Uric Acid	0.224	4.46
09.	Citric Acid	0.213	4.67
10.	Serum Albumin	0.223	4.47
11.	CEA	0.222	4.48
12.	Cyfra-21-1	1	Analyte response

Table. 5.1. Selectivity coefficient (k_{sel}) with respect to possible interferents

TH-2627_166106107

Table 5.2. A detailed account of the comparative analytical performances of recently reported cyfra-21-1 based OC sensors.

Sl. No.	Sensor probe design	LDR	DL	Real sample		Detection technique	Redox couple requirement	References
1.	BSA/anti-CYFRA-21-1/APTES/ZrO_2 /ITO	2 –16 ng/mL	0.08 ng/mL	Not reported	ELISA	CV	5 mM $[Fe(CN)6]^{3-/4-}$	(Kumar et al. 2015)
2.	BSA/anti-CYFRA-21-1/APTES/nHfO_2/ITO	2 –18 ng/mL	0.21 ng/mL	Not reported	ELISA	CV	5 mM $[Fe(CN)6]^{3-/4-}$	(Kumar et al. 2016a)
3.	BSA/anti-CYFRA-21-1/APTES/ZrO_2–RGO/ITO	2 –22 ng/mL	0.122 ng/mL	Not reported	ELISA	DPV	5 mM $[Fe(CN)6]^{3-/4-}$	(Kumar et al. 2016b)
4.	BSA/anti-Cyfra-21-1/L-Cys-$La(OH)_3$/ITO	0.001-10.2 ng/mL	0.001 ng/mL	Yes	Artificial Saliva	DPV	5 mM $[Fe(CN)6]^{3-/4-}$	(Tiwari et al. 2017)
5.	BSA/anti-CYFRA-21-1/APTES/nHfO_2@RGO/ITO	0-30 ng/mL	0.16 ng/mL	Not reported	ELISA	DPV	5 mM $[Fe(CN)6]^{3-/4-}$	(Kumar et al. 2018c)
6.	**SPE/AuNP/GdHCF/GO /Anti-Cyfra**	**2 – 50 ng/mL**	**0.6 ng/mL**	**Yes**	**Human Saliva**	**DPV**	**Redox couple free**	**This Work**

TH-2627_166106107

The calculated k_{sel} values (table 5.2) for interfering molecules were extremely low (< 1), indicating that the fabricated sensor is highly selective towards CYFRA-21-1 detection.

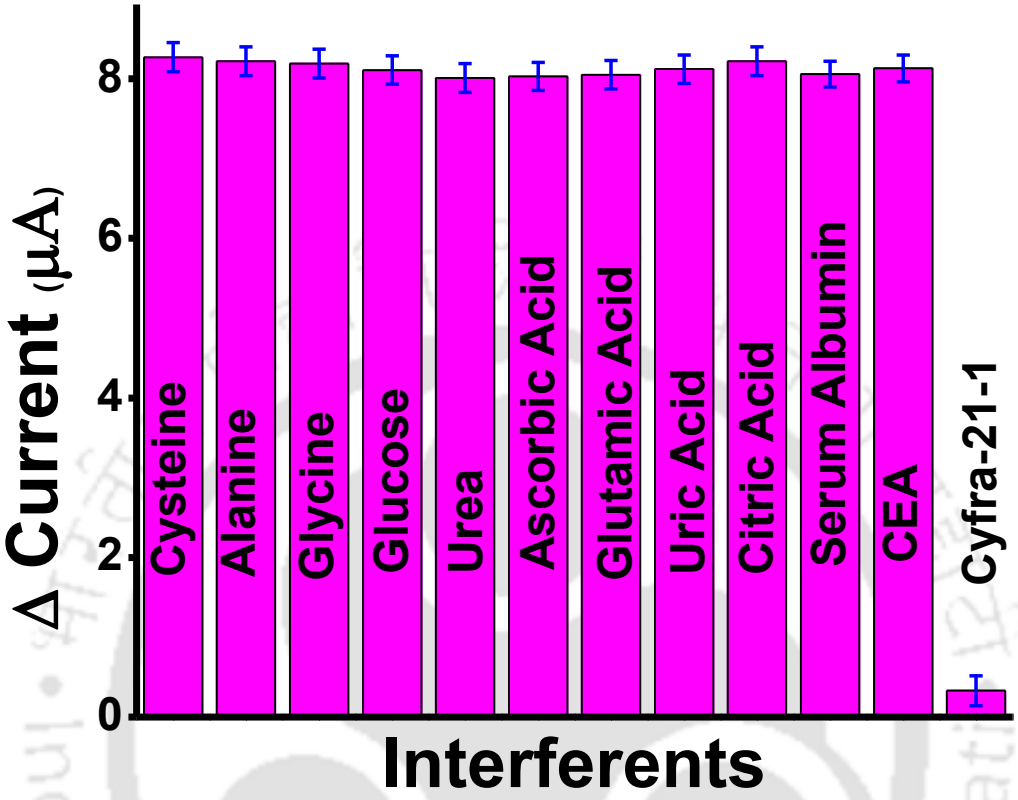

Figure 5.9: Interference study of SPE/AuNP/GdHCF/GO/Anti-CYFRA-21-1 sensor.

Figure 5.9 shows the comparatives histograms obtained from DPV responses of CYFRA-21-1 and different interfering molecules at the sensor probe.

3.5. Real sample analysis

For OC patient, a continuous CYFRA-21-1 level monitoring is very much required to assess the prognosis, therefore, we have tested SPE/AuNP/GdHCF/GO/Anti-CYFRA-21-1 sensor for real sample analysis. Initially, we have tested the performance of SPE/AuNP/GdHCF/GO/Anti-CYFRA-21-1 sensor using spike and recovery real sample analysis method. In this method, a healthy 28 year male volunteer provided saliva for sensing. The saliva was collected into a 1.95 mL PBS containing vial and

TH-2627_166106107

mixed throughly. It was then tested for CYFRA-21-1 sensing. Similar amount of CYFRA-21-1 was spiked into the electrochemical cell and calibration curve was obtained. Based on the dose dependent CYFRA-21-1 detection in saliva, a calibration plot was obtained which shows the linear regression equation as follows: ΔI (μA) = 8.871(± 0.377) – 1.146 (± 0.074) Conc [CYFRA-21-1 (ng/mL)] with the correlation coefficient of 0.912. The LOD of 0.97 (± 0.01) ng/mL was obtained in saliva based on the standard deviation of three times consecutive analyses of the blank (95% confidence level; n=3), which shows the fabricated sensor is powerful for real sample analysis and highly reproducible. The results of these experiments were analyzed and % recoveries of CYFRA-21-1 were calculated using equation 5.

$$\% \text{ recovery} = \frac{[S]\text{CYFRA} - [B]\text{CYFRA}}{[SS]\text{CYFRA}} \quad \ldots\ldots\ldots\ldots (5)$$

Where, $[S]_{CYFRA}$ and $[B]_{CYFRA}$ are the analytical responses of CYFRA-21-1 in spiked and blank saliva, respectively, and $[SS]_{CYFRA}$ is the analytical response of CYFRA-21-1in PBS solution.

Sample	Spiked	Recovered	RSD %	% Recoveries
1.	2	1.97 ± 0.12	1.12	98.50 %
2.	5	4.77 ± 0.32	3.02	95.40%
3.	10	9.73 ± 0.21	2.04	97.30 %
4.	20	17.70 ± 1.92	1.04	88.50%
5.	30	26.85 ± 2.02	1.06	89.50 %
6.	40	39.05 ± 2.11	2.21	97.62 %
7	50	45.23 ± 3.16	1.07	90.46 %
8.	60	46.80 ± 1.21	2.15	78.00 %

Table. 5.3. Percentage recovery of cyfra antigen in real sample

TH-2627_166106107

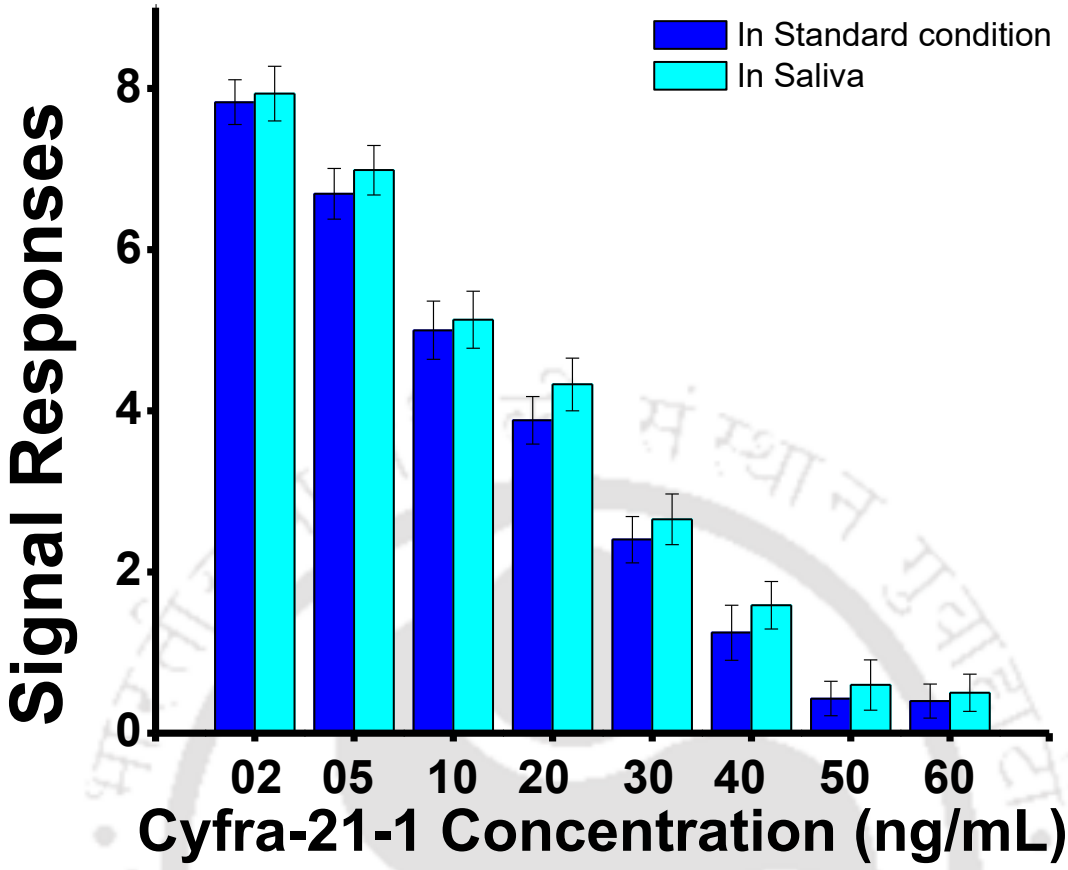

Figure 5.10: SPE/AuNP/GdHCF/GO/Anti-CYFRA-21-1 sensor real sample analysis.

Intrestringly, the SPE/AuNP/GdHCF/GO/Anti-CYFRA-21-1 sensor showed 88.50% to 98.50% recoveries in the range of 02 ng/mL to 50 ng/mL (Figure: 5.10)

3.6. Reproducibility and stability studies

For the commercial viability of a sensor, it must have to be highly reproducible and stable (Mahato et al. 2018b). In this regard, we have tested our sensor for reproducibility by checking the current responses with 5 seperate electrodes, prepared using similar protocol. The reproducibility of the sensor was evaluated, which showed the RSD < 3.32% (n = 3) and probe to probe RSD was < 4.8% even when the same fabrication process was followed. This minor variation was most likely due to the negligible variation in the sensor

TH-2627_166106107

fabrication process and handling errors. We have also tested long-term stability of our sensor while keeping the sensor system in a refrigerator at 4° C, it was observed that the sensor retained almost 93.21 ± 2 % (RSD < 3.1 %) of its original response over 10 weeks. Over the period, current decreased with time, suggesting that, the developed SPE/AuNP/GdHCF/GO/Anti-CYFRA-21-1 sensor is stable up to 10 weeks.

4. Conclusions

With the above study, we conclude that GdHCF NPs can be synthesized with a facile, fast, and stable process of microwave irradiations. GdHCF NPs were physically characterized using XRD, TEM, EDX, Raman, and FTIR spectroscopy. The SPE, SPE/GdHCF, SPE/AuNP/GdHCF, SPE/AuNP/GdHCF/GO, and SPE/AuNP/GdHCF/GO/Anti-CYFRA-21-1 sensor surface modificaions were further characterized using electrochemical techniques and tested for development of POC CYFRA-21-1 electrochemical sensor. The SPE/AuNP/GdHCF/GO/Anti-CYFRA-21-1matrix showed the sensing of CYFRA-21-1 with a wide LDR of 02-50 ng/mL and LOD of 0.63 ng/mL (±0.05) (RSD< 4%, 95 %), which is comparable to be applied for clinical implication. The immunosensor was able to recover 88.50% to 98.50% signal in the real saliva sample. To the best of our knowledge this is the first report where SPE/AuNP/GdHCF/GO nanocomposite was used to detect OC. The sensor was able to detect the CYFRA-21-1 upto 10 weeks. The sensor system fabricated has many outstanding features such as; simplicity, rapidity, label-free and low-cost detection, hence it could be a method of choice for OC detection in POC applications.

TH-2627_166106107

5. ***References***

Agrawal B, Chandra P, Goyal RN, Shim YB (2013) Detection of norfloxacin and monitoring its effect on caffeine catabolism in urine samples. Biosens Bioelectron 47:307–312.

Ajayan PM (1999) Nanotubes from carbon. Chem Rev 99:1787–1800.

Alkotyfan K, Wiegand S, Müller HH, et al (2010) Cyfra 21-1 as a tumor marker for follow-up of patients with squamous cell carcinoma of the oropharnyx. Anticancer Res 30:2291–2296.

Arya SK, Bhansali S (2011) Lung cancer and its early detection using biomarker-based biosensors. Chem Rev 111:6783–6809.

Baranwal A, Kumar A, Priyadharshini A, et al (2018) Chitosan: An undisputed bio-fabrication material for tissue engineering and bio-sensing applications. Int J Biol Macromol 110:110–123.

Brawley OW (2009) Oropharyngeal cancer, race, and the human papillomavirus. Cancer Prev Res 2:769–772.

Brocklehurst P, Kujan O, O'Malley LA, et al (2013) Screening programmes for the early detection and prevention of oral cancer. Cochrane database Syst Rev Wiley.

Céruse P, Rabilloud M, Charrié A, et al (2005) Study of Cyfra 21--1, a tumor marker, in head and neck squamous cell carcinoma. Ann Otol Rhinol Laryngol 114:768–776.

Chandra P (2015) Electrochemical Nanobiosensors for Cancer Diagnosis. J Anal Bioanal Tech 6.

Chandra P, (2016) Nanobiosensors for personalized and onsite biomedical diagnosis. The Institution of Engineering and Technology, Stevenage, London.

TH-2627_166106107

Chandra P, Zaidi SA, Noh HB, Shim YB (2011) Separation and simultaneous detection of anticancer drugs in a microfluidic device with an amperometric biosensor. Biosens Bioelectron 28:326–332.

Choudhary M, Yadav P, Singh A, et al (2016) CD 59 Targeted Ultrasensitive Electrochemical Immunosensor for Fast and Noninvasive Diagnosis of Oral Cancer. Electroanalysis 28:2565–2574.

Gonzalez MV, Artimez ML, Rodrigo L, et al (1997) Mutation analysis of the p53, APC, and p16 genes in the Barrett's oesophagus, dysplasia, and adenocarcinoma. J Clin Pathol 50:212–217.

Ignat M carbon nanotubes. A.Farcas,A.Vasile,E. Propovici, (2008) Calixarene-modified multi-wall carbon nanotubes Stud Surf Sci Catal 174:389–392.

Jasuja K, Berry V (2009) Implantation and Growth of Dendritic Gold Nanostructures on Graphene and Raman Enhancement. ACS Nano 3:2358–2366.

Kawaguchi H, Ohno S, Miyazaki M, et al (2000) CYFRA 21-1 determination in patients with esophageal squamous cell carcinoma: Clinical utility for detection of recurrences. Cancer 89:1413–1417.

Kumar A, Purohit B, Mahato K, et al (2019a) Design and Development of Ultrafast Sinapic Acid Sensor Based on Electrochemically Nanotuned Gold Nanoparticles and Solvothermally Reduced Graphene Oxide. Electroanalysis 32:59 – 69

Kumar A, Purohit B, Mahato K, Chandra P (2019b) CHAPTER 11. Advance Engineered Nanomaterials in Point-of-care Immunosensing for Biomedical Diagnostics. Immunosensors RSC 238–266.

Kumar A, Purohit B, Maurya PK, et al (2019c) Engineered Nanomaterial Assisted Signal-

TH-2627_166106107

amplification Strategies for Enhancing Analytical Performance of Electrochemical Biosensors. Electroanalysis 31:1615–1629.

Kumar A, Sharma S, Pandey LM (2018a) Nanoengineered material based biosensing electrodes for enzymatic biofuel cells applications. Mater Sci Energy Technol 1:38–48.

Kumar S, Ashish, Kumar S, et al (2018b) Effect of Brownian motion on reduced agglomeration of nanostructured metal oxide towards development of efficient cancer biosensor. Biosens Bioelectron 102:247–255.

Kumar S, Ashish, Kumar S, et al (2018c) Effect of Brownian motion on reduced agglomeration of nanostructured metal oxide towards development of efficient cancer biosensor. Biosens Bioelectron 102:247–255.

Kumar S, Kumar S, Tiwari S, et al (2016a) Highly sensitive protein functionalized nanostructured hafnium oxide based biosensing platform for non-invasive oral cancer detection. Sensors Actuators B Chem 235:1–10.

Kumar S, Kumar S, Tiwari S, et al (2015) Biofunctionalized Nanostructured Zirconia for Biomedical Application: A Smart Approach for Oral Cancer Detection. Adv Sci 2:1500048.

Kumar S, Sharma JG, Maji S, Malhotra BD (2016b) Nanostructured zirconia decorated reduced graphene oxide based efficient biosensing platform for non-invasive oral cancer detection. Biosens Bioelectron 78:497–504.

Kumar S, Sharma JG, Maji S, Malhotra BD (2016c) A biocompatible serine functionalized nanostructured zirconia based biosensing platform for non-invasive oral cancer detection. RSC Adv 6:77037–77046.

Mahato K, Kumar A, Maurya PK, Chandra P (2018a) Shifting paradigm of cancer diagnoses

TH-2627_166106107

in clinically relevant samples based on miniaturized electrochemical nanobiosensors and microfluidic devices. Biosens Bioelectron 100:411–428.

Mahato K, Maurya PK, Chandra P (2018b) Fundamentals and commercial aspects of nanobiosensors in point-of-care clinical diagnostics. 3 Biotech 8:149.

Malhotra R, Patel V, Vaqué JP, et al (2010) Ultrasensitive electrochemical immunosensor for oral cancer biomarker IL-6 using carbon nanotube forest electrodes and multilabel amplification. Anal Chem 82:3118–3123.

Malhotra R, Urs AB, Chakravarti A, et al (2016) Correlation of Cyfra 21-1 levels in saliva and serum with CK19 mRNA expression in oral squamous cell carcinoma. Tumor Biol 37:9263–9271.

Mandal R, Baranwal A, Srivastava A, Chandra P (2018) Evolving trends in bio/chemical sensor fabrication incorporating bimetallic nanoparticles. Biosens Bioelectron 117:546–561.

Mehrotra R, Gupta DK (2011) Exciting new advances in oral cancer diagnosis: avenues to early detection. Head Neck Oncol 3:33.

Noh HB, Lee KS, Chandra P, et al (2012) Application of a Cu-Co alloy dendrite on glucose and hydrogen peroxide sensors. Electrochim Acta 61:36–43.

Nugent AG, Moore CE (2010) Adolescent awareness of risk factors associated with head and neck cancer vs lung cancer. Laryngoscope 120:S170.

Oliver-Tolentino MA, Vázquez-Samperio J, Arellano-Ahumada SN, et al (2018) Enhancement of Stability by Positive Disruptive Effect on Mn-Fe Charge Transfer in Vacancy-Free Mn-Co Hexacyanoferrate Through a Charge/Discharge Process in Aqueous Na-Ion Batteries. J Phys Chem C 122:20602–20610.

TH-2627_166106107

Patton LL, Epstein JB, Kerr AR (2008) Adjunctive Techniques for Oral Cancer Examination and Lesion Diagnosis: A Systematic Review of the Literature. J Am Dent Assoc 139:896–905.

Pickering V, Jordan RCK, Schmidt BL (2007) Elevated salivary endothelin levels in oral cancer patients—a pilot study. Oral Oncol 43:37–41.

Prasad A, Mahato K, Chandra P, et al (2016) Bioinspired Composite Materials: Applications in Diagnostics and Therapeutics. J Mol Eng Mater 04:1640004.

Punyani SR, Sathawane RS (2013) Salivary level of interleukin-8 in oral precancer and oral squamous cell carcinoma. Clin Oral Investig 17:517–524.

Rajkumar K, Ramya R, Nandhini G, et al (2015) Salivary and serum level of CYFRA 21-1 in oral precancer and oral squamous cell carcinoma. Oral Dis 21:90–96.

Scully C, Bagan J V, Hopper C, et al (2008) Oral cancer: current and future diagnostic techniques. Am J Dent 21:199–209.

Shao Y, Wang J, Wu H, et al (2010) Graphene based electrochemical sensors and biosensors: a review. Electroanalysis 22:1027–1036.

Siegel R, Naishadham D, Jemal A (2012) Cancer statistics for hispanics/latinos, 2012. CA Cancer J Clin 62:283–298.

Tiwari S, Gupta PK, Bagbi Y, et al (2017) L-cysteine capped lanthanum hydroxide nanostructures for non-invasive detection of oral cancer biomarker. Biosens Bioelectron 89:1042–1052.

Verma S, Singh A, Shukla A, et al (2017) Anti-IL8/AuNPs-rGO/ITO as an Immunosensing Platform for Noninvasive Electrochemical Detection of Oral Cancer. ACS Appl Mater Interfaces 9:27462–27474.

TH-2627_166106107

Wang J (2005) Carbon nanotube based electrochemical biosensors: A review. Electroanalysis 17:7–14.

Yadav SK, Agrawal B, Chandra P, Goyal RN (2014) In vitro chloramphenicol detection in a Haemophilus influenza model using an aptamer-polymer based electrochemical biosensor. Biosens Bioelectron 55:337–342.

Zhang Z, Chen H, Xing C, et al (2011) Sodium citrate: A universal reducing agent for reduction / decoration of graphene oxide with au nanoparticles. Nano Res 4:599–611.

Zhong L ping, Zhang C ping, Zheng J wei, et al (2007) Increased Cyfra 21-1 concentration in saliva from primary oral squamous cell carcinoma patients. Arch Oral Biol 52:1079–1087.

TH-2627_166106107

Chapter – VI

Summary and future works

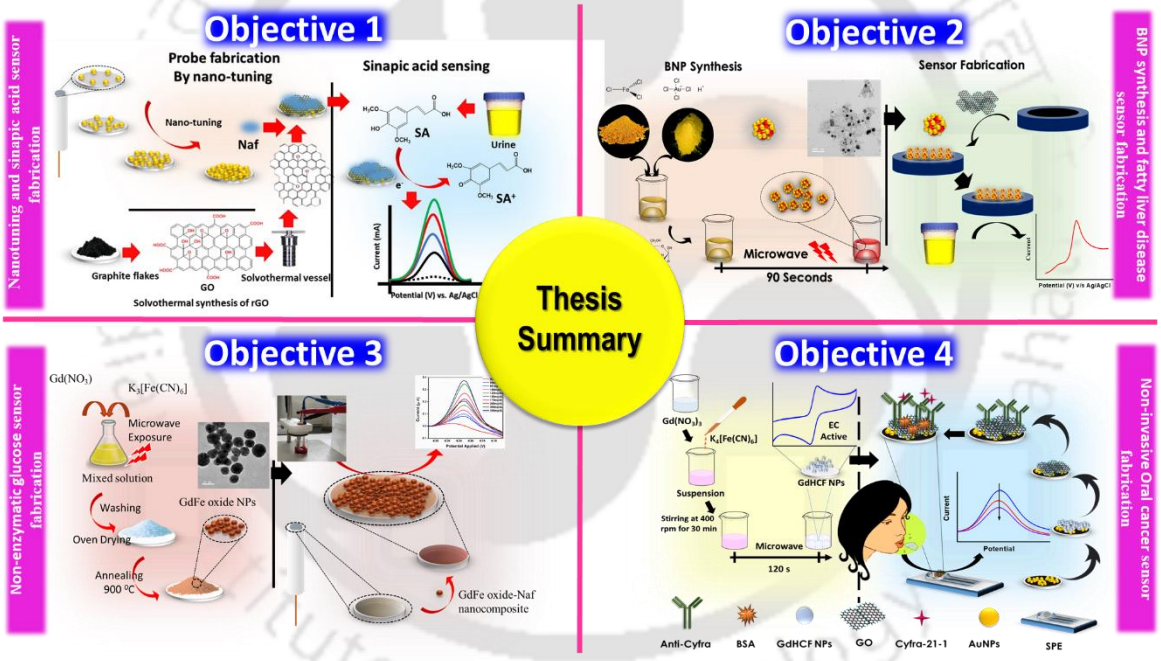

TH-2627_166106107

1. Thesis Summary

In the present thesis, sensor fabrication strategies incorporating advance engineered NMs and nano composites has been investigated to obtain the better biosensing with amplified signal generation.

In the chapter I, fundamentals about biosensing has been discussed. A brief description of biosensor type based on bioreceptor and transducer has been elucidated. Current challenges to electrochemical sensor and their possible solutions are also described. Signal amplification strategies using various NMs and sensor surface functionalization steps are briefly discussed. Based on the introduction and literature review four research objectives were formulated that are discussed below.

In the first objective (Chapter II), we have developed an ultrafast first electrochemical sensor for sinapic acid based on nanocomposite comprising electrochemically tuned gold nanoparticles (EAuNPs) and solvothermally reduced graphene oxide (rGO). The synthesized EAuNPs, rGO, and EAuNPs-rGO nanocomposite were characterized using X-ray diffraction (XRD), transmission electron microscopy (TEM), selected area electron diffraction (SAED), particle size analysis, and Raman spectroscopy. A proof-of-concept electrochemical sensor for sinapic acid was developed based on synthesized EAuNPs-rGO nanocomposite, which was characterized by electrochemical techniques such as cyclic voltammetry (CV) and electrochemical impedance spectroscopy (EIS). The developed sensor detected SA with a linear dynamic range (LDR) between 20 µM and 200 µM and detection limit (DL) of 33.43 (±0.21) nM (RSD<3.32%). To show the useful purpose of the sensor probe in clinical applications, sinapic acid was detected in human urine samples, which showed the percentage recovery between 82.8% and 93.34%. Interferences due to various molecules such as L-cystine, glycine, alanine, serum albumin, uric acid, citric acid,

TH-2627_166106107

ascorbic acid, and urea were tested. Long-term stability of sensor probe was examined, which was found to be stable up to 6 weeks.

In the second objective (Chapter III), we developed for the first time a microwave assisted, one pot, direct, and facile synthesis of monodispersed iron and gold bimetallic nanoparticles (BNP_{Au-Fe}) using glucose as a reducing agent in merely 90 s. The as such synthesized BNP_{Au-Fe} were thoroughly characterized using UV-Vis, XRD, TEM, EDX, elemental mapping, and raman spectroscopy. These BNP_{Au-Fe} were further impregnated to reduced graphene oxide (rGO) and coated onto glassy carbon electrode (GCE) to develop a sensor probe for label free electrochemical detection of acetaminophen. The sensor probe was systematically characterized by cyclic voltammetry (CV) and electrochemical impedance spectroscopy (EIS). The BNP_{Au-Fe}-rGO nanocomposite matrix showed the sensing of acetaminophen with a wide dynamic range between 50 and 800 nM with detection limit (DL) of 0.14 nM (±0.05) nM (RSD< 4.12%) that was lower compared to previously reported acetaminophen sensors. To show the practical application of the sensor probe, acetaminophen was detected in human urine samples, which showed the percentage recovery between 86.65% and 91.32%. To the best of our knowledge, this is the first report where BNP_{Au-Fe} impregnated rGO was used to detect acetaminophen. Interferences due to various molecules such as glucose, serum albumin, glycine, glutamic acid, alanine, citric acid, and ascorbic acid were tested individually and in mixed sample. Long-term stability of sensor probe was examined, which was found to be stable up to 10 weeks.

In the third objective (Chapter IV), we studied for a non-enzymatic glucose sensor based gadolinium iron oxide ($GdFeO_3$) NPs, which were synthesized using household microwave oven. $GdFeO_3$ NPs were physically characterized using UV-Vis, XRD, TEM, EDX, STEM and FTIR spectroscopy. The $GdFeO_3$ NPs were doped with nafion to form a

TH-2627_166106107

nanocomposite ($GdFeO_3$-Naf), which was characterized by electrochemical techniques and tested for proof-of-concept non-enzymatic glucose electrochemical sensor. Unlike to other non-enzymatic glucose sensor the $GdFeO_3$-Naf nanocomposite did not require any mediator for sensing and need very low potential to detect glucose. It showed the sensing of glucose with a wide LDR of 66-350 mg/dL and LOD of 9.59 (±0.05) mg/dL (RSD< 4%) that is clinically comparable for glucose sensors. Moreover, the sensor was capable to detect the glucose in real blood samples and results were comparable to classical hexokinase method of glucose determination. To the best of our knowledge, this is the first report where $GdFeO_3$-Naf was used to detect glucose non-enzymatically. Selectivity was determined with possible interfering agents and the sensor was able to sense the glucose up to 12 weeks.

In the fourth objective (Chapter V), we have tried to synthesize Gadolinium hexacyanoferrate (GdHCF) NPs with a facile, fast, and stable process of microwave irradiation. GdHCF NPs were physically characterized using XRD, TEM, EDX, Raman, and FTIR spectroscopy. A non -invasive, self-signal generating, mediator less, oral cancer sensor has been developed using GdHCF NPs onto SPE. The SPE, SPE/GdHCF, SPE/AuNP/GdHCF, SPE/AuNP/GdHCF/GO, and SPE/AuNP/GdHCF/GO/Anti-CYFRA-21-1 sensor surface modifications were characterized using electrochemical techniques and tested for development of proof-of-concept CYFRA-21-1 electrochemical sensor. The SPE/AuNP/GdHCF/GO/Anti-CYFRA-21-1 sensor matrix showed the sensing of CYFRA-21-1 with a wide LDR of 02-50 ng/mL and LOD of 0.63 ng/mL (±0.05) (RSD< 4%, 95 %), which is comparable to be applied for clinical implication. To the best of our knowledge this is the first report where SPE/AuNP/GdHCF/GO nanocomposite was used to detect oral cancer. The sensor was able to detect the CYFRA-21-1 up to 10 weeks.

TH-2627_166106107

Conclusively, this research work has provided new findings towards signal enhancement of electrochemical biosensors with the help of novel metal and metal oxide NPs and their nanocomposite.

2. Future Work

The current research work can be extended to:

- The future directions of these findings can lead to development of a portable hand-held diagnostic device using applied metal and metal oxide nanocomposites.
- There is a possibility of deciphering the mathematical model of electrocatalysis occurring after nanocomposite application while sensor fabrication.
- A new bimetallic novel nanocomposite can be attained that can further enhance the developed sensor.
- The metal and metal oxide nanocomposites that are used for sensor development can be studied for their biocompatibility.
- A wearable sensor can be developed using discussed metal and metal oxide nanocomposite that can be used for real-time measuring diagnostic device.
- A smart circuit-based sensor can be developed that can be integrated with smartphones.
- The developed sensors can be tried for pilot project testing to examine their commercial viabilities.

TH-2627_166106107

Annexures

TH-2627_166106107

Other Research Publications

TH-2627_166106107

Biosensors and Bioelectronics 148 (2020) 111815

Contents lists available at ScienceDirect

Biosensors and Bioelectronics

journal homepage: http://www.elsevier.com/locate/bios

Clinically comparable impedimetric immunosensor for serum alkaline phosphatase detection based on electrochemically engineered Au-nano-Dendroids and graphene oxide nanocomposite

Kuldeep Mahato, Buddhadev Purohit, Ashutosh Kumar, Pranjal Chandra *

Laboratory of Bio-Physio Sensors and Nano-bioengineering, Department of Biosciences and Bioengineering, Indian Institute of Technology Guwahati, Guwahati, 781039, India

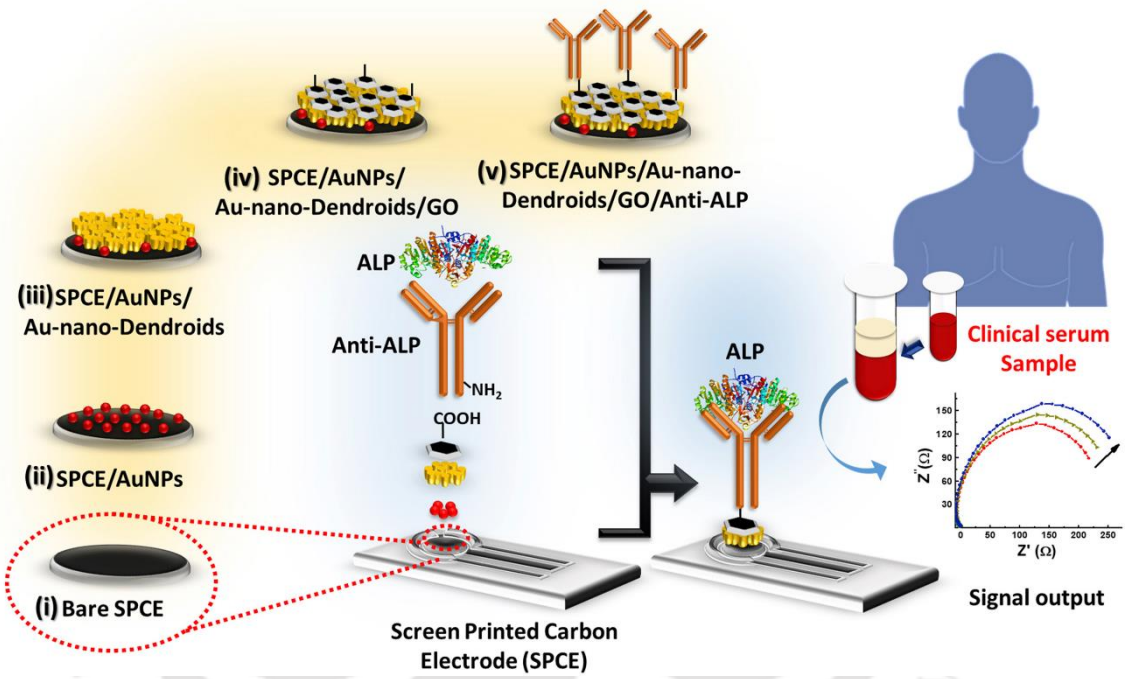

Abstract: In this work, we demonstrate label-free electrochemical impedance spectroscopy (EIS) based alkaline phosphatase (ALP) detection using gold nanoparticles (AuNPs), electrochemically engineered Au-nano-Dendroids, and graphene oxide (GO) nanocomposite. These nanomaterials were sequentially deposited on to the screen-printed carbon electrode (SPCE) and antibodies against ALP (anti-ALP) were immobilized using carbodiimide bioconjugation process. The sensor probe has been characterized extensively using TEM, EDX, SAED, XRD, FE-SEM, FTIR, DIC, and electrochemical techniques. The analytical performance of fabricated biosensor has been evaluated using EIS, where linear dynamic range and limit of detection were obtained to be 100–1000 U/L and 9.10 (±0.12) U/L, respectively. The developed biosensor showed high selectivity towards ALP with negligible interference (k_{sel} « 1; n = 3) due to coexisting molecules. The sensor probe has successfully recovered ALP between 108.84% and 172.50% (n = 3) in human serum samples. The sensor has been used to estimate ALP in clinical serum samples, where the level was found to be 83.15 U/L and was comparable with standard technique used in the hospitals. The shelf life, stability, and reproducibility have also been evaluated.

Mahato, K., Purohit, B., **Kumar, A.**, & Chandra, P. (2019). Clinically comparable impedimetric immunosensor for serum alkaline phosphatase detection based on electrochemically engineered Au-nano-dendroids and graphene oxide nanocomposite. *Biosensors and Bioelectronics*, 111815.

TH-2627_166106107

www.nature.com/scientificreports

SCIENTIFIC REPORTS

OPEN

Design of commercially comparable nanotherapeutic agent against human disease-causing parasite, *Leishmania*

Received: 17 October 2017
Accepted: 15 May 2018
Published online: 11 June 2018

Anupriya Baranwal, Adarsh Kumar Chiranjivi, Ashutosh Kumar, Vikash Kumar Dubey & Pranjal Chandra

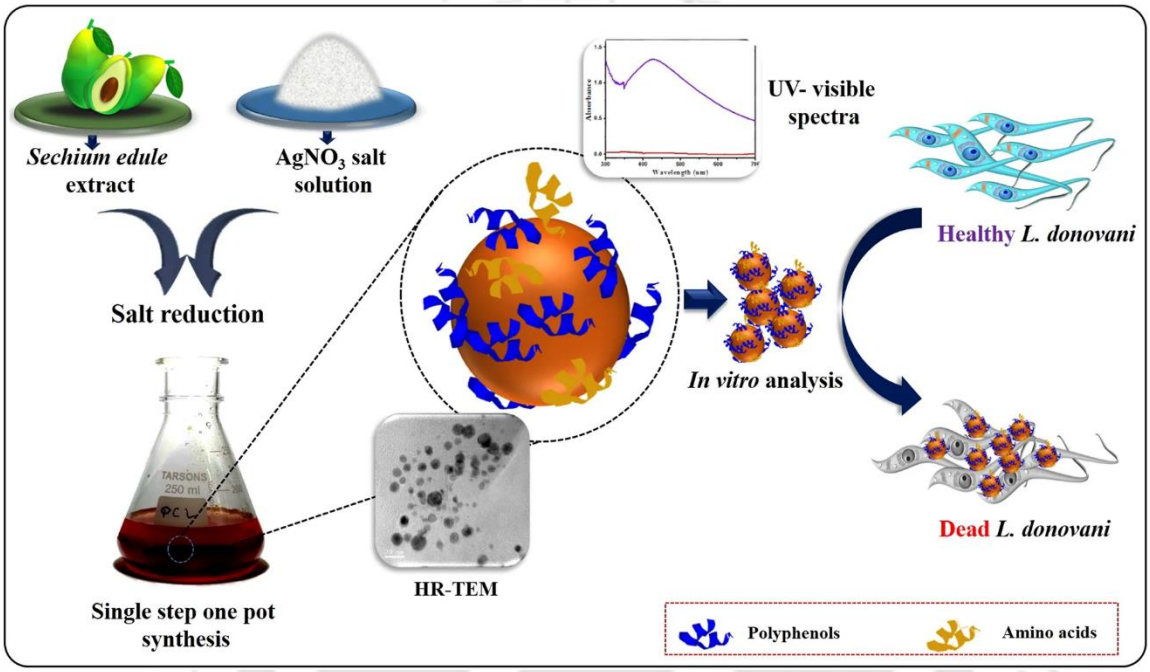

Abstract: Nanotherapeutic agents (NTA) play a crucial role in clinical medicine, if their unique properties are well understood and well exploited. In this direction, we report synthesis and characterization of highly potent phytofabricated silver nanoparticles (AgNPs) using *Sechium edule*, which served the purpose of both reducing and capping agent. The designed AgNPs were characterized using UV-Vis spectroscopy, XRD, FTIR, HR-TEM, and TGA techniques. The formation of AgNPs was also confirmed using electrochemistry, which to the best of our knowledge has never been reported before for biosynthesized nanoparticles. The antileishmanial potential of AgNPs was examined on the clinical isolates of *Leishmania donovani* promastigote cells in an *in vitro* experimental setting. A dose dependent killing activity of the AgNP was observed with an IC_{50} value of 51.88 ± 3.51 µg/ml. These results were also compared using commercially available drug, miltefosine. Furthermore, the clinical applicability of AgNP, as antileishmanial agent was proven by testing them against normal mammalian monocyte cell line (U937). The results were statistically analyzed and no significant toxicity of AgNPs on the normal mammalian cells was observed.

Baranwal, A., Chiranjivi, A. K., **Kumar, A.,** Dubey, V. K., & Chandra, P. (2018). Design of commercially comparable nanotherapeutic agent against human disease-causing parasite, Leishmania. *Scientific reports*, *8*(1), 8814.

TH-2627_166106107

Microchimica Acta (2019) 186: 658
https://doi.org/10.1007/s00604-019-3773-2

ORIGINAL PAPER

Sputtering enhanced peroxidase like activity of a dendritic nanochip for amperometric determination of hydrogen peroxide in blood samples

Buddhadev Purohit[1] · Kuldeep Mahato[1] · Ashutosh Kumar[1] · Pranjal Chandra[1]

Received: 23 April 2019 / Accepted: 16 August 2019 / Published online: 29 August 2019
© Springer-Verlag GmbH Austria, part of Springer Nature 2019

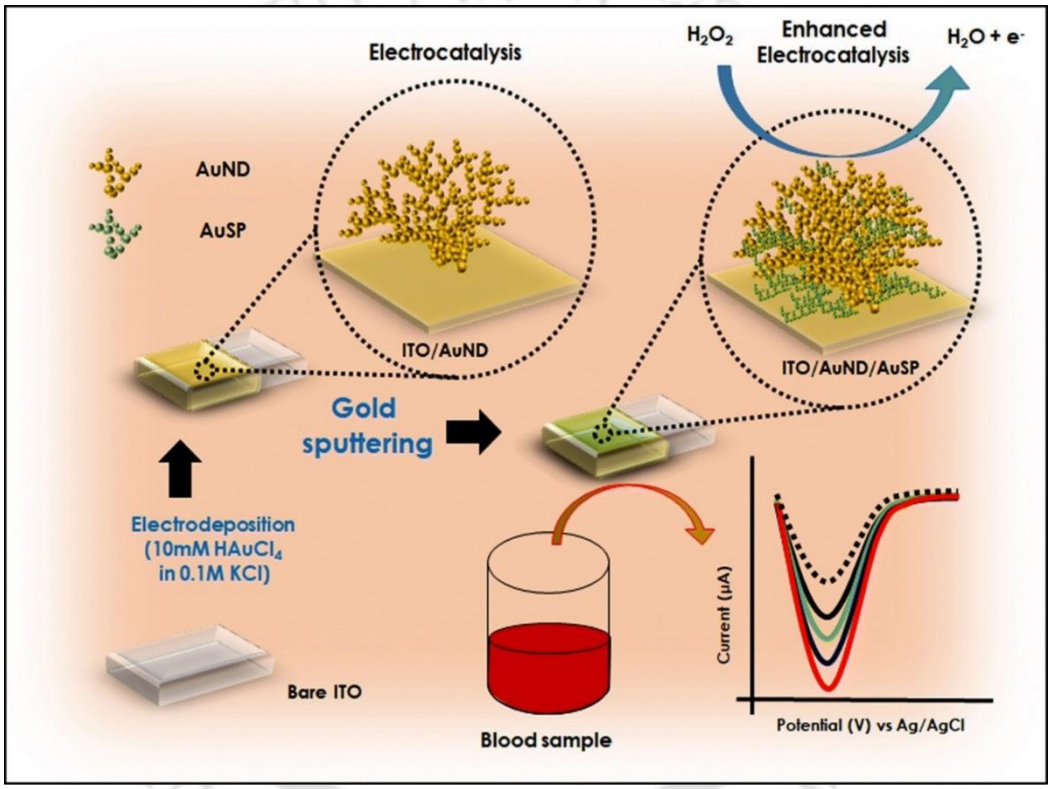

Abstract: A nonenzymatic electrochemical nanoprobe is described for the fast determination of hydrogen peroxide (H_2O_2). A sputtered indium tin oxide electrode with a nano-hierarchical 3D gold structure is used. The nanoprobe was characterized by SEM, EDX, TEM, SAED, and electrochemical techniques. Figures of merit include (a) a fast response time (≤ 1.0 s), (b) two linear dynamic ranges that extend from 10^{-12} M to 10^{-10} M and from 10^{-10} M to10^{-5} M; and (c) a low limit of detection of 9.8×10^{-13} M. The nanoprobe works in the clinical range and was applied for trace analysis of H_2O_2 in spiked blood samples, and recoveries ranged between 90 and 96%. It has negligible response ($p < 0.001$, for $n = 3$) toward glucose, citric acid, ascorbic acid, uric acid, glycine, and alanine. The shelf-lifetime is found to be 12 weeks.

Purohit, B., Mahato, K., **Kumar, A.**, & Chandra, P. (2019). Sputtering enhanced peroxidase like activity of a dendritic nanochip for amperometric determination of hydrogen peroxide in blood samples. *Microchimica Acta*, *186*(9), 658.

TH-2627_166106107

Full Paper Wiley Online Library ELECTROANALYSIS

DOI: 10.1002/elan.201900551

Novel Sensing Assembly Comprising Engineered Gold Dendrites and MWCNT-AuNPs Nanohybrid for Acetaminophen Detection in Human Urine

Buddhadev Purohit,[a] Ashutosh Kumar,[a] Kuldeep Mahato,[a] and Pranjal Chandra*[a]

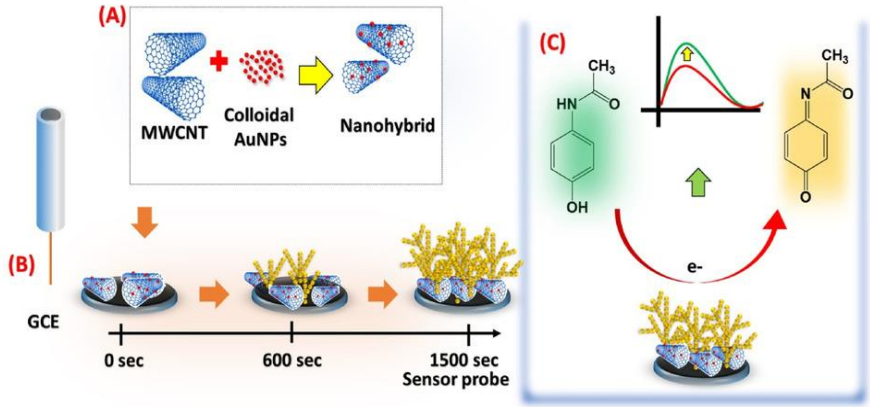

Abstract: A layered nanohybrid comprising of multi walled carbon nanotubes (MWCNT)-gold nanoparticles (AuNPs) has been designed as a matrix for the development of Au dendritic nanostructures (AuDN) with enhanced catalytic activity. The developed sensor matrix was thoroughly characterized by scanning electron microscope (SEM), transmission electron microscope (TEM), and energy dispersive X-ray spectroscopy (EDX). The developed sensor probe MWCNT-AuNPs/AuDN over glassy carbon electrode (GCE) was used for the label free detection of acetaminophen (AP), a commonly used drug associated with hepatotoxicity when overdosed, as a model molecule. The final sensor probe was characterized by cyclic voltammetry (CV), electrochemical impedance spectroscopy (EIS), linear sweep voltammetry (LSV), and differential pulse voltammetry (DPV). The sensor shows excellent analytical performances with a linear dynamic range (LDR) of 100 to 7500 nM, and a low limit of detection (LOD) of 2.12 (±0.03) nM, which is better than recently reported AP sensors. The practical application / clinical possibilities of the final sensor were evaluated by real sample analysis in human urine by spike and recovery method, where the AP recoveries were found in between 92 % to 96 %. The sensor probe shows negligible response towards co-existing interfering molecules like glucose, urea, uric acid and various amino acids, which are commonly found in real samples ($p<0.001$, $n=3$). The shelf life of the sensor probe was evaluated and found to be stable for 8 weeks. The fabricated sensor probe using MWCNT-AuNPs/AuDN is easy to fabricate, simple, robust, and able to detect AP in urine with high recoveries shows its possibilities to be used in clinical settings.

Purohit, B., **Kumar, A.**, Mahato, K., & Chandra, P. Novel sensing assembly comprising engineered gold dendrites and MWCNT-AuNPs nanohybrid for acetaminophen detection in human urine. *Electroanalysis*.

TH-2627_166106107

List of Publications

1. **Ashutosh Kumar,** Swati Sharma, Lalit Mohan Pandey, and Pranjal Chandra: *Nanoengineered material based biosensing electrodes for enzymatic biofuel cells applications*. Material Science for Energy Technology, 2018; 1(1):38-48.

    - Awarded for the best article of the year

2. **Ashutosh Kumar,** Buddhadev Purohit, Pawan Kumar Maurya, Lalit Mohan Pandey, and Pranjal Chandra: *Engineered Nanomaterial Assisted Signal-amplification Strategies for Enhancing Analytical Performance of Electrochemical Biosensors*. Electroanalysis 2019; 31(9) 1615-1629.

3. **Ashutosh Kumar,** Buddhadev Purohit, Kuldeep Mahato, Riddhipratim Mandal, Ananya Srivastava, and Pranjal Chandra: *Gold-Iron Bimetallic Nanoparticles Impregnated Reduced Graphene Oxide Based Nanosensor for Label-Free Detection of Biomarker Related to Non-Alcoholic Fatty Liver Disease*. Electroanalysis 2019; 31(12) 2417-2428.

4. **Ashutosh Kumar,** Buddhadev Purohit, Kuldeep Mahato, Sharmili Roy, Ananya Srivastava, and Pranjal Chandra: *Design and Development of Ultrafast Sinapic Acid Sensor Based on Electrochemically Nanotuned Gold Nanoparticles and Solvothermally Reduced Graphene Oxide*. Electroanalysis 2020; 32(1) 59-69.

5. **Ashutosh Kumar,** Buddhadev Purohit, Kuldeep Mahato, and Pranjal Chandra: *A self-reporting and label-free non-invasive electrochemical biosensor for oral cancer detection.* Advanced Science (Manuscript submitted)

6. **Ashutosh Kumar,** Buddhadev Purohit, Kuldeep Mahato, and Pranjal Chandra: *Self signal generating bimetallic nano system for enzyme-less detection of glucose in blood.* Biosensors and Bioelectronics (Manuscript submitted)

7. **Ashutosh Kumar,** Buddhadev Purohit, Kuldeep Mahato, and Pranjal Chandra: *Gold nano star impregnated graphitic carbon nitride for serotonin detection in biological fluids.* Sensors and Actuators B (Manuscript submitted)

TH-2627_166106107

8. **Ashutosh Kumar,** Buddhadev Purohit, Kuldeep Mahato, and Pranjal Chandra: *A non-invasive uric acid sensor based on gold nano star impregnated reduced graphene oxide*. Microchimica Acta (Manuscript submitted)

9. **Ashutosh Kumar,** Silveri Maheshwari, Kuldeep Mahato, Buddhadev Purohit, VGM Naidu, Ananya Srivastava, and Pranjal Chandra: *In-vitro haemolysis and anti-cancer activity of one pot microwave assisted synthesized zirconium oxide nanoparticles.* Applied Nanoscience (Manuscript submitted)

10. Kuldeep Mahato, **Ashutosh Kumar,** Pawan Kumar Maurya, and Pranjal Chandra: *Shifting paradigm of cancer diagnoses in clinically relevant samples based on miniaturized electrochemical nanobiosensors and microfluidic devices*. Biosensors & Bioelectronics 2018; 100 411-428.

11. Buddhadev Purohit, **Ashutosh Kumar,** Kuldeep Mahato; and Pranjal Chandra. A novel label-free electrochemical immunosensor based on Au nanodendrite–graphene–chitosan nanocomposite for ultrasensitive detection of cancer biomarker in serum samples. Biosensors and Bioelectronics (Manuscript Submitted).

12. Buddhadev Purohit, **Ashutosh Kumar,** Kuldeep Mahato; and Pranjal Chandra Electrochemically nanoengineered three-dimensional Au-Cu bimetallic dendrite for acetaminophen detection in urine samples. *Microchimica Acta (Manuscript submitted)*

13. Buddhadev Purohit, **Ashutosh Kumar,** Kuldeep Mahato; and Pranjal Chandra. Au dendritegraphene nano-conjugate based novel electrochemical immunosensor for CYFRA-21-1 detection in human saliva samples. Biosensors and Bioelectronics (Manuscript under preparation).

14. Anupriya Baranwal, **Ashutosh Kumar,** A. Priyadharshini, Gopi Suresh Oggu, Ira Bhatnagar, Ananya Srivastava, and Pranjal Chandra: *Chitosan: An undisputed bio-fabrication material for tissue engineering and bio-sensing applications*. International Journal of Biological Macromolecules 2018; 110 110-123.

15. Buddhadev Purohit, **Ashutosh Kumar,** Kuldeep Mahato, and Pranjal Chandra: *Smartphone assisted personalized diagnostics devices and wearable sensors*. Current Opinion in Biomedical Engineering 2020; 13 42-50.

TH-2627_166106107

16. Buddhadev Purohit, **Ashutosh Kumar,** Kuldeep Mahato, and Pranjal Chandra: *Electrodeposition of metallic nanostructures for biosensing applications in health care*. Journal of Scientific Research 2020; 64 (1) 68-73.

17. Buddhadev Purohit, **Ashutosh Kumar,** Kuldeep Mahato, and Pranjal Chandra: *Novel sensing assembly comprising engineered gold dendrites and MWCNT-AuNPs nanohybrid for acetaminophen detection in human urine*. Electroanalysis 2020; 32 (03) 561-570.

18. Kuldeep Mahato, Buddhadev Purohit, **Ashutosh Kumar,** and Pranjal Chandra: *Clinically comparable impedimetric immunosensor for serum alkaline phosphatase detection based on electrochemically engineered Au-nano-Dendroids and graphene oxide nanocomposite*. Biosensors & Bioelectronics 2020; 148 111815.

19. Anupriya Baranwal, Adarsh Kumar Chiranjivi, **Ashutosh Kumar,** Vikash Kumar Dubey, and Pranjal Chandra: *Design of commercially comparable nanotherapeutic agent against human disease-causing parasite, Leishmania*. Scientific Reports 2018; 8 8814.

20. Buddhadev Purohit, Kuldeep Mahato, **Ashutosh Kumar,** and Pranjal Chandra: *Sputtering enhanced peroxidase like activity of a dendritic nanochip for amperometric determination of hydrogen peroxide in blood samples*. Microchimica Acta 08/2019; 186(9) 658.

21. Buddhadev Purohit, Kuldeep Mahato, **Ashutosh Kumar,** and Pranjal Chandra: *Repurposing of Waste: Developing sensors from laboratory waste materials.* Asia Pacific Biotech News; 23(12) 1-2.

22. Ridhima Wadhwa, Taru Aggarwal, Noopur Thapliyal, **Ashutosh Kumar,** Priya, Pooja Yadav, Vandana Kumari, Boda Sai Charan Reddy, Pranjal Chandra, and Pawan Kumar Maurya: *Red blood cells as an efficient in vitro model for evaluating the efficacy of metallic nanoparticles*. 2019; 9(7) 279.

TH-2627_166106107

Book Chapters

23. **Ashutosh Kumar,** Budhhadev Purohit, Kuldeep Mahato, and Pranjal Chandra: *CHAPTER 11. Advance Engineered Nanomaterials in Point-of-care Immunosensing for Biomedical Diagnostics*. Immunosensors, 08/2019: pages 238-266; ISBN: 978-1-78801-437-3.

24. **Ashutosh Kumar,** Sharmili Roy, Ananya Srivastava, Mastan Mukram Naikwade, Buddhadev Purohit, Kuldeep Mahato, V.G.M. Naidu, and Pranjal Chandra: *Nanotherapeutics: A Novel and Powerful Approach in Modern Healthcare System*. Nanotechnology in Modern Animal Biotechnology: Concepts and Applications, 07/2019: pages 148-158; Elsevier. ISBN: 9780128188231.

25. **Ashutosh Kumar,** Budhhadev Purohit, Kuldeep Mahato, Supratim Mahapatra, Ananya Srivastava, and Pranjal Chandra: *Bio-Nano-Interface Engineering Strategies of AuNPs Passivation for Next-Generation Biomedical Applications in Biointerface Engineering: Prospects in Medical Diagnostics and Drug Delivery*, 2020: pages 215-231; ISBN: 978-981-15-4789-4.

26. Kuldeep Mahato, **Ashutosh Kumar,** Buddhadev Purohit, Supratim Mahapatra, Ananya Srivastava, and Pranjal Chandra: *Nanomaterial Functionalization Strategies in Bio-Interface Development for Modern Diagnostic Devices in Biointerface Engineering: Prospects in Medical Diagnostics and Drug Delivery*, 2020: pages 195-214; ISBN: 978-981-15-4789-4.

27. Kuldeep Mahato, Buddhadev Purohit, **Ashutosh Kumar,** and Pranjal Chandra: *Paper based biosensors for clinical and biomedical applications: Emerging engineering concepts and challenges in Paper Based Sensors Comprehensive Analytical Chemistry*; ISBN: 978-044-464-346-9.

28. Kuldeep Mahato, Buddhadev Purohit, **Ashutosh Kumar,** Ananya Srivastava, and Pranjal Chandra: *Next-Generation Immunosensing Technologies Based on Nano-Bio-Engineered Paper Matrices in Immunodiagnostic Technologies from Laboratory to Point-Of-Care Testing*, 2020: pages 93-110; ISBN: 978-981-15-5823-8.

29. Buddhadev Purohit, **Ashutosh Kumar,** Kuldeep Mahato, Sharmili Roy, and Pranjal Chandra: *Cancer Cytosensing Approaches in Miniaturized Settings Based*

TH-2627_166106107

on Advanced Nanomaterials and Biosensors. Nanotechnology in Modern Animal Biotechnology: Concepts and Applications, 07/2019: pages 133 -147; Elsevier. ISBN: 9780128188231.

भारतीय प्रौद्योगिकी संस्थान गुवाहाटी • Indian Institute of Technology Guwahati •

TH-2627_166106107

List of conferences

1. **Ashutosh Kumar**, Kuldeep Mahato, Buddhadev Purohit, Monalisha Ghosh Dastidar, Sharmili Roy, Vikash Kumar Dubey, Pranjal Chandra *. Designing potent metal nanoparticles against parasite causing human infectious disease at Recent Advancements in Biochemical Engineering and Biotechnology (RABEB-2019), Indian Institute of Technology (BHU) Varanasi on 15-16th March 2019. Page number: 90-91.

2. **Ashutosh Kumar,** Buddhadev Purohit, Kuldeep Mahato, Sharmili Roy Majumdar, Ananya Srivastava, Pranjal Chandra*. A Novel Sensor for Label Free Detection of Sinapic Acid Based on Electrochemically Tuned Gold Nanoparticles and Reduced Graphene Oxide Nanocomposite at International Conferencen of Nanomaterials and Nanotechnology (ICANN), Indian Institute of Technology Guwahati on 18-21 December 2019. Page number: K1240

3. Buddhadev Purohit, Kuldeep Mahato, **Ashutosh Kumar**, Monalisha Ghosh Dastidar, Sharmili Roy, Pranjal Chandra *. Design of engineered dendritic nanochip for electrochemical characterisation of biologically important small molecules at Recent advancements in biochemical engineering and biotechnology (RABEB-2019), Indian Institute of Technology (BHU) Varanasi on 15-16th March 2019. Page number: 97-98.

4. Sharmili Roy, Monalisha Ghosh Dastidar, Buddhadev Purohit, **Ashutosh Kumar,** Kuldeep Mahato, Shrikrishnan N Joshi, Pranjal Chandra *. Design of chitosan-metal sheet based engineered nanocomposites matrix for bacterial preservation at Recent advancements in biochemical engineering and biotechnology (RABEB-2019), Indian Institute of Technology (BHU) Varanasi on 15-16th March 2019. Page number: 93-94.

5. Monalisha Ghosh Dastidar, **Ashutosh Kumar,** Kuldeep Mahato, Buddhadev Purohit, Sharmili Roy, Lalit M Pandey, Pranjal Chandra*. Design of metallic nanoparticle-conducting monomer nanocomposites for their bioelectronic properties at Recent Advancements in Biochemical Engineering and Biotechnology (RABEB-2019), Indian Institute of Technology (BHU) Varanasi on 15-16th March 2019. Page number: 95-96.

TH-2627_166106107

List of media coverages

1. Vigyan Prasar, Government of India
http://www.vigyanprasar.gov.in/isw/Nano-chip-made-from-laboratory-waste-can-help-in-diagnosis-of-diseases.html

2. The Hindu Business Line
https://www.thehindubusinessline.com/news/science/nano-chip-made-from-laboratory-waste-can-help-in-diagnosis-of-diseases/article29331811.ece

3. Biotecnika Times
https://www.biotecnika.org/2019/09/indian-scientists-develop-nano-chip-from-laboratory-waste-to-diagnose-diseases/

4. Down to Earth
https://www.downtoearth.org.in/news/health/nano-chip-made-from-laboratory-waste-can-help-in-diagnosis-of-diseases-66527

5. Newsroom
https://newsroom24x7.com/2019/09/04/nano-chip-made-from-laboratory-waste-can-help-in-diagnosis-of-diseases/

6. Sputnik News
https://sputniknews.com/society/201909061076737012-indian-scientists-fabricate-nano-chip-made-from-lab-waste-for-diagnosis-of-diseases/

7. The India Saga/ Daily hunt News
https://m.dailyhunt.in/news/india/english/the+india+saga-epaper-indsaga/iit+guwahati+scientists+reused+laboratory+waste+to+design+nanosensor-newsid-136393186

8. Research stash News
https://www.researchstash.com/2018/07/16/popular-vegetable-can-help-prepare-a-cure-for-kala-azar/

9. Biotech times News
https://biotechtimes.org/2018/07/16/popular-vegetable-can-help-prepare-a-cure-for-kala-azar/

10. The Hindu Business line News
https://www.thehindubusinessline.com/news/science/popular-vegetable-can-help-prepare-a-cure-for-kala-azar/article24433753.ece

Media highlights of anti-leishmaniasis nanotherapeutic paper

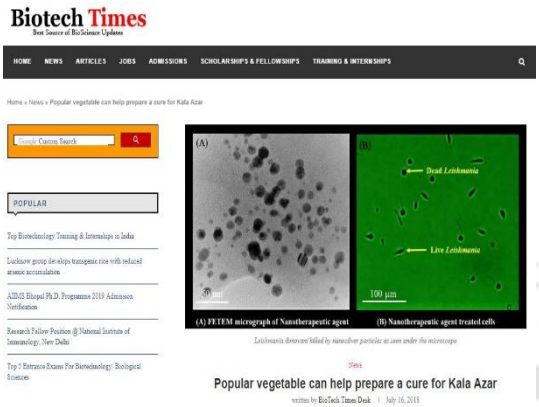

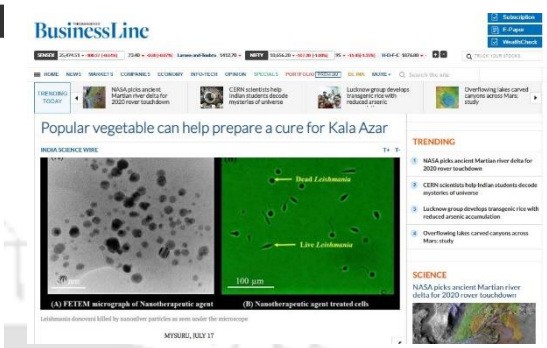

Media highlights of hydrogen peroxide paper

Review

Wiley Online Library

ELECTROANALYSIS

DOI: 10.1002/elan.201900216

Engineered Nanomaterial Assisted Signal-amplification Strategies for Enhancing Analytical Performance of Electrochemical Biosensors

Ashutosh Kumar,[a, b] Buddhadev Purohit,[a, b] Pawan Kumar Maurya,[c] Lalit Mohan Pandey,[b] and Pranjal Chandra*[a, b]

Abstract: The design and development of modern biosensors for sensitive and selective detection of various biomarkers is important in diversified arenas including healthcare, environment, and food industries *etc.* The requirement of more robust and reliant biosensors lead to the development of various sensing modules. The nanomaterials having specific optical, electrical, and mechanical strength can pave the way towards development of ultrafast, robust, and miniaturized modules for biosensors. It can provide not only the point-of-care applicability but also has tremendous commercial as well as industrial justification. In order to improve the performance of the sensor systems, various nanostructure materials have been readily studied and applied for development of novel biosensors. In the last few years, researchers are engaged on harnessing the unique atomic and molecular properties of advance-engineered materials including carbon nanotubes, graphene nanosheets, metal nanoparticles, metal oxide nanoparticles, and their nano-conjugates. In view of such recent developments in nanomaterial engineering, the current review has been formulated emphasizing the role of these materials in surface engineering, biomolecule conjugation, and signal amplification for development of various ultrasensitive and robust biosensors having commercial as well as industrial viability. Attention is given on the electrochemical biosensors incorporating various nanomaterials and their conjugates. Importance of nanomaterials in the analytical performance of the various biosensor has also been discussed. To put a perceptive insights on the importance of various nanomaterials, an extended table is incorporated, which includes probe design, analyte, LOD, and dynamic range of various electrochemical biosensors.

Keywords: Biosensors · Electrochemistry · Nanoengineering · Nanomaterials · Signal amplification

1 Introduction

Early diagnosis of any disease is extremely important and is of interest to all individuals globally [1]. Among all type of biomedical instruments, biosensors are considered very effective for disease diagnosis due to its robustness, small size, user-friendly operation, and ability to be a tool for personalized diagnosis [2–4]. The biosensor is an analytical device that uses different biochemical reactions facilitated by enzymes, antibodies, cell-organelles, and proteins to detect the physiological changes in the form of quantifiable electrical/optical/thermal signals [5,6]. In general, its main constituents comprise of bio-receptor element, transducer, amplifier, and processor with output display [7]. The mechanism of sensing involves the process where target analyte encounters bio-receptor element, a stimulus is generated and transducer transforms it into a decipherable signal, which is further enhanced by amplifier and processor in the form of an output signal [8]. The major benefits of biosensor that make them superseding over conventional lab-based detection techniques are; requirement of very little sample, miniaturization ability, as well as the robustness that prevalently make them more appropriate for commercial acclamation [9]. Recently, modern biosensing devices are escalating their horizon by confronting multitudinous medical complications for providing accurate and selective diagnosis. In spite of the tremendous promise of biosensors in biomolecular analysis, they sometime suffer due to high limit of detection (LOD), less sensitivity, narrow dynamic range, and short shelf life, which limits their applications in commercial perspective. To address these limitations, several works have been done towards development of advance engineered nanomaterials (NM) and their com-

[a] A. Kumar, B. Purohit, P. Chandra
Laboratory of bio-physio sensors and nanobioengineering, Department of Biosciences and Bioengineering, Indian Institute of Technology Guwahati, Guwahati, 781039, Assam, India
Tel. (Off.): +91(0)-361-258-3207/(Lab): +91(0)-361-258-3218
Fax: +91(0)-361-258-2249
E-mail: pchandra13@iitg.ac.in
[b] A. Kumar, B. Purohit, L. M. Pandey, P. Chandra
Department of Biosciences and Bioengineering, Indian Institute of Technology Guwahati, Guwahati, 781039, Assam, India
[c] P. K. Maurya
Department of Biochemistry, Central University of Haryana, Mahendragarh, 123031, Haryana, India

© 2019 Wiley-VCH Verlag GmbH & Co. KGaA, Weinheim

TH-2627_166100107

Full Paper

Wiley Online Library

ELECTROANALYSIS

DOI: 10.1002/elan.201900406

Design and Development of Ultrafast Sinapic Acid Sensor Based on Electrochemically Nanotuned Gold Nanoparticles and Solvothermally Reduced Graphene Oxide

Ashutosh Kumar,[a] Buddhadev Purohit,[a] Kuldeep Mahato,[a] Sharmili Roy,[a] Ananya Srivastava,[b] and Pranjal Chandra*[a]

Abstract: We report for the first time sinapic acid (SA) sensing based on nanocomposite comprising electrochemically tuned gold nanoparticles (EAuNPs) and solvothermally reduced graphene oxide (rGO). The synthesized EAuNPs, rGO, and EAuNPs-rGO nanocomposite were characterized using X-ray diffraction (XRD), transmission electron microscopy (TEM), selected area electron diffraction (SAED), particle size analysis, and Raman spectroscopy. A proof-of-concept electrochemical sensor for SA was developed based on synthesized EAuNPs-rGO nanocomposite, which was characterized by electrochemical techniques such as cyclic voltammetry (CV) and electrochemical impedance spectroscopy (EIS). The developed sensor detected SA with a linear dynamic range (LDR) between 20 μM and 200 μM and detection limit (DL) of 33.43 (±0.21) nM (RSD < 3.32 %). To show the useful purpose of the sensor probe in clinical applications, SA was detected in human urine samples, which showed the percentage recovery between 82.6 % and 92.8 %. Interferences due to various molecules such as L-cystine, glycine, alanine, serum albumin, uric acid, citric acid, ascorbic acid, and urea were tested. Long-term stability of the sensor probe was examined, which was found to be stable up to 6 weeks. The sensor fabricated using EAuNPs-rGO nanocomposite has many attractive features such as; simplicity, rapidity, and label-free detection; hence, it could be a method of choice for SA detection in various matrices.

Keywords: Nanotuning · gold nanoparticles · sinapic acid · rGO · electrochemical sensor

1 Introduction

Nowadays, replacing the nutritional supplements with natural food has attracted researchers to investigate the levels of chemicals/biochemicals in fruits, vegetables, and other agricultural resources along with various supplementary drugs having health benefits. Among various nutritional supplements, SA has gained huge interest in human health due to its excellent antioxidant activity. SA majorly found in rapeseed, red wine, coffee, tea leaves, various kinds of citrus fruits including lemon and Indian gooseberry, canola oil, vegetables, whole grains or cereals, etc. [1,2]. It has been reported that SA could be considered as a preservative of cosmetics, pharmaceuticals, and various foods [3]. Moreover, numerous studies have also been reported about the useful applications of SA as therapeutic agents in various oxidative stress related diseases like depression, inflammation, and atherosclerosis. Even in cancer diagnosis, levels of SA provides better understandings about the disease diagnosis and prognosis [4]. Furthermore, a low level of SA in body fluids is also related to human behavior such as depression, anxiety, and neurological disorders viz. Alzheimer's and Parkinson's disease [5]. This clearly shows the importance of the SA in food as well as in various clinical conditions. In view of such importance, several analytical methods have been developed for its detection in diverse samples. Conventionally, SA has been detected using high-pressure liquid chromatography (HPLC), liquid chromatography – mass spectrometry (LC-MS), and gas chromatography-mass spectrometry (GC-MS) techniques [6,7]. These techniques are extremely powerful and provide reliable detection of SA, but they are complicated, tedious, less sensitive, require bulky instruments, expensive reagents, and involve multiple steps; hence not appropriate for quick onsite analysis of SA. It is, therefore, desirable to develop a facile, robust, sensitive, selective, and economically feasible method for SA detection that can be operated on-site. SA has a unique chemical structure composed of various functional groups that can be oxidized/reduced at a certain electrode

[a] A. Kumar, B. Purohit, K. Mahato, S. Roy, P. Chandra
Laboratory of Bio-physio Sensors and Nanobioengineering, Department of Biosciences and Bioengineering, Indian Institute of Technology Guwahati, Guwahati, 781039, Assam, India
E-mail: pchandra13@iitg.ac.in
[b] A. Srivastava
Department of Pharmacology and Toxicology, NIPER Guwahati, Guwahati, 781125, Assam, India

© 2019 Wiley-VCH Verlag GmbH & Co. KGaA, Weinheim

TH-2627_166106107

Full Paper

Wiley Online Library

ELECTROANALYSIS

DOI: 10.1002/elan.201900337

Gold-Iron Bimetallic Nanoparticles Impregnated Reduced Graphene Oxide Based Nanosensor for Label-free Detection of Biomarker Related to Non-alcoholic Fatty Liver Disease

Ashutosh Kumar,[a] Buddhadev Purohit,[a] Kuldeep Mahato,[a] Riddhipratim Mandal,[a] Ananya Srivastava,[b] and Pranjal Chandra*[a]

Abstract: We report for the first time a microwave assisted, one pot, direct, and facile synthesis of monodispersed iron-gold bimetallic nanoparticles ($BNP_{Au\text{-}Fe}$) using glucose as a reducing agent in merely 90 s. The as such synthesized $BNP_{Au\text{-}Fe}$ were thoroughly characterized using UV-Vis, XRD, TEM, EDX, elemental mapping, and raman spectroscopy. These $BNP_{Au\text{-}Fe}$ were further impregnated with reduced graphene oxide (rGO) and coated onto glassy carbon electrode (GCE) to develop a sensor probe for label free electrochemical detection of acetaminophen, which is considered to be a most potent biomarker related to non-alcoholic fatty liver disease. The sensor probe was systematically characterized by cyclic voltammetry (CV) and electrochemical impedance spectroscopy (EIS). The $BNP_{Au\text{-}Fe}$-rGO nanocomposite matrix showed the sensing of acetaminophen with a wide dynamic range between 50 and 800 nM with detection limit (DL) of 0.14 nM (±0.05) nM (RSD < 4.12 %) that was lower compared to previously reported acetaminophen sensors. To show the practical application of the sensor probe, acetaminophen was detected in human urine samples, which showed the percentage recovery between 86.65 % and 91.32 %. To the best of our knowledge, this is the first report where $BNP_{Au\text{-}Fe}$ impregnated rGO was used to detect acetaminophen. Interferences due to various molecules such as glucose, serum albumin, glycine, glutamic acid, alanine, citric acid, and ascorbic acid were tested individually and in mixed sample. Long-term stability of sensor probe was examined which was found to be stable up to 12 weeks. The sensor fabricated using $BNP_{Au\text{-}Fe}$-rGO nanocomposite has many attractive features such as; simplicity, rapidity, and label free detection, hence it could be a method of choice for acetaminophen detection in clinical settings.

Keywords: Bimetallic nanoparticles · rGO · Electrochemistry · Nanosensor · Acetaminophen · Liver disease · Urine

1 Introduction

Over the last few decades, the amalgamation of nanosciences and biotechnology has had a significant impact on biomedical applications, including bio- imaging, biosensing, and targeted drug delivery [1–3]. Recent advancements in application of nanomaterials (NM) in interdisciplinary research diaspora has transformed the paradigm of sensing of analytes of biological importance due to their exceptional optoelectronic properties [4–6]. Moreover, it has been perceived that chemical structure, active surface area, surface charge, quality of crystal structure and orientation of crystal in nanoparticles, *etc.*[7–10] cumulatively effect electron transfer in electrochemical sensors [6]. To accomplish the accurate sensing; they are progressively being engaged in development of modern sensors because of their unique electro-catalytic behaviour [11,12]. The synthesis of advanced engineered NM and their composites for the faster electron transfer at the transducing surface can pave a new dimension in the designing of enhanced modern sensors [13–15]. Among various engineered NM, mono-metallic *viz.* gold, silver, and platinum, are comprehensively considered as potent matrix materials that have been utilized to design many electrochemical sensors [16]. Recently, there has been increase in the researches on the development of NM having two or more than two metals to get the synergistic properties of constituent elements [17]. Bimetallic nanoparticles particularly of iron and gold ($BNP_{Au\text{-}Fe}$) has been widely synthesized which require several complex synthetic procedures. There are number of reports on the

[a] A. Kumar, B. Purohit, K. Mahato, R. Mandal, P. Chandra
Laboratory of Bio-Physio Sensors and Nanobioengineering, Department of Bioscience and Bioengineering, Indian Institute of Technology Guwahati, Guwahati-781039, Assam, India
Fax: +91361-258-2249
Phone: +91361-2583207
E-mail: pchandra13@iitg.ac.in
pranjalmicro13@gmail.com
[b] A. Srivastava
Department of Pharmacology and Toxicology, NIPER Guwahati, Guwahati-781125, Assam, India

Supporting information for this article is available on the WWW under https://doi.org/10.1002/elan.201900337

© 2019 Wiley-VCH Verlag GmbH & Co. KGaA, Weinheim

TH-2627_166106107

Materials Science for Energy Technologies 1 (2018) 38–48

Contents lists available at ScienceDirect

Materials Science for Energy Technologies

journal homepage: www.keaipublishing.com/en/journals/materials-science-for-energy-technologies

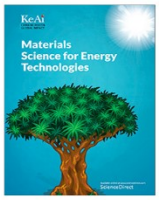

Nanoengineered material based biosensing electrodes for enzymatic biofuel cells applications

Ashutosh Kumar, Swati Sharma, Lalit Mohan Pandey *, Pranjal Chandra *

Department of Bioscience and Bioengineering, Indian Institute of Technology Guwahati, Guwahati, Assam 781039, India

ARTICLE INFO

Article history:
Received 12 March 2018
Revised 9 April 2018
Accepted 9 April 2018
Available online 2 May 2018

Keywords:
Biosensing electrodes
Glucose biofuel cells
Nano materials
Nanotubes
Graphene
Conducting polymers

ABSTRACT

In the last few decades, biofuel cells have been explored extensively as an emerging technology and achieved the status of critical research endeavours among the intellectual communities working on power crisis across the world. The researchers around the globe are concentrating on harnessing the unique atomic and molecular properties of advance engineered materials, including nanotubes, nanosheets, nanoparticles and conducting polymers, on account of their capability to aid in the generation of efficient electricity from biological substrates using numerous biocatalysts. Because of the enhancement of nanotechnology, substantial milestones have been achieved in the realm of the biofuel cell, even though it is still challenging to uphold the performance of these cells. Implementation of nano materials and conducting polymers for biofuel cell assembly has been widely anticipated as an effective and capable approach to attain high power generation. In this review, we have documented the relevant and exciting methodologies used in the development of the enzyme based biofuel cells (EBC), focused on glucose as biofuel, using different nano materials utilized for EBC and emphasized the revolutions in this field. Every aspect of biofuel cell system including the fundamentals, charge transfer as well as the role of nano materials and conducting polymers in matrix development of electrode materials and its fabrication has been elucidated. To summarize the latest trend an extensive table has been incorporated including bio-sensing electrode, the enzymatic system mediator and output power density.
© 2018 The Authors. Production and hosting by Elsevier B.V. on behalf of KeAi Communications Co., Ltd. This is an open access article under the CC BY-NC-ND license (http://creativecommons.org/licenses/by-nc-nd/4.0/).

Contents

* Corresponding authors.
E-mail addresses: lalitpandey@iitg.ernet.in (L.M. Pandey), pchandra13@iitg.ernet.in (P. Chandra).

https://doi.org/10.1016/j.mset.2018.04.001
2589-2991/© 2018 The Authors. Production and hosting by Elsevier B.V. on behalf of KeAi Communications Co., Ltd.
This is an open access article under the CC BY-NC-ND license (http://creativecommons.org/licenses/by-nc-nd/4.0/).

TH-2627_166106107

Biography

Ashutosh Kumar is currently a research scholar at the Laboratory of Bio-Physio Sensors and Nano-bioengineering, Department of Biosciences and Bioengineering, Indian Institute of Technology Guwahati, India. He hails from Siwan, Bihar. He holds a degree of Integrated Masters of Technology (M.Tech.) in Nanotechnology from Central University of Jharkhand, Ranchi, India 835205.

He has qualified in GATE 2017 with the percentile of 95+. He was selected for prestigious Summer Research Fellowship from Indian Academy of Sciences, Banglore. After M. Tech, he joined Indian Institute of Technology Guwahati for his doctoral studies under the supervision of Dr. Pranjal Chandra, Professor (Assist.) and Ramanujan Fellow. His research work is centered at the development of nano-biosensors based on metal and metal oxides nanocomposites. During his PhD tenure, he has published more than 25 high impact articles in various Journals including Biosensors and Bioelectronics, Journal of Biological Macromolecules, Electroanalysis, Scientific Reports, Current Opinion in Biomedical Engineering, Microchimica Acta, 3-Biotech etc. He is also an invited reviewer of prestigious scientific journals such as Material Science and Energy Technology, Elsevier, Sensors International, Elsevier, etc.

Contact:

S/O Sri M. M. Pandey
Pandey Bhawan
Siwan
Email: akpandeyiitg@gmail.com
Phone: +917638038121